



TECHNISCHE
UNIVERSITÄT
DARMSTADT

**Microfluidic systems based on electroactive polymers
technology**

**at the Electrical Engineering
and
Information Technology Faculty**

of the Technischen Universität Darmstadt

submitted in fulfilment of the requirements for the
degree of Doktor-Ingenieurs (Dr.-Ing.)

Doctoral thesis by

Susana Solano Arana (M.Sc.)

First assessor: Prof. Ph.D. Thomas P. Burg

Second assessor: Prof. Ph.D. Herbert Shea

Darmstadt 2022 (year of the viva voce)

Solano Arana, Susana: Microfluidic systems based on electroactive
polymers technology

Darmstadt, Technische Universität Darmstadt,

Thesis published in TUpriints in 2023

urn: nbn:de:tuda-tuprints-240442

Date of the viva voce 12.10.2022

Published under CC BY-SA 4.0 International

<https://creativecommons.org/licenses/>

ERKLÄRUNGEN LAUT PROMOTIONSORDNUNG

§ 8 Abs. 1 lit. c PromO

Ich versichere hiermit, dass die elektronische Version meiner Dissertation mit der schriftlichen Version übereinstimmt.

§ 8 Abs. 1 lit. d PromO

Ich versichere hiermit, dass zu einem vorherigen Zeitpunkt noch keine Promotion versucht wurde. In diesem Fall sind nähere Angaben über Zeitpunkt, Hochschule, Dissertationsthema und Ergebnis dieses Versuchs mitzuteilen.

§ 9 Abs. 1 PromO

Ich versichere hiermit, dass die vorliegende Dissertation selbstständig und nur unter Verwendung der angegebenen Quellen verfasst wurde.

§ 9 Abs. 2 PromO

Die Arbeit hat bisher noch nicht zu Prüfungszwecken gedient.

Darmstadt, den 28.06.2022 (Tag der Einreichung)

(Susana Solano Arana)

ACKNOWLEDGEMENT

I would like first to express my most sincere gratitude to Prof. Dr.-Ing. Helmut F. Schlaak, who allowed my employment at the Department of Microtechnology and Electromechanical Systems (MEMS) through the Marie Curie Project MICACT. His expertise was invaluable in formulating the research questions and methodology. Prof. Dr.-Ing. Helmut F. Schlaak was committed to my work with all his strengths until the end and for so I will always have him in a special part of my memory.

I would like to acknowledge my colleagues from my secondment in the LMTS: Soft Transducers group in EPFL for their wonderful collaboration, specially to Dr. Samuel Rosset, Dr. Alexandre Poulin and Dr. Samuel Schlatter. I felt very integrated in the group from the very beginning of my stayed. I would particularly like to single out my supervisor, Prof. Ph.D. Herbert Shea. I want to deeply thank you for your patient support and for all of the opportunities I was given to further my research.

Words cannot express my gratitude to Prof. Ph.D. Thomas P. Burg for inspiring my interest in the development of innovative technologies and new projects. Thanks for allowing my employment in the IMNS group and for letting me join the group. I am also thankful to my IMNS colleagues for the nice time we have spent together.

This work would not have been possible without the help and support of my MEMS group colleagues. Special thanks to the EAP colleagues Florentine Förster-Zügel, Florian Klug and Holger Mößinger. Your insightful feedback pushed me to sharpen my thinking and brought my work to a higher level. Many thanks to our technical assistant, Bernhard Jochem and to our dear Ms Matt, your help and assistance was essential for the technical aspects of this thesis and the emotional support was indispensable for the continuation of this work.

Thanks should also go to the dream team, Johannes Bieker, Christian Nakic and Sarah Wicker. I could not have undertaken this journey without our coffee pauses and dancing classes together. I really enjoyed each second.

Most importantly, none of this could have happened without my family and friends. My parents and brothers, who offered their encouragement via our videocalls on Sundays. This gave me the strength to fight against the research issues during the week. Your belief in me has kept my spirits and motivation high during this process.

Finally, I would like to specially dedicate this work to Blanco. Giving up was not an option being by your side. Your day by day love and invaluable support have allowed me to push this work until the end.



ABSTRACT

Dielectric elastomer actuators (DEAs) have been widely investigated for more than 30 years. Lately, several fabrication methods have successfully allowed the creation of very thin elastomer and electrode layers. The development of attractive applications, in which DEAs offer advantages over conventional technologies, is thus necessary for the advance of the technology. In this work, new biocompatible microfluidic devices based on DEAs are developed.

In the first part of this thesis, several prototypes of peristaltic pumps of single layer dielectric elastomer actuators are designed, manufactured and characterized. Although these prototypes were not able to produce fluid flow, novel insights into the capabilities of Electroactive Polymer technology were gained.

In the second part of this work, a pumping micromixer as a novel application of dielectric elastomer stacked actuators is manufactured. The pumping micromixer is based on peristaltic movements, which gently act as a mixer and a pump for microfluidics. Experimental data show a maximal flow rate of 21.5 $\mu\text{L}/\text{min}$ at 10 Hz. Image analysis at the outlet proves a 50/50 mixing when all actuators are functioning at the same pace and voltage.

The performance of the pumping micromixer is further studied with the Finite Element Method, using the COMSOL Multiphysics[®] software. Simulations demonstrate the versatility of the pumping characteristics of such a microdevice, from very few $\mu\text{L}/\text{min}$ to mL/min, and from a very low pressure in the range of Pa to hundreds of kPa, by only changing the duty cycle, phase shift and actuation frequency.

KURZFASSUNG

Dielektrische Elastomeraktoren (DEAs) werden seit mehr als 30 Jahren intensiv untersucht. In letzter Zeit ist es durch neue Herstellungsverfahren gelungen, sehr dünne Elastomer- und Elektroden-schichten zu erzeugen. Die Entwicklung attraktiver Anwendungen, in denen DEAs Vorteile gegenüber konventionellen Technologien bieten, ist daher für die Weiterentwicklung der Technologie notwendig. In dieser Arbeit werden neue biokompatible mikrofluidische Systeme auf der Basis von DEA entwickelt.

Im ersten Teil dieser Arbeit werden mehrere Prototypen von peristaltischen Pumpen aus einlagigen dielektrischen Elastomeraktoren entworfen, hergestellt und charakterisiert. Obwohl die hergestellten Prototypen keine Pumpleistung erzielen konnten hiermit neue Erkenntnisse über die Möglichkeiten der EAP-Technologie gewonnen wurden.

Der zweite Teil der Arbeit befasst sich mit der Herstellung und Charakterisierung einer Mikropumpe mit Mischer als neuartige Anwendung von dielektrischen Elastomer-Stapelaktoren. Dieses neue System basiert auf peristaltischen Bewegungen, die für das schonende Pumpen und Mischen in der Mikrofluidik geeignet sind. Experimentell ermittelte Daten zeigen eine maximale Flussrate von 21,5 $\mu\text{l}/\text{min}$ bei 10 Hz. Die Bildanalyse am Auslass des Mixers beweist eine 50/50 Mischung, wenn alle Aktoren mit der gleichen Geschwindigkeit und Spannung arbeiten.

Die Leistung des pumpenden Mikromischers wurde mit der Finite-Elemente-Methode unter Verwendung der COMSOL Multiphysics[®] Software weiter untersucht. Die Simulationen zeigen die Vielseitigkeit der Pumpeigenschaften eines solchen Mikrogeräts mit einem Durchfluss im Bereich von sehr wenigen $\mu\text{l}/\text{min}$ bis zu einigen ml/min und einem Druck im Bereich von wenigen Pa bis zu Hunderten von kPa, indem nur das Tastverhältnis, die Phasenverschiebung und/oder die Betätigungsfrequenz der einzelnen Aktoren geändert werden.

LIST OF CONTENTS

ACKNOWLEDGEMENT	III
ABSTRACT	V
KURZFASSUNG	VI
LIST OF ABBREVIATIONS.....	1
LIST OF SYMBOLS	3
1. INTRODUCTION TO ELECTROACTIVE POLYMERS TECHNOLOGY	7
1.1. Fundamentals of Electroactive Polymers	7
1.2. Materials in Electroactive Polymers	9
1.2.1. Dielectric	9
1.2.2. Electrodes.....	17
1.3. Lifetime of actuators	18
1.4. Comparison to other technologies	19
1.5. Applications of Electroactive Polymers	20
1.6. Motivation to use Electroactive Polymers in microfluidics	21
1.7. Content and structure of this work	22
2. PERISTALTIC MICROPUMPS.....	25
2.1. Fundamentals of microfluidic pumps	26
2.2. Types of micropumps	28
2.2.1. Non-mechanical micropumps	28
2.2.2. Mechanical micropumps	29
2.3. Single-layer peristaltic pump – type 1 liquid film	33
2.3.1. Working principle	34
2.3.2. Analytical model.....	36
2.3.3. DEA fabrication - liquid film method.....	39
2.3.4. Characterization	41
2.4. Single-layer peristaltic pump – type 1 solid film.....	51
2.4.1. DEA fabrication - solid film method	51
2.4.2. Characterization	54
2.5. Single-layer peristaltic pump – type 2 solid film.....	57
2.5.1. Working principle	58
2.5.2. Analytical model.....	59
2.5.3. Geometry and fabrication	60
2.5.4. Characterization	61
2.6. Conclusions and discussion	65
3. CONCEPT OF A PUMPING MICROMIXER.....	70
3.1. Fundamentals of micromixers	70
3.1.1. Classification of micromixers	72

3.1.2.	Pumping micromixers	79
3.2.	Concept of a DEA micromixer	80
3.2.1.	Geometry	81
3.2.2.	Materials	82
3.2.3.	Working principle	84
4.	FABRICATION OF A PUMPING MICROMIXER	87
4.1.	Fabrication of dielectric stacked actuators.....	87
4.1.1.	Fundamentals of Dielectric Stacked Actuators	87
4.1.2.	Fabrication technique for DESA	89
4.1.3.	Fabrication of a pumping micromixer	93
4.1.4.	Micromixer connections	95
4.2.	Characterization	97
4.2.1.	Characterization of the layer thickness.....	97
4.2.2.	Characterization of the electrical connection	98
4.2.3.	Deformation of the layers	99
4.3.	Experimental results of pumping micromixer	102
4.3.1.	Flow rate	102
4.3.2.	Mixing of fluids.....	106
4.4.	Improved pumping designs and outlook.....	112
4.4.1.	Encapsulated micromixer.....	112
4.4.2.	T-type pumping micromixer.....	114
4.4.3.	Array of microfluidic mixers	116
4.5.	Applications	117
4.5.1.	Limitations of the micromixer	117
4.6.	Conclusion	118
5.	SIMULATIONS WITH THE PUMPING MICROMIXER	121
5.1.	Displacement versus electric field	121
5.1.1.	Modules and parameters	122
5.1.2.	Displacement results.....	123
5.2.	Fluid dynamic characterization.....	125
5.2.1.	Solid mechanics module.....	126
5.2.2.	Laminar flow module	128
5.2.3.	Fluid-structure interaction	129
5.2.4.	Definition of mesh.....	129
5.2.5.	Results	131
5.3.	Conclusion	143
6.	SUMMARY AND CONCLUSIONS.....	147
6.1.	Micropump prototypes	147
6.2.	Pumping micromixer	149
	REFERENCES	154
	LIST OF PUBLICATIONS	170

A.	APPENDIX - TRANSPORT PHENOMENA IN MICROFLUIDICS	173
	Conservation of mass	173
	Conservation of momentum	173
	Conservation of energy	175
B.	APPENDIX - TRANSPORT PHENOMENA IN MICROMIXERS	177
C.	APPENDIX - LIQUID FILM FABRICATION METHOD	181
	LIST OF FIGURES	187
	LIST OF TABLES	194



LIST OF ABBREVIATIONS

Abbreviation	Meaning	Page ¹
DEA	Dielectric Elastomer Actuator	v
EAP	Electroactive Polymer	1
PDMS	Polydimethylsiloxane	8
PMMA	Poly(Methacrylic Acid Methyl Ester)	9
VHB	Very High Bond	9
DBP	Dibutyl Phthalate	10
TPP	Triphenyl Phosphate	10
PEG	Polyethylene Glycol	10
NERD	Novel Electrode Resistance Degradation	19
EAC	Electroactive Ceramics	20
SMA	Shape Memory Alloys	20
EM	Electromagnetic	20
DEG	Dielectric Elastomer Generators	21
EPFL	École Polytechnique Fédérale de Lausanne	34
EHD	Electro Hydro-Dynamic	28
PET	Polyethylene Terephthalate	40
RTV	Room Temperature Vulcanizing	43
LDPE	Low-Density Polyethylene Polymer	53
PZT	Lead Zirconate Titanate or Pb(Zrti)	80
DESA	Dielectric Elastomer Stacked Actuator	81
SWCNT	Single-Wall Carbon Nanotubes	85
MWCNT	Multi-Wall Carbon Nanotubes	85
PLA	Polylactic Acid	97
CCD	Charge-Coupled Device	107
CMOS	Complementary Metal Oxide Semiconductor	107
RGB	Red-Green-Blue	108
PAA	Polyacrylic Acid	183
PVA	Polyvinil Alcohol	185

¹ Page on which each one is first used and defined.



LIST OF SYMBOLS

Symbol	Meaning
ΔA	Change in area of the actuator
Δz	Change in thickness of the actuator
A_0	Initial area of the actuator
z_0	Initial thickness of the actuator
V	Applied voltage
p	Maxwell pressure
ε_0	Permittivity of free space
ε_r	Permittivity of the dielectric
E	Electric field
S_a	Active strain
Y	Young's Modulus
F	Applied force
k	Spring constant or constant of proportionality
L	Total length of the probe
L_0	Initial length of the probe
W_s	Total energy density
W_{iso}	Isochoric strain energy density
W_{vol}	Volumetric strain energy density
S	Second Piola-Kirchhoff stress tensor
p_p	Volumetric stress
C	Right Cauchy-Green tensor
J	Volume ratio
V_d	Deformed volume
V_0	Initial volume
\bar{I}_1, \bar{I}_2	Invariants of the isochoric right Cauchy-Green tensor

λ	Stretch ratio
L_d	Deformed length of the probe
\hat{N}_a	Principal referential directions
\bar{C}	Modified right Cauchy-Green stretch tensor
P	First Piola-Kirchhoff stress tensor
σ	Cauchy stress tensor
C_{pq}	Fitting parameters in the Mooney-Rivlin model
D_m	Constant related to the volumetric response
$C_{10}, C_{01}, C_{20}, C_{02}, C_{11}$	Mooney-Rivlin's five parameters
μ	Shear modulus
I_m	Material constant in the Gent model
C_v	Specific heat capacity
σ_{ce}	Electrical conductivity
K_t	Thermal conductivity
ε_r''	Imaginary part of the complex permittivity
Re	Reynolds number
ρ	Density of the fluid
v	Velocity of the fluid
D	Diameter of the channel
μ_d	Dynamic viscosity of the fluid
D_e	Equivalent diameter of a rectangular tube
a	Length of the major side of the rectangular section
b	Length of the minor side of the rectangular section
λ_{1a}	Stretch after actuation in direction 1
λ_{2a}	Stretch after actuation in direction 2
λ_{1ps}	Prestretch in direction 1
λ_{2ps}	Prestretch in direction 2
r_a	Active ratio
E_{bd}	Electrical breakdown field
R_s	Series resistance

U	Operating voltage
Z	Electrical impedance
G_p	Conductivity of the dielectric
d	Distance between plates in a capacitor
$\Delta\varphi$	Phase shift
D	Duty cycle
f	Actuation frequency
V_T	Terminal electrodes voltage
V_G	Ground electrodes voltage
ν	Poisson's ratio
Q	Maximum flow rate
\dot{V}	Volumetric flow rate
v	Velocity vector
s	Boundary coordinate
n	Outward-pointing unit normal to the boundary
ΔP	Back pressure
g	Gravity constant
β	Thermal expansion
c	Concentration of species
D	diffusivity
r_g	Generation rate of the species per volume
k_B	Boltzmann constant
σ_p	Radius of the particle p



1. INTRODUCTION TO ELECTROACTIVE POLYMERS TECHNOLOGY

Polymers are flexible, light-weighted, and easy to handle and to fabricate at a large scale with a high quality. Some polymers respond to a stimulus by changing their mechanical properties. This increases their versatility in multiple fields. Applying magnetic fields, electric fields, chemical, pneumatic, optic or temperature changes have been reported to cause a change in shape or size in certain polymers.

The polymers deformation caused by an electric field is one of the most employed methods. Some examples of polymers, which react when voltage is applied to the material, are piezoelectric polymers, electrostrictive polymers and dielectric polymers.

Piezoelectric and electrostrictive polymers have, at the elementary domain scale, a permanent dipole moment. Piezoelectric polymers have a linear dependence between the stress and the electric field, while electrostrictive polymers have a quadratic dependence.

Electroactive polymers, which are the materials used in this work, were discovered at the beginning of the 1990s by Ronald E. Pelrine and Roy D. Kornbluth [1] [2] [3]. Not only can these polymers deform mechanically while an electric field is applied, but they also provide an electric signal when a deformation is performed on the material. This property is very interesting in terms of reversibility. They can work as actuators, as sensors and as generators. They have a huge range of applications, some of which are: robotics and artificial muscles, optical systems, drug delivery and energy harvesting applications.

This chapter is devoted to the fundamentals, material properties and main applications of electroactive polymers.

1.1. FUNDAMENTALS OF ELECTROACTIVE POLYMERS

As mentioned in the previous section, electroactive polymers (EAPs) are a type of electro stimulated materials that deform when an electric field is applied. Electroactive polymers can be divided into two main types: dielectric EAPs, in which the deformation of the material is induced by coulombic or electrostatic forces between two electrodes; and ionic EAPs, in which the deformation is obtained due to the migration of free ions caused by an electric field. In the present work, the focus is on the dielectric EAPs and their properties. Only dielectric EAPs are relevant in the present work and will be described in this section.

A dielectric elastomer actuator (DEA) consists of an elastic dielectric sandwiched between two compliant electrodes. When voltage is applied to the electrodes, the actuator expands in area (ΔA) and contracts in thickness (Δz) due to the electrostatic forces, exhibiting a high strain. The deformation is mainly obtained due to the electrostatic interaction between two electrodes with opposite electric charge. In Figure 1.1, the working principle of a DEA is shown.

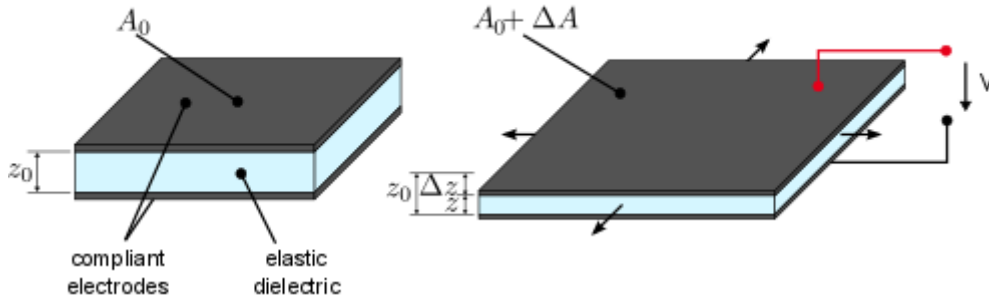


Figure 1.1: Dielectric elastomer actuators working principle: in light blue, the elastic dielectric material and, in grey, compliant electrodes. In the left layout, the actuator is at zero voltage. The geometry of the actuator is defined by an initial area A_0 and an initial thickness of z_0 . The right layout represents the actuator when a voltage V is applied between the electrodes. The initial area A_0 expands, ending up in $A_0 + \Delta A$, while the final thickness is $z_0 - \Delta z$.

It is possible to estimate the electrostatic pressure exerted on a DEA sandwiched between two compliant electrodes, according to the Maxwell pressure equation:

$$p = \varepsilon_0 \varepsilon_r E^2 = \varepsilon_0 \varepsilon_r \frac{V^2}{z_0^2} \quad \text{Eq 1.1}$$

where p is the Maxwell pressure, ε_0 is the permittivity of free space, ε_r the dielectric constant, E is the electric field, z_0 the initial dielectric thickness and V the applied voltage (in the order of a few kV for typical EAPs). The active strain S_a also depends on the stiffness or Young's Modulus Y of the material:

$$S_a = \frac{1}{Y} \varepsilon_0 \varepsilon_r \frac{V^2}{z_0^2} \quad \text{Eq 1.2}$$

As it can be observed in equation 1.2, in electroactive polymers the strain is proportional to the square of the electric field and to the dielectric constant, while inversely proportional to the Young's modulus of the dielectric. In general, the applied electric field in this technology is close to $100 \text{ V}/\mu\text{m}$ to obtain a significant strain in the material, and normally closely below the breakdown strength of the dielectric.

Equation 1.2 is a simplification, considering only small strains with free boundary conditions. The model also considers that the dielectric material is an ideal rubber, which means that it is an incompressible material and has a Poisson's ratio of 0.5. The needed model for larger strains is more complicated due to the hyperelastic properties of this kind of elastomers.

The simplest fabrication method of an EAP actuator is based on a pre-stretched membrane, usually of polydimethylsiloxane (PDMS) or acrylics supported by two rigid frames, which hold the pre-stretch. On top and bottom of this elastic elastomer compliant electrodes are deposited by brush-coating [4], spraying [5], stamping [6], laser ablation [7] or electrodeposition [8] with the desired geometry of the final actuator. Figure 1.2(a) shows a diagram of the elements needed to fabricate a basic circular actuator and the final single-layer actuator device obtained after assembling these parts Figure 1.2 (b).

Single-layer actuators provide a high deformation in the x and y directions due to the pre-stretching of the dielectric film along this plane. The force obtained with these actuators is rather small. Different actuator configurations have been already proposed to increase the stroke [9] [10] of single layer actuators: some examples of these configurations [11] are the so-called spider, roll, tube, diaphragm, extender, and bowtie.

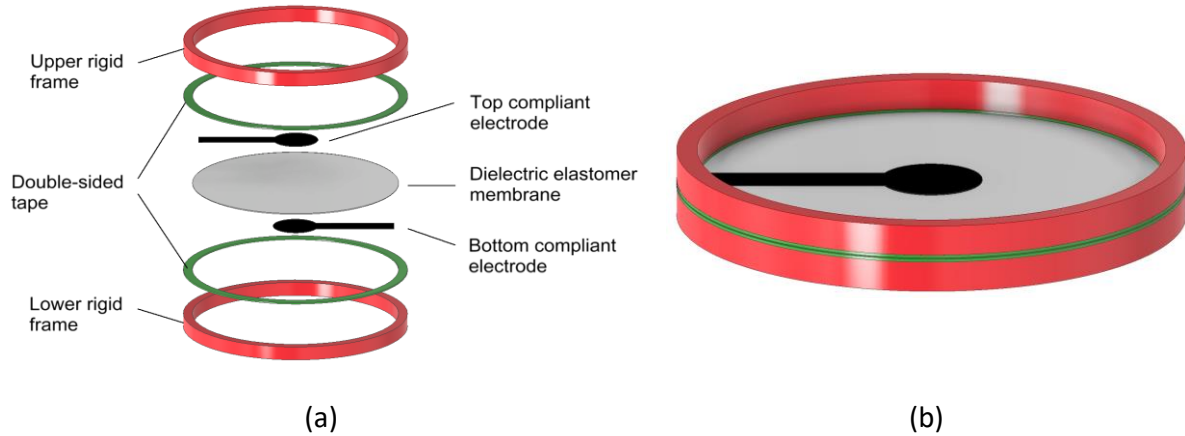


Figure 1.2: (a) Elements needed to fabricate a single layer EAP: two rigid holding frames (normally made of PMMA); two rings of a double-sided tape, the top electrode, followed by the elastomer layer and the bottom electrode. (b) Assembled elements to form a single layer EAP. The bottom electrode is not visible in the layout.

1.2. MATERIALS IN ELECTROACTIVE POLYMERS

As mentioned in section 1.1, dielectric actuators consist basically of an elastic dielectric sandwiched between two compliant electrodes. In the following section the properties of the materials necessary to manufacture electroactive polymers, as well as their fabrication processes, are detailed.

1.2.1. DIELECTRIC

The first dielectric material used as electroactive polymer was an acrylic band (VHB, very high bond) from the company 3M[®]. This material is provided as a double-sided adhesive tape of different thicknesses. The properties of this type of material are both high permittivity and high strain when voltage is applied. Some other materials that can be used as dielectric for electroactive polymers are polyurethanes [12][13] and polydimethylsiloxane (PDMS).

Table 1.1: Requirements for the dielectric material in terms of material properties, actuator performance and market requirements: high (H) or low (L).

Material properties	Permittivity (H)	Breakdown strength (H)	Young's modulus (L)	Thickness (L)
Actuator performance	Dielectric losses (L)	Viscoelastic losses (L)	Operating voltage (L)	Stroke/Force (H)
Market requirements	Price (L)	Reproducibility (H)	Availability (H)	Environment (H)

The main desirable properties for the dielectric in terms of actuation performance are those maximizing the strain in Eq 1.2 (low Young's modulus, high permittivity), plus some related to the application of the electric field (high breakdown strength, high durability, high stroke, high actuation force, relatively low operating voltage and finally low viscoelastic and dielectric losses).

The fundamental industrial requirements for actuators are price, reproducibility, availability and environmental sustainability. Table 1.1 summarizes the main properties related to the EAP desired characteristics.

Polyurethanes have been rejected due to their high Young's modulus, their slow response speed and their high flammability, although they have a significantly higher relative permittivity than the other materials and higher breakdown strength. Polyurethane dielectrics were improved in terms of the electromechanical actuation. Small molecular plasticizers like Dibutyl Phthalate (DBP) and Triphenyl Phosphate (TPP) and oligomer plasticizers like Polyethylene Glycol (PEG) and PMG were introduced in the polyurethane matrix to decrease its Young's modulus, thus leading to a decrease of its relative permittivity [14]. The results were not sufficient to compete with the properties of PDMS. In Table 1.2, the general values for acrylics, polyurethanes, silicones and silicone film are shown.

Table 1.2: Parameters of different materials used as dielectric in EAP systems

Elastomer type	Young's modulus [MPa]	Breakdown field [$V\mu\text{m}^{-1}$]	Relative permittivity	Response speed
Acrylic	0.2-3	55-412	4.8	ms to s
Polyurethane	17	160	7.0	ms to s
Silicone	0.1-1	80-130	2.8-3.7	μs to ms
Elastosil Film	1	80-100	2.8	μs to ms

For some applications a higher strain of the PDMS is needed. In order to optimize the performance of the EAP actuators, great efforts have been made by researchers to improve the relative permittivity of the dielectric (normally in the range of $\epsilon_r \sim 3$) without increasing significantly its Young's modulus. Some of the techniques used are based on mixing metal oxides in the PDMS [15][16][17] or high-permittivity liquids [18], covalent grafting of dipoles [19][20] and the use of functional copolymers [21][22]. When using the abovementioned techniques, the consequences are normally changes in the mechanical and electrical properties of the material: some examples are an increase of the stiffness (higher Young's modulus) or lower electrical breakdown strength. Other authors used carbon black as well as other carbon-based fillers to improve the acrylic elastomers performance [23].

HYPERELASTIC MATERIALS

Polydimethylsiloxane is a hyperelastic material. Hyperelastic materials are a kind of material that responds elastically when it is exposed to very high strains. In the case of single membrane actuators, they are often even pre-stretched before voltage is applied. In general, the relationship between the exerted force and the deformation of the material is described by the Hooke's law. Hooke's law shows that, within certain limits, the necessary force to stretch an elastic object (a metal spring) is directly proportional to the extension of the spring.

$$F = k(L - L_0) \quad \text{Eq 1.3}$$

where F states for the force, k is the spring constant or the constant of proportionality, normally given in N/m, L is the total length and L_0 the initial length.

In Figure 1.3 the force-strain curve for an elastomer is shown. It can be appreciated that at low forces the linear behaviour between force and strain follows the Hooke's law (region a). As the material is more stretched, the linearity of the relationship is lost and a curve (close to a plateau) region is observed (region b). In region a, the material is hard; in region b, it gets softer; in region c, it develops a strain-hardening behaviour. The two first parts of the material curve can be modelled with the classic hyperelastic models (Mooney-Rivlin or Gent model), but the last region of the curve is challenging to explain and to predict.

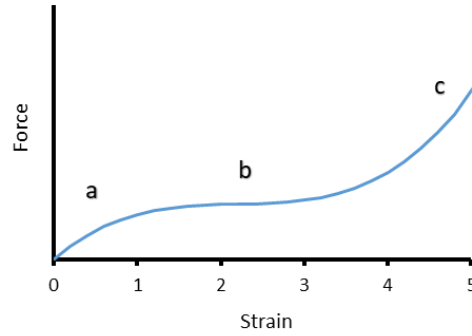


Figure 1.3: Relation between force and strain for elastomers. Region a follows a linear behaviour, the Hooke's law for springs (the material in this region can be considered "hard"). In region b, the material gets softer and a plateau region is observed. In region c, no model is able to determine the relation between force and strain [24].

In this thesis, the dielectric material is assumed to be an incompressible hyperelastic solid, since the elastic effect is predominant compared to the visco-elastic one. The stress state in the hyperelastic material is determined by taking the derivatives of the strain energy density with respect to the strain components.

HYPERELASTIC MODELS

In this section, the hyperelastic models used to predict the behaviour of the elastomers in this thesis are explained. They are important for the production of the stress-strain curve to characterize the volumetric deformation of the dielectric. Assuming the near incompressibility of the material, the total energy density W_s for a nearly incompressible material is

$$W_s = W_{iso} + W_{vol} \quad \text{Eq 1.4}$$

where W_{iso} is the isochoric strain energy density and W_{vol} is the volumetric strain energy density. The second Piola-Kirchhoff stress tensor S [25] is described as

$$S = -p_p J C^{-1} + 2 \frac{\partial W_{iso}}{\partial C} \quad \text{Eq 1.5}$$

where p_p is the volumetric stress, C is the right Cauchy-Green tensor (Eq 1.13), and J is the volume ratio. The volume ratio is defined as the ratio between the deformed volume V_d and the initial volume V_0 . The second term of Eq 1.5 can be further developed to

$$S = -p_p J C^{-1} + 2 \left(J^{-2/3} \left(\frac{\partial W_{iso}}{\partial \bar{I}_1} + \bar{I}_1 \frac{\partial W_{iso}}{\partial \bar{I}_2} \right) I - J^{-4/3} \frac{\partial W_{iso}}{\partial \bar{I}_2} C - \left(\frac{\bar{I}_1}{3} \frac{\partial W_{iso}}{\partial \bar{I}_1} + \frac{2\bar{I}_2}{3} \frac{\partial W_{iso}}{\partial \bar{I}_2} \right) C^{-1} \right) \quad \text{Eq 1.6}$$

Where \bar{I}_1 and \bar{I}_2 are invariants of the isochoric right Cauchy-Green tensor. \bar{I}_1 and \bar{I}_2 can be expressed in terms of the stretch ratio λ as:

$$\bar{I}_1 = J^{-2/3} I_1, \quad I_1 = \lambda_1^2 + \lambda_2^2 + \lambda_3^2 \quad \text{Eq 1.7}$$

$$\bar{I}_2 = J^{-4/3} I_2, \quad I_2 = \lambda_1^2 \lambda_2^2 + \lambda_2^2 \lambda_3^2 + \lambda_3^2 \lambda_1^2 \quad \text{Eq 1.8}$$

In the present work, the stretch ratio λ is defined as a measure of the magnitude of deformation. Mathematically, the stretch ratio of a material under uniaxial tension is defined as $\lambda = L_d/L_0$, where L_d is the deformed length of the probe and L_0 is its original length. In a multiaxial stress experiment, the principal stretches $\lambda_a = L_a/L_{0a}$ (where $a = 1, 2, 3$ in the principal referential directions \hat{N}_a) have the same directions as the principal stresses. The strain energy density and stresses are often expressed in terms of the stretch ratio λ .

Figure 1.4: shows the deformation of a cube. In Figure 1.4:(a), the undeformed cube and its original dimensions L_{0a} are shown. In Figure 1.4: (b), the external forces F_a deform the cube leading to new dimensions $L_a = L_{0a} \cdot \lambda_a$.

If the assumption of incompressibility is not formulated, it is common to split the deformation into volumetric and isochoric contributions, introducing a modified right Cauchy-Green stretch tensor \bar{C} associated with volume-preserving transformation. The modified right Cauchy-Green tensor can be expressed as

$$\bar{C} = J^{-2/3} C \quad \text{Eq 1.9}$$

The first Piola-Kirchhoff stress tensor P and the Cauchy stress tensor σ can be expressed as a function of the second Piola-Kirchhoff stress tensor as

$$P = FS \quad \text{Eq 1.10}$$

$$\sigma = J^{-1} F S F^T \quad \text{Eq 1.11}$$

Where F is the deformation gradient.

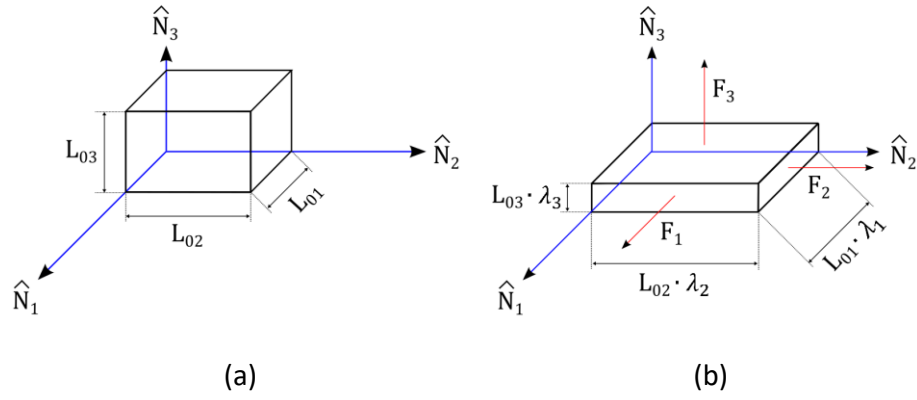


Figure 1.4: (a) Undeformed cube. (b) Deformation of the cube under external forces F_a .

The stress tensor for multiaxial stress experiments can be expressed as

$$S = \sum_{a=1}^3 S_a \hat{N}_a \otimes \hat{N}_a \quad \text{Eq 1.12}$$

where S_a represents the principal values of the second Piola-Kirchhoff stress tensor and \hat{N}_a represents the principal referential directions and the right Cauchy-Green tensor in the following form:

$$C = \sum_{a=1}^3 \lambda_a^2 \hat{N}_a \otimes \hat{N}_a \quad \text{Eq 1.13}$$

The second Piola-Kirchhoff stress tensor can be expressed in terms of the principal stretches:

$$S_a = \frac{-p_p J}{\lambda_a^2} + 2 \left(J^{-2/3} \left(\frac{\partial W_{iso}}{\partial \bar{I}_1} + \bar{I}_1 \frac{\partial W_{iso}}{\partial \bar{I}_2} \right) - J^{-4/3} \frac{\partial W_{iso}}{\partial \bar{I}_2} \lambda_a^2 - \frac{1}{\lambda_a^2} \left(\frac{I_1}{3} \frac{\partial W_{iso}}{\partial \bar{I}_1} + \frac{2I_2}{3} \frac{\partial W_{iso}}{\partial \bar{I}_2} \right) \right) \quad \text{Eq 1.14}$$

For uniaxial and biaxial tests, the relationship between stress and stretch can be determined. As mentioned above, considering incompressibility of the material ($J = 1$), the principal stretches for the uniaxial deformation of an isotropic hyperelastic material are given by:

$$\lambda_1 = \lambda, \lambda_2 = \lambda_3 = \lambda^{-1/2} \quad \text{Eq 1.15}$$

The deformation gradient is given by:

$$F = \begin{pmatrix} \lambda & 0 & 0 \\ 0 & \frac{1}{\sqrt{\lambda}} & 0 \\ 0 & 0 & \frac{1}{\sqrt{\lambda}} \end{pmatrix} \quad \text{Eq 1.16}$$

For uniaxial extension $S_2 = S_3 = 0$, suppressing the volumetric stress p_p :

$$S_1 = 2 \left(\frac{1}{\lambda} - \frac{1}{\lambda^4} \right) \left(\lambda \frac{\partial W_{iso}}{\partial \bar{I}_{1uni}} + \frac{\partial W_{iso}}{\partial \bar{I}_{2uni}} \right), \quad P_1 = \lambda S_1 \text{ and } \sigma_1 = \lambda^2 S_1 \quad \text{Eq 1.17}$$

The isochoric invariants \bar{I}_{1uni} and \bar{I}_{2uni} can be expressed in terms of the principal stretch λ as:

$$\bar{I}_{1uni} = \left(\lambda^2 + \frac{2}{\lambda} \right) \quad \text{Eq 1.18}$$

$$\bar{I}_{2uni} = \left(2\lambda + \frac{1}{\lambda^2} \right) \quad \text{Eq 1.19}$$

The principal stretches for the equibiaxial deformation of an isotropic hyperelastic material are given by:

$$\lambda_1 = \lambda_2 = \lambda, \lambda_3 = \lambda^{-2} \quad \text{Eq 1.20}$$

For equibiaxial extension $S_3 = 0$, the volumetric stress p_p can be eliminated to give:

$$S_1 = S_2 = 2 \left(1 - \frac{1}{\lambda^6} \right) \left(\frac{\partial W_{iso}}{\partial \bar{I}_{1bi}} + \lambda^2 \frac{\partial W_{iso}}{\partial \bar{I}_{2bi}} \right), \quad P_1 = \lambda S_1 \text{ and } \sigma_1 = \lambda^2 S_1 \quad \text{Eq 1.21}$$

The invariants \bar{I}_{1bi} and \bar{I}_{2bi} are then:

$$\bar{I}_{1bi} = \left(2\lambda^2 + \frac{1}{\lambda^4} \right) \quad \text{Eq 1.22}$$

$$\bar{I}_{2bi} = \left(\lambda^4 + \frac{2}{\lambda^2} \right) \quad \text{Eq 1.23}$$

In the following sections, the hyperelastic models used during the analysis of the elastomers of this thesis are explained in more detail. First, the strain energy function for each hyperelastic model is defined. Then, for each particular expression of the strain energy function the first Piola-Kirchhoff stress tensor P is deduced to reach the final expression of the model.

A. Mooney-Rivlin model with five parameters

The Mooney-Rivlin hyperelastic model [26] [27] with five parameters is used in chapter 6 for the COMSOL Multiphysics® simulations. The higher the number of parameters in the model, the better curve fitting matching the simulations with experimental data is obtained. For Mooney-Rivlin

model, 3, 5 and 7 fitting parameters are possible. The right selection of number of parameters is necessary, as more parameters may lead to convergence issues. For a given strain, the stress state is determined as the derivative of the strain energy density with respect to the strain components. The strain energy function of the Mooney-Rivlin hyperelastic constitutive model is expressed as a function of the strain invariants I_1 , I_2 and the volume ratio J . The strain energy density function is given as:

$$W = W(I_1, I_2, J) = W(I_1, I_2) + U(J) \quad \text{Eq 1.24}$$

The strain energy function can be extended considering the fitting parameters C_{pq} in the Mooney-Rivlin model:

$$W_{iso} = \sum_{p,q=0}^N C_{pq} (\bar{I}_1 - 3)^p (\bar{I}_2 - 3)^q + \sum_{m=1}^M D_m (J - 1)^{2m} \quad \text{Eq 1.25}$$

where D_m are material constants related to the volumetric response. Considering the assumption of incompressible material or $J=1$, the last term of the expression is zero. The form of the strain energy density function for five parameters of the Mooney-Rivlin model is given as:

$$W_{iso(5)} = C_{10}(\bar{I}_1 - 3) + C_{01}(\bar{I}_2 - 3) + C_{20}(\bar{I}_1 - 3)^2 + C_{02}(\bar{I}_2 - 3)^2 + C_{11}(\bar{I}_1 - 3)(\bar{I}_2 - 3) \quad \text{Eq 1.26}$$

where C_{10} , C_{01} , C_{20} , C_{02} , and C_{11} are the Mooney-Rivlin's five parameters.

From the strain energy density expression (Eq 1.26), it is possible to obtain the expressions for the first and second Piola-Kirchoff stress tensor. First, the general equation for the second Piola-Kirchoff stress tensor S for the uniaxial case is needed (Eq 1.17). The derivatives of the strain energy density function of the five-term Mooney-Rivlin model (Eq 1.26) with respect to the isochoric invariants \bar{I}_1 and \bar{I}_2 are:

$$\frac{\partial W_{iso(5)}}{\partial \bar{I}_1} = C_{10} + 2C_{20}(\bar{I}_1 - 3) + C_{11}(\bar{I}_2 - 3) \quad \text{Eq 1.27}$$

$$\frac{\partial W_{iso(5)}}{\partial \bar{I}_2} = C_{01} + 2C_{02}(\bar{I}_2 - 3) + C_{11}(\bar{I}_1 - 3) \quad \text{Eq 1.28}$$

Introducing these terms into the general equation for the second Piola-Kirchoff stress tensor S for the uniaxial case (Eq. 1.17):

$$S_{1_{uni}} = 2 \left(\frac{1}{\lambda} - \frac{1}{\lambda^4} \right) \left(\lambda(C_{10} + 2C_{20}(\bar{I}_{1_{uni}} - 3) + C_{11}(\bar{I}_{2_{uni}} - 3)) + C_{01} + 2C_{02}(\bar{I}_{2_{uni}} - 3) + C_{11}(\bar{I}_{1_{uni}} - 3) \right) \quad \text{Eq 1.29}$$

By using the relation between the first and the second Piola-Kirchhoff stress tensor ($P_1 = \lambda S_1$) and regrouping the terms in the previous equation, the first Piola-Kirchhoff stress tensor for the uniaxial case is expressed as:

$$P_{1_{uni}} = 2(1 - \lambda^{-3}) \left(\lambda C_{10} + 2\lambda C_{20}(\bar{I}_{1_{uni}} - 3) + \lambda C_{11}(\bar{I}_{2_{uni}} - 3) + C_{01} + 2C_{02}\bar{I}_{2_{uni}} + C_{11}(\bar{I}_{1_{uni}} - 3) \right) \quad \text{Eq 1.30}$$

If needed, the uniaxial isochoric invariants $\bar{I}_{1_{uni}}$ and $\bar{I}_{2_{uni}}$ can also be expressed in terms of the principal stretch λ by using equations Eq 1.18 and 1.19, leading to an expression where the first Piola-Kirchhoff stress tensor $P_{1_{uni}}$ only depends on the principal stretch λ and the five material parameters of Mooney-Rivlin C_{10} , C_{01} , C_{20} , C_{02} and C_{11} .

For the biaxial case, the derivatives of the strain energy density function of the five-term Mooney-Rivlin model respect to the isochoric invariants \bar{I}_1 and \bar{I}_2 (Eq 1.28 and 1.29) are introduced into the expression of the second Piola-Kirchhoff stress tensor S for the biaxial case (Eq. 1.21), leading to:

$$S_{1_{bi}} = 2 \left(1 - \frac{1}{\lambda^6} \right) \left((C_{10} + 2C_{20}(\bar{I}_{1_{bi}} - 3) + C_{11}(\bar{I}_{2_{bi}} - 3)) + \lambda^2 (C_{01} + 2C_{02}(\bar{I}_{2_{bi}} - 3) + C_{11}(\bar{I}_{1_{bi}} - 3)) \right) \quad \text{Eq 1.31}$$

Considering the relation $P_{1_{bi}} = \lambda S_{1_{bi}}$ and regrouping the terms in Eq 1.32, the first Piola-Kirchhoff stress tensor for the biaxial case is expressed as:

$$P_{1_{bi}} = 2(\lambda - \lambda^{-5}) \left(C_{10} + 2C_{20}(\bar{I}_{1_{bi}} - 3) + C_{11}(\bar{I}_{2_{bi}} - 3) + \lambda^2 C_{01} + 2\lambda^2 C_{02}(\bar{I}_{2_{bi}} - 3) + \lambda^2 C_{11}(\bar{I}_{1_{bi}} - 3) \right) \quad \text{Eq 1.32}$$

The biaxial isochoric invariants $\bar{I}_{1_{bi}}$ and $\bar{I}_{2_{bi}}$ can also be expressed in terms of the principal stretch λ by using equations Eq 1.22 and 1.23. Thus, the first Piola-Kirchhoff stress tensor for the biaxial case $P_{1_{bi}}$ only depends on the principal stretch λ and the five material parameters of Mooney-Rivlin C_{10} , C_{01} , C_{20} , C_{02} and C_{11} .

For all the above-mentioned formulations, the Cauchy stress tensor σ can be easily obtained for the uniaxial and biaxial cases by using the equations $\sigma_1 = \lambda P_1$ or $\sigma_1 = \lambda^2 S_1$.

B. Gent model

The Gent model [28] is used in section 2.3.2 where the Sylgard[®] 186 hyperelastic material is modelled. The Gent model is based on the first invariant I_1 and two material constants: the shear modulus μ and I_m . I_m measures a limiting value for $I_1 - 3$. The strain energy density for the Gent model can then be expressed as:

$$W(I_1) = \frac{-\mu I_m}{2} \ln \left[1 - \frac{I_1 - 3}{I_m} \right] \quad \text{Eq 1.33}$$

To obtain the first and second Piola-Kirchoff stress tensors, the procedure is the same as in the Mooney-Rivlin case. First, the derivatives of the strain energy density with respect to the first and second invariant are needed. In the Gent model, only the first invariant \bar{I}_1 is in the strain energy density included. Then,

$$\frac{dW_{iso}}{d\bar{I}_1} = \frac{\mu}{2} \cdot \frac{I_m}{I_m - \bar{I}_1 + 3} \quad \text{Eq 1.34}$$

For the uniaxial case, this derivative is included in the general equation for the second Piola-Kirchoff stress tensor S (Eq. 1.17):

$$S_{1uni} = 2 \left(\frac{1}{\lambda} - \frac{1}{\lambda^4} \right) \left(\lambda \left(\frac{\mu}{2} \cdot \frac{I_m}{I_m - \bar{I}_{1uni} + 3} \right) \right) \quad \text{Eq 1.35}$$

Simplifying the above expression and considering the relation $P_{1uni} = \lambda S_{1uni}$, the first Piola-Kirchoff stress tensor for the uniaxial case in the Gent model is expressed as:

$$P_{1uni} = \mu(\lambda - \lambda^{-2}) \left(\frac{I_m}{I_m - \bar{I}_{1uni} + 3} \right) \quad \text{Eq 1.36}$$

Following the same steps for the biaxial case, the first Piola-Kirchoff stress tensor for the biaxial case in the Gent model is:

$$P_{1bi} = \mu(\lambda - \lambda^{-5}) \left(\frac{I_m}{I_m - \bar{I}_{1bi} + 3} \right) \quad \text{Eq 1.37}$$

As mentioned for the Mooney-Rivlin model, the Cauchy stress tensor σ can be obtained for the uniaxial and biaxial cases by using the equations $\sigma_1 = \lambda P_1$ or $\sigma_1 = \lambda^2 S_1$. In the formulas, the first isochoric invariant \bar{I}_1 for both uniaxial and biaxial cases can be expressed in terms of the principal stretch λ by using equations Eq 1.18 and 1.22, respectively. All these steps lead to Gent model expressions where the only parameters are the principal stretch and the constant material parameters, μ and I_m .

1.2.2. ELECTRODES

EAP actuators work as deformable capacitors, consisting of a dielectric and two electrodes, as previously stated. The main properties for suitable electrodes are: high conductivity, so that the actuator or capacitor can charge and discharge fast; stability in time; deformability, so that they do not impede the deformation of the elastic dielectric. EAP electrodes with these properties are commonly named as compliant electrodes.

Some types of electrodes already used are: graphite powders, ionically conductive water-based polymers, conductive fillers distributed in an elastomer binder material and thin metal films.

In the first case, graphite or carbon powder electrodes are directly sprayed [29] or brushed [30] on the top and bottom surface of the elastomer without the need of a binder (like another elastomer) [31]. This method is in general used for multilayer or stacked actuators where the following layer of dielectric protects the electrodes to fly away from the elastomer.

The conductive fillers are basically graphite [32], carbon black particles mixed in oil, gel or a low Young's modulus elastomer. The result is a composite with a high conductivity and flexibility. The amount of filler tends to be the minimum to obtain the desired conductivity without compromising the elasticity of the material obtained. The low percolation threshold and the dispersion of the particles in the matrix are some of the factors that should be taken into account when fabricating these composites [33][34][35].

Thin metal film electrodes are extremely conductive electrodes, but often not compliant. Only when the metal film is very thin (much more than the abovementioned electrodes) is it possible to avoid the two main negative effects: the passivation of the elastomer and the creation of cracks in the electrodes when the deformation occurs. Researchers [1][36] have used gold electrodes in form of zig-zag using photolithography to overcome the cracking problem. Other authors have used ion implantation to get an extremely thin film, in the range of 10 nm, Ti-ion [37], gold [38], Ti and Pd implantations and by depositing silver electrodes by magnetron sputtering [39]. These techniques have also the inconvenient that increase the production cost of the EAP, in comparison to the other techniques.

1.3. LIFETIME OF ACTUATORS

In order to be able to use the technology of EAP in an industrial scale, it is necessary that the EAP as actuators, sensors or energy harvesting systems are reproducible in time and also that the technology can be used for long periods of time.

Researchers have focused their investigations in the possible degradation of the materials of the EAP, elastomers and electrodes, under high cycle numbers of actuation and different conditions.

In general, to obtain very high strains, researchers actuate EAP near the electrical breakdown field strength. As a consequence, a shorter lifetime is expected. An electric breakdown occurs when the initially negligible current flowing in a dielectric material suddenly rises extremely. This sudden increase can have various causes, but all of them lead to thermal destruction [40].

There are different explanation models for the increase of the flowing current. The first free charge carriers of an electrically induced breakdown originate from the electrodes and penetrate the dielectric material from there. Areas can now be created where the material has a lower density. In these areas, electrons have a longer free path length and can be accelerated so strongly by the applied electric field, that further free electrons can be generated by impact ionization. The thicker the material sample, the higher the probability that such events occur. Therefore, many materials show decreasing breakthrough strength with increasing sample thickness [41].

The more charge carriers are created in the dielectric material and travel through it, the more the material heats up and supports the second type of electric breakdown: the thermally induced

breakdown [42]. How fast the material heats up depends on the specific heat capacity c_v , the heat generated and the heat dissipated through the material:

$$C_v \frac{dT}{dt} - \text{div}(K_t \text{grad}T) = \sigma_{ce} E^2 \quad \text{Eq 1.38}$$

The generated Joule heat depends on the applied field E and the electrical conductivity σ_{ce} of the material. The amount of heat dissipated is determined by the thermal conductivity K_t . The electrical conductivity in an applied alternating field is composed of the DC conductivity and the conductivity due to polarization $\omega \varepsilon_0 \varepsilon_r''$, where ε_r'' represents the imaginary part of the complex permittivity. Therefore, dielectric materials have higher breakdown strengths for DC voltage than for AC voltage.

Defining the electrical breakdown field strength allowed the development of the EAP technology. Matysek et al. [43] used a setup based on 16 stacked actuators which were measured by a laser displacement sensor. Voltage and current were continuously monitored for each actuator. The end of the lifetime measurement was based on measurements of the current of the actuators. When the current in the actuator has a value lower than 75 % of its maximum, the actuator is defined to reach the end of its lifetime. Frequencies of 10, 100 and 200 Hz were used for the measurements and 45.5, 445 and 462 million cycles were obtained, respectively. They also checked the lifetime of the actuators depending on the used contact material to connect the stack layers: graphite, silver grease and a mixture of both. The mixture of graphite and silver grease featured a higher life time.

Zhang et al. [44] fabricated different dielectric materials changing the stoichiometric imbalance of the reagents, the network structure, the mechanical properties and the electric characteristics to know the influence of these properties on the ageing of the material.

In general, researchers have focused their attention in determining the lifetime of the actuators based on the breakdown strength of the dielectric. It is also important to consider the time degradation of the electrodes when using EAPs. With this purpose, Rosset et al. [45] developed a new system to characterize the electrodes of one single layer actuator. The so-called NERD setup (Novel Electrode Resistance Degradation) is able to characterize the degradation of compliant electrodes during actuation. The circular actuator is connected to a high voltage power supply and to a four-wire resistance measurement system. The strain of the actuator is measured by using a camera and image study analysis. The actuators were made of Sylgard[®] 186 membrane with carbon composite electrodes. They reached over 350k cycles with 1500 V for the first 100k cycles, then 1850 V for another 100k cycles and finally 2000 V for the last 150k cycles. They measured the electrodes resistance along the experiment. As far as the actuation stretch keeps lower than 10 %, the resistance stays stable.

1.4. COMPARISON TO OTHER TECHNOLOGIES

In the previous sections of this chapter, the main characteristics of EAPs have been introduced. The necessary requirements of dielectric polymers, electrodes and ultimately of EAP actuators, in terms of material properties, degradation, life cycle, actuator performance and market requirements have been outlined. In this section, a comparison between EAP and other technologies that are currently in use, for example electroactive ceramics (EACs), shape memory

alloys (SMAs) and electromagnetic (EM) actuation, is made. These technologies are often used for the same applications as EAPs. Thus, an overview of their main advantages and disadvantages helps to understand potential applications of EAPs.

In Table 1.3, properties such as actuation, force and speed of response are shown. The data correspond to the dielectric EAPs, considered in this thesis, not to the ionic EAPs.

Table 1.3: Comparison of the properties of EAP with other technologies like SMA, EAC and EM (adapted from [46]).

	EAP	SMA	EAC	EM
Actuation strain	> 300 %	<8 %	0.1 – 0.3 %	50 %
Force	0.1 – 25 MPa	200 MPa	30 – 40 MPa	0.1 MPa
Reaction speed	μ s	ms to min	μ s	μ s
Driving voltage	10 – 150 V/ μ m	1 – 10 V	50 – 800 V	0 – 120 V
Fracture behaviour	Resilient, elastic	Resilient, elastic	Fragile	Resilient

On the one hand, the table shows that the actuation strain of EAPs [47][48] is at least one order of magnitude higher than the one of SMA, EAC and EM technologies. With respect to reaction speed or response time, EAP is much superior to SMA and comparable to EAC and EM. EAP actuators are also able to last a higher number of cycles and have an elastic behaviour that makes them last longer than the remaining technologies. On the other hand, the low obtained forces and the high driving voltages are the main disadvantages of the EAP technology. However, obtained forces have been improved lately by introducing new geometries [49][50], while driving voltages have been reduced by new manufacturing processes (see more details in section 1.6).

1.5. APPLICATIONS OF ELECTROACTIVE POLYMERS

As mentioned before, dielectric elastomer actuators can work as actuators, sensors and energy harvesting devices or generators. Therefore, they offer a huge variety of applications. At the early stages of this technology, EAPs were used as artificial muscles or soft robots. EAPs are ideal for this application due to their dual acting-sensing response, their high deformation, the biocompatibility of the materials in use, the low cost of the technology and the low weight, that could greatly reduce the weight of classic robots and prosthesis.

The application of EAP as actuators in robots is especially relevant for aerospace applications or in situations in which the presence of human beings is not recommended or possible. The main idea is to have small, soft, low cost robots, with good mobility and dexterity or in other words, collaborative robots.

Some of the first fabricated microrobots were FLEX 1 [51], FLEX 2 [11], Skitter [52] and MERbot [53]. These are the so-called walking robots, inspired on animals. The FLEX robots are based on six legs, a tripod gait and a lightweight but rigid body. FLEX 1 had a Bowtie actuator in each leg and FLEX 2 had spring roll actuators on its legs instead of the Bowtie one.

EAP demonstrators mimicking insects [54] have already been fabricated with this technology. Flies [55][56], worms [57] and fishes [58][59] are some of the lately animal-based actuators fabricated as microrobots.

After this application was first explored, EAPs were used for brand-new applications like: small-motors [60][61] using EAP at their resonance frequency; Braille displays [62][63] in order to

decrease the price of the current devices using EAP; for sound generation as loud speakers [64][65], due to the very high range of frequencies of EAPs; and silicone tuneable lenses [66].

The EAP technology has also been used as sensors. Since EAPs are soft capacitors, a change of capacitance can be detected and modify to react to a stimulus. The company Stretchsense [67] bases its work and research in using EAP as sensors in different devices. Some examples are gloves, which can reproduce with high fidelity the finger motion and a sport rehabilitation or/and training suit. The suit is equipped with plenty of EAPs as sensors that provide information about the movements of the body in order to analyse sportive performance, injuries, etc.

As energy harvesting systems, EAPs work inversely to actuators. The energy harvesting system is deformed by an external force and therefore it generates an electric field, due to the charge and discharge of the capacitor. Some examples of EAPs as generators or dielectric elastomer generators (DEGs) are buoy generators and heel-strike generators [68], which take advantage of the human's walking motion to continuously store energy. Maas et al. [69][70][71] studied the parameters that influence the energy harvesting devices and the involved mathematic modelling. They proposed some examples suitable for small rivers. The company SBM-offshore [72] has fabricated prototypes of DEG for ocean waves energy harvesting.

1.6. MOTIVATION TO USE ELECTROACTIVE POLYMERS IN MICROFLUIDICS

The use of DEAs in biocompatible devices, for instance devices inside the body or in contact with cells, was rejected in the past due to the high voltage required in order to get the needed actuation of the DEAs.

The investigations towards the decrease of the driving voltage are leading to a reduction of the applied voltage from few kV to a couple of hundreds of Volts, using technologies like 3D-printing. Poulin et al. [73] reported lateral strains up to 7.5 % with films of 3 μm thickness, fabricated using pad printings of the dielectric with an applied voltage of 245 V. Matysek et al. [74] fabricated 5 μm thick dielectric films in a multilayer DEA by spin coating, actuated by applying 150 V. Töpper et al. [75] produced 200 nm thick films using molecular beam deposition and used driving voltages between 1 to 12 V. However, the actuation strain in this case was limited by the stiffness of gold-sputtered electrodes. The development of thin films will not only allow the use of DEAs with biocompatible applications (due to the decrease of the actuation voltage), but also the simplification of the electronics used to control the actuators [76].

Some of the characteristics offered by the EAP technology are relevant to microfluidics, like biocompatibility [77], flexibility, soft materials, non-expensive technology, high frequency actuation, portability and long term usage.

Previous work has been related to the use of DEAs in the biological field. Several research groups work in the mechanical stimulation of cell cultures by means of EAPs. The group of Prof. Shea [78] works in the fabrication of the so-called "minigyms for cells", where it is possible to stretch cells and analyse the impact of stretching versus time at different frequencies and strains, by the implementation of culture cells on top of a dielectric elastomer actuator, previously coated with a passive membrane. Costa et al. [79] fabricated a bioreactor with EAP. The bioreactor is based on electrically deformable membranes with a tuneable curvature holding a liquid inside. The EAP membrane is stretched and the biological liquid or cells on top of it get deformed when voltage is

applied, mimicking the deformation of the cells in a human body. The advantage of this method, with respect to other previously exposed, is that cells not only suffer from uniaxial or biaxial stretch but also out-of-plane stretch, due to the membrane curvature.

Micropumps for drug delivery is a potential application where EAP materials can report better performance than the current technologies. The aim in all drug delivery applications is to take the therapeutic substance to the target and deliver it at the right time and in the right dose, thus improving the therapeutic index and reducing side effects, which in turn lead to better disease treatments. Much of the pioneering work in this area has been carried out by Zhang et al. [80]. Electrostrictive polyvinylidene-fluoride trifluoroethylene has been used to realize a microfluidic pump.

The aim of this thesis is to demonstrate that EAPs can be used to build robust microfluidic systems and these are capable of competing with existing technologies.

1.7. CONTENT AND STRUCTURE OF THIS WORK

In this work, prototypes of microfluidic devices fabricated out of electroactive polymers are presented. Single-layer EAPs are used to develop two micropump prototypes and stacked actuators are utilized to create a more complex microfluidic device: a pumping micromixer.

Chapter 2 presents the fundamentals and various working principle mechanisms of micropumps and, in more detail, of peristaltic pumps. Two prototypes of single-layer EAPs peristaltic pumps are studied. Both types of peristaltic pumps are based on a single prestressed diaphragm made of elastomer material. The prototypes, named peristaltic pump - type 1 and type 2, differ in the working principle. These prototypes are fabricated with two different methods:

- 1) Liquid elastomer film - manufactured in the LMTS group in EPFL.
- 2) Solid elastomer film - produced in the MEMS group in TU-Darmstadt.

An analytical model, an electromechanical and fluid dynamic characterization of the first and second prototype designs are included in this chapter.

Chapters 3, 4 and 5 are devoted to the pumping micromixer made out of dielectric stacked actuators.

Chapter 3 begins with a short description of the types of micromixers and their actuation principle. Finally, the ultimate configuration prototype for the pumping micromixer with its materials, working principle and design completes the chapter.

Chapter 4 focuses on the fabrication method, the electrical connection techniques and the electromechanical and fluid dynamical characterization of the pumping micromixer. First experimental results regarding the walls deformation, the fluid flow and the mixing are also part of this chapter.

In chapter 5, the pumping micromixer explained in chapter 3 and fabricated in chapter 4 is further analysed by using COMSOL Multiphysics® simulation software. Firstly, electromechanical simulations of the deformation of stacked actuators are performed. Then, the fluid dynamic

behaviour of the pumping chamber actuators is analysed at different duty cycles, phase shifts and frequencies. Finally, the pressure at the outlet of the channel in the pumping chamber is determined. This chapter provides an insight of the potential of the pumping micromixer at diverse phase shift and frequency configurations.

Chapter 6 gives an overview of the whole thesis, including the main results and the discussion of the results obtained.

In summary, this work is structured as follows:

Chapter 2 – Fabrication and characterization of single-layer electroactive polymer peristaltic pumps (2 working principles)

Chapter 3 – Concept of a pumping micromixer out of dielectric elastomer stacked actuators

Chapter 4 – Fabrication and characterization of the pumping micromixer

Chapter 5 – COMSOL Multiphysics® simulations of the pumping micromixer

Chapter 6 – Conclusions and discussion of this work



2. PERISTALTIC MICROPUMPS

In patients, the concentration of drugs or chemical agents should remain constant and within very precise levels to provide a specific therapeutic effect. High fluctuations of the drug concentration may lead to non-desired side-effects in patients. Therefore, the dose, duration, frequency of application, toxicity and side-effects must be considered and adapted for each patient.

Drug delivery pumps are medical devices designed to deliver medications, fluids, or nutrients directly into a patient's bloodstream or other part of the body, such as the digestive tract or epidural space. Drug delivery pumps can provide controlled and precise delivery of medications, which is particularly important for patients who require ongoing treatment, such as those with diabetes, cancer, or chronic pain. These pumps can be programmed to deliver medication at a specific rate or in specific amounts over a certain period of time, depending on the patient's individual needs. Some common types of drug delivery pumps include insulin pumps, infusion pumps, syringe pumps, and enteral feeding pumps.

Insulin pumps can deliver insulin at flow rates ranging from 0.025 $\mu\text{L/hr}$ to 25 $\mu\text{L/hr}$ and the pressure generated is typically less than 140 Pa [81]. Infusion pumps can deliver fluids and medications at rates ranging from a few millilitres per hour up to several hundred millilitres per hour. Infusion pumps are designed to generate pressure varying from a few kPa up to 700 kPa in some high-pressure applications [82]. Syringe pumps deliver medication at a rate as low as 0.1 mL/hr up to 150 mL/hr [83].

The human body contains several types of peristaltic pumping systems commonly known as biological pumps, such as the veins, esophagus, intestines, ureter, uterus, and bile duct. When any of these organs malfunction, external pumps are required to compensate for inadequate fluid transport. The diversity of fluids involved in each biological process and their specific properties necessitates a specific fluid flow and pressure range for proper organ function. To illustrate this, a comparison of these parameters in the veins, esophagus, and intestines is presented below [84].

Human veins and muscles utilize muscular contractions and valves to propel blood through the veins towards the central part of the body. Skeletal muscles, which are responsible for body movement, indirectly compress veins to circulate blood from the extremities towards the core of the body. Considering the vena cava dimensions approximately 20-30 mm diameter and 40 cm length, the flow rate for this particular vein varies between 2-3 L/min with a pressure of 12-17.3 kPa [85][86].

The human esophagus and the intestine, which are both part of the gastrointestinal tract, use propulsive peristalsis to facilitate transportation. Furthermore, the intestine exhibits stationary peristalsis, employing pendular mixing motions to enhance nutrient absorption. The linear velocity of the fluids in the esophagus is in the range between 2-5 cm/s with a pressure varying from 1.33 kPa to 6 kPa [85][87]. In the intestine, however, the fluids flow at a linear velocity of 0.001-0.5 cm/s and a pressure ranging from 5-16.6 kPa [85][88].

The aforementioned reveals a significant variation in the fluid flow rate and pressure range for biological, medical, and pharmaceutical applications. In this thesis, the focus is on drug delivery

system application meaning a flow rate from few $\mu\text{L}/\text{min}$ up to few mL/min and a pressure from hundred pascals to a few kilopascals. It is clear that for drug delivery applications, the use of high-precision devices is necessary. Moreover, design requirements, such as small size, biocompatibility, sufficient displacement to achieve desired flow rates, generating enough pressure for fluid movement, safe operation for an extended time, stable flow rates, and low power consumption, are desired.

Micropumps are an emerging technology with potential impact on the biomedical field. However, their reliability, biocompatibility, power consumption, and integration with other microfluidic systems require comprehensive evaluation.

In this chapter, the fundamentals of micropumps and an analysis of micropumps technology are included. Moreover, this chapter studies the fabrication of two different biocompatible micropumps out of single-layer electroactive polymers as drug delivery systems. Various prototypes with different actuation concepts and manufacturing techniques are presented in this chapter. Although both types of micropumps failed to produce fluid flow, the developed actuation concepts and manufacturing techniques may serve as a foundation for a range of other EAP-based devices.

2.1. FUNDAMENTALS OF MICROFLUIDIC PUMPS

The equations that rule the movement of a homogeneous fluid are the conservation equations: conservations of mass, conservation of momentum and conservation of energy. They provide information about the velocity, the pressure and the temperature field in a channel, which are very significant properties in the microfluidic field. Inside channels, and more specifically in micropumps, the fluids flow following these rules. The governing equations are summarized in Appendix A.

Microfluidic pumps or micropumps are small devices capable of providing a constant and precise flow in a laminar regime without generating turbulences. A laminar regime or laminar flow occurs when a fluid flow in parallel layers without contact or interaction between them. In contrast, in a turbulent regime, the fluid layers do not travel in parallel but intertwine chaotically.

The Reynolds number Re can be used to determine whether the transport of a fluid belongs to a laminar or to a turbulent regime. It refers to the relation between inertial and viscous forces in a fluid inside a channel. The Reynolds number is mathematically expressed as:

$$Re = \frac{\rho v D}{\mu_d} \quad \text{Eq 2.1}$$

where ρ is the density of the fluid, v its velocity, D the diameter of the channel and μ_d the dynamic viscosity of the fluid. Therefore, the flow is not only determined by the fluid properties, but also by the channel geometry.

For values of the Reynolds number below 2300, the laminar flow tends to dominate. In a laminar flow, the viscous forces are dominant respect to the inertial forces. A transition regime is observed

for values of the Reynolds number in the range between 2300 and 4000. Both laminar and turbulent flow cohabit in this range and it is difficult to establish a clear boundary between them. Finally, the turbulent regime dominates for values of the Reynolds number over 4000. Here, inertial forces are predominant. These ranges are defined for a channel with a circular shape. The Reynolds number thresholds between regimes vary depending on the geometry of the channel cross-section, due to the distinct interaction of the fluid layers with the channel walls.

The fabrication techniques used in this work only permit the manufacturing of rectangular channels. Thus, the equivalent diameter is used to calculate the corresponding circular cross-section from a rectangular one. The equivalent diameter refers to the diameter of a circular tube that, for a given flow, provides the same pressure loss or resistance as its equivalent rectangular duct. A round shape provides less friction to the fluid. Therefore, the equivalent diameter of a rectangular shape is lower than the diameter of the circle with the same area. The equivalent diameter D_e of a rectangular tube can be calculated following the Huebscher equation [89]:

$$D_e = 1.3(a \cdot b)^{0.625} / (a + b)^{0.25} \quad \text{Eq 2.2}$$

where D_e corresponds to the equivalent diameter in mm, a is the length of the major side of the rectangular section in mm and b is the length of the minor of the rectangular section in mm side or the height.

Table 2.1: Fluid rate for various fluids in laminar (Re = 1, Re = 1000), transient (Re = 3000) and turbulent (Re = 4000) regimes.

	Dynamic viscosity (kg/(m·s))	Density (kg/m ³)	Channel diameter (μm)	Fluid linear velocity (cm/s)			
				Re = 1	Re = 1000	Re = 3000	Re = 4000
Water	8.940E-04	1000	20	4.5	4470	13410	17880
			300	0.3	298	894	1192
			1000	0.1	89	268	358
Ethanol	1.074E-03	789	20	6.8	6806	20418	27224
			300	0.5	454	1361	1815
			1000	0.1	136	408	544
Oil	8.100E-02	920	20	440	440217	1320652	1760870
			300	29.3	29348	88043	117391
			1000	8.8	8804	26413	35217

The small size of micropumps and the low fluid speed typically lead to a very low Reynolds number, in the range from 1 to 100. For example, Table 2.1 compares the fluid velocity (in cm/s) of various fluids for three characteristic channel diameters (20 μm, 300 μm and 1000 μm) and three regimes: laminar (Re = 1, Re = 1000), transient (Re = 3000) and turbulent (Re = 4000). Three common substances are chosen for the calculations: water, ethanol and oil (from lowest to highest viscosity). All fluid density and viscosity parameters are given for 25°C.

Table 2.1 highlights the differences between laminar and turbulent regimes on these channel diameter scales. The velocities of the laminar, transient and turbulent regimes for the chosen substances range from a couple of cm/s to several thousand m/s. Considering the size of the microdevices, it is evident that it is extremely difficult for fluids to flow in these devices in transient or turbulent regimes. Thus, only laminar regime is feasible. Moreover, in viscous fluids such as oils, even in laminar regime, the flow within small channels (e.g., a 20 μm diameter) is 440 cm/s. Here,

it is demonstrated that in these microdevices the viscous forces are much larger than the inertial forces, and therefore viscous fluids are extremely difficult to move within the channels.

In the next section, micropumps able to transport fluids at laminar regime for biological, chemical and medical applications are described.

2.2. TYPES OF MICROPUMPS

Micropumps, in contrast to common MEMS-devices, used to be fabricated by scaling down the macropumps and using their main working principle. Now, micropumps are fabricated with a great amount of different operating principles. In general, they are classified in two main categories: mechanical and non-mechanical pumps.

Mechanical pumps normally use elements like check-valves or vibrating membranes to deliver a constant fluid flow in each pump cycle, while non-mechanical pumps transform another energy form to kinetic energy giving a momentum to the fluid. Mechanical pumps have a greater size and deliver larger flow rates than non-mechanical pumps.

2.2.1. NON-MECHANICAL MICROPUMPS

Some examples of non-mechanical micropumps are magneto-hydro-dynamic [90], electro-hydro-dynamic [91], electro-osmotic [92], chemical [93], osmotic-type [94], capillary-type [95], electrowetting [96] and bubble-type micropump [97]. Within this section electro-hydro-dynamic pumps and electrokinetic pumps are further explained.

Electro-hydro-dynamic (EHD) pumps are based on electrostatic forces acting on dielectric fluids [91]. These pumps can be categorized into three main types: induction pump [98], injection pump [99] and ion-drag pump [100].

The EHD induction pump consists in inducing charge at the material interface. A traveling wave of electric field drags the induced charges along the wave direction. A fluid velocity of several hundred micrometres per second can be achieved with this pump type.

In the EHD injection pump, the Coulomb force is responsible for moving ions injected from one or both electrodes by means of electrochemical reactions. Richter et al. [99] demonstrated this pump principle with micromachined silicon electrodes. Furuya et al. [101] used electrode grids, standing perpendicular to the device surface, in order to increase the pressure gradient. This pump can deliver 0.12 ml/min with a drive voltage of 200 V.

The ion-drag pump based its working principle on the direct injection of free charges into a dielectric fluid medium. A sharp corona source, or emitter electrode, is used to inject ions and an oppositely charged electrode, known as a collector electrode, attracts them. The flow of ions between the anode and cathode drags the adjacent fluid and causes a net flow to occur. This type of EHD pumping was the first to be investigated by the scientific community and is therefore well documented [100] [102]. However, the biggest downside to this type of pumping is that it deteriorates and dulls the emitter electrode as more and more of its material is injected into the fluid. In addition, over time the additional charges present in the working fluid damage the unique electrical properties of the dielectric fluid, causing the pumping performance to decline and fail.

Therefore, although this type of pumping has been studied much more extensively than the other types of EHD pumping and is capable of relatively high-pressure generation, its use is not recommended for processes requiring continuous or long-term operation [91].

Electrokinetic pumps [103] move conductive fluid by means of an electrical field. The electrokinetic phenomenon can be divided into electrophoresis [104] and electro-osmosis [105]. Electrophoresis is the effect by which charged species in a fluid are moved by an electrical field relative to the fluid molecules. In contrast to electrophoresis, electro-osmosis is the pumping effect of a fluid in a channel under the application of an electrical field. A surface charge exists on the channel wall. The surface charge comes either from the wall property or the adsorption of charge species in the fluid. In the presence of an electrolyte solution, the surface charge induces the formation of a double layer on the wall by attracting oppositely charged ions from the solution. An external electrical field forces the double layer to move.

Although the pressure and the fluid flow in these kinds of pumps are very high, the fluids need to have specific electrical properties to allow the movement. Thus, these pumps are not practical for the majority of medical and pharmaceutical applications.

2.2.2. MECHANICAL MICROPUMPS

Mechanical micropumps examples are electrostatic [106], piezoelectric [107], thermo-pneumatic [108], shape memory alloy [109], bimetallic [110] and ionic conductive polymer film [111]. In this section, the focus is on the piezoelectric and the thermo-pneumatic types.

Figure 2.1(a) shows a schematic of a piezoelectric diaphragm pump [112]. A membrane fabricated with a piezoelectric material deforms while voltage is applied. The displacement of the membrane generates a change in pressure due to the increase/decrease of the volume in the chamber. By deforming the piezoelectric membrane with a certain frequency, the fluid flows inside the chamber and then outside the chamber leading to a constant flow. In this type of pump, any kind of fluid can be pumped without requiring any special property, unlike the previous pumps shown.

Advantages of piezoelectric actuation based micropump are their fast response and simple structure, which however provides large actuation forces. The main drawbacks are a high actuation voltage and a complex fabrication process.

The thermo-pneumatic [108] type actuation mechanism for micropumps is also an important category in the mechanical type micropump classification. This kind of mechanism can be based on either vibrating diaphragm or peristaltic movement.

Figure 2.1(b) shows a schematic view of a thermo-pneumatic micropump. The air inside the air chamber is periodically and alternatively heated and cooled using a combination of heater and cooler. The air chamber and pump chamber are separated by a diaphragm. The expansion and compression of air in the air chamber causes the pumping of liquid in the pump chamber with the help of inlet and outlet valves.

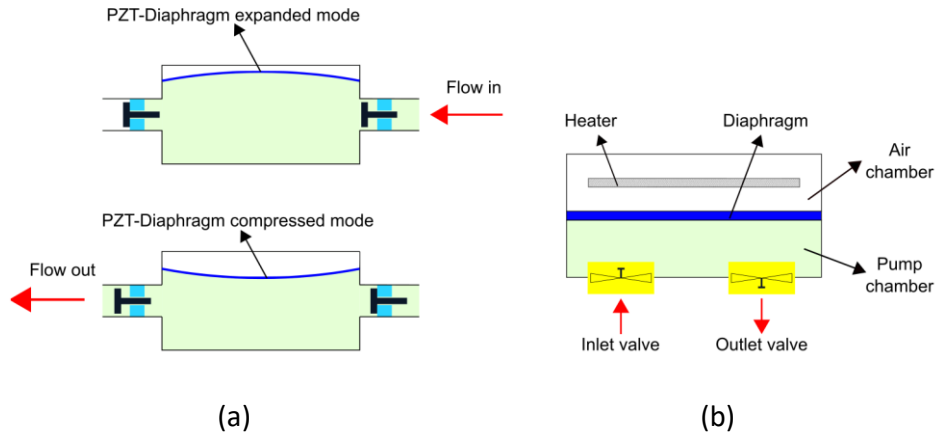


Figure 2.1: (a) Layout of a piezoelectric diaphragm pump (adapted from [112]). (b) Schematic view of a thermo-pneumatic micropump (adapted from [108]).

Some of the advantages present in the thermo-pneumatic pumps are: 1) they can be easily fabricated using soft lithography techniques and 2) despite the very small actuation of the diaphragm, the membrane undergoes very large deflections.

CONFIGURATIONS FOR MECHANICAL MICROPUMPS

Mechanical micropumps have different configurations depending on the actuation principle on which they are based or the power/fluid flow needed for each application. Some configurations of mechanical micropumps are rotary pumps, check-valve pumps, valveless rectification pumps and peristaltic pumps.

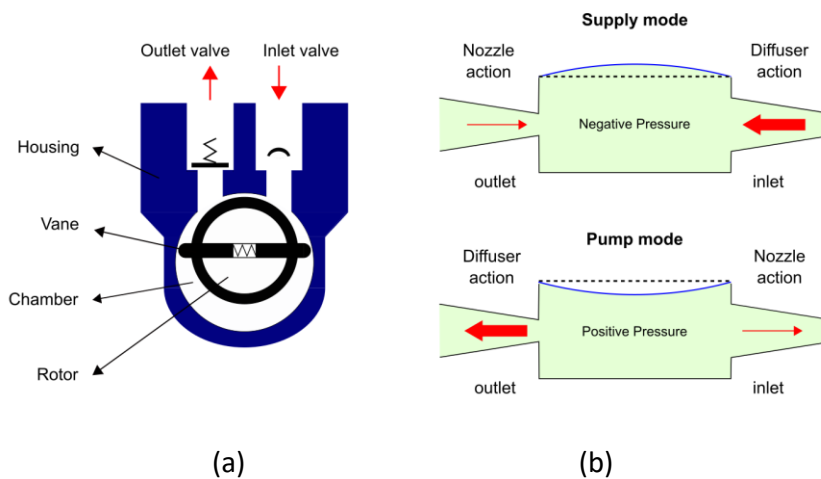


Figure 2.2: (a) Rotary pump. (b) Valveless rectification pump.

In a rotary pump, the fluid is retained in a chamber and then discharged in a smooth flow by the movement of a rotor with a vane. All types of fluids can be pumped with this configuration, only exceptions are corrosive fluids which could damage the chamber. If dealing with high viscous fluids, the only limitation can be the minimum speed necessary to fill the casing, in order to successfully move the maximal quantity of fluid while the rotor moves.

The design of the rotatory pump is simple, as it can be observed in Figure 2.2(a). It is mainly based on a chamber, two valves -inlet and outlet valves-, a housing and a rotor. The rotary pumps include: a cam-and-piston, an internal-gear, a lobular, a screw and vane pumps.

Check-valve pumps are a very typical macroscale pump type and, for this reason, they were the first miniaturised type in microscale pumps. In general, a check-valve pump has a pump chamber, two check-valves and an actuator unit.

Valveless rectification pumps are similar to check-valve pumps, however, instead of using check-valves to control how the fluid flows, they use rectifying geometries such as a nozzle/diffuser or a Tesla structure. This also prevents the fluid from flowing backwards. Figure 2.2 (b) shows a valveless rectification pump. The upper drawing represents the pump in the supply mode, where the fluid is introduced in the chamber. The bottom layout represents the pump mode, where the positive pressure created due to the diaphragm membrane deformation allows the liquid to flow out the chamber through the diffuser element. Various researchers [113][114] have reported that flow rectification is not achievable in laminar flow for the nozzle/diffuser type of pump, whereas Gamboa et al. [115] proved in his studies that the flow for Tesla structure is achievable for Reynolds number higher than 200. New structures for the valveless rectification pumps such as bifurcation and triangles, as well as low frequency actuation ranges, are promising to reduce the Reynolds number [116]. Nonetheless, the results obtained are still far from the Reynolds numbers needed for biological applications, normally in the range of 1-10.

The last type of pump described in this section is peristaltic pump [117]. Peristaltic pumps, unlike check-valves, do not require the presence of external valves or passive valves for the flow rectification. The peristaltic pump consists of at least 3 chambers. These chambers move in a wave propagating motion leading to a displacement of the fluid in pulses in the desired direction.

In this work, peristaltic micropumps are chosen for the fluid transport. In the next section, the main reasons and characteristics of peristaltic micropumps for biological applications are described.

PERISTALTIC MICROPUMPS OUT OF ELECTROACTIVE POLYMERS

The aim of the work presented here is to develop microfluidic devices able to transport biological, pharmaceutical and medical fluids in a controlled and precise fashion.

Non-mechanical micropumps, such as electro-hydro-dynamic and electro-osmotic pumps, are very precise and gentle to fluids. In addition, they can achieve high fluid flow and high pressure. The main drawback of these micropumps is the electrical properties of the fluids required to induce the flow. This is not suitable for most medical and pharmaceutical fluids.

In mechanical micropumps, however, fluids do not need to fulfil special electrical properties to be transported. External power is supplied to the micropump to enable fluid flow. These micropumps provide high pressure, high flow rates and minimal backflow. However, some of the operating principles of these pumps are critical for biological applications. For example, in rotary pumps, fluids containing cells can be damaged or in check-valve pumps, fluids can clog the system and cause high pressure losses. In nozzle/diffuser pumps, laminar flow at low Reynolds is difficult to achieve and reverse flow is a critical problem. This behaviour can lead to extreme cellular fatigue, causing the cells to die or behave differently than usual.

To overcome these issues, peristaltic micropumps are here chosen as the ideal pump for biological applications. In a peristaltic pump, the fluid is only in contact with the walls of the tubing and chambers used for pumping. Thus, it is a very gentle fluid transport method. This allows the fluid to keep a high purity, avoiding contamination. It is very useful in medical and pharmaceutical applications, where sensitive fluids containing cells, bacteria and drugs need to be pumped. It also favours the use of peristaltic pumps with delicate or fragile liquids rather than with other pump designs, for example rotatory pumps.

Peristaltic micropumps are considered as very precise pumps for dosing applications. Moreover, they are easy to clean due to the lack of external parts like seals or valves. Here, only the tubing needs to be cleaned or replaced to avoid contamination when different fluids are used. This results in reduced maintenance times and reduced downtime.

Examining the actuation method utilized in peristaltic pumps is important for assessing the capabilities and possibilities of such systems. Actuators can be evaluated and compared based on three key parameters: the force they can exert, the displacement they can achieve, and their frequency response. Pneumatic and hydraulic actuators are capable of producing large forces and large displacements, but their frequency response is typically low, around a few Hz. Conversely, piezoelectric actuators have a high frequency response, in the range of hundreds of MHz and above, but they typically produce small displacements in the micrometer range. Dielectric Elastomer Actuators fall in between, with small forces, typically on the order of few newtons, but large displacements, in the range of millimeter to centimeters, and frequency response of up to 1 kHz, which makes them well-suited for high-speed pumping applications. This allows precise flow rate control in addition to high flow rate capability.

Dielectric elastomer actuators are a promising technology for pumping applications in the medical and pharmaceutical fields. One of the main advantages of DEAs is their high energy density (up to $0.4 \text{ J}\cdot\text{cm}^{-3}$), which allows them to generate a large amount of force for a given volume. This makes them well suited for use in small, portable medical devices, such as wearable pumps for administering drugs. For magnetic actuators the energy density is in the range of $0.01\text{-}0.1 \text{ J}\cdot\text{cm}^{-3}$. Piezoelectric actuators, on the other hand, typically have lower energy density, typically in the range of $10^{-4}\text{-}10^{-3} \text{ J}\cdot\text{cm}^{-3}$.

The lifetime of DEAs is very high, lasting over hundred thousand cycles of actuation. This directly impacts the overall performance and reliability of the peristaltic pump. A long lifetime is highly desirable as it allows for the pump to function consistently and effectively over a prolonged period of time. This is especially important for applications such as medical and pharmaceutical use, where the pump must be reliable and operate consistently for long periods of time. It ensures the pump can operate for a long time without the need for frequent maintenance or replacement. This results in lower costs, increased reliability, and greater convenience for users.

DEAs also have a simple structure and can be fabricated using low-cost and scalable methods. This makes them an attractive option for commercialization and mass production of medical devices, which can help to reduce costs and increase accessibility.

The biocompatibility of dielectric elastomer actuators has been extensively studied and has been found to be favourable. This is due to the use of non-toxic and biocompatible materials, such as silicone, in their construction. As a result, DEAs do not elicit adverse reactions or cause harm to living tissue or biological fluids when in contact.

Additionally, DEAs are operated at relatively high voltage, which is required to create the large electrostatic forces that cause the DEA to deform, this high voltage operation can be a major drawback of DEAs, as it requires specialized power electronics and safety measures to ensure safe operation.

Due to the above reasons, the peristaltic pump configuration actuated by the action of dielectric elastomer actuators is the desired pump type used within this thesis. In the following sections, two peristaltic pump prototypes are described and characterized. Both types of peristaltic pumps are based on a single prestressed diaphragm made of an elastomer material.

In the peristaltic pump prototypes (chapter 2) and also in the pumping micromixer (chapters 3, 4 and 5), the actuator elements are driven by rectangular signals with a phase shift to produce peristaltic motions of contraction and relaxation, like the ones occurring in some organs in the human body. Segments of the alimentary canal alternately contract and relax, allowing the food to be transported (Figure 2.3).

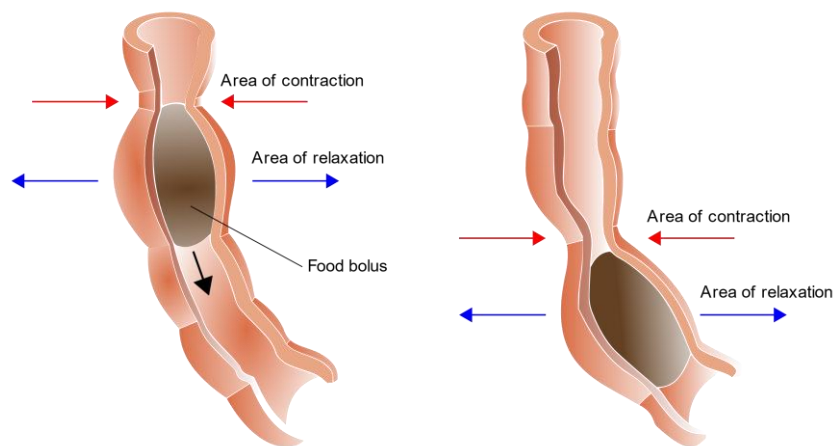


Figure 2.3: Layout of the peristalsis in the human body (based on [118]).

In this chapter, the prototypes, named peristaltic pump – type 1 and type 2, differ in the working principle. In the peristaltic pump – type 1, three actuators located in series below the channel and in the fluid flow direction generate a propagation wave of the fluid. This prototype is fabricated with two different methods:

- 1) Liquid elastomer film (section 2.3)
- 2) Solid elastomer film (section 2.4)

The peristaltic pump type – 2 (section 2.5), however, is based on two arrays of three actuators located in parallel to the channel. The pressure difference acquired along the channel allows the fluid movement. Type 2 is fabricated with the solid elastomer film method.

2.3. SINGLE-LAYER PERISTALTIC PUMP – TYPE 1 LIQUID FILM

In this section, the peristaltic pump – type 1 fabricated with the liquid film method is described. Its working principle, an analytical model and its characterization are included here.

This work was performed in the École Polytechnique Fédérale de Lausanne (EPFL) in Neuchâtel (Switzerland) in the LMTS group directed by Prof. Herbert Shea.

2.3.1. WORKING PRINCIPLE

The main principle of the design of the peristaltic pump – type 1 is a single membrane made of an elastomer. On top and bottom of this membrane, electrodes are located in series, leading to three actuators (with the same shape) located in a line (more details in Figure 2.4). On top of these actuators, a rectangular cross-section channel of a much softer elastomer is located. The channel contains the fluid (Figure 2.5).

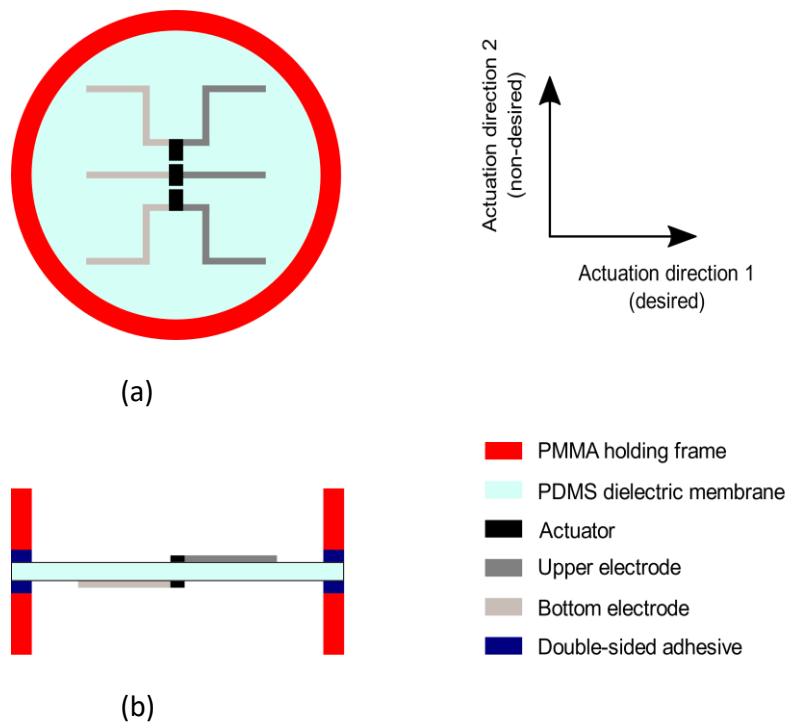


Figure 2.4: Geometry of the proposed peristaltic pump. (a) Top view and (b) cross-section of the device.

By applying voltage to the driving electrodes, a decrease in the elastomer thickness is observed but also an expansion in area, due to the main DEA principle. The channel -directly in contact to the actuators- moves at the same pace. While actuating the actuators with different phases, the difference of pressure acquired along the channel allows the fluid to flow.

As above mentioned, DEAs expand in area. For this application, only the expansion in the perpendicular direction to the channel length is needed. Thus, the optimization of actuator expansion (section 2.3.2) in this direction is critical to maximize the potential of the peristaltic pump. A scheme of the actuation directions is shown in Figure 2.4(a). The arrows show the direction of the actuation. Direction 1 is the main actuation direction (or desired direction), while direction 2 is the secondary direction.

Figure 2.4(a) represents the top view of the device. The red circles are rigid frames (PMMA). They hold the membrane prestretch with the help of a double-sided tape. Details about the materials

in use and the fabrication are explained in section 2.3.3 and in Appendix C. Figure 2.4(b) shows the cross-section view of the device: the passive and active width, excluding the frame zone. This figure is meant to provide a visual representation of the location of the electrodes in the device.

Figure 2.5 shows the channel structure in detail. The soft PDMS channel is depicted in dark green. Figure 2.5(a) presents the top view of the device with the fluid inlet and outlet. The device is symmetrical. Hence, the fluid inlet and outlet are reversible. Figure 2.5(b) displays the cross-section of the complete device. Here, the inner width of the channel and the width of the actuators coincide in size and in vertical position.

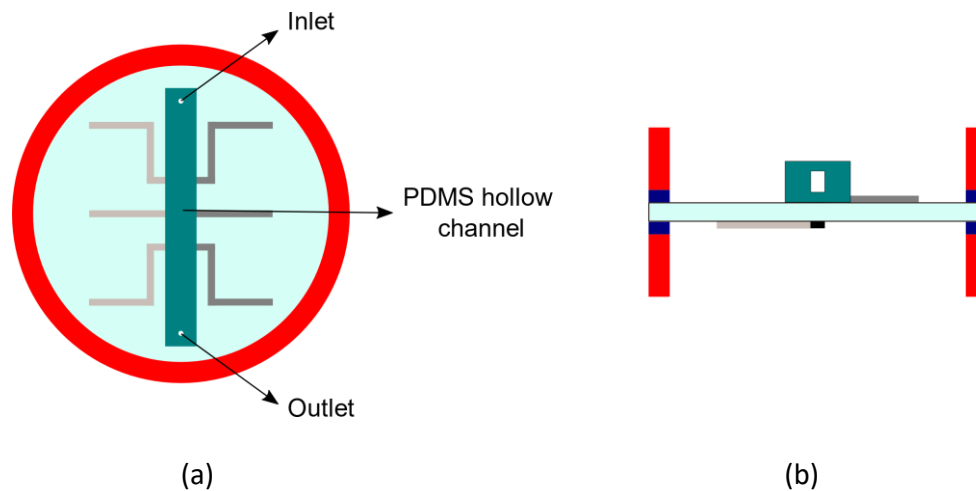


Figure 2.5: (a) Top view of the device with the hollow channel on top of the actuators. (b) Cross-section of the full device.

The diameter of the membrane is determined by the fabrication process. The electrode deposition method, based on stamping the electrode material on top of the elastomeric membrane, requires a circular device of 38.5 mm diameter. Thus, the devices larger than 38.5 mm or devices with non-circular distributions are not possible. The actuator width is determined by the minimum acceptable width of the electrodes possible with the stamping method (2 mm) and the length of the actuators is determined considering the total distance and the required space for connecting the necessary tubing posterior to the fabrication of the device and the possibility to increment the number of chambers in the future.

The maximal deformation of an actuator takes place on its border, i.e., on the line that separates the actuation region and the passive region. For this reason, the channel has the same width as the actuators, so that its walls expand at their maximum during actuation.

The materials for the fabrication of the actuators are Sylgard[®] 186 from Dow Chemicals [119] and, for the electrode, a homemade mixed of carbon black and solvents.

After all the geometry values and materials for the device are chosen, it is necessary to optimize the deformation of the actuators in the perpendicular direction of the fluid flow, to allow a greater deformation of the channel and thus, an increase in the pumping action. The PDMS membrane is bidirectionally prestressed in order to increase the actuation in one direction and decrease it in the other direction. Previous research has shown that a greater prestress of the membrane in the opposite direction than the desired one, leads to an increase of the deformation in the desired direction while applying voltage.

As demonstrated earlier in the hyperelastic section (section 1.2.1), it is challenging to predict the deformation of the PDMS due to its non-linear behaviour at very high strains. In the following section, an analytical model based on the Gent model for hyperelastic materials (section 1.2.1 B) is used to determine the deformation in the x and y axis of the actuator based on the applied voltage, the properties of the elastomer and the geometry of the actuator. This helps to predict how much deformation is theoretically expected in the actuators and the optimized values of prestretch in both directions.

By knowing the maximum deformation of the actuators and the maximum deformation of the channel, it is possible to first predict the volume difference when the actuators are turned on versus when they are turned off. Using the net volume, it is possible to predict the maximum fluid flow rate possible for this system under specific conditions of frequency and sequence of actuation of the actuators. Thus, it becomes feasible to predict the potential of these devices, compare them with other technologies, and contrast them with experimentally derived values.

2.3.2. ANALYTICAL MODEL

The analytical modelling of the actuation is done using a MATLAB[®] script where parameters like optimum prestretching values, stretch after actuation and failure modes, are calculated. The script and the modelling corresponds to the proposed model of Rosset et al. [120][121]. The deformation of the dielectric material is modelled with the considerations of a hyperelastic material following the Gent Model for Sylgard[®] 186 PDMS, described in section 1.2.1 B.

The first optimization done is the calculation of the optimum stretch after actuation, λ_{1a} . The stretch, λ , here is defined as the ratio between the final thickness after actuation and the initial thickness after manual prestretch. The first index represents the direction of actuation (1 for the desired actuation direction, perpendicular to the fluid flow), while the second index indicates actuation a .

The active region is defined as the width of the actuator, while the passive region is the width where there is no actuator. Obtained from the calculations at different prestretches, the active ratio r_a or the ratio between the active region and the total region (active region plus passive region) is derived.

Table 2.2. Fixed parameters for the optimization

Geometry		
Thickness after prestretch	50	μm
Actuator length	3.2	mm
Actuator width	2	mm
Active ratio (r_a)	0.01:0.01:0.99	
Gent model parameters		
Jm	16.62	
μ	365000	Pa
Electrical parameters		
E_{bd}	100	V/ μm
Relative permittivity	2.5	
Voltage	0:100:5000	V

The failure modes considered are divergence of the Gent model, loss of tension in the membrane and compression in the actuation direction. The values used for this optimization, in terms of geometry, Gent model and electrical parameters, are summarized in Table 2.2.

The minimum prestretch in the direction 1 is defined as the uniaxial case. The membrane is prestretched along direction 2 and allowed to relax along the other directions. The minimum prestretch in the direction 2 is predefined with a minimum value of 1. For simplicity, it is considered that the length of the actuator does not influence the final results.

After the calculations, it is concluded that the greater actuation is obtained when the active region or actuator width is small and there is a big passive zone where the actuator can expand. The optimum ratio obtained is 0.12, for which the optimum prestretch ps values obtained are $\lambda_{1ps} = 0.7027$ and $\lambda_{2ps} = 2.54$ for the actuation direction (1) and the perpendicular direction (2), respectively. The maximal theoretical stretch obtained after actuation is $\lambda_{1a} = 1.269$ or, in other words, a deformation of 26.9 % the initial width in the direction 1.

A second script is used in order to have a wide vision of all the possible prestretches and the stretch obtained with a fix value of optimization ratio (r_a). The combinations under study are the prestretches values using a fixed value for the ratio active width/total width of 0.12. The total amount of stretches after actuation obtained is 32955, plotted in Figure 2.6.

The regions not plotted are due to failure of the actuation. From blue to red, the colour bar shows the stretch obtained after actuation (λ_{1a}) in the desired direction, perpendicular to the fluid channel. The greater stretch after actuation, according to the data previously shown, is displayed in the box in the figure, together with the optimal prestretch. The darker red ellipsoidal region shows the maximal actuation range possible. The prestretch ranges where the actuation stretch is over 20 % are:

$$0.56 < \lambda_{1ps} < 1.08$$

$$1.46 < \lambda_{2ps} < 3.50$$

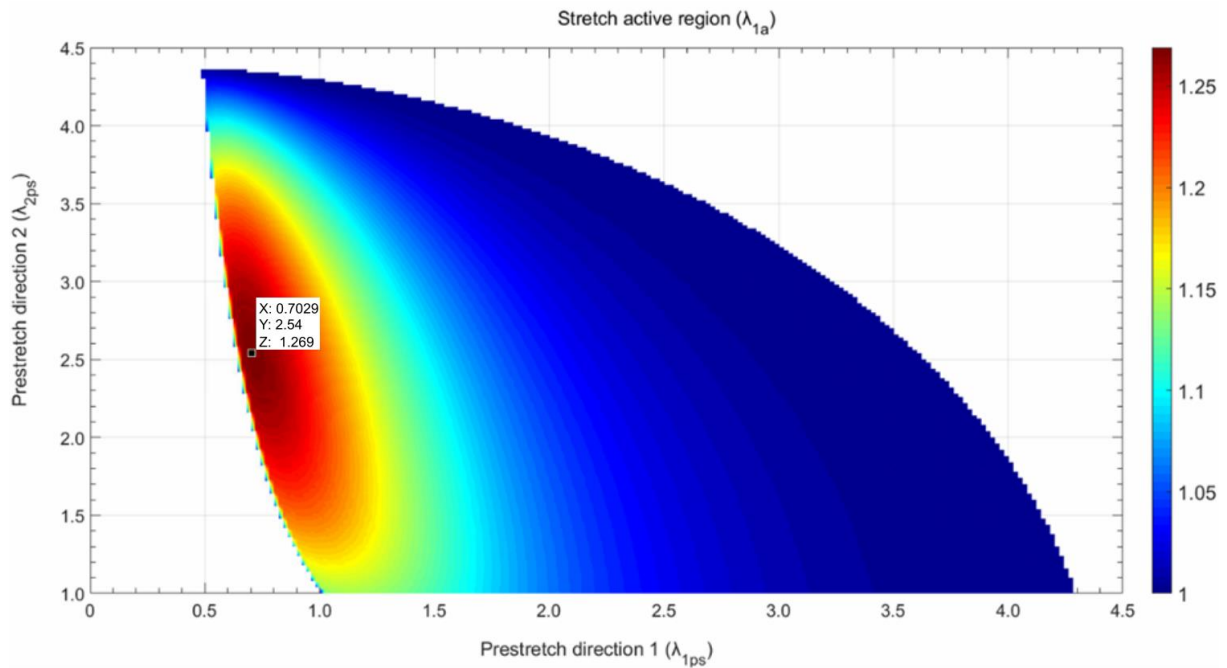


Figure 2.6: Actuation stretch obtained for different bidirectional prestretches from 0 to 4.5 for direction 1 and from 1 to 4.5 for direction 2. The actuation stretch obtained is in the range between 1 and 1.269 (right bar).

To decrease the probability of failure and add some tension to the above prestretch of $\lambda_{1ps} = 0.72$ in the actuation direction, the values considered for the prestretch are $\lambda_{1ps} = 0.90$, for prestretch in actuation direction, and $\lambda_{2ps} = 2.2$, for the perpendicular direction. This leads to a stretch after actuation of $\lambda_{1a} = 1.24$, i.e., 24 % deformation.

The maximum possible deformation of the actuator allows the calculation of the optimum fluid flow obtained under ideal operating conditions. To assess the pumping conditions, the difference in initial chamber volume and final chamber volume, or in other words, the net volume, needs to be calculated.

The initial chamber volume corresponds to the dimensions of a single actuator chamber: 3.2 mm length, 2 mm width and 0.5 mm height (channel height). This results in a volume of 3.2 μL . As the actuator expands in area, the chamber volume increases. Assuming only a lateral deformation of 24 % of its initial width, the final chamber volume is 3.968 μL . The volume difference between activated and deactivated actuator is the fluid volume able to flow. Thus, 0.768 μL is the maximal expected net volume.

Following the considerations from Schimmelpfennig [122] for a three chamber peristaltic pump and a high flow rate sequence, the pumping sequence is as follows:

Actuator 1	Actuator 2	Actuator 3	
1	0	1	Step 1
1	1	0	Step 2
0	1	1	Step 3

Regardless of the total number of chambers, in the high flow rate sequence, two chambers are consistently closed (indicated as 1) while the other chambers remain open (represented by 0). When there are three chambers, this results in two chambers being closed and one chamber being open throughout the cycle. The pattern begins with “1 0 1”, and the closed chambers move from left to right in n steps, where n corresponds to the total number of chambers. The high flow rate sequence produces $n-2$ boluses of fluid during a time period of n steps. The flow rate Q can be calculated using the formula $Q = ((n-2)/n)Q_0$, whereas Q_0 corresponds to the channel volume divided by one step time. For the particular case of three chambers, the flow rate is then $Q = Q_0/3$. The pump transports only 1/3 its chamber volume per cycle.

Based on the factors above mentioned and the peristaltic pump's design, the flow rate results in 0.256 $\mu\text{L}/\text{cycle}$. Considering a 1 Hz actuation frequency, the expected fluid flow corresponds to 15.36 $\mu\text{L}/\text{min}$ or a linear velocity of 15.36 mm/min (for a channel of 2 mm width and 0.5 mm height).

Following the calculations for the Reynolds number and for the equivalent diameter described in section 2.1 for the diverse fluids, a very low Reynolds number is obtained. A very laminar regime is expected in this micropump. Thus, these pumps turn out to be unsuitable for high viscous fluids like oil. Table 2.3 shows the Reynolds number for diverse fluids at 25°C considering a linear velocity of 15.36 mm/s and an equivalent diameter of 1.03 mm.

Table 2.3: Calculated Reynolds number for 1 Hz actuation and diverse fluids.

Fluid	Density (kg/m ³)	Dynamic viscosity (kg/(m·s))	Reynolds number
Water	1000	8.940E-04	0.295
Ethanol	789	1.074E-03	0.194
Oil	920	8.100E-02	0.003

2.3.3. DEA FABRICATION - LIQUID FILM METHOD

The fabrication method of these actuators follows the standard fabrication method for dielectric elastomer actuators done by the EPFL group “LMTS: Soft Transducers Lab” in Neuchâtel, led by Prof. Shea. A detailed protocol and video with the general fabrication method was previously published by Rosset et al. [123].

The fabrication of the full device, including the channel, is described in Appendix C of this work. In this section, the key features of the fabrication are highlighted.

The elastomer membrane is made of Sylgard® 186 from Dow Chemical®. Sylgard® 186 is based on two components, A and B, and the mixing ratio used is 10:1, respectively. To produce a homogeneous film, the PDMS mixture is cast with a variable gap applicator on top of a Polyethylene Terephthalate (PET) substrate. To enhance the cross-linking, the film is heated for 1 hour at 80°C. After casting, the thickness of the films is $95 \pm 2 \mu\text{m}$.

The membrane is prestretched according to the values obtained during the analytical modelling. The prestretching is done bidirectionally in the directions 1 and 2, with magnitudes of 0.9 and 2.2, respectively. To hold the prestretch, a double frame of polymethyl methacrylate (PMMA) 3 mm thick is attached to the membrane.

After prestretching, the elastomer thickness is $47 \pm 2 \mu\text{m}$ thick. This thickness measurement is essential to avoid electrical breakdown, in case the membrane is thinner than expected. The dielectric breakdown for Sylgard® 186 is 100 V/ μm . This leads to a maximal applied voltage of 4700 V for a 47 μm thick membrane.

The electrode material is based on a mixture of carbon black, silicone elastomer and isooctane. The electrodes are pad printed on top and bottom of the prestretch elastomer membrane. Due to the polymeric composition of the electrodes, their cross-linking is crucial. This is done by heating the electrodes 1 hour at 80°C. The thickness of the electrode with this method is approximately 3 μm .

Figure 2.7(a) presents the device after depositing the electrodes. To achieve the calculated active ratio ($r_a = 0.12 = \frac{2 \text{ mm active width}}{16.7 \text{ mm total width}}$), PMMA frames are bonded on top and bottom of the membrane (Figure 2.7(b)).

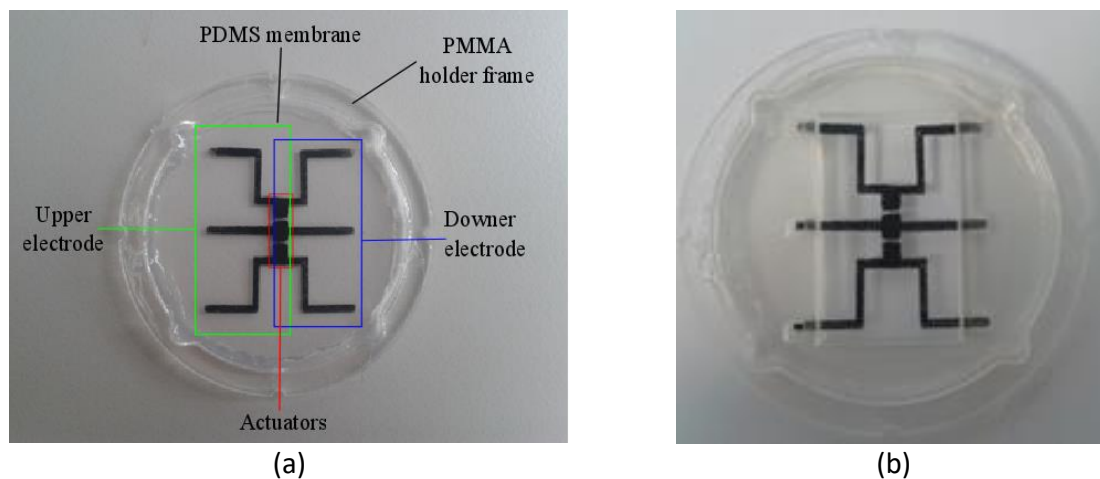


Figure 2.7: (a) Photo of the preliminary device. (b) Preliminary device with the PMMA frames on top and bottom to obtain the exact active ratio.

For this peristaltic pump, the channel should also be flexible and with a low Young's modulus. The microfluidic channel deforms due to the actuator displacement at the bottom of the channel. Therefore, PDMS is also used for the channel but with a much lower Young's modulus than that

of the elastomer layer of Sylgard[®] 186, MED4086 from NuSil[®] [124]. The properties of this material are found in Appendix C, Table C.1.

For the fabrication of the channel, three PDMS layers are needed: top (50 μm thick), wall (500 μm thick) and bottom (50 μm thick). The fabrication is based on the lamination process:

- 1) Cast the PDMS layers as thin films
- 2) Laser cut - for defining the shape of each layer
- 3) Plasma O₂ - for bonding the layers

In Figure 2.8, cross-sections of the device are represented. On the left, the dielectric membrane with the top and bottom electrodes and the channel located above. On the right, each layer of the channel and their final thickness. In the figure, the inside hollow of the channel corresponds to the width of the actuators.

Finally, the device is both electrically and fluidically connected by using flexible tubes.

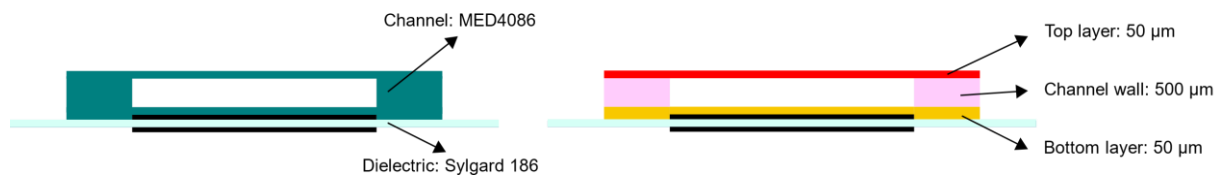


Figure 2.8: Cross-section of the channel geometry: consisting of a layer of 50 μm at the bottom, a channel wall of 500 μm and a layer of 50 μm at the top.

2.3.4. CHARACTERIZATION

A. Characterization of the deformation

In this section, the deformation of the actuators with respect to the applied electric field is under study. The measurement setup consists of:

- A 4-channel high voltage power supply
- A Dino-Lite digital USB-microscope
- A LabVIEW program

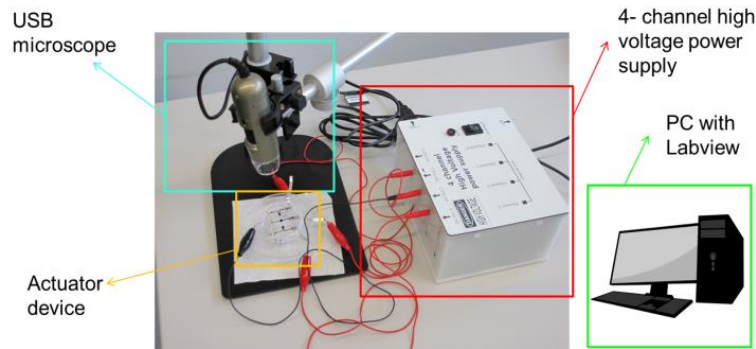


Figure 2.9: Measurement setup for characterizing the displacement of the actuators.

The 4-channel voltage supply was developed during the Peta-Pico-Voltron Project [125]. It is controlled by a LabVIEW program. The LabVIEW program synchronizes the voltage with the image captured by a Dino-Lite digital USB-microscope. Thus, the displacement/stretch of the actuator at a certain voltage is determined. Figure 2.9 shows an image of the measurement setup with a description of its elements.

The first measurements are devoted to the knowledge of the amount of stretch obtained at different electric fields in the directions 1 and 2.

Figure 2.10 and Figure 2.11 display the values obtained. On the top left of the figures, an image of the actuator with red arrows pointing in the direction of the actuation is shown. The measured actuator is the one in the middle of the membrane. In this device, the actuators are held with a prestretch of $\lambda_{1ps} = 0.9$ and $\lambda_{2ps} = 2.2$, and an active ratio $r_a = \frac{2 \text{ mm}}{38.5 \text{ mm}} = 0.05$.

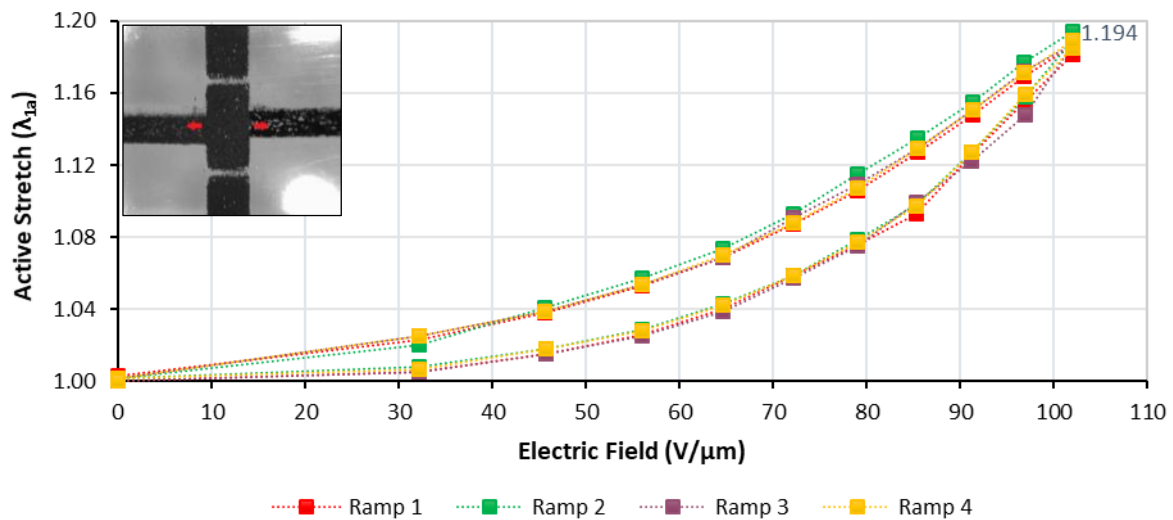


Figure 2.10: Actuation stretch versus voltage in the direction 1 of actuation or desired direction. Rectangles correspond to measurement points, while dotted lines are only a visual guidance. On the top left of the graph, a photo of the device with red arrows along direction 1 is shown.

The voltage-deformation hysteresis curves are shown. The ramps are taken in 11 points from 0 V to a maximal voltage of 5000 V (102 V/μm) and back from 5000 V to 0 V. In each point, the applied voltage stays constant for 5 seconds and then switch to the next value of the ramp. All ramps show very similar values of actuation stretch for the same voltages. For each ramp, the active stretch (y

axis) during charging is lower than the active stretch during discharging. The deformation of the actuators is retained when moving from a high to low voltage (discharging). DEAs are well-known for their rapid response to an electric field. Thus, this can be caused by a poor electrical connection between electrodes and power supply.

The middle actuator presents the following stretches at the maximal voltage ($V= 5000 \text{ V}$, $102 \text{ V}/\mu\text{m}$) of:

- $\lambda_{1a} = 1.194$ (desired direction, perpendicular to the fluid flow)
- $\lambda_{2a} = 1.048$ (fluid flow direction)

The theoretical analysis shows a maximal actuation in the desired direction of $\lambda_{1a} = 1.24$ (section 2.3.2) for an active ratio of $r_a = 0.12$ and an electric field of $100 \text{ V}/\mu\text{m}$. It corresponds to 5 % more deformation in the theoretical results than in the real case. Moreover, the parameters used for the middle actuator are meant to have better results than that of the theoretical prediction due to 1) a lower active ratio $r_a = 0.05$, i.e., more passive region to expand and 2) a higher electric field $102 \text{ V}/\mu\text{m}$.

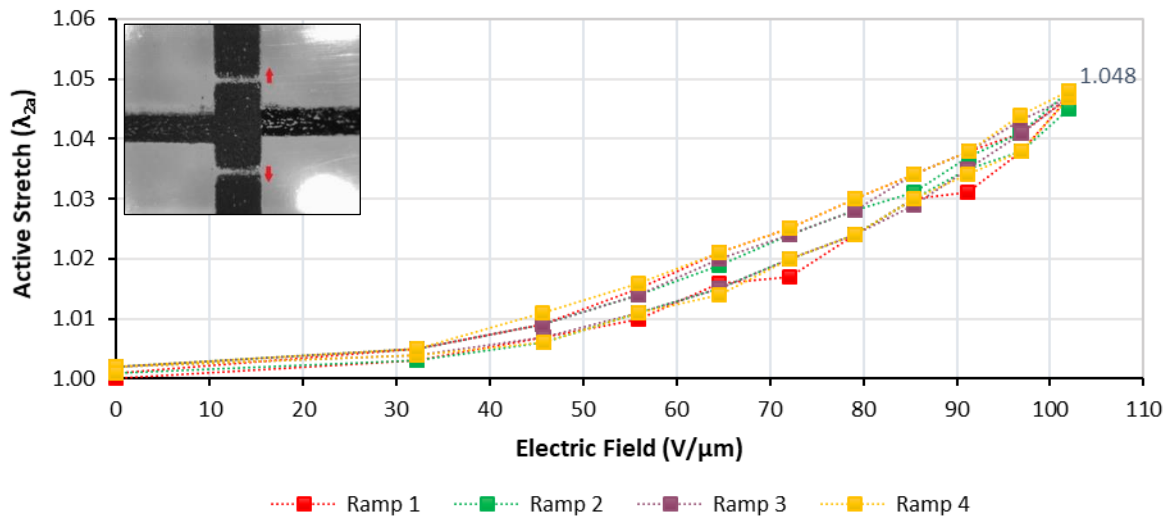


Figure 2.11: Actuation stretch versus voltage in the direction 2 of actuation. Rectangles are measurement points, while dashed lines are only a visual guidance. On the top left of the graph, a photo of the device with red arrows along direction 2 is shown.

In the next step, the same actuator is tested with an active ratio of $r_a = \frac{2 \text{ mm}}{16.7 \text{ mm}} = 0.12$. To do so, a PMMA frame is located on top of the elastomer to reduce the passive region width (from 36.5 mm to 14.7 mm). A PMMA laser cut frame with an inner hollow (a rectangle with a Room Temperature Vulcanizing or RTV double sided tape) is attached both on top and bottom of the membrane.

Figure 2.12 shows a graph with the values of the middle actuator without the frame or $r_a = 0.05$ (NF, measured first), and with the frame or $r_a = 0.12$ (F). As it can be observed in the graphs, the actuator with the frame has a slightly bigger actuation than the one without the frame. According to the theory, this is not possible: the more passive region there is around the actuator, the more actuation stretch should be obtained.

A possible explanation to this phenomenon is that the actuator performance improves over time. This has already been proven in the case of dielectric stacked actuators when the actuation increases with a certain number of actuations at the beginning, leading to a high increase of the deformation during the life cycle.

From this point on, since there is not a big difference between having a frame or not, the following devices are manufactured with a frame in order to give more rigidity to the system.

The analytical model as it is formulated is useful to characterize the performance of a single actuator only surrounded by passive region. The designed peristaltic pump is based on three actuators located in series. Therefore, it is important to know the influence of one actuator on the following when only one of them is active.

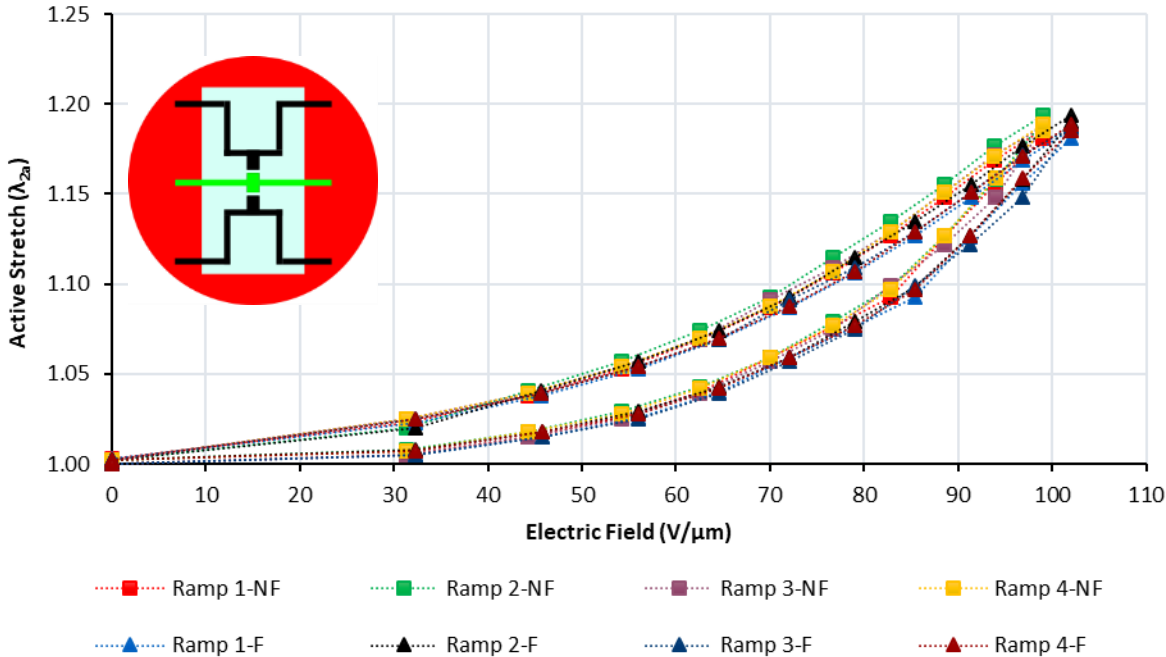


Figure 2.12: Characterization of the deformation of the actuator with active ratio 0.12 (frame, F) and active ratio 0.05 (no frame, NF). Dotted lines are only a visual guidance. On the top left of the graph, a layout of the device with frame is shown. The middle or measured actuator is highlighted in green.

The deformation produced by the upper actuator on the remaining actuators is measured with the measurement setup shown in Figure 2.9. In Figure 2.13, the upper actuator (in green) is actuated, while the measurement points are coloured with the same colour as in Figure 2.14, for a better understanding of the data. Here, only the displacement in the desired direction and the ascending ramps (from 0 until $100 V/\mu m$) are represented for clarity.

The actuation in the above part of the second actuator (red line) shows a maximal deformation of 14 % in the direction 1 at $99 V/\mu m$. For the lower part of the second actuator (green line) the deformation is 10 %. For the third actuator the deformation is 4.1 % and 1.4 % for the upper part (purple line) and for the lower part (yellow line), respectively.

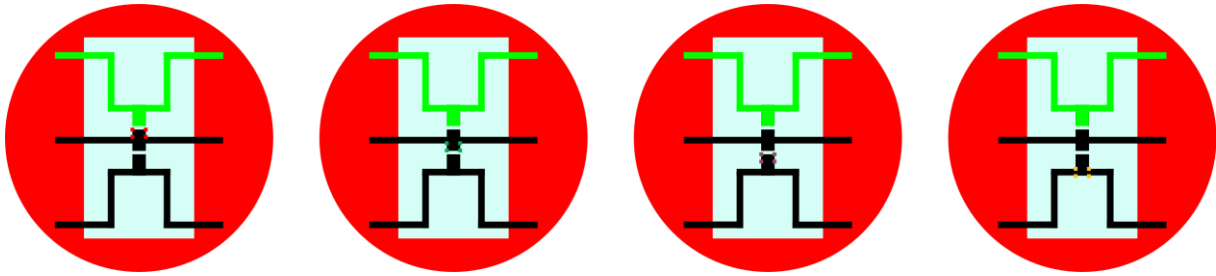


Figure 2.13: Layouts of the points taken for the measurement of interaction between actuators.

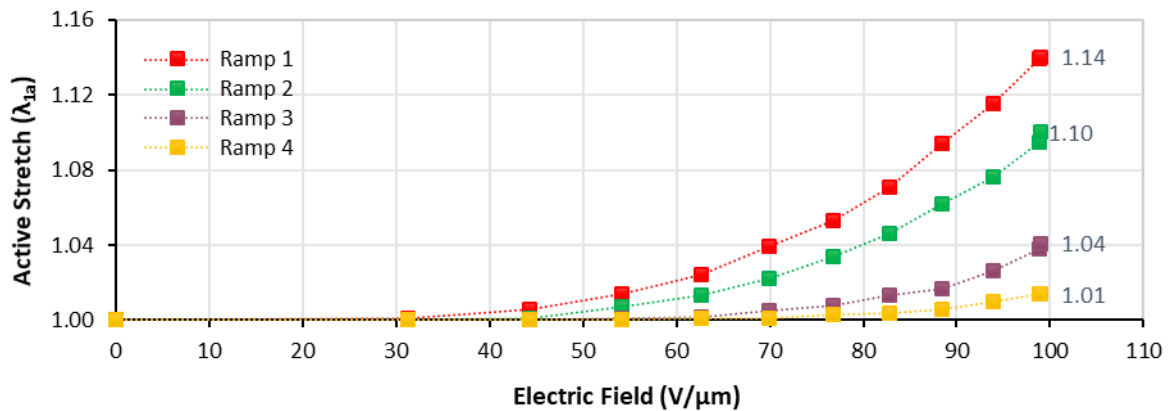


Figure 2.14: Deformation in the desired direction induced by the first actuator of the remaining actuators. Dotted lines are only a visual guidance.

For the fabrication of the following actuator devices, the actuators geometry does not change, except for the separation between the actuators in the direction 2, which is changed to 5.2 mm. Based on Figure 2.14 for this new geometry, the deformation of the following actuator when the previous one is actuated is 4.1 % (values in Ramp 3). Here, the distance between the two actuators is 5.2 mm.

A thinner actuator of 40 μm is fabricated with the mentioned separation between actuators and an increase of the actuation of the actuators is observed. The maximal deformation in this case is the same as the one obtained by the mathematical analysis for a 50 μm thickness: 24 %, Figure 2.15. This could be explained due to the less passivity surrounding the actuators. The distance from one actuator to the next one is greater; thus, the non-activated electrodes exert less inhibition to the deformation of the active electrodes. Some simplifications of the analytical model are: 1) the length of the actuator has no influence and 2) the distance to the next actuator is not evaluated, only one actuator is considered.

The image processing of the results also shows that the actuator at this deformation (24 %) presents a loss of tension where wrinkles are present in the actuator. In Figure 2.15, a picture of the bottom actuator with a deformation of 24 % is shown.

When the voltage V is large or the axial force P is compressive and of a large magnitude, the stress in the plane of the elastomer may cease to be tensile. This loss of tension causes the elastomer to buckle out of the plane, so that the elastomer does no longer generate a force of actuation. This

out-of-plane deformation creates instabilities which could end up in a failure mode of the actuator [126].

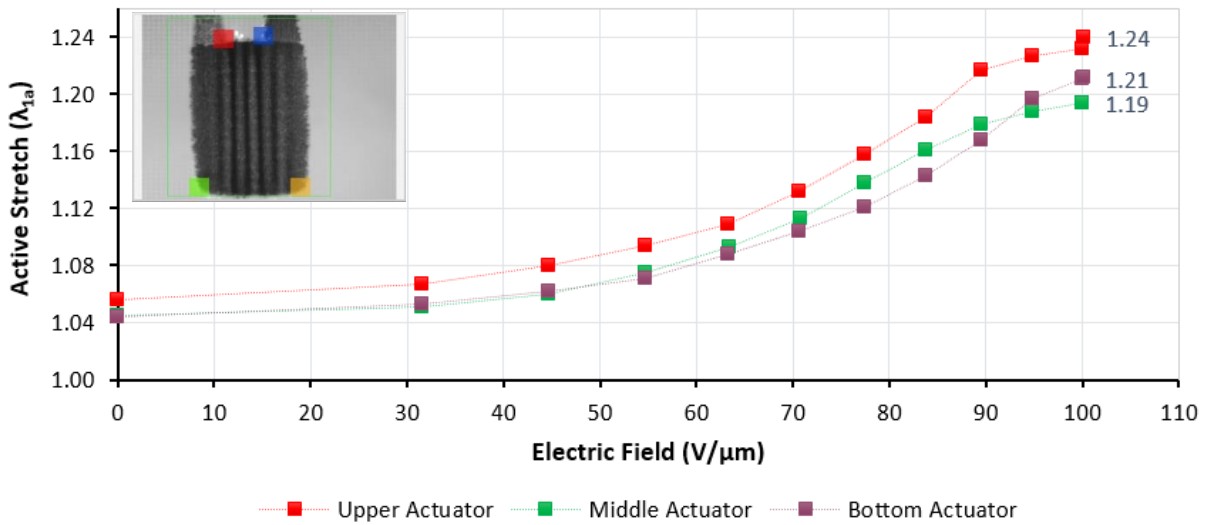


Figure 2.15: Deformation in the desired actuation direction of a thinner membrane (40 μm). Dotted lines are only a visual guidance. A picture of the bottom actuator with a deformation of 24 % and its loss of tension is shown (top left).

After several ramps, some deformation at 0 V remains from the previous ramp. Figure 2.16 shows an example of that remaining stretch. While Ramp 1 starts at 0 V with zero deformation, Ramp 2 starts with 4 % deformation at 0 V, corresponding to the latest value of deformation of the Ramp 1. A similar behaviour is observed for Ramp 3 and Ramp 4. In the dielectric layer, static charges remain after the cycle is finished and therefore, a small deformation stays constant, unless long periods of time elapse between a ramp and the following one. The behaviour shown in Figure 2.16 corresponds to the upper actuator of a 40 μm thick membrane device submitted to an electric field.

The channel, described in section 2.3.3 and in Appendix C, is located on top of the membrane and the displacement of the channel is characterized with the measurement setup previously shown. The attachment between channel and the elastomer membrane is only done by direct contact of both surfaces.

Figure 2.17 shows the difference in deformation when the channel is located on the membrane (C) and without the channel (NC). A loss of 8-9 % of deformation occurs when the channel is located on top of the membrane.

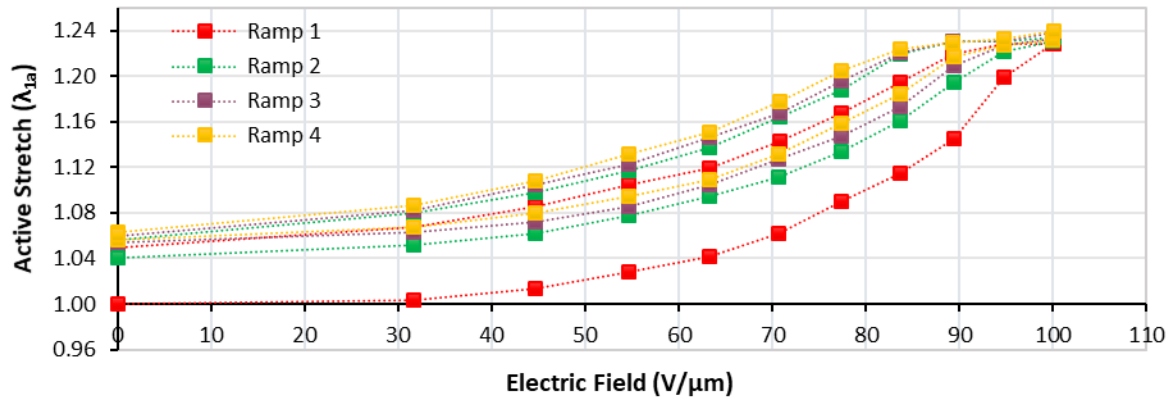


Figure 2.16: Series of ramps of the upper actuator of a 40 μm thick membrane device submitted to an electric field. Stretch obtained after four ramps in an actuator.

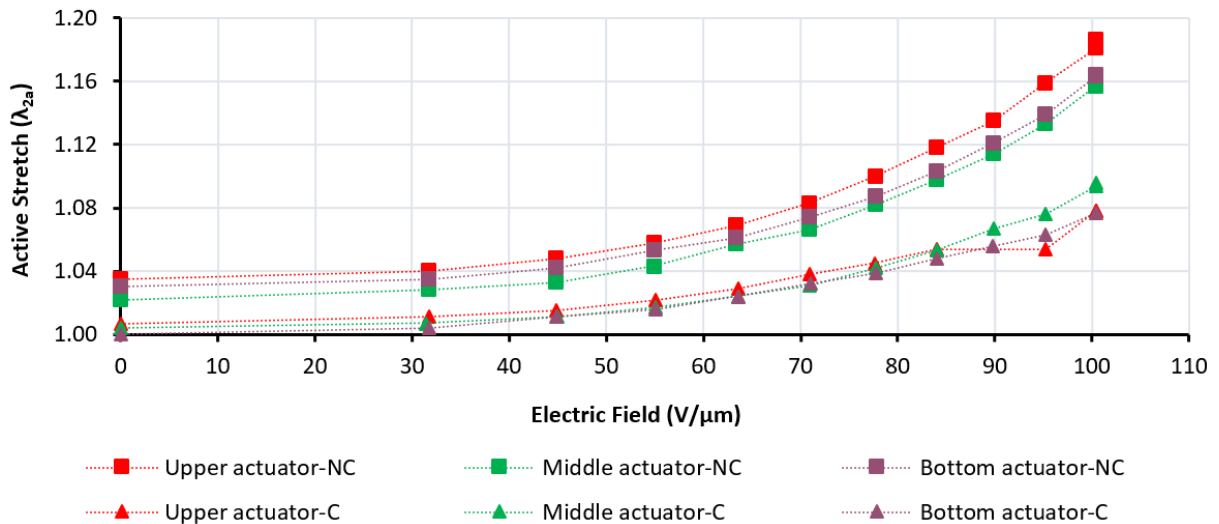


Figure 2.17: Characterization of the displacement of the actuation with channel (C, triangles) and without channel (NC, rectangles). Dotted lines are only a visual guidance.

Although the deformation is significantly smaller than expected, the channel is filled with DI water. The actuators at 100 $\text{V}/\mu\text{m}$ mimic a peristaltic motion at a constant frequency of 1 Hz, with a phase shift of $1/3$ ($\Delta\varphi = 120^\circ$) and a duty cycle of 0.5. Figure 2.18 represents three propagation waves of the device in red, blue and yellow, respectively. No movement of the liquid is observed during this demonstration. No leaking of the fluid is observed either.

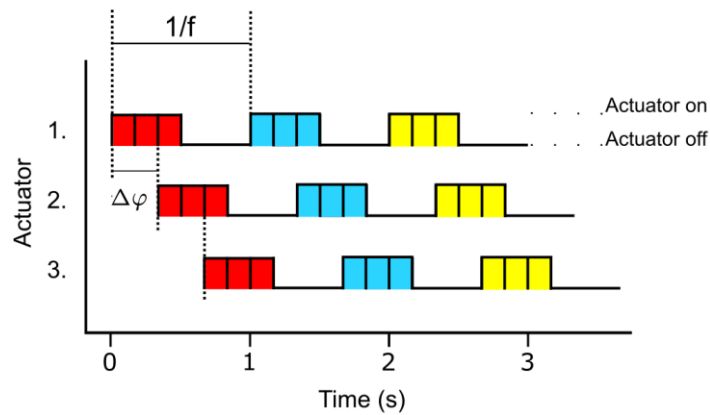


Figure 2.18: Configuration for the peristaltic pump at 1 Hz frequency, 0.5 duty cycle and 1/3 phase shift.

To prove the adhesion, the channel is separated. In doing so, part of the upper electrode and the channel are separated from the elastomer membrane. This indicates a strong adhesion between the channel and the electrode. A representation of this is shown in Figure 2.19. Here, the top electrode is visible in black and the bottom electrode in grey.

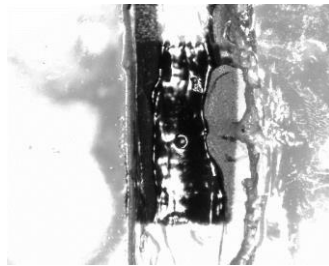


Figure 2.19: Actuator after detaching the channel. A part of the top electrode is also detached with the channel.

As previously mentioned, the bottom layer of the channel significantly decreases the performance of the actuators. Therefore, channels with thinner bottom layers (40 μm , 30 μm , 20 μm and 10 μm thick) are fabricated. Thinner bottom layers (less than 10 μm thick) with high quality cannot be handled with the channel manufacturing method proposed here. In the following, the deformation of the actuators with these channels is analysed. The deformation, in this case, is in the same range as for the 50 μm thick bottom layer (Figure 2.17). Thus, the microdevices obtained by reducing the thickness of the bottom layer do not pump fluids.

In the next steps, the channel is only manufactured using the top layer and the wall layer, omitting the bottom layer. The purpose here is to increase the deformation of the actuator and thus, the channel deformation.

Regarding the electrical connections, the ground electric connection is always coupled to the upper electrode. This prevents the liquid to be in direct contact with the high voltage.

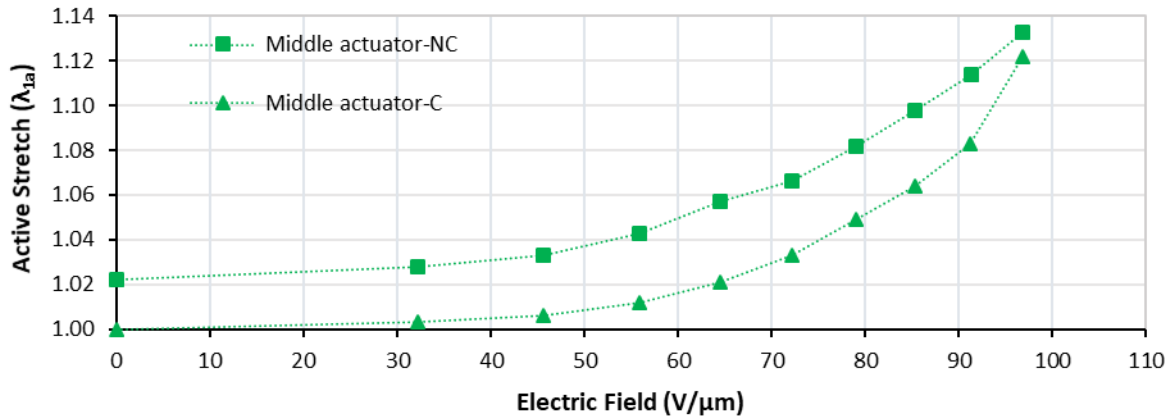


Figure 2.20: The deformation of the actuator with the channel (C, only top layer and wall) is reduced between 0.1 % and 1 % of the maximal deformation obtained without the channel (NC).

The deformation of the actuator with the channel (only top layer and wall layer) is approximately reduced between 0.1 % and 1 % of the maximal deformation obtained without the channel. Figure 2.20 shows the difference of deformation. In this case, the actuation without channel is much less than previously measured, most probably because the elastomer membrane is much thicker than the previous ones and hence, more voltage is necessary to achieve the same deformation.

B. Fluid flow characterization

In this section, the fluid flow in the single layer peristaltic pump - type 1 is investigated. Here, the channel only consists of a top layer and a channel wall layer. Due to the lack of bottom layer, the top electrodes of the actuators are connected to ground. DI water is introduced into the channels through the fluidic connection explained in Appendix C. The actuators perform at 4.5 kV, 1/3 phase shift, 0.5 duty cycle and 1 Hz, following the pattern described in Figure 2.18.

The fluid flow is characterized by video recording. A Dino-Lite digital USB-microscope records the fluid displacement inside the channel. Five microfluidic micropumps are tested. The video recording proves a displacement of the fluid for all tested microfluidic micropumps.

Figure 2.21 shows an example of a recording. Two video frames of the actuators with a channel on top are represented. Considering the channel dimensions (2 mm width and 0.5 mm height) and assuming the fluid to cover the full channel volume, the flow rate corresponds to 0.83 μL/min. This value is one order of magnitude lower than the theoretically calculated value in section 2.3.2, 15.36 μL/min. The passivation of the channel walls leads to a decrease of the net volume pumped by the system.

Although the transport of fluids with these devices has been proven, continuous flow measurements are not possible. The actuators suffer a dielectric breakdown after a couple of minutes of operation. This only occurs when the actuators operate with DI water flowing in a channel without a bottom layer.

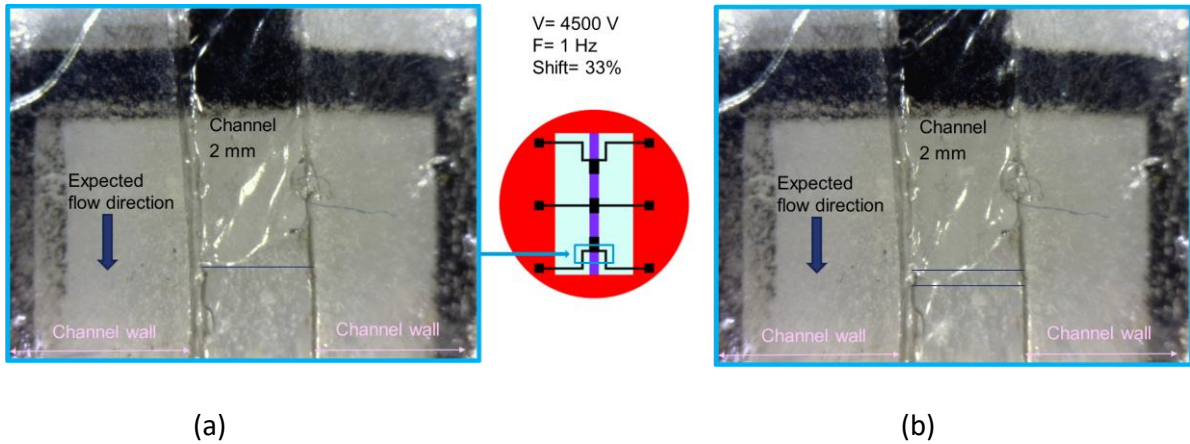


Figure 2.21: Video frames where the actuators are driven at 4500 V with 1 Hz frequency and 1/3 phase shift. Blue lines point out the difference of the meniscus from one frame to the next one. The time difference between (a) and the (b) is 21.58 seconds.

In Figure 2.22, the video recording of the fluid flow shows the generation of bubbles inside the channel. These are generated when the actuation occurs at 4500 V. This phenomenon can be explained by the generation of H_2 and O_2 due to the electrolysis of water. DI water leaks from the dielectric layer towards the high voltage electrode. The formation of bubbles causes the movement of the fluid to become unsteady and therefore cannot be measured accurately. Moreover, the dielectric membranes with a high prestretch are systematically getting broken.

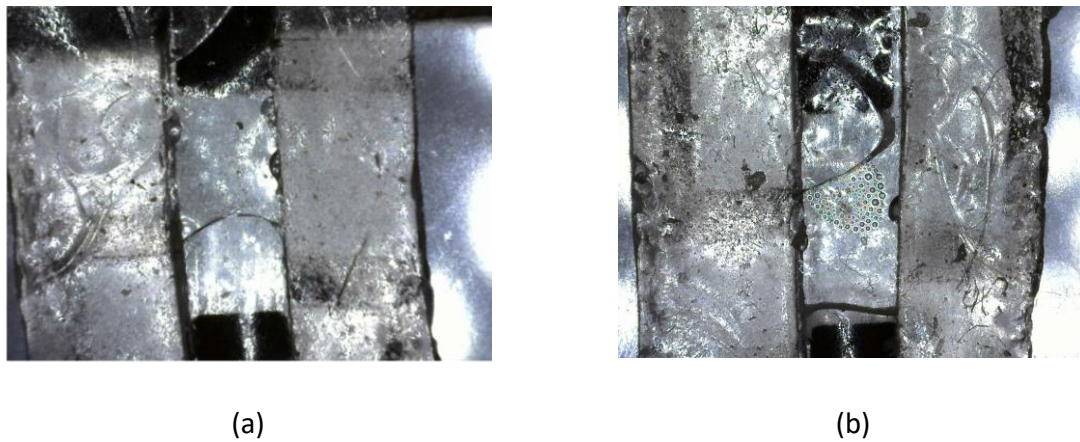


Figure 2.22: Photos of the channel filled with DI water. (a) The meniscus of the fluid can be seen. (b) Bubbles in the fluid are shown. The displacement of the fluid towards the outlet can be observed.

It can be concluded that this device, as it is fabricated, is not suitable for pumping liquids. A channel without a bottom layer is needed for the device to pump. The lack of a bottom layer allows, however, DI water to diffuse through the membrane, leading to a fast breakdown of the actuator. Therefore, no further experiments are developed with these materials and fabrication technique.

In the following sections, different materials and methods for the fabrication of the peristaltic pump – type 1 are investigated.

2.4. SINGLE-LAYER PERISTALTIC PUMP – TYPE 1 SOLID FILM

To achieve larger deformation of microchannels with a top, a wall and a bottom layer, the solid film method was investigated. The solid film Elastosil® E2030 was used as a new EAP material for the fabrication of the peristaltic pump prototype – type 1. The working principle of this new peristaltic pump, named here single-layer peristaltic pump – type 1 solid film, corresponds to that explained in the previous section 2.3. Furthermore, a new fabrication process is established for single layer actuators. This work was performed in the MEMS group of TU-Darmstadt.

2.4.1. DEA FABRICATION - SOLID FILM METHOD

In this section, the fabrication method for single-layer dielectric elastomer based on solid film is explained. The elastomeric layer is an industrially fabricated 50 µm thick PDMS film, manufactured by the company Wacker, named Elastosil® E2030. At the moment, Elastosil® E2030 films have the best characteristics as dielectric materials for EAP actuators in terms of electrical and mechanical properties. Table 2.4 summarizes the main properties of the silicone Elastosil® E2030 [127].

Table 2.4: Characteristics of Elastosil® E2030 for DEA fabrication [127].

Property	Value
Tensile strength	6.0 N/mm ²
Elongation	450 %
Tear strength	10 N/mm
Dielectric strength	80 - 100 kV/mm

The Elastosil® E2030 solid film supported by a PET layer is cut in a rectangular shape and prestretched with a homemade device. The pre-stretched membrane is attached to 3 mm PMMA frames to maintain the pre-stretch. The frames are 6 cm square with a frame width of 1 cm. These frames are attached at the top and bottom to the elastomeric layer. 3M® double-sided adhesive tape 96042 is used for this purpose.

Figure 2.23(a) shows a photo of a single-layer peristaltic pump type 1- solid film without the channel. Contrary to the electrode stamping method, in this electrode deposition method (explained later in this section), the device and actuator geometry are not restricted. Thus, the PMMA holding frames are squares of 6 cm x 6 cm, with a 1 cm width. The elastomer layer has a surface of 4.6 cm x 4.6 cm after prestretching. The three actuators have the same passive width, enhancing a similar actuation stretch of the actuators. The actuators, as in the previous peristaltic pump prototype, have 3.2 mm length and 2 mm width. Figure 2.23(b) and (c) show layouts of the top and front view of the device for a better interpretation of the photo. In the figure, the connection of the ground electrodes to each other can be noticed. The driving electrodes are individually connected.

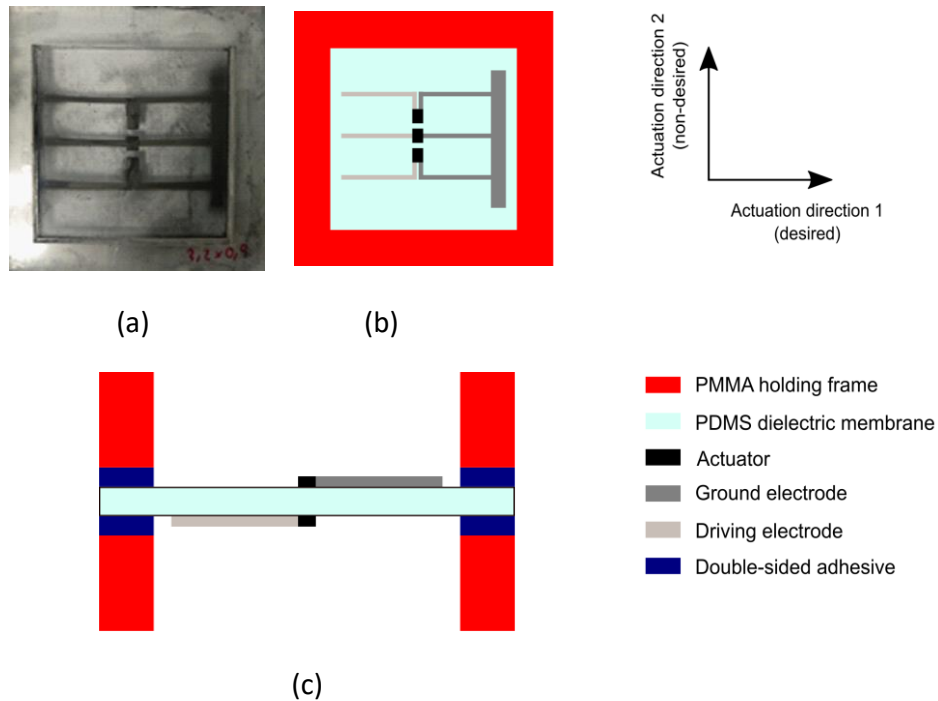


Figure 2.23: Single-layer peristaltic pump – type 1 solid film without the channel. (a) Photo of the device. (b) Layout of the top view and (c) of the cross-section of the device.

Due to its high conductivity, flexibility and bonding to the dielectric material, graphite powder (MF 2/99,5-99,9E, NGS Naturgraphit GmbH) was selected as electrode material. Table 2.5 summarizes the main properties of the electrode. Two deposition methods are investigated: brushing graphite powder and spraying a solution of graphite powder with isopropanol.

A. Brushing the electrodes

A 125 μm thick PET mask with the desired shape of the electrodes, is laser cut. Then it is cleaned with a solution of isopropanol to eliminate all the dust and particles generated after the cutting. The mask is located on top of the prestretched elastomer membrane and with a soft brush; graphite powder (MF 2/99,5-99,9E, NGS Naturgraphit GmbH) is brushed until the complete area of electrodes is sufficiently covered.

Table 2.5: Main properties of the graphite used for the electrodes.

Electrode	MF 2/99,5-99,9E
Particle size (μm)	X50 < 2
Electrode conductivity (S/m)	20
Sheet resistance, one layer (kOhm/sq)	10

B. Spraying the electrodes

A 3 mm PMMA frame is used as a mask with the shape and geometry of the electrodes. On top of it, a double-sided tape 96042 by 3M[®] is located with a PET layer to cover the rest of the actuator, avoiding contamination of the free area of the device, like for example the PMMA holding frame.

The spraying is done automatically with an automatic spray station, explained in section 4.1.2 The material used is a solution of graphite powder (MF 2/99,5-99,9E, NGS Naturgraphit GmbH) in

isopropanol. As this is a well-known and automatic process, the advantages of this method over the previous one are the control of the electrode thickness and the homogeneity of the layer.

Figure 2.24 summarizes the fabrication method for a single layer actuator with the solid film method. The electrical connection is the same as the one described in Appendix C.

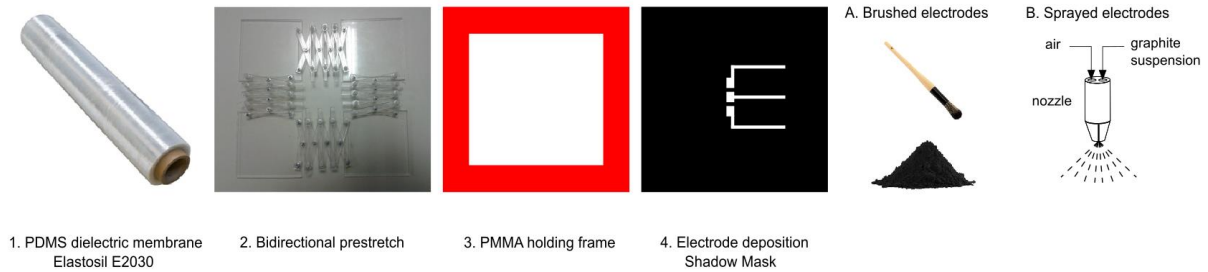


Figure 2.24: Fabrication process of a single layer DEA. From left to right: first PDMS Elastosil E2030 membrane (1); bidirectional prestretch with a homemade device (2); attachment of a PMMA holding frame (3); and electrode deposition (4). Two possible methods for electrode deposition are shown: brushing the electrodes (A) and spraying the electrodes (B).

CHANNEL FABRICATION

The channel fabrication method described in section 2.3.3 and detailed in Appendix C, is also used here. The material used for the channel is Elastosil® P7670. The properties of this material are described in section 3.2.2 in Table 3.3. This material presents similar properties as those of MED4086 and it is easier to handle in terms of crosslinking time and temperature.

For all connections, the tube is a low-density Polyethylene polymer (LDPE) 0.5 mm inner diameter tubing and 1 mm outer diameter from RCT Reichelt Chemietechnik GmbH and biologically compatible. The previous connection technique, described in Appendix C, provides a continuous leakage of the fluid. Two different techniques are investigated: 1) Self-sealing the tubing to the channel by gluing it with PDMS and 2) using a glass connector.

A. Self-sealing PDMS

The first method is based on one of the most interesting properties of PDMS, self-sealing. PDMS serves as an adhesive for multiple materials and also to itself. A great number of pumps and valves have already been fabricated using irreversible self-sealing PDMS [128][129].

In this method, the tube is attached and sealed to the channel using PDMS in liquid form and which is later cross-linked. No leakage is observed when introducing a fluid into the channel. However, the position of the tube is not practical for filling.

B. Glass connector

This method is based on a glass connector on top of the top PDMS layer. The glass connector is cut out of a glass wafer of 750 μm thickness. A thin-film of chromium is sputter-deposited on the glass wafer and patterned using UV-lithography and wet etching to mark the locations for the connector. An ultrasonic drill is then used to cut the 1.5 mm diameter circle and a wafer dicing

saw is used to cut the rectangle shapes. Only by processing one glass wafer, 64 connectors are fabricated.

When the glass connectors are fabricated, the top PDMS layer and the glass connector are exposed to O₂ plasma, 30 seconds at 100 W is enough for a strong adhesion. After applying force to them, they are introduced in an oven at 80°C for 30 minutes to get a strong bonding. The tubing is connected to the glass connector and therefore to the PDMS channel. To provide stability to the system, a few droplets of Elastosil® P7670 are located on top of the channel to fix the tube in the desired position. No leakage is observed after introducing the liquid with a syringe through the tubing.

2.4.2. CHARACTERIZATION

The characterization of the deformation versus voltage is done by applying voltage with the measurement setup described in section 4.2.1 for the micromixer. The images of the deformation of the actuators are recorded via a high-speed camera (Optronis CR 3000x2 – HighSpeedKamera).

A. Influence of the electrode deposition method

As mentioned above, two different methods for the deposition of electrodes are used: spraying and brushing the electrodes. The measurements are done via DC voltage, the applied voltage being held during 15 seconds. The brushing electrodes method proves to make the actuator fail at lower electric field than the spraying electrodes method.

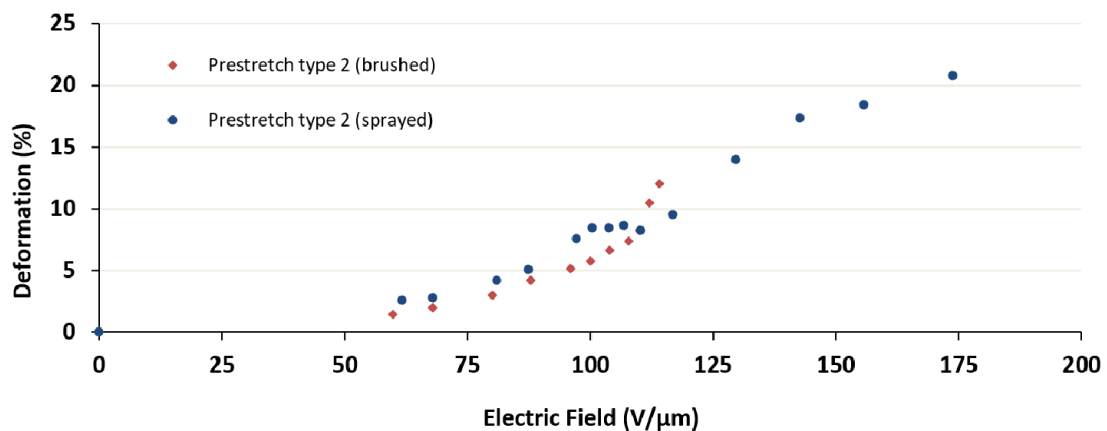


Figure 2.25: Relation between the deformation of a prestretched membrane and the electric field for two different electrode deposition methods: sample brushing (in red) and sample spraying (in blue) electrodes.

As it can be observed in Figure 2.25, the brushed sample with a prestretch of 1.2 x 2.7 gets a maximal deformation of 11.97 % at 113 V/μm. These measurements are repeated for a total of 8 samples. The samples break down before achieving the 113 V/μm or they break at this electric field.

For the sprayed electrodes, the prestretch used is also 1.2 x 2.7 and the maximal deformation is 20.77 % at 174 V/μm, leading to a much superior deformation and electric field only by changing the deposition method of electrodes. Figure 2.25 shows a plot with the deformation versus electric field for the two best samples obtained.

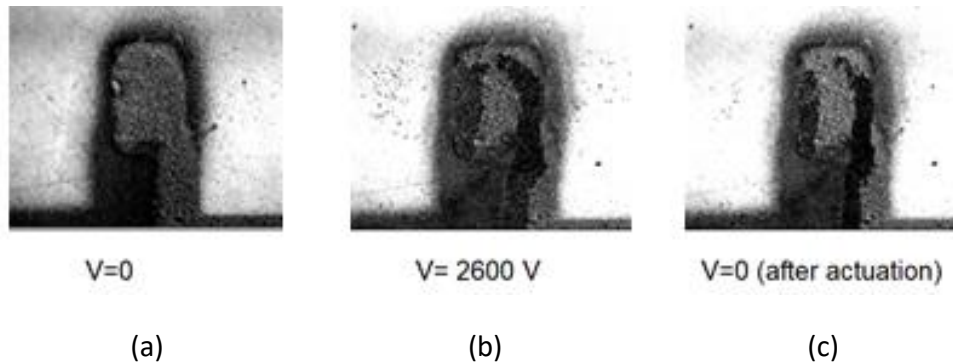


Figure 2.26: Photographs of the actuator. (a) Actuator at zero voltage. (b) Deformation of the actuator at applied voltage of 2600 V or 174 V/ μm . (c) Actuator at zero voltage after a previous actuation.

The electrode layers are measured with the resistance measurement setup described in section 4.2.2. The sheet resistance obtained is 15 kOhm/ \square , close to 12 μm thick layer. For stacked actuators fabricated in the MEMS group, the elastomer layers are 50 μm thick and the deformation is 5 % in the thickness direction. For the current single layer actuator, due to the prestretch, the final thickness of the elastomer layers is between 15 and 30 μm , so the electrodes thickness influence is much greater.

During the measurements at a high electric field, where also a high deformation is observed, the thicker electrode layers show a different behaviour than the thinner electrode layers. In the thicker layers, the graphite powder particles accumulate at the edges of the electrodes during high voltage application, leading to an increase of the edges thickness and a decrease of the middle-centred part of the electrodes. When no electric-field is applied, the electrodes do not recover its initial shape in thickness. Figure 2.26 shows photographs of the mentioned phenomenon. As it can be noticed in Figure 2.26 (b), the electrode layers crack and particles accumulate at the edges of the actuator.

When these cracks appear in the bottom electrode of these actuators, the graphite particles do not longer stay attached to the membrane and fall down due to gravity effects. These are the small spots that can be observed next to the electrodes in the photographs. For stacked actuators, this problem never occurs due to the accumulation of dielectric layers, impeding the loss of electrode particles.

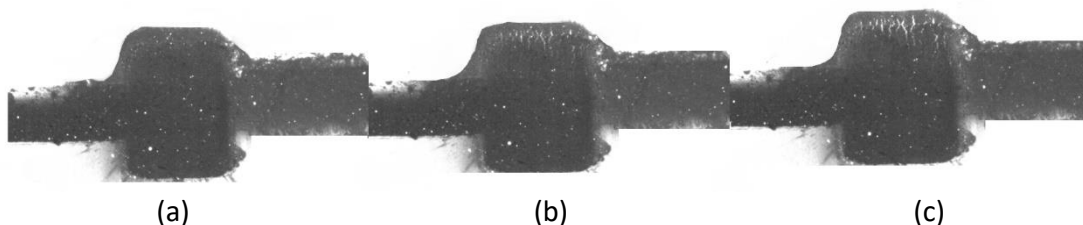


Figure 2.27: Three photographs of the actuator at (a) 0 V, (b) 2400 V and (c) 2750 V.

At high voltage, other actuators present a linear block displacement of the electrode layers. This displacement disconnects of the electrodes, impeding further deformation of the actuator at

much higher voltages. An example of this is shown in Figure 2.27. As it can be observed, the top of the electrode expands to form these cracks which are not in contact with the other cracks.

B. Influence of the prestretch

Förster-Zügel et al. [130] studied the dependence between the thickness of the elastomer and the electrode shape with the electrical breakdown of Elastosil® E2030 film. Various films were studied with a prestretch of 1.5 and without prestretch. They showed dielectric breakdown strengths between 96 and 200 V/μm during operation, depending on the applied voltage, prestretch and the setup of the actuators. This study used films of 30 μm initial thick. When the membranes were deformed with $\lambda = 2$, the highest dielectric breakdown was obtained.

Iannarelli et al. [131] studied the effects of the 0 %, 20 % and 50 % prestretch of the membrane and the thickness dependency of Elastosil® E2030 of 100, 76 and 54 μm thick membranes in the short and long term. They demonstrated that the films exposed to a larger prestretch have an enhancement of the dielectric breakdown, in some of the cases; they doubled the dielectric breakdown of the membranes without prestretch. They concluded that, in the long term, the higher prestretch membranes suffer from a lower lifetime performance.

In this section, a pair of prestretched values is studied, in order to elucidate the maximal deformation of the membranes before their dielectric breakdown. The prestretches are summarized in Table 2.6.

Table 2.6: Different prestretch for the elastomer made out of Elastosil® E2030

	Prestretch type 1	Prestretch type 2
λ_{1ps}	0.9	1.2
λ_{2ps}	2.2	2.7
Initial thickness (μm)	50	50
Final thickness (μm)	25.25	15.43

The first prestretch is based on the previous prestretch of Sylgard® 186, studied in the analytical model above shown in section 2.3.2. The second prestretch is based on other researchers' studies where they point out that this prestretch, here named type 2, offers a better actuator performance. Figure 2.28 presents two plots of the different prestretches. For the prestretched type 1, the maximal deformation is 11.56 % at 111 V/μm, while for the second prestretch type mentioned above, 20.77 % at 174 V/μm.

The dielectric breakdown values obtained in these measurements agree with the results that previous researchers have acquired for Elastosil® E2030 [132] [101]. Moreover, it is well known in the dielectric elastomer actuators field, that the dielectric breakdown field strength of the elastomer increases when the thickness of the material decreases. The dielectric breakdown field strength inversely depends on the thickness of the material, in accordance with the results obtained in Figure 2.28. The red triangles in that figure, which correspond to the larger prestretch and thus the thinner elastomer membrane, works until 174 V/μm, whereas the blue rhombi with a thicker membrane due to the smaller prestretch hold the actuation until an electric field of 111 V/μm.

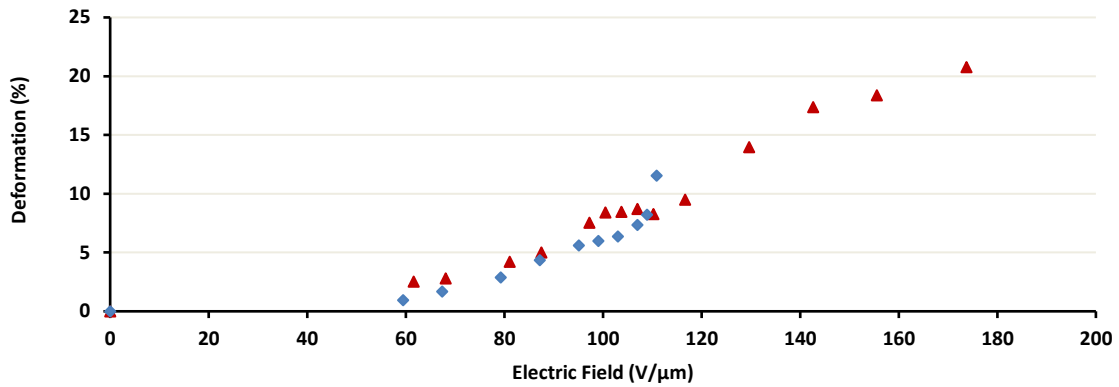


Figure 2.28: Relation between the deformation of a prestretched membrane and the electric field with two different prestretches: prestretched 1, in blue (0.9 x 2.2) and prestretched type 2, in red (1.2 x 2.7). Measurements are taken until samples suffer from an electrical breakdown.

Deformation with the channel:

A channel with the same geometry as the one stated in section 2.3.3 is located on top of the PDMS membrane. The channel differs only in the material properties. For this particular case, PDMS Elastosil® P7670 is in use. The material used for the channel is softer than that from the elastomer layer, this helps to prevent a loss in displacement of the actuators.

The deformation at the highest electric field corresponds to 7.5 % in the perpendicular direction to the channel. The channel in this case has the top, wall and bottom layer. As previously demonstrated for peristaltic pump – type 1- liquid film method (deformation 9.4 % in the perpendicular direction to the channel), this deformation is not enough for pumping fluids. The prototype does not successfully accomplish its goal although the materials in use have better mechanical and electrical properties than that of the liquid film method.

The design of single-layer peristaltic pump – type 1, fabricated with the materials with the best performances at the moment, does not result in a working device. Although the analytical values for the deformation indicates a sufficient volume change for generating a flow, the channel incorporation to the elastomer layer enormously decreases the actuators performance.

2.5. SINGLE-LAYER PERISTALTIC PUMP – TYPE 2 SOLID FILM

Herein, a new prototype for a microfluidic device is proposed, named peristaltic pump - type 2. The working principle of this peristaltic pump slightly differs from its predecessor. Although it is also based on a single layer EAP, here the actuators are not located below the channel, but parallel to it. Six actuators are needed and located in an array: two parallel groups of 3 actuators in series. The channel is located in the middle, between the two groups of actuators.

In the following sections, the working principle of this prototype, an analytical model to anticipate the actuation stretch obtained after voltage application and the characterization of the prototype in terms of deformation of the actuators, are explained in detail.

2.5.1. WORKING PRINCIPLE

The operating principle of this design concept of a peristaltic pump is a single membrane made of an elastomer. On top and bottom of this membrane, two arrays of electrodes are located in parallel, forming six electroactive polymer actuators. In between this actuator array, a channel of a softer elastomer is located. Upon voltage application, the actuator displacement contracts the channel. This decreases the channel width, reducing the channel volume. The actuators perform in a frequency, duty cycle and phase shift that creates a change of pressure along the channel. The fluid is expected to travel inside the channel due to this change in pressure.

The advantage of this prototype over the previous one is that the channel is closed by the operation of the actuators. Thus, the pressure and fluid flow are expected to increase in this prototype.

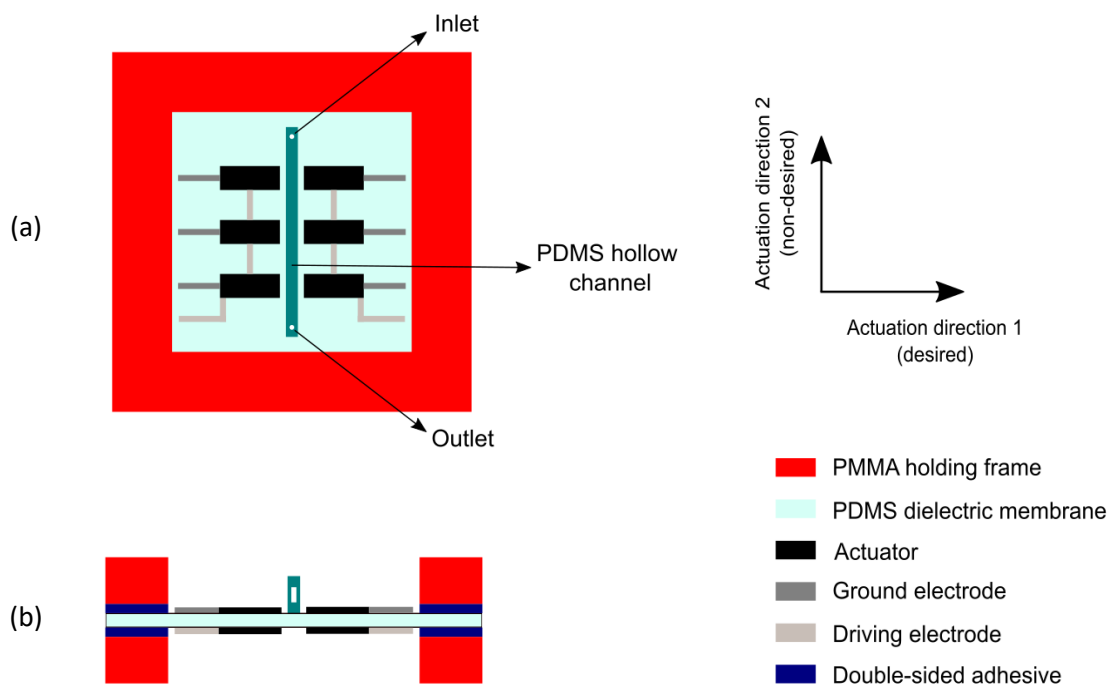


Figure 2.29: (a) Top view of the single-layer peristaltic pump – type 2 solid film with the channel on top of the elastomer layer. (b) Cross section of the device.

The actuation is again favoured in the perpendicular direction of the flow in order to close and open the channel. The membrane is bidirectionally prestretched to enhance the actuation in one direction and decrease it in the other direction.

Figure 2.29 presents a schematic of the geometry and location of the actuators in the peristaltic pump – type 2. In the figure, the channel is represented in green. The red colour represents the PMMA frame of 3 mm thickness used to hold the prestretch of the dielectric membrane. More details about this design are explained in the following sections.

2.5.2. ANALYTICAL MODEL

In this section, the deformation after applying an electric field to the actuators is studied. The actuator geometry is designed after the analysis of the stretch with respect to the active ratio.

MATLAB scripts of section 2.3.2 are used here to model the behaviour of the actuators upon voltage application [120]. For this modelling, the deformation of Elastosil® E2030 is characterized for the prestretch type 2 (Table 2.6) or prestretch 2.7 times in the channel flow direction and 1.2 times in the perpendicular direction to the channel flow. This prestretch has previously proved a better performance for 50 μm thick Elastosil® E2030, (more details in section 2.4.2).

Figure 2.30 shows a graph of the relation between the prestretch direction 1, in the perpendicular direction to the fluid flow (the desired actuation direction) and the active ratio. The active ratio, defined as the ratio between the width of the actuator and the total width of the device, is represented from 0 to 1 against the prestretch in direction 1, from 0 to 1.8. The stretch after actuation obtained is displayed with a colour code. The colour bar gets from 1 to 1.31, or from blue to yellow. The prestretch in direction 2 is fixed at 2.7.

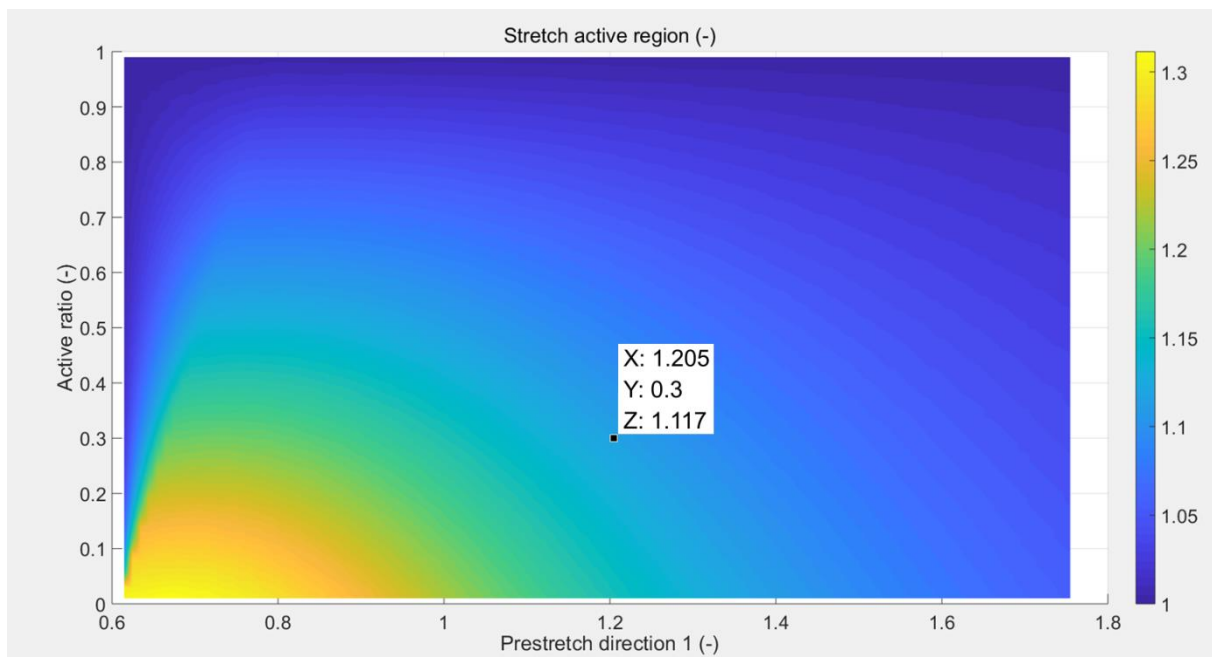


Figure 2.30: Active ratio versus prestretch in the direction 1 for the prototype 2. Prestretch in the direction 2 is constant, with a value of 2.7. The active ratio, defined as the ratio between the width of the actuator and the total width of the device, is represented from 0 to 1 against the prestretch in direction 1, from 0 to 1.8. The stretch after actuation obtained is displayed with a colour code. The colour bar gets from 1 to 1.31, or from blue to yellow.

White parts in the graph belong to failures in calculation. Failure modes considered are divergence of the Gent model, loss of tension in the membrane and compression in the actuation direction.

As depicted in Figure 2.30, in the prestretch in direction 1 the lower the active ratio, the greater the stretch upon actuation. Considering 10 mm width for each actuator, or by having two of them in parallel, a total active region of 20 mm and a passive region of 40 mm, the active ratio is 0.3. In

Figure 2.30, an active ratio of 0.3 in a 1.2 x 2.7 prestretch membrane leads to an actuation stretch of 1.117 or 11.7 % deformation of each actuator at maximal voltage. The Gent model analysis concludes that each actuator of 10 mm is ideally deforming 1170 μm in the desired axis, or half of it in the direction towards the channel, 585 μm . The opposite actuator will mirror it by moving 585 μm in the direction of the channel. Ideally, the actuation of the parallel actuators leads to the fully closing of the channel.

This model only considers one actuator deforming in a passive region. In practice, since both actuators act in opposite directions, it is expected to have less actuation than that predicted by the analytical model.

Here, assuming that the actuators fully close the channel, considering the change in volume in a chamber of 1 mm width, 0.5 mm height and 3.2 mm length and the peristaltic pump three chambers (only 1/3 of the net volume is transported per cycle [122]), the fluid flow expected in ideal conditions for this peristaltic pump is 0.53 $\mu\text{L}/\text{cycle}$.

The fluid flow for a frequency of 1 Hz is then 31.8 $\mu\text{L}/\text{min}$. This results in approximately the double of the flow rate expected for the peristaltic pump type 1 (15.36 $\mu\text{L}/\text{min}$). The reason for it is the fully closing of the chamber upon actuation.

2.5.3. GEOMETRY AND FABRICATION

The analytical model helps to understand the potential of the device in an ideal situation and the possibility to optimize the active ratio to maximize the actuator deformation towards the channel.

Figure 2.29 shows a layout of the device. In the figure, the channel is represented in green. The channel has 1 mm width and 500 μm height. The red colour represents the PMMA frame of 3 mm thickness used to hold the prestretch of the dielectric membrane.

As in the previous device, a prestretched elastomer membrane made of Elastosil[®] E2030 with a higher prestretch in the non-desired direction is held by a 3 mm thick square PMMA frame. The PMMA is attached to the membrane by a double-sided tape 96042 by 3M[®]. Electrodes are sprayed on top and bottom of the prestretched membrane, following the findings of the previous section. Electrodes are based on a solution of isopropanol and graphite powder (MF 2/99,5-99,9E, NGS Naturgraphit GmbH). After spraying, the isopropanol evaporates and the graphite powder stays attached to the membrane.

The prototype has three actuators in series located in parallel to other three actuators in series. In between the two arrays, a soft PDMS channel of 1 mm width and 55 mm length, is located. The working principle of this prototype is based on the closing of the channel by the lateral expansion of the parallel actuators towards the channel, when voltage is applied, creating a propagating wave.

The geometry of the device and actuators, and the prestretch used for the membrane are summarized in Table 2.7.

Table 2.7: Geometry details about the actuator design

	Prestretch type 2	Final Thickness (μm)	15.43
λ_{1ps}	1.2	Actuator width (mm)	10
λ_{2ps}	2.7	Actuator length (mm)	4
Initial Thickness (μm)	50	Distance between actuators in series (mm)	5

The fabrication process, materials, connections and tubing for this prototype match to the one explained in section 2.4.1 and correspond to the solid film manufacturing method.

The study of the influence of parameters like the prestretch in both directions and the electrode deposition methods in section 2.4.2, concludes that the prestretch of 1.2×2.7 and an electrode deposition method based on spraying an isopropanol-graphite solution provide a better performance of the actuators, thus, these findings are used in this prototype. In Figure 2.31, a photo of the resulting fabricated device without the channel and a layout of the prototype design based on the parameters in Table 2.7 are shown.

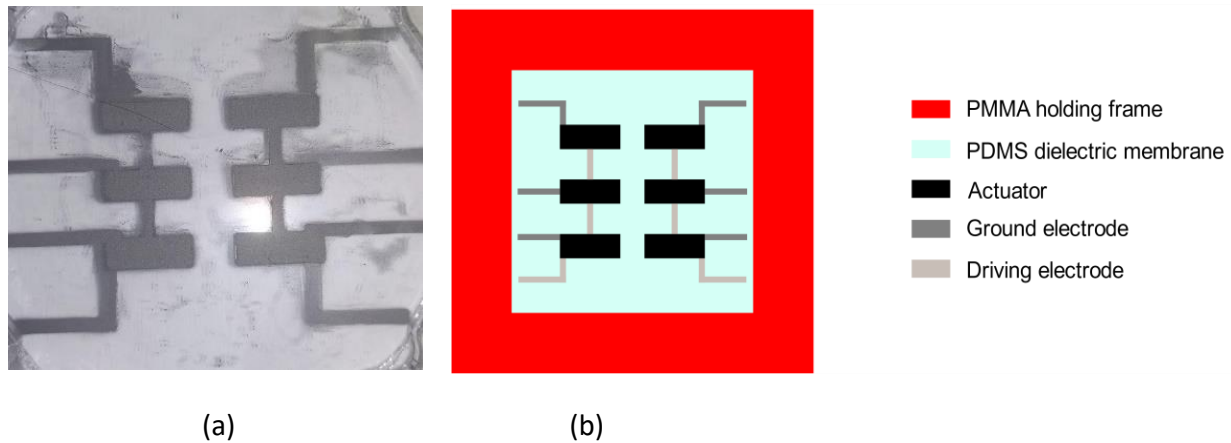


Figure 2.31: (a) Photo of a prototype for the peristaltic pump 3. The prototype has three actuators in series located in parallel to other three actuators in series with an active ratio of 0.3. (b) Layout of the prototype with its legend.

2.5.4. CHARACTERIZATION

To investigate the fluid flow as a function of the width, the deformation of the actuators with and without a channel is studied. The measurement setup corresponds to that from section 4.2.1.

First, measurements of the performance of only one actuator (the one in the middle) and of two actuators at the same time, are performed. Figure 2.32 shows a graph where the deformation versus the electric field is represented, the middle actuator: alone (purple) and for 2 actuators at the same time (red). The initial membrane thickness is $50 \mu\text{m}$. After prestretching 1.2×2.7 , the thickness corresponds to $15.43 \mu\text{m}$. The maximum electric field applied to the sample is $165 \text{ V}/\mu\text{m}$.

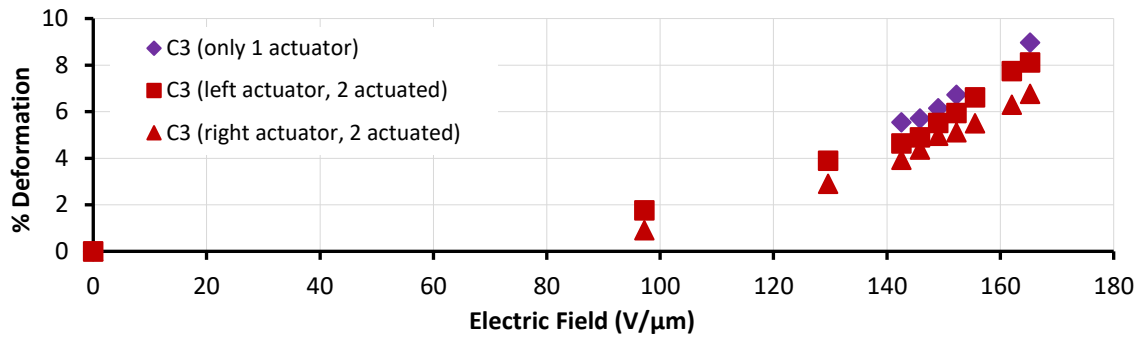


Figure 2.32: Deformation versus electric field for the middle actuator at the left when it is the only actuator working (in purple), left actuator when two actuators at the same time are actuating (red squares), and right actuator when two actuators are acting at the same time (red triangles).

The maximal deformation is obtained, as expected, for the single actuator in the middle at the left, the deformation obtained is 8.97 %. For two actuators at a time, the left actuator presents a deformation of 8.12 %, while the right actuator shows a deformation of 6.77 % at the maximal electric field applied 165 V/μm. The edge of the left actuator expands 406 μm to the right and the edge of the right actuator deforms 338.5 μm to the left. Both edges get closer by 744.5 μm.

Experimental deformation values are lower than those obtained by the analytical method. The analytical method predicts a deformation of 11.7 % for an active ratio of 0.3 of one actuator deforming, while the experimental value obtained is 7.44 %, in this case, with two actuators performing at the same time. For a single actuator, the active ratio is $r_a = 10 \text{ mm}/60 \text{ mm} = 1/6$. The theoretical deformation resulted from the analytical model, represented in Figure 2.30, is 16.2 %, much higher than the one experimentally achieved for a single actuator, 8.97 %.

In the following, the deformation of the actuators with a channel is investigated. A channel of 1 mm width and 55 mm length is fabricated and attached to the middle part of the device, in between the parallel actuators. The channel material is PDMS Elastosil® P7670. The channel has a passive wall of 6 mm width, surrounding both sides of the channel. The 1 mm wide channel is located in between the two actuators with a distance of 2.5 mm from the centre of the channel to the edge of the actuators.

Figure 2.33 presents the deformation versus electric field for the same device with and without the channel on top of the membrane, for the actuator located in the middle. The figure represents 4 sets of data: 2 for the actuation of only one actuator in the middle with and without channel, and 2 for the two actuators in parallel located in the middle of the device, with and without channel. Graphs in red represent the device without channel and in blue, with the channel. Square marks are devoted to the deformation of the actuator at the left of the channel and triangles to the actuator at the right of the channel.

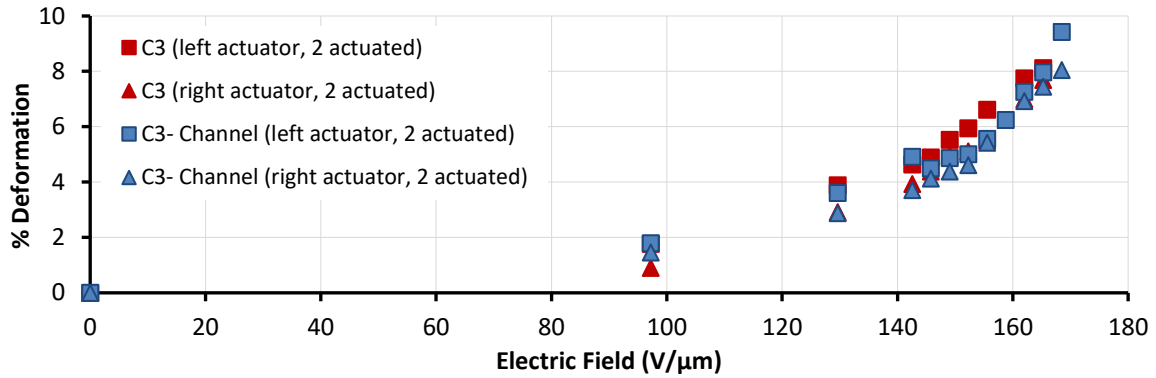


Figure 2.33: Deformation versus electric field for the two actuators in the middle with and without the channel on top of the elastomeric membrane in blue and red, respectively.

At an electric field of 165 V/μm, the maximal electric field applied to the actuators without the channel, the prototype with channel presents a slightly lower deformation than that of the device without channel. The difference in deformation between the left actuator without channel, 8.12 %, and the same actuator with the channel, 7.98 %, is 0.14 %. For the right actuator at an electric field 165 V/μm, the deformation without the channel is 7.70 % and with the channel 7.45 %. For both actuators, there is a slightly different deformation with and without the channel, not very remarkable.

The deformation of the channel is also tested. The deformation of the actuators is not directly translated in a deformation of the channel due to the channel wall of 6 mm between the actuators and the channel.

Figure 2.34 displays the deformation of the channel respect to the electric field applied to the actuators. As it can be observed, the curve follows a similar behaviour to that of the actuators. The maximal deformation of the channel is 0.46 mm or 46 % of its total width. Photos of the channel are taken at each electric field and its deformation is afterwards analysed.

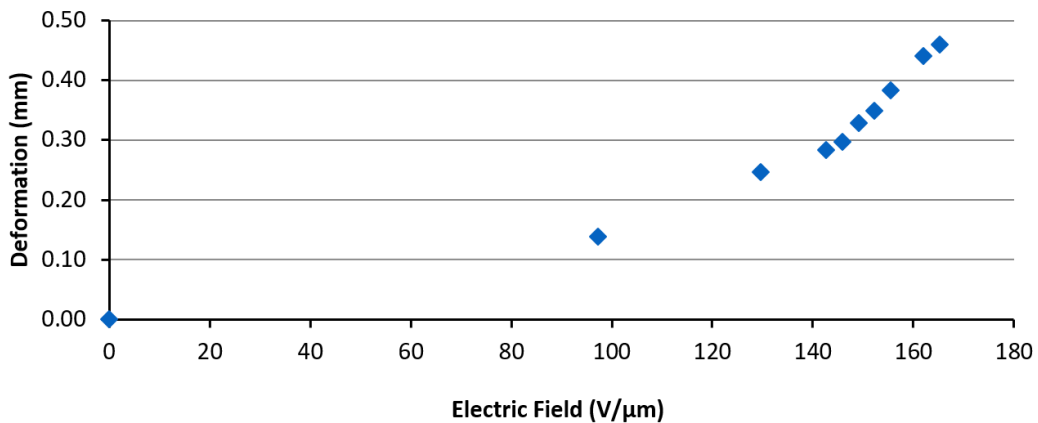


Figure 2.34: Deformation of the channel of 1 mm width and 55 mm length.

To achieve a completely closed channel, different channel widths (300 μm, 600 μm and 1000 μm) have been tested. Moreover, the channel height has also been reduced (300 μm and 500 μm) to make the change in volume due to the width shrinking more significant.

Tubing and connectors are added to the system following the procedures exposed in Appendix C. DI water is the fluid chosen for testing. Diverse configurations of frequency, duty cycle and phase shift are in use. The fluid flow is characterized by video recording via a high-speed camera (Optronis CR 3000x2 – HighSpeedKamera). For all the combinations above exposed, no pumping of the fluid is obtained. However, a forward-backward fluid movement is observed.

Figure 2.35 shows two photographs of the 1000 μm wide and 500 μm height channel. On the left, the channel at non-actuation state and on the right, channel when both middle actuators are subjected to an applied electric field of 152 $\text{V}/\mu\text{m}$. The deformation of the channel is 0.34 mm (1/3 its initial width). According to the assumption of 1/3 of the net volume being transported per cycle [122], more details in section 2.3.4. B, the fluid flow expected in these conditions for this peristaltic pump is 0.23 $\mu\text{L}/\text{cycle}$. However, the actuation leads to a deformation of the channel and to the wrinkling of the top layer of the channel which can be observed in the image at 152 $\text{V}/\mu\text{m}$. The top layer of the channel buckles down, resulting in a non-homogeneous deformation of the channel. Thus, it is difficult to predict the real change in volume of the microfluidic channel.

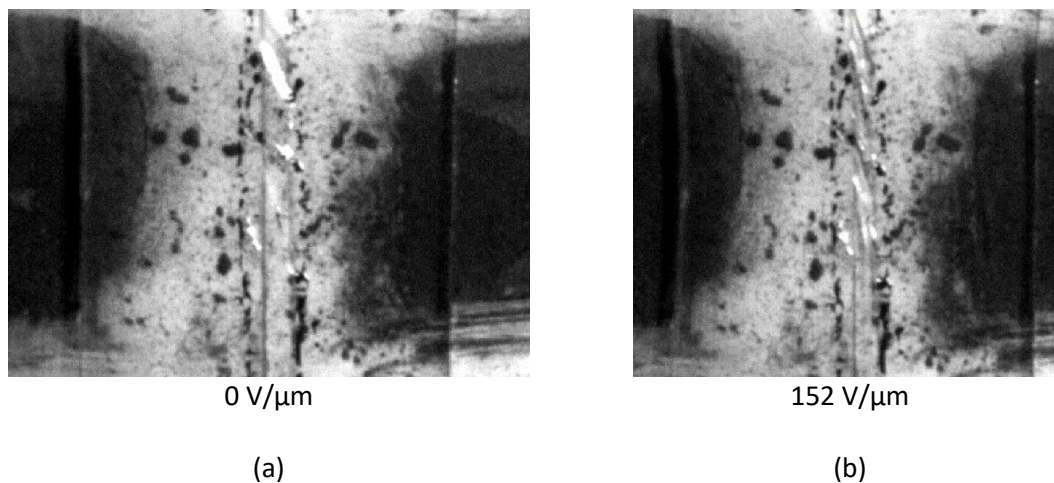


Figure 2.35: Image of the channel on top of the membrane. (a) Actuators at 0 $\text{V}/\mu\text{m}$. (b) Channel when the actuators are subjected to an electric field of 152 $\text{V}/\mu\text{m}$.

This behaviour also occurs in the rest of the fabricated channels. Moreover, the deformation in width of the channel decreases when reducing the channel width. This is due to the symmetry of the device. The middle point between the actuators in parallel has a null displacement and has its maximum at the electrodes edge.

The findings of these experiments suggest that the channel walls are not displacing uniformly when actuation occurs. As PDMS is a hyperelastic material, due to the direct contact of the actuators, the bottom layer of the channel deforms 1/3 its initial width. However, the walls and top layer of the channel may remain without a deformation or with a very little deformation, leading to a channel with a trapezoidal geometry. Consequently, the change in volume when actuating the actuators is not high enough to allow the fluid to flow. This actuator displacement leads to a forward-backward fluid movement so small that it cannot produce a fluid flow.

It seems possible that the lack of fluid flow is also affected by the distance in length between the actuators. This distance, based on the values obtained in section 2.3.4 A, is related to the influence of one actuator over the following in terms of deformation. The channel, in the space between

one actuator and the next, barely deforms, leading to a volume where the fluid stays still. This could in fact impede the propagation wave necessary for the fluid movement along the channel.

Investigations on the channel deformation of hyperelastic materials and on the distance between actuator elements have not been found in literature and thus, these results should be interpreted with caution.

2.6. CONCLUSIONS AND DISCUSSION

In this chapter, two different peristaltic pump prototypes have been tested. Both prototypes are based on microfluidic channels which are deformed by single EAP layer actuators.

The first prototype design, named peristaltic pump type 1 - liquid film, is based on a mechanical pump type and three DEAs. The pump deforms a channel on top of these actuators with a certain frequency and phase shift, allowing the fluid to flow. Some of the prototype parameters like the width of the actuators, the width of the channel and the diameter of the full device are limited by the fabrication method, in particular the electrode stamping method.

An analytical method is used to determine the requirements of prestretch of the elastomer membrane to enhance the actuation after the application of voltage to the actuators. It provides values for the bidirectional prestretch: $\lambda_{1ps} = 0.9$, in the actuation direction; and $\lambda_{2ps} = 2.2$, for the perpendicular direction. This is translated to a deformation after actuation of 24 %.

The deformation of the actuators, fabricated according to the values obtained by the analytical method, is measured and analysed. The influence of the deformation along the length, not predicted by the analytical model, is evaluated. This leads to a distance between actuators of 5.2 mm.

The full device with the channel is under analysis. The deformation obtained when the channel is on top of the actuators decreased dramatically the performance of the actuators by 9 % deformation. No fluid flow is observed. The deformation decreases only from 0.1 to 1 % when there is no bottom layer in the channel. Fluid is introduced in the system and pumping of the fluid is observed. The liquid flows in the channel. Unfortunately, DI water leaks through the DEA-membrane leading to the electrolysis of water and the generation of H_2 and O_2 . The membranes are systematically getting broken in a very short period of time. Therefore, it is not possible to do long time measurements of the pump flowing.

To overcome this issue, the system needs a channel with a bottom layer. Thus, the single-layer peristaltic pump-type 1 is fabricated with better performance materials and fabrication method. The prototype is named as single-layer peristaltic pump - type 1 solid film. This displacement turns out to be insufficient for pumping fluids along the channel. Results have proven that the deformation of the actuators with these materials leads to a lower deformation of the channel, resulting in an invalid device for pumping microfluidics, although materials with a theoretical better performance are used.

Given the characterizations previously done for peristaltic pump – type 1, a new design is proposed. The single layer peristaltic pump – type 2 is based on the coupling of two parallel arrays of actuators where a channel is located in the middle space between the arrays. When the actuators stretch, the channel deforms in its width and thus, in volume. The advantage of this

prototype respect to the previous one is the working principle. Here, the actuators in parallel perform to fully close the channel. Thus, a higher flow rate and pressure is expected.

The analytical modelling of the deformation leads to an actuation stretch of $\lambda_{1a} = 1.11$ at 168 V/ μm . The experimental results confirm that the channel does not inhibit much the deformation of the actuators. The bottom layer of the channel with a 1 mm width, deforms 1/3 its width. This deformation should be sufficient for the pumping of the fluid; however, no fluid flow is observed. This inconsistency may be due to two facts: 1) the non-uniform deformation of the channel and 2) the distance in length between actuators.

The channel made of PDMS is displaced due to the force applied by the actuators to its bottom layer. Considering the hyperelastic behaviour of PDMS, it is to assume that only the bottom layer decreases its width, whereas the wall and top layers do not modify their shape. As a result, the change in volume when actuating the actuators is not high enough to allow the fluid to flow. To overcome this issue, a channel with a combination of elastic and rigid walls could indeed permit the fluid flow.

The use of a longer distance between actuators in series, characterized to avoid the influence of one actuator on the following (in section 2.3.4 A), may be linked to fluid flow problems in the pumps. Along the length between actuators, the channel does not deform and therefore, the fluids do not move. This steady fluid volume between actuators may avoid the propagation wave. Further investigations regarding the ideal distance between actuators to enhance the fluid flow could elucidate whether the deformation of the channels with the actuators as manufactured is sufficient.

Although the peristaltic pumps manufactured in this chapter have failed to function properly, it is possible to compare their theoretical fluid flow with that of other technologies to understand the potential of these systems. The peristaltic pumps made from dielectric elastomer in this thesis, specifically referred to as type 1 and type 2, have a theoretical fluid flow rate of 15.36 $\mu\text{L}/\text{min}$ and 31.8 $\mu\text{L}/\text{min}$, respectively, at a potential of 5 kV and a frequency of 1 Hz.

Cazorla et al. [133] fabricated a low voltage silicon micro-pump based on piezoelectric actuation principle and they could achieve a flow rate of 3.5 $\mu\text{L}/\text{min}$ at 24 V and 1 Hz actuation frequency using water as pumping fluid. Piezoelectric actuation offers high-frequency fluid flow and pressure, is reliable and durable, and is easy to integrate into microfluidic systems. However, it has limited displacement and deformation capabilities and requires the implementation of a relatively high voltage and electrical power consumption.

Thermo-pneumatic actuation offers simple and low-cost fabrication, is suitable for portable and disposable microfluidic devices, and can generate low-frequency fluid flow and pressure. Hamid et al. [134] used the thermo-pneumatic actuators with a single chamber using polyimide as the membrane material to obtain a flow rate as low as 0.0125 $\mu\text{L}/\text{min}$ at 10 Hz using water as pumping fluid.

In 2015, Shaegh et al. [135], fabricated a micropump based on one thermal expansion actuator at a frequency of 5 Hz, producing a flow rate of 85 $\mu\text{L}/\text{min}$ using water. As it can be observed, thermal expansion actuation provides high-pressure fluid flow and is simple and low-cost to fabricate. However, it also has limited displacement and deformation capabilities and is sensitive to environmental temperature fluctuations.

In general, the time response of thermal expansion actuators is relatively slow compared to other types of microfluidic actuators, such as piezoelectric or electromagnetic actuators. This is because the thermal expansion process is a relatively slow process, and it takes time for the actuator to reach its maximum expansion or contraction.

Ehsani et al. [136] used electromagnetic actuation mechanism to develop a micropump able to provide a flow rate of 0.055 $\mu\text{L/s}$ at a frequency of 1 Hz. Electromagnetic actuation provides low fluid flow but high pressure and is suitable for integration into microfluidic systems, but it has limited displacement and deformation capabilities and requires high electrical power consumption, while also being sensitive to environmental magnetic field fluctuations.

In terms of flow rate, the peristaltic pumps fabricated here are expected to have a higher flow rate than those actuated by electromagnetic and thermal expansion technologies. The electroactive polymer peristaltic pumps, in particular, are expected to provide an even higher flow rate than the piezoelectric pumps, thanks to the electroactive polymers' large deformation at their resonance frequency.

It is worth noting that piezoelectric actuators generally operate in the range of hundreds of volts, whereas electroactive polymers require a few kilovolts of voltage application. These factors should be considered when selecting the appropriate actuation technology for a particular microfluidic application.

It is important to mention that piezoelectric actuators typically operate within the range of hundreds of volts, while electroactive polymers require several kilovolts, which requires specialized equipment for the application of such high voltages.

The findings of this chapter reveal that, currently, piezoelectric actuators exhibit superior characteristics compared to electroactive polymers in the development of micropumps. Nonetheless, the potential of electroactive polymer technology is continuously being researched to reduce the required electric potential and enhance the deformation of the actuators, as well as their lifespan.

While the prototypes developed in this chapter were not successful in achieving fluid flow, valuable insights into the capabilities of EAP technology were gained through the investigation. For instance, the deformation of actuators, the impact of actuators on each other, the deformation of a channel on top of actuators, the comparison between analytical model and experimental and the development of new fabrication processes for microfluidic devices. These findings can be used to develop new devices. Some of the most relevant properties of the here produced prototypes are:

- Biocompatible channel (PDMS)
- Channel can be easily detached/attached (Changing samples)
- Channel can be fully closed
- Device which deforms a channel almost (46 %) unidirectional.
- Transparent
- Possibility to increase the number of actuators

The proposed configurations do not succeed in pumping fluids. However, the microfluidic devices can hold fluids inside an elastomeric, biocompatible channel and stretch this channel and

compress with a maximal deformation of 33 % for a 1 mm channel width. The deformation is controlled with the applied voltage. For this reason, a deformation from 0 % to 33 % of a fluid in a direction is possible.

Here, a different application for the fabricated devices is proposed: cell stretchers. In the human body, cells are continuously being stretched. For example, in blood vessel walls the cells are deformed at a rate of once per second by the blood flow. At the moment, the influence of the mechanical forces on cells is a hot topic in the medical field. The knowledge of the change of behaviour of cells in proliferation and gene expression, due to their continuous deformation, may play a key role in illnesses such as cancer, lung disease and heart disease, as well as muscle disorders.

Researchers have already used this property of EAPs in the field of cell stretching [78][137][138]. The difference in this case is that the fluids are held in a channel, contrary to that already used where the cells are deposited directly on top of an elastomeric layer on top of the actuators, without a top cover to protect the fluids. With this configuration a higher deformation is observed.

The prototypes fabricated in this chapter can be used for this purpose. Moreover, as the influence on the deformation of one actuator over the following one has also been studied with the distance, several deformation sequences are possible with the prototypes. There is the possibility to fabricate three different inlets and outlets to introduce different prototypes to measure this deformation: for example, a reference probe in the middle without stretching and two probes in upper and bottom electrode to study different deformations with time. As explained in section 1.3, the lifetime of EAP is very high, lasting over hundred thousand cycles of actuation, would allow plenty of cycles, considering there is no need for very high frequency deformation of cells.

Figure 2.36 shows the proposed system for the analysis of the deformation of cells with the prototypes above mentioned. Interesting is, due to the versatility of the channel fabrication, that a single device can introduce several different types of channel for diverse measurements.

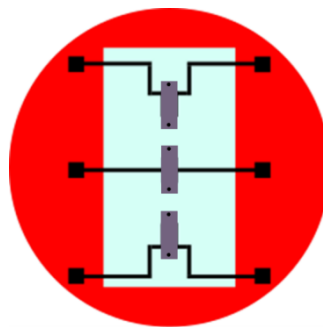


Figure 2.36: Configuration of one channel with multiple inlets and outlets to introduce one or several fluids and allowing different deforming conditions.



3. CONCEPT OF A PUMPING MICROMIXER

Micromixers are cost-saving devices in the chemical production of expensive substances. In a great number of processes, the cost of the catalyst is the main constriction. Using micromixers greatly decreases the amount of catalyst needed and avoids extra costs. Micromixers are also promising in the case of explosives or flammable substances. The reaction energy is highly reduced because micromixers reduce the needed volume of reactants, the explosiveness of the reactions decreases, allowing safer experiments [139]. Mixing is the main process in most microfluidic devices for medical diagnostics, proteomics, genetic sequencing, chemistry production and drug discovery.

In the following chapter, the fundamentals and a short description of the types of micromixers in research and their actuation principle are included. Moreover, the final configuration prototype for the pumping micromixer made of dielectric elastomer actuator is described, including the materials, the working principle and the design.

3.1. FUNDAMENTALS OF MICROMIXERS

Mixers are devices consisting of at least two inlets and one outlet. They homogenize the properties of the substances conveyed through the inlets. Some of these properties are: the phase, the temperature, the density and the viscosity of the substances.

To mix, at least two different substances with different properties must be in contact. They are commonly referred to as solvent and solute. A solvent is a substance, usually a liquid, in which other materials are dissolved to form a solution or, in other words, to form a homogeneous fluid. A solute is a substance that can be dissolved by a solvent to create a solution. A solute can be a gas, a liquid or a solid. The solvent, or the substance that dissolves the solute, breaks up the solute and distributes the solute molecules equally. This creates a homogeneous mixture, or a solution that has the same properties everywhere. The diffusive layer is defined as the boundary region between the solvent and the solute.

Depending on the mixing volume or the amount of solute and solvent that can be mixed, the mixing ranges are: macromixing, mesomixing and micromixing [140][141]. Micromixers operate in the microscale, with volumes ranging from microlitres to millilitres. In a micromixer device, at least one of its channel geometries should not be greater than 500 μm (width, height or length). In general, both width and height are in the microscale range, and length in the millimetre range.

Parameters such as mixing quality or efficiency and speed are critical in characterizing the functionality of micromixers. The mixing quality or mixing efficiency is a measure of the homogeneity of a mixture. The coefficient of variation is used to calculate it. The coefficient of variation is the ratio of the standard deviation of the chemical composition of the samples in the mixing chamber to the arithmetic mean of the samples. The closer this value is to 0, the more uniform the mixture is. A coefficient of variation of 0 means a mixing quality of 100 %, i.e. the best mixing condition.

The mixing speed refers to processes in which mixers with an external energy are used to increase the mixing quality. This parameter determines the speed of the mixer agitator. This agitator can consist of several paddles, a mixer drum or a mixer pan, among others. The optimum mixing speed strictly depends on the design of the mixer and on the solute and solvent in used.

As previously analysed in Table 2.1 in chapter 2, the small size of microfluidic channels leads to a laminar (Reynolds < 2300) regime. Here, mixing components is tedious due to the lack of turbulence.

Mixing in micromixers is only possible due to the free movement of molecules through the fluids. The transport phenomena due to the molecules free displacement in a laminar flow are: a) Molecular diffusion, based on the random motion of molecules in the fluid, b) Taylor dispersion based on the increase in the diffusivity of the particles through the fluid layers due to a non-constant velocity field in the channel and c) Chaotic advection or the complex behaviour a fluid particle can attain, driven by the Lagrangian dynamics of the flow. More details about these transport phenomena can be found in Appendix B.

To enhance the molecule displacement and thus the mixing in micromixers, the need of special channel configurations and designs is necessary, as opposed to designs for the macro and meso scale. In micromixers, the mixing can be obtained by increasing the time that the layers solute-solvent are in contact or by enhancing the contact area between the solute-solvent layers. These disturbances are not predicted by the Reynolds number. To achieve these, some of the possibilities are:

- Passive elements to enhance the contact between solute-solvent layers
- Increasing the length of the mixing channel (section 3.1.1A)
- Increasing the mixing time or the time both solute and solvent are in the mixing chamber/channel (section 3.1.1A)
- Active micromixers (section 3.1.1B)

When using a micromixer at very low Reynolds number, the use of passive elements results beneficial to increase the contact between the fluid layers and thus, to generate local disturbances in the fluid chamber. Some elements to enhance the mixing at a micro scale are: nozzle/diffuser structures [142], obstacles or solid elements attached to the channel [143], the addition of curvatures or any disturbance element [144] that locally separates the parallel layers of the laminar flow and makes them intertwine. These passive geometries enhance the mixing by slightly inducing a transverse flow inside the channel.

Figure 3.1 shows two structures to increase the turbulences in a microchannel. In Figure 3.1(a) a nozzle structure is presented. The fluid layers represented as red arrows indicate the laminar flow of the fluid. The layers are orientated parallel to the channel walls. It is clear that the narrowing of the channel inhibits the parallel distribution of the layers. The upper and lower layers collapse with the channel walls leading to disturbances inside the channel. This behaviour enhances the distribution of the particles in the channel, thus, increasing the mixing efficiency. Similar behaviour occurs in Figure 3.1(b). The fluid layers travel in parallel along the channel until the obstacle with a triangle shape appears. Then, the upper layers collapse with the triangle side causing a chaotic

behaviour. This chaos favours the contact between the upper layers and the rest of layers. An increase in the mixing efficiency is therefore obtained.

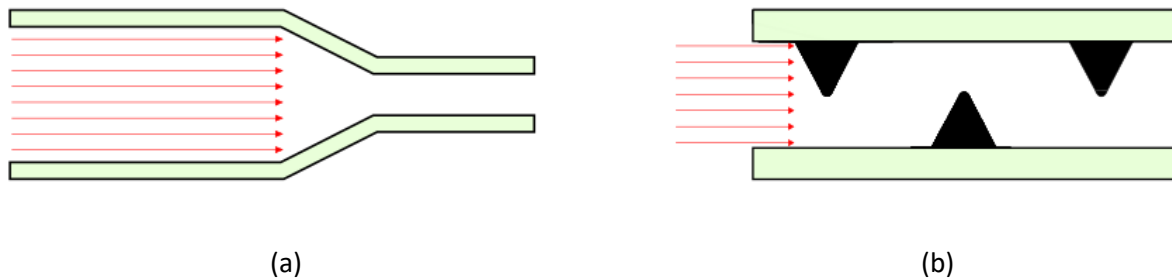


Figure 3.1: (a) Channel with a nozzle structure. (b) Channel with obstacles or passive elements.

In the following section, active and passive micromixers are explained in detail. In addition, some of the effects for turbulence generation outlined above are defined and investigated in more detail. Among others, the influence of the channel length, Reynolds number, the use of obstacles and active micromixers are analysed.

3.1.1. CLASSIFICATION OF MICROMIXERS

Micromixers are classified into two main types depending on the strategy they use to enhance the mixing: active and passive [145][146]. Active micromixers need external energy sources to improve the mixing quality and speed, while passive micromixers are mainly based on the geometry of the microchannels for fluid mixing.

A. Passive micromixers

The mixing mechanism of passive micromixers is only based on the contact between solute and solvent layers. Molecular diffusion transport phenomena are the only form to achieve the mixing. In laminar flow, these are molecular diffusion, Taylor dispersion and chaotic advection. To enhance these phenomena, passive micromixers often include passive elements or obstacles like the ones shown in Figure 3.1. The solute-solvent contact time also influences the time molecules have to move and enable the mixing. The contact time can be affected due to 1) the length of the mixing channel and 2) the inlets fluid velocities or the time the solute and solvent are in the mixing chamber. Both the nature of the contact and its time length influence the resulting mixing efficiency. Later in this section, these parameters are evaluated.

Passive micromixers have advantages like stable operation, easy integration and low-cost manufacture. Faster mixing time within the laminar regime can be achieved by decreasing the mixing path and increasing the interfacial area. Depending on the mixing principle, passive micromixers can be further classified into parallel lamination [147], sequential lamination [148], sequential segmentation [149], segmentation based on injection [150], and focusing micromixers [151]. Here only parallel lamination is explained in more detail.

Parallel lamination micromixers are based on the increase of the contact area between solute and solvent and the decrease of the striation thickness, dividing each the solute and solvent into a

certain number of streams and thereafter unifying them in a single stream. The simplest version of a parallel lamination mixer is a channel with two inlets, one for the solute and the other one for the solvent flow. To this family of passive micromixers belong the Y-micromixer [152] and T-micromixer type [153].

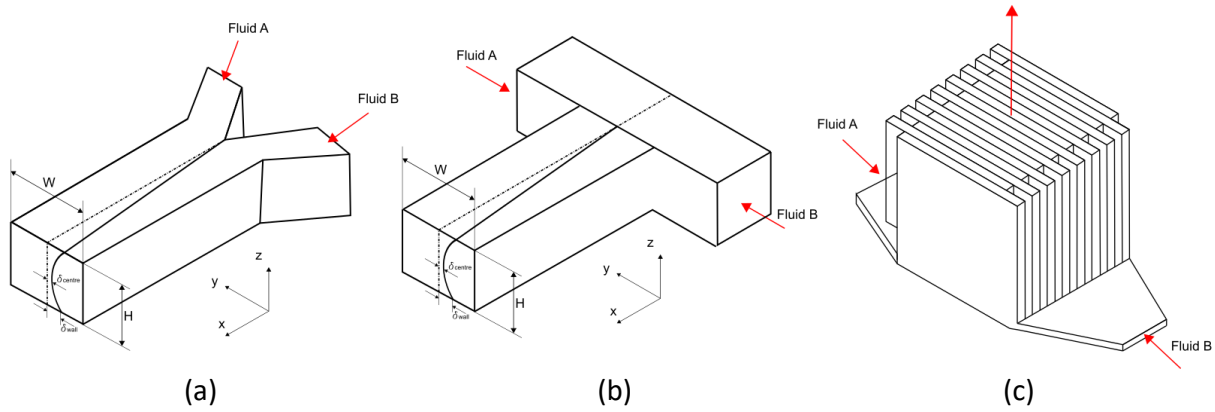


Figure 3.2: Passive micromixers; (a) Y-form, (b) T-form and (c) interdigitated parallel lamination.

In Figure 3.2 parallel lamination micromixers are shown, they are based only on the molecular diffusion of the solvent and solute. In this chapter, due to the symmetry of the devices presented, solute and solvent can indistinctly be represented by Fluid A or Fluid B. Here, for each micromixer one inlet is meant for the solvent and the other inlet for the solute.

In Figure 3.2(b), a laminar T-shaped micromixer is shown, while Figure 3.2(a) presents a Y-shaped micromixer. Both T-shaped and Y-shaped micromixers have only one entrance for the solvent and one entrance for the solute, leading to a single exit with the resulting mixture. Figure 3.2(c) shows an interdigitated parallel lamination micromixer. This micromixer has an inlet for the solute subdivided in multiple substreams and a single entrance for the solvent, also split in various substreams. As it can be observed from the layouts, the interdigitated lamination channels are thinner than the Y-type and T-type and there is a very significant increase of the interface area between the solvent and the solute in each substream, increasing the efficiency and molecular diffusion of the mixer. Hessel et al. [154] studied the different geometry systems and designs like rectangular, triangular, and slit-type, for different interdigital micromixers. Other well-known types of passive micromixers are multi-laminating flow configuration [155] and modified Tesla structures [156].

Here, some of the parameters that enhance the mixing are evaluated. These are the length of the mixing channel, the passive elements or obstacles and the Reynolds number.

The length of the mixing channel in a passive micromixer has a great influence in the mixing efficiency. The longer the channel is, the higher mixing efficiency is expected. Obviously, upon a length where the mixing efficiency is 100 %, there is no longer a channel length effect. Depending on parameters like the diffusion coefficient of the molecules, the optimal length of the channel to obtain 100 % mixing efficiency varies.

Rao et al. [158] performed COMSOL Multiphysics® simulations of a passive micromixer T-type. They studied the influence of the length of the mixing channel on the mixing efficiency. The mixing channel was 200 μm in height, 200 μm in width and 10.4 mm in length. The solvent was DI water

and the solute was an ink. The properties of both fluids for the simulations are summarized in Table 3.1.

Table 3.1: Parameters used for the COMSOL Multiphysics® simulation [158].

Property	Value
Diffusion Coefficient	$3.23 \cdot 10^{-10} \text{ m}^2/\text{s}$
Viscosity (DI water)	$2.646 \cdot 10^{-4} \text{ kg/m s}$
Viscosity (Ink)	0.001 kg/m s
Density (DI water)	1000 kg/m^3
Density (Ink)	998 kg/m^3

For the simulations, both the conservation equations (Appendix A) and the transport of species equations (Appendix B) were used. Figure 3.3 shows the concentration distribution of the solute in red and the solvent in blue along the T-type micromixer. For this simulation, a Reynolds of 100 was used, a very laminar regime. The concentration of ink in mol/m^3 ranges from 0 mol/m^3 (100 % DI water) and 1 mol/m^3 (100 % ink). Thus, a 0.5 mol/m^3 indicates a 100 % mixing efficiency. This can be observed in the colour bar in Figure 3.3. In Figure 3.3(a), three cross section images of the concentration distribution are shown: at the beginning, at the middle and at the end of the mixing channel. The first corresponds to the junction, where both inlets are in contact for the first time. There it is possible to see that the solute and solvent are separate. The second cross section is at the middle of the channel length (5.2 mm after junction). A more homogeneous cross section is observed, but still not a concentration of 0.5 mol/m^3 (100 % mixing efficiency). It is also to be noticed that the fluids at the walls are not mixed at this point. The last cross section is at 10.4 mm from the junction, i.e., at the micromixer outlet. This section shows a concentration close to the 0.5 mol/m^3 , 88 % mixing efficiency. At this section in the T-type image, it can be appreciated that the edges of the walls at this section have a different colour than that of the 0.5 mol/m^3 .

Regarding the effect of introducing passive elements inside the mixing channel, Rao et al. [158] studied the effect of diverse geometries on the mixing efficiency. They simulated the influence of a circle, a diamond, an ellipse and two triangles (one with a vertex pointing towards the outlet and one with a vertex pointing towards the opposite direction) as obstacles in the fluid's junction. They stated that the diamond geometry has the highest impact on the mixing efficiency. Figure 3.3(b) proves the significant increase of mixing efficiency along the length with the diamond-shaped obstacle. In the figure, the same T-type micromixer as for Figure 3.3(a) is simulated. All fluid properties and parameters are the same as in the previous case, the only difference here is the introduction of a passive element at the T-junction, a diamond-shaped element. Three cross section layouts at the same distances as before prove the effectiveness of such passive elements. In the T-type micromixer image, it can be seen how, at a length much shorter as the middle of the channel (5.2 mm), a mixing efficiency of 100 % is achieved. This confirms that the use of passive elements or obstacles in the mixing channel enhances the mixing efficiency and allows the fabrication of smaller devices. In this particular case, only half of the length is necessary to achieve a 100 % mixing efficiency.

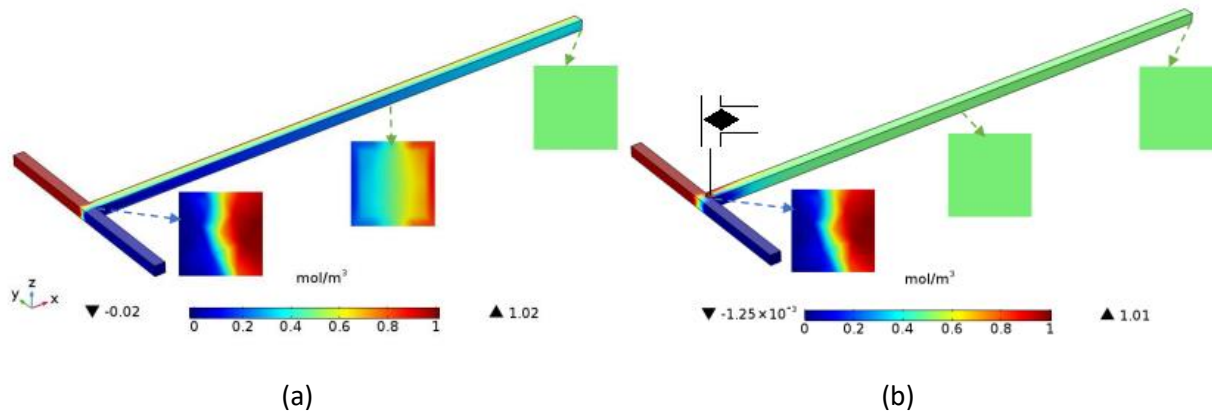


Figure 3.3: Concentration distribution profiles in a T-type passive micromixer: (a) without an obstacle and (b) with a diamond shape passive element. Adapted and modified from [158].

The relation between the Reynolds number and the mixing efficiency in T-micromixers has been widely studied. At very laminar flows, researchers have distinguished three subregimes or phenomena. At very low Reynolds numbers, $Re < 50$ the fluid layers remain segregated and mixing is only caused by molecular diffusion, named stratified flow regime. From $50 < Re < 150$, at the T-junction a secondary flow is generated due to the collision of the inlets in a form of small vortices, named vortex regime. Mixing is slightly increased due to the increase of the contact surface caused by the secondary flow. The layers remain separated here, as in the previous case. From $Re > 150$, another phenomenon appears at the junction: the engulfment regime. This regime interrupts the parallel fluid layers flow at the junction and multiple vortical effects are observed. Vortices in this regime allow the particles to travel from one side of the channel wall to the opposite wall. The increase of the mixing efficiency at this level is enormous. The limits for the Reynolds number at each subregime are estimated, varying as a function of the shape and size of the micromixer and the fluid properties.

Rao et al. studied the impact of the Reynolds number on the mixing efficiency for the T-micromixer exposed above with and without obstacles. For simplicity, here only the T-micromixer without obstacles is shown. Simulations of mixing efficiency at various Reynolds numbers are performed. Reynolds numbers in a very laminar range are chosen, from 0.1 up to 100. Here, the Reynolds number is defined for the fluid flowing through the mixing channel and thus, properties like the viscosity and the density are continuously varying with the length due to the mixing. Simulations allow the calculation of these values at every cross section through the mixing length.

Figure 3.4 presents the mixing efficiency obtained at the end of the mixing channel (at 10.4 mm). At this length, with a very low Reynolds number (0.1), the maximal mixing efficiency is achieved, 100 %. Molecular diffusion here predominates and the extremely long residence time (the time that the fluids are in the mixing channel) increases the probabilities that the molecules with their free displacement generate a homogeneous mixing. In the range from 0.1 to 10 Reynolds number, the mixing efficiency drops dramatically until approximately 80 %. This confirms the stratified flow regime, both solvent and solute fluid layers flow side by side and there is only a small amount of mass transfer perpendicular to the main flow. The residence time in this range is shorter than for the previous case, decreasing the mixing efficiency.

In the Figure 3.4, from Reynolds number 10 until 100 an increase of the mixing efficiency is observed although the contact time between solvent and solute becomes shorter at higher Reynolds number. The increase of the mixing efficiency in this range is attributed to the transverse secondary flow induced in the junction where both inlets get in contact, in this case at a higher speed than in the previously. The contact of the two inlets at higher speeds allows the generation of small vortices in this section, which gradually increase the mixing efficiency. These results are in accordance with the simulation and experimental data for T-micromixers from Bothe [159], Orsi [160], Hoffmann [161] and Fani [162].

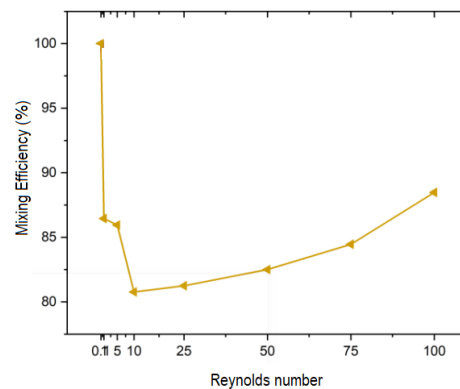


Figure 3.4: Mixing efficiency at 10.4 mm channel length (outlet) at different Re values. Adapted and modified from [158].

Figure 3.5 shows an experiment from Hoffmann et al. of a T-type micromixer [161]. In their research, a T-type micromixer with a geometry of $0.6 \times 0.27 \times 10$ mm (width, height and length of the mixing channel) is investigated. The solvent and solute used in this research also differ from those in the previous one. Here, a system with HCl, as solvent, and NaOH with dye disodium fluorescein, as solute, is used. The flow of fluorescein particles is visible through the channel by means of fluorescence microscopy. This allows studying the particle path along the length of the mixing channel. They determined the vortex regime for their micromixer in the range of $50 < Re < 150$ and the engulfment regime for $Re > 150$.

Figure 3.5 presents three cross sections of two of the above exposed regimes at various lengths of the mixing channel. First, $Re=150$ or vortex regime, where three distances in the mixing channel are evaluated at 0.5 mm, 5 mm and 10 mm. It can be observed that the fluorescein particles, in grey in the images, are flowing towards the interface solvent/solute in the middle of the images. As the length of the mixing channel increases, the amount of the particles in the middle of the section increases. The diffusion of the molecules here is the key element for mixing.

They also analysed the behaviour of the fluorescein particles at the engulfment regime at $Re=250$ and at the same channel lengths as before. Here, the generation of multiple vortices can be observed at the very beginning of the mixing channel (0.5 mm length). These vortices increase their dimension along the length of the channel. It is visible how the particles flow from outside to inside the vortices, thus increasing the mixing efficiency.

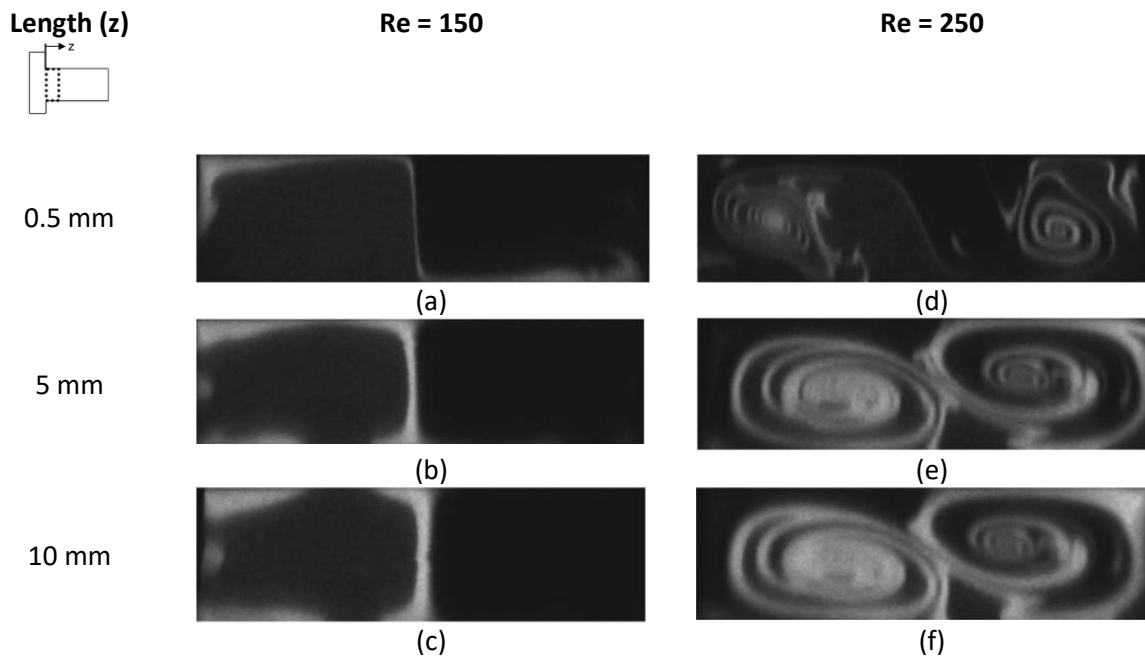


Figure 3.5: Cross sections of the mixing channel at Reynolds = 150 (vortex regime), at various lengths (a) 0.5 mm and (b) 5 mm and (c) 10 mm and at Reynolds= 250 (engulfment regime), at (d) 0.5 mm, (e) 5 mm and (f) 10 mm Adapted and modified from [161].

This section demonstrates the possibility of mixing fluids at very low Reynolds numbers without using an external energy source. Here, some passive mechanisms have been evaluated to enhance mixing efficiency in a passive micromixer. Their influence on the mixing efficiency has been studied. This is achieved by modifying the mixing channel length, the Reynolds number, including obstacles or interleaving the solute-solvent layers using an interdigitated parallel lamination micromixer. All these passive elements and mechanisms can also be integrated into active micromixers.

B. Active micromixers

Active micromixers use external energy sources to enhance the mixing efficiency and to reduce the residence time, i.e., the time fluids spend in the mixing channel. Active micromixers use the geometry of a passive micromixer and, in addition, increase the diffusion of particles through the mixing channel by applying external energy.

Energy can be applied primarily for one of these purposes: 1) to directly move the solute molecules using, for example, an electric field, as in the case of electroosmosis, or 2) by periodically changing the geometry of the mixing channel, for example, using piezoelectric membranes or electroactive polymers. In the latter, the walls of the mixing channel move, generating local turbulences and breaking the parallel displacement of the fluid layers. This phenomenon increases the generation of vortices in the mixing channel and thus the particle distribution and homogeneity in the fluids. The pumping micromixer proposed in this work enhances its mixing by changing the geometry of the mixing channel. This is achieved by using the Electroactive Polymer technology.

Some energy sources typically used include ultrasonic vibration [163], electro kinetic energy [164], and piezoelectric vibrating membranes [165]. The main drawbacks of active micromixers are the

high amount of parts and the difficulties in the fabrication process, as well as in the integration with other microfluidic systems.

As a summary, active micromixers based on the thermal response of a membrane are very powerful in terms of actuation pressure, but their processes tend to be very slow and therefore, the actuation frequencies are significantly low. Pneumatic actuators are a common type of microactuators in the fabrication of micromixers. Their main drawbacks consist of the high amount of parts needed and the volume required for actuating. The actuation frequency depends on the external pressure supply and switching system, and in general is between 0.1 Hz and 1 Hz. On the contrary, electrostatic and piezoelectric microactuators work at a very high frequency. Although the strains generated tend to be small, stacking piezoelectric and electrostatic actuators lead to an increase of the strain. Depending on the application, the geometry of the micromixer and the fluids to mix, the frequency needed to improve the mixing efficiency varies.

Figure 3.6 shows two examples of active micromixers: (a) a thermopneumatic micromixer and (b) a piezoelectric micromixer. The thermopneumatic micromixer [166] works with two integrated thermopneumatic actuators out of phase in combination with four micro check-valves. The fluid A is pumped through its inlet-channel to a common channel with the fluid B, which arrives to the same spot with the same conditions as the Fluid A. Then, both fluids get mixed in the mixing channel and arrive to a reservoir. Due to the pulsatile flow, there is a disturbance which improves the mixing efficiency in the mixing channel, similarly to that of the sequential lamination. Here, fluid A and fluid B can be either the solute or the solvent due to the symmetry of the geometry.

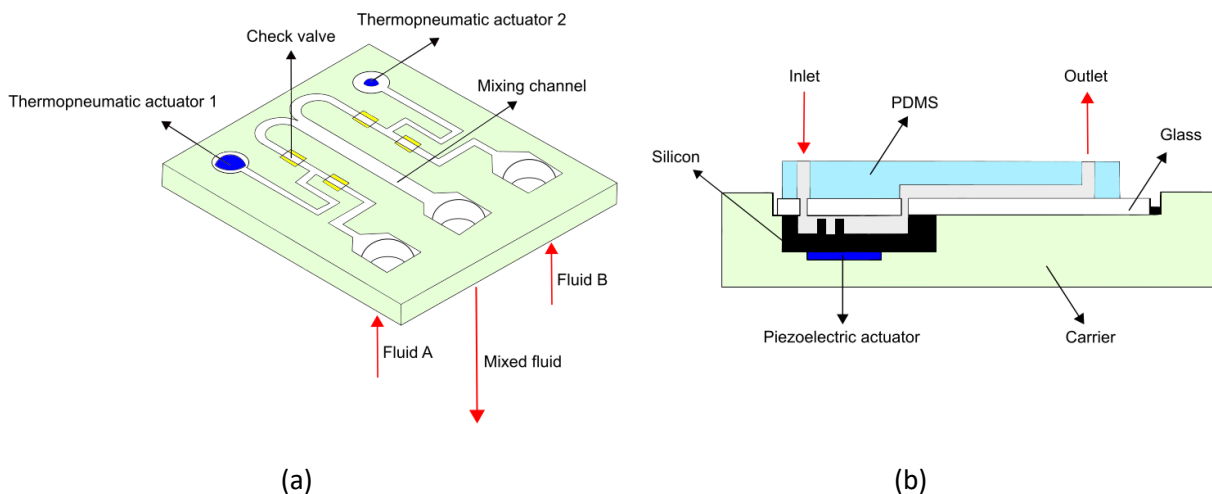


Figure 3.6: (a) Concept of an active micromixer based on pressure-driven disturbance. The fluids are delivered by integrated micropumps. Thermopneumatic actuators [167] drive the pump and generate the pressure disturbance. (b) Sketch of an active micromixer based on pressure-driven disturbance. The fluids are delivered by hybrid-integrated piezoelectric micropumps [168].

The working principle of each pump is based on an integrated thermopneumatic actuator and two valves. The microheaters in the system generate vapour bubbles. The bubbles act like a piston and move the fluid out. Thanks to the check-valves, the fluid flows to the outlet direction. Once the heat is removed, these bubbles condensate. By repeating this procedure of bubble creation, a continuous flow is obtained. The two fluids A and B flow towards a long channel where both get mixed and move to a single outlet.

The hybrid-integrated piezoelectric micropump [168] is based on a Y-type design. A valveless diaphragm pump, a piezoelectric actuator, drives the fluid from the inlet to the mixing channel and afterwards to the outlet point. The fluid flow is typically between 20 nl/s to 200 nl/s, and the pressure up to 5.0 kPa.

In this subsection, a general overview of micromixers has been exposed. Further details can be found in the research of Lee et al. [169]. They wrote a compilation of the recent advances in the micromixer field with a great number of examples and their main application.

3.1.2. PUMPING MICROMIXERS

For some applications, it is necessary to use a device where liquids are pumped in, mixed and then pumped out; some of these applications are drug delivery of substances and reagents for chemical analysis.

Based on the technologies above mentioned for micromixers, diverse pumping micromixers have already been developed. The advantages of pumping micromixers are the simplification of parts needed for the mixing, where neither external valves nor pumps are required, and the increase of the mixing quality or efficiency, because the micromixers are often active micromixers.

Yoon et al. [170] presented an AC electroosmosis pumping micromixer. Electroosmosis works under an applied electric field, where the movement of counterions in the diffusion layer favours the movement of the surrounding liquid molecules due to the viscous effect. They got a mixing efficiency over 90 % for a combination of mixing and pumping. They investigated the mixing efficiency and flow rate depending on the height of the microchannel.

Some examples of pumping micromixers are the ones presented in Figure 3.7: a thermopneumatic and a piezoelectric pumping micromixer. Tseng et al. [171] also developed a pumping micromixer out of pneumatic actuators. The micromixer is shown in Figure 3.7(a). The micromixer has four PDMS membranes and two pneumatic microvalves. Samples are pumped to an annular channel from two different reservoirs. Thereupon, the membranes deform allowing the fluid to mix and to pump the mixed fluid out of the device by peristalsis. The rotatory pump has a flow rate of 165.7 $\mu\text{L}/\text{min}$ at a driving frequency of 17 Hz and an air pressure of 207 kPa.

Sheen et al. [172] fabricated a piezoelectric pumping micromixer, illustrated in Figure 3.7(b). The micromixer has a Y-type entrance and two regions with obstacles to favour the contact between the fluid A and B and to generate vortices to increase the mixing between species. The chamber works as a valveless micropump. A PZT actuator diaphragm membrane generates an increase and a decrease of the chamber volume, generating a flow. The maximum flow rate obtained is 50 $\mu\text{L}/\text{min}$ at 50 V and 2.2 kHz, with a mixing efficiency of 84 %.

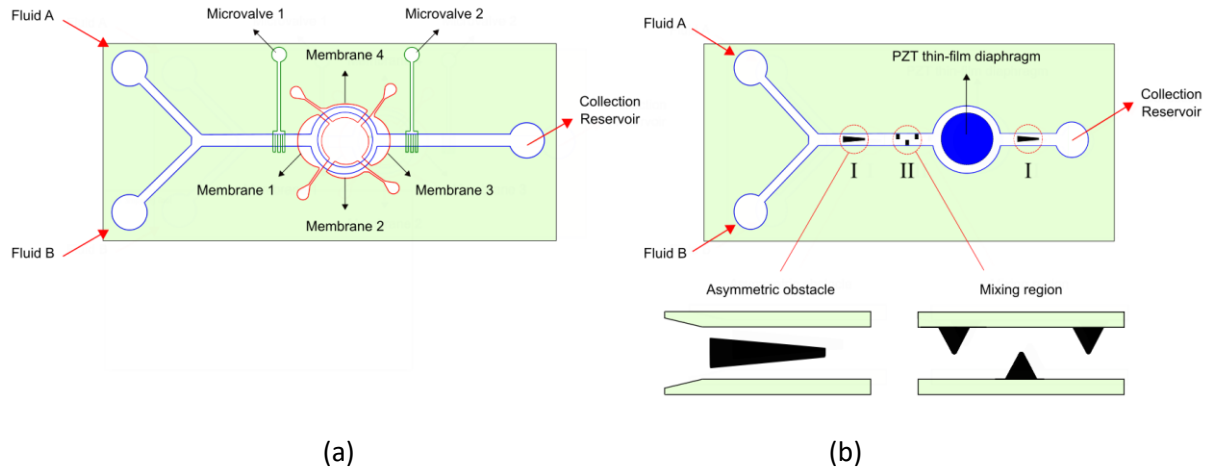


Figure 3.7: (a) Schematic illustration of a pumping micromixer composed of a Y-shaped microchannel, four PDMS membranes and two pneumatic microvalves [171]. (b) Schematic diagram of a pumping micromixer including two asymmetrical obstacles and one mixing region with triangular-wave structures.

3.2. CONCEPT OF A DEA MICROMIXER

The realization of a pumping micromixer pursued in the context of this work with the help of dielectric elastomer stacked actuators has the primary goal of demonstrating a new field of application for dielectric elastomer actuators (DEA). In contrast to discrete linear actuators, often found in literature, this is a fully integrated fluid system. Due to the novelty of this application for dielectric elastomer actuators, the first functional models are to prove the suitability and feasibility of the system. Miniaturization and further characterization of the systems can be further studied in the future.

As mentioned previously, the design of a micromixer consists not only in the scaling down of a mixer due to the dominance of surface effects over the volumetric ones, the very laminar regime is also a challenge for the design of micromixers. In micromixers, due to their small size, the shear stress increases in spite of the very low speed rates. Mixing in a laminar regime is a common step in multiple biological processes due to the high viscosity of substances and the very low flow rate. Micromixers can also be used as microreactors; in this case, the chemical reaction does not depend on the size of the device but on the reaction speed.

In this work, a pumping micromixer fabricated out of the electroactive polymer technology is proposed. In the past, the fabrication of DEA micromixers was not considered due to the small deformation of a single layer DEA. Thanks to the stacking of thin layers and prestretched membranes, it is possible to achieve a larger displacement with lower voltages.

What makes Dielectric Elastomer Stacked Actuator (DESA) micromixers interesting for these applications is the biocompatibility [173][174] of the used materials (PDMS and graphite) and the actuation principle, on which the micromixer is based, the peristalsis. The micromixer not only mixes, but also pumps the fluids into and out of the device, decreasing the number of external devices required. By changing the actuation frequency of the DEA, different mixing ratios and flow rates can be achieved.

3.2.1. GEOMETRY

The geometry of the micromixer is based on a peristaltic pump previously developed by Lotz [175]. The micromixer is 33 mm long and 25 mm wide. It is based on twelve stacked actuators distributed in: two different pumping chambers (chambers 1 and 2) consisting of four parallel actuators each and a mixing chamber (chamber 3) made of four parallel actuators. The size of the actuators in the pumping chambers (chambers 1 and 2) is 3 mm length and 6 mm width, while in the mixing chamber the actuators have 3 mm length and 15 mm width. The distance between parallel actuators is 1 mm.

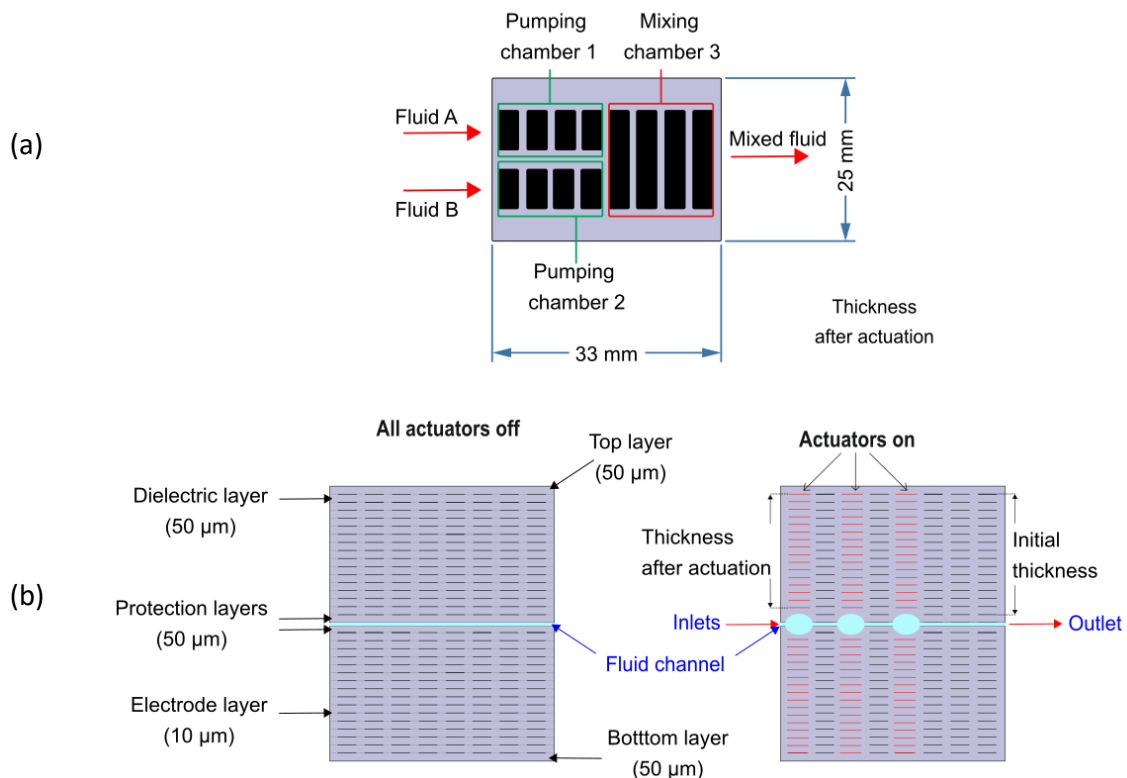


Figure 3.8: (a) Top view of the micromixer with two pumping chambers (green boxes) and one mixing chamber (red box), each consisting of 4 actuated regions. (b) Working principle of the micromixer: cross sectional views of the micromixer when all the actuators are off (left) and when the voltage in some actuators is applied (right), where a change in the fluid channel height is observed.

In Figure 3.8, a layout of the micromixer is shown. Above, the top view of the micromixer with two pumping chambers (green boxes) and one mixing chamber (red box), each consisting of 4 actuated regions can be observed. The lower drawings show the working principle of the micromixer: profile views of the micromixer when all the actuators are off (left); cross sectional view when the voltage in some actuators is applied (right), where a change in the fluid channel volume is observed.

The micromixer is formed by a total of 30 actuation layers. The layers are disposed in 15 layers of 50 μm of elastomers sandwiched between electrodes, a protective PDMS layer (50 μm) to prevent the contact of the liquid with the actuators, the empty fluid channel (40 μm) and a symmetrical number of layers to form the bottom part of the device. Table 3.2 summarizes the main geometric parameters of the micromixer.

In order to increase the diffusive mixing of the solute and solvent, the interfacial area could be increased or the thickness of the solute and solvent layers decreased. Since the length of the mixing chamber in the micromixer is small, the diffusive mixing is increased due to the high gradient of concentration in a short distance. In the microchannel, the difference between height and width leads to a low aspect ratio, the mixing of solute and solvent is also favoured due to the increase of contact of both substances. On the other hand, a low aspect ratio leads to a decrease in the dispersion factor, which leads to a decrease of the Taylor dispersion phenomenon (relation shown in Eq 3.6).

It is possible to increase the diffusion coefficient by increasing the fluids temperature or decreasing their viscosity, but in practice this does not provide a very significant change in diffusion.

For this particular design, the width of the channel is 3 mm and the initial height 40 μm . The thin layer channel increases the parallel contact surface between solvent and solute.

Table 3.2: Summary of the geometry of the system.

Micromixer	
Length	33 mm
Width	25 mm
Number of protective layers	2
Thickness of protective layers	50 μm
Channel height	40 μm
Total stacked actuators	12
Single actuators in a stack	15+15
Thickness of dielectric layer	50 μm
Thickness of electrode layer	10 μm
Distance between stacked actuators	1 mm
Pumping Chambers (2)	
Stacked actuators per inlet	4
Actuators length	3 mm
Actuators width	6 mm
Mixing Chamber	
Number of stacked actuators	4
Actuators length	3 mm
Actuators width	15 mm

3.2.2. MATERIALS

As mentioned in section 1.1, an electrostatic actuator must have good mechanical and electrical properties, in order to be more efficient. On the other hand, for the manufacturing of a micromixer other properties such as biocompatibility and light-weight are important.

Although some other materials have shown better properties in terms of deformation versus voltage, as the fabrication process is based in this case on stacking automatically single layers of actuators, other properties of the materials like rapid curing at low temperature for the dielectric and easy application and homogeneity for the electrodes are fundamental.

C. Dielectric elastomer

In a material search, Elastosil® P7670, whose material properties suggest suitability for dielectric elastomer stacked actuators, was considered the most appropriate elastomer for the fabrication process. The main reason for it is the demand for low stiffness and a short curing time. Elastosil® P7670 is developed by Wacker GmbH for the use in prostheses, which also indicates its high degree of biocompatibility.

In terms of mechanical properties, Elastosil® P7670 has a low Young modulus of 165 kPa, and with regard to electrical properties, a relative permittivity of 3. Elastosil® P7670 does not have a high electrical breakdown. Dielectric elastomer actuators are normally operated with the highest possible electric field. If the electric field exceeds the electrical breakdown, the material irreversibly breaks, so it is critical to know this value before actuation. For Elastosil® P7670, the electrical breakdown is 46 V/μm [176], while for other elastomers this value is near 115 V/μm [132], for example Elastosil® film E2030 (also from Wacker). Elastosil® P7670 is provided as a two-component silicone and cross-links at 80 °C during 2 minutes.

D. Electrodes

Electrodes play an important role in dielectric elastomer actuators. As already suggested in section 1.2.2, a high electrostatic pressure can only be achieved if the electrodes do not impede the expansion of the dielectric, contrary to the electrodes in a classical plate capacitor.

In the special case of dielectric elastomer stacked actuators, the electrode must also be as thin as possible. Practically all electrode materials create a conductive surface by the juxtaposition and superposition of individual particles. When stretched, the particles can glide past each other up to a certain limit without losing contact with each other. However, the thickness of the conductive layer does not change. In the stacking actuator, the electrode layers therefore represent a thickness-invariant part of the total thickness.

Matysek et al. [177] show that the electrode should therefore not contribute more than 10 % of the thickness of an actuator, so that the deflection of the actuator is also not affected by more than 9 %. In addition to these mechanical-geometric properties, the electrical properties of the electrodes are of course particularly important.

The most common material used as electrodes are carbon-based. The carbon can be present in three different configurations: graphite, carbon black and carbon nanotubes.

Graphite is the natural, mineral form of carbon. The crystal atoms are arranged in parallel layers, in a hexagonal structure. This anisotropic crystal structure is macroscopically reflected in the distinctly anisotropic mechanical and electrical properties of graphite. Commercial graphite powder consists of angular particles with a diameter between 2 μm and 50 μm, depending on the fineness of the powder.

Carbon black is an industrial product and is mainly used as a filler to adjust the mechanical properties of polymers, for example as printing cartridges. Due to pyrolytic production from hydrocarbons, carbon black consists of spherical aggregates. These primary particles with a diameter of about 100 nm agglomerate to particles with a diameter of about one order of magnitude higher as the graphite particles. However, these electrodes are too thick for multilayer

actuators. Kovacs et al. [178] developed a process to apply the industrial carbon black (Ketjenblack EC) so thinly to the dielectric that the electrode practically consists of only one particle layer.

Carbon nanotubes are the above-mentioned third configuration of carbon with a hexagonal crystal lattice. Two basic types of nanotubes are described: single wall carbon nanotubes (SWCNT) consist of only one lattice wall, whereas multi wall carbon nanotubes (MWCNT) can have up to 50 coaxial lattice walls. The tube shape leads to an extreme aspect ratio: the typical diameter for SWCNT is less than 5 nm, for MWCNT about 50 nm. The length can be several micrometres for both types.

Extremely thin conductive layers of SWCNT have already been used on EAPs as electrode material. The SWCNTs are sprayed on by airbrush in various layer thicknesses. The film thicknesses range from 5 nm to 250 nm with film sheet resistances between 20 kΩ/sq and 0.1 kΩ/sq [179][180][181]. Like all nanoparticles, carbon nanotubes and especially SWCNT have a very large specific surface area. This leads to a very strong agglomeration of the primary particles. The carbon nanotubes can therefore only be brought into a solution by using dispersing agents, which often leads to reducing the conductivity.

After analysing the characteristics of these three materials, natural graphite has the best electrical properties and is the easiest to process for the fabrication of stacked actuators by spraying.

Table 3.3: Properties of the dielectric and electrode material

Dielectric	Wacker Elastosil® P7670 A/B
Young Modulus (kPa)	165
Relative Permittivity, ϵ_r	3
Tensile Strength (N/mm ²)	1.8
Tensile Strain (%)	600
Electrode	MF 2/99,5-99,9E
Particle size (µm)	X50 < 2
Conductivity (S/m)	20
Sheet resistance, one layer (kOhm/sq)	10

The materials used for the fabrication of the micromixer are Elastosil® P7670 PDMS from Wacker GmbH, for the dielectric and the passive layers, and flake graphite powder MF2/99,5.99,9E from NGS Naturgraphit GmbH for the electrodes. Some of the relevant properties of the dielectric and electrode materials are summarized in Table 3.3.

3.2.3. WORKING PRINCIPLE

The proposed pumping micromixer corresponds to the active micromixers type. Active micromixers need external energy sources to improve the mixing quality and speed. For this prototype, an electric field is applied to the actuators to enhance the mixing and also to allow the fluid to flow: the DEA technology is used for this purpose. The shape of the micromixer is similar to a Y-type passive micromixer. Y-shaped micromixers have only one entrance for the solvent and one entrance for the solute, leading to a single exit with the resulting mixture.

The mixing and pumping of the fluids are based on peristaltic movements. Peristalsis involves an actuation principle where energy is transferred from the periodic motion of the walls to a fluid volume. Actuator elements are driven by rectangular signals with a phase shift to produce

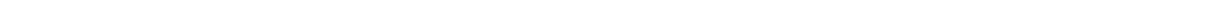
peristaltic motions of contraction and relaxation like the ones occurring in some organs in the human body, where segments of the alimentary canal alternately contract and relax allowing the food to travel inside the body (Figure 2.3).

Some of the advantages of the peristalsis (section 2.2.2) are that the fluid that has to be transported only comes in contact with the walls of the pump. The contamination of the fluids can be avoided, which is convenient in medical applications to inhibit the contact of the DNA or other biologic substances with non-biocompatible substances. In peristaltic systems there are no rotating elements. Therefore, high relative velocities, which might cause cavitation, are not expected. This is a highly important feature if the transported fluid separates under the influence of high flow velocities such as suspensions.

The working principle of the micromixer is based on the opening and closing of the channel walls between the actuators. When the voltage is applied, the actuators expand in area and compress in thickness. By reducing the thickness of the stacked actuators, the volume of the channel increases. A controlled activation and deactivation of the stacked actuators following the opening and closing schemes for peristaltic pumps, generates a phase shift between the activated chambers and thus, a positive fluid flow towards the outlet. This produces a pressure gradient that makes the fluid flow along the device. Previous works revealed that, although during one period of sinusoidal excitation the liquid volume is flowing in both directions, the net pumped fluid volume at the outlet after one period is non-zero, indicating successful fluid pumping.

The channel walls are initially opened with a height of $40\ \mu\text{m}$ due to the manufacturing process. The deformation of the stacked actuators is approximately 5 % when a voltage of 1500 V is applied to the electrodes. Each dielectric layer, as explained before, has a thickness of $50\ \mu\text{m}$. Therefore, the channel height changes from $40\ \mu\text{m}$ to $40\ \mu\text{m} + \Delta z$ when the actuation occurs, leading to an increase in height of the passive state height. When the voltage is switched off, the actuators return to the passive state and partially close the channel. This considerable change in volume in the chambers, mostly due to the change in height of the actuators, directly creates pressure differences in the whole system, allowing the fluid to flow.

The twelve actuator elements are driven by rectangular signals with a variable phase shift which causes a peristaltic motion through the whole device. The fluid flows through the channel in the middle of the micromixer, firstly into the pumping chamber, afterwards into the mixing chamber and then out of the device. In the next chapter, the fabrication and characterization of this device is investigated.



4. FABRICATION OF A PUMPING MICROMIXER

During the development of this thesis a pumping micromixer out of dielectric elastomer actuator (DEA) has been fabricated. The micromixer belongs to the category of active micromixers, i.e., the mixing of the fluids is not only provided by the geometry of the micromixer (Y-type), but also by the walls movements around the fluid, increasing the mixing efficiency of the fluids, or in other words, an external energy is applied to the system to enhance the mixing.

In the previous chapter, the mechanisms to optimize the mixing in micromixers have been reported. In addition, the working principle, geometry and materials of the pumping micromixer have been presented in detail. In the following chapter, the fabrication method, the electrical connection techniques and the electromechanical and fluid dynamical characterization of the pumping micromixer are presented. Moreover, the most relevant results of pumping and mixing are exposed.

4.1. FABRICATION OF DIELECTRIC STACKED ACTUATORS

The fabrication method for stacked actuators in TU-Darmstadt highly differs from the previous fabrication methods exposed in chapter 2. The automatization of the fabrication process for stacked actuators greatly increases the variety of devices to fabricate. Within this section, the fabrication method for a pumping micromixer with the automatic system is explained in detail.

4.1.1. FUNDAMENTALS OF DIELECTRIC STACKED ACTUATORS

In order to decrease the applied voltage and to increase the actuator force, we assemble single layer DEAs on one another to obtain dielectric elastomer stacked actuators (DESA) or multi-layer stacks: each single layer is electrically connected in parallel. The fabrication of stacked actuators allows a higher displacement in the z -direction in comparison with the single layer technology due to the large number of layers.

The change in thickness Δz is defined as the difference between the actual thickness z and the initial thickness z_0 . The static deflection of a stacked actuator with n layers and Young's modulus Y can be calculated as:

$$\frac{\Delta z}{z_0} = \frac{p}{Y} = n \frac{1}{Y} \varepsilon_0 \varepsilon_r \frac{V^2}{z_0^2} = n \frac{1}{Y} \varepsilon_0 \varepsilon_r E^2 \quad \text{Eq 4.1}$$

where p is the Maxwell pressure, ε_0 the permittivity of free space, ε_r the dielectric constant, E the electric field, z_0 the initial dielectric thickness and V the applied voltage (in the order of a few kV for typical DEA).

Figure 4.1 shows in detail the deformation of stacked actuators. It can be observed how the applied voltage in Figure 4.1(a), allows the deformation in z , or the reduction of thickness of the whole device, according to Figure 4.1(b), thanks to the individual decrease in thickness of each

layer. Unlike single layer DEA, in dielectric elastomer stacked actuators the dimension of interest is the change in thickness.

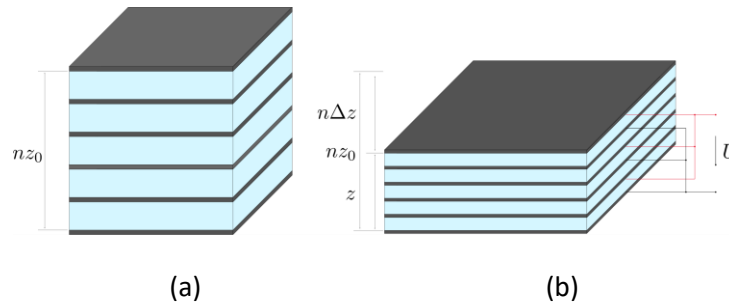


Figure 4.1: Dielectric stacked actuator working principle: in blue, the elastic dielectric material and, in grey, the compliant electrodes. After applying voltage to the stacked actuator (a), an area deformation of the dielectric occurs and thus, thanks to the conservation of volume, a decrease in thickness of the dielectric takes place (b).

Some advantages of using stacked actuators are the decrease of the applied electric field, the increase of the deformation in z , the increase of the stroke and the robustness of the final actuator compared to a prestretched single layer actuator. There is no need to prestretch the dielectric to obtain a higher stretch upon actuation.

In order to manufacture these multilayer systems, researchers have developed different fabrication techniques. These can be classified in two main groups: 1) Single-layer folding film and 2) layer-by-layer deposition methods.

The single-layer folding film method uses a continuous strip of the dielectric layer. The dielectric layer is coated with compliant electrodes on both sides. This forms a single dielectric elastomer layer. Afterwards, this coated strip is folded up several times forming a structure. The dielectric layer can be a prefabricated film, for example, E2030 Elastosil® from Wacker or a film fabricated with the liquid elastomer.

While Carpi et al. [182] used mould casting to fabricate rectangular and circular cross-section folded DESA, Maas et al. [183] developed a fully automated method based on a prefabricated film, E2030 Elastosil®. This allows very high-quality actuators with homogeneous and reproducible properties. They reported stacked actuators of 200 layers with an active area of 64 mm² and 3.5% deformation when applying an electrical field strength of 50 V/μm. The main drawback of this folding processes is the lack of adhesion between the stacked layers, which can lead to delamination under tensile load. Thus, researchers have used polymer-based electrodes to solve this adhesion issue, but as a result an increase of the stiffness of the final stacked has been observed.

In layer-by-layer deposition methods, the dielectric and the electrode layers are alternatively stacked. The dielectric layer as liquid-form can be structured using various methods. One of these methods is the so-called doctor blading, in which a blade with a certain gap transports the dielectric liquid on top of a substrate. This gap or distance between the blade and the passive layer corresponds to the final thickness of the dielectric layer. The company CT Systems AG uses this technology for the automatic fabrication of dielectric elastomer stacked actuators. A more precise liquid deposition method is the spin coating method. Here, a disc rotates at various speeds leading to a very homogeneous and reproducible layer thickness. Matysek et al. [184] developed an

automatic process to fabricate stacked actuators based on depositing the dielectric layer by spin coating and afterwards spraying the electrodes.

In this chapter, the micromixer devices are manufactured with the method developed by Matysek and the research group of Schlaak. In the following section, this process for the micromixer is explained in detail.

4.1.2. FABRICATION TECHNIQUE FOR DESA

The technology used in this thesis for the production of dielectric stacked actuators is based the layer-by layer manufacturing technique developed by Jungmann [185], and followed by its linear automatization by Matysek and Lotz [184]. The process is based on three steps: dielectric deposition, elastomer crosslinked/heating step and electrode deposition.

A. Dielectric deposition

First, PDMS Elastosil® P7670 [186] components A and B, each in a single syringe, are automatically mixed in a mixer, with ratio 1:1, and deposited on top of a plate disc. The disc can move along all the stages of the fabrication process. The stacked actuator grows in height on the centrifugal plate along the processes. Different sizes of this disc are available in order to save material, depending on the required diameter of the final version of the actuator. Some of the parameters that are modifiable in the dielectric deposition process are:

- Mixing ratio of PDMS
- PDMS dispensed dose
- Speed of PDMS dispensed
- Disc speed and acceleration

The first step is the spin coating of the PDMS: the mixture of PDMS is deposited on top of the disc surface, with a controlled amount and speed. The most important requirement for this step is obtaining a reproducible homogeneous layer thickness that does not change even during the production of 50 or more layers. The disc rotates in ramps at four different speeds, from lower to higher rotational speed, in order to cover the disc surface with the elastomer material and get the desired thickness. The fastest speed provides the final thickness of the elastomer layer. The various influencing variables on the thickness of the dielectric in a spin coating process are: a constant rotational speed, duration of the spin coating process, the Newtonian behaviour of the material to be spun on, a constant density and viscosity. This process proves to produce layer thicknesses in a range between 5 μm and 100 μm . Figure 4.2 shows a schematic of this first step of the fabrication process: the dielectric deposition.

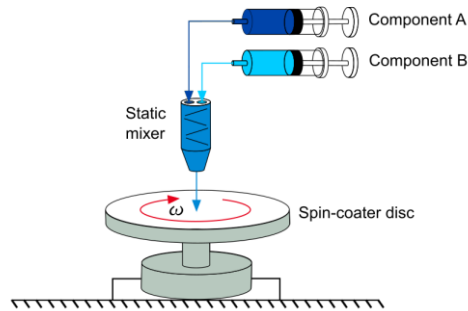


Figure 4.2: First step of the fabrication of DESA at Technische Universität Darmstadt, the spin coating process. The PDMS, in two syringes each with a component of it, namely A and B, is unified by a PET mixer. The resulting mixture is deposited on top of a spin-coater disc which rotates to provide the desired thickness. Adapted and modified from [175].

B. Elastomer crosslinked /Heating step

The second step is a heating step for curing and crosslinking the PDMS. The disc travels to a new stage, a metallic platform descends and surrounds the disc. While the disc rotates to uniformly propagate the heat on the disc, the heating element (a radiation source) starts operating. The temperature and the duration of the heating is controlled by LabVIEW program. The disc has a temperature sensor to ensure that the disc is not overheated. In case it happens, the process is automatically turned off. The temperature range available is between 0 and 150 °C. Two heating stages are available in the system.

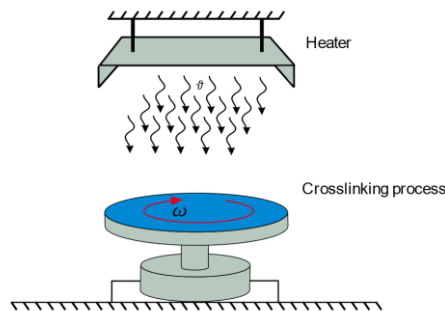


Figure 4.3: Elastomer crosslinking step. The disc arrives to a new stage, the heating area. The heating device descends and covers the spin coater disc surface. While the disc slowly rotates, the heater crosslinks the elastomer. Adapted and modified from [175].

In Figure 4.3, the heating system is shown. The heating device descends and covers the spin coater disc surface and heats while the disc is slowly rotating (around 10 rpm).

C. Electrode deposition

The third step is the electrode deposition on top of the crosslinked elastomer. The rotatory disc arrives to a new closed stage. The electrode material is sprayed as a suspension by means of a two-substance nozzle. Using a suspension allows the precise control of the sprayed particle quantity via the measurable particle concentration in the volume of liquid held.

A thin metallic mask with the desired shape of the electrodes moves down and locates directly on top of the elastomer membrane without touching it. The electrode suspension is atomized in a point nozzle by means of the atomizing air. A second forming air stream transforms the resulting round spray cone into a flat jet covering the entire actuator diameter. After the spraying of the electrodes, compressed air is ejected from the bottom to ensure the evaporation of the electrode solvents while the disc is gently rotating. The previous step of heating the disc helps the adhesion of the electrode to the elastomer and the solvents evaporation.

The system has two stations for spraying, each with a separate electrode solution tank and two mask holders. Therefore, four different electrode shapes are possible for one actuator.

The interaction of atomizing pressure, forming pressure and nozzle opening, as well as the speed with which the nozzle is moved over the the elastomer surface, must be precisely matched to achieve a uniform electrode quality. The variable parameters in this step are: number of paths of the nozzle, time of spraying, distance in the y -direction for spraying and distance z from the mask to the elastomer layer.

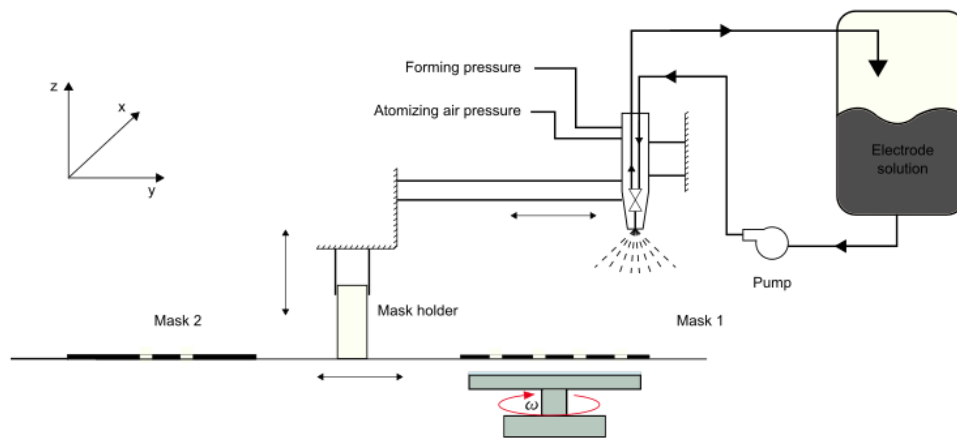


Figure 4.4: Third step in the fabrication of DESA: spraying the electrodes. The spin coater disc is located in the new stage position. A mask holder supports two different masks, named Mask 1 and Mask 2. The desired mask is located on top of the elastomer layer. To do so, the desired mask moves first in the y -axis to the right position, vertically aligned to the spin coater disc. Then the mask moves down in the z -axis towards the elastomer layer in the spin coater disc until there is no gap between the dielectric layer and the mask. A tank holds the electrode suspension. The electrode suspension flows to the spray unit or nozzle by the action of a pump. The electrode solution enters the nozzle. While the nozzle head is moving in the y -direction, the electrode solution gets spread out of the nozzle and deposits on the elastomer layer with the mask shape. Adapted and modified from [175].

Figure 4.4 shows a schematic of the spraying stage. First, a tank holds the suspension of graphite-isopropanol. Then, a pump agitates the suspension 15 seconds before the spraying takes place, in order to mix the suspension. At the same time, the electrode-mask moves down to locate on top of the dielectric layer. From one layer to the next one, the displacement in the z -axis of the mask decreases to stay always at the same distance of the elastomer layer. This gap distance is the thickness of the elastomer plus the thickness of the electrode.

Afterwards, a valve opens and while the nozzle is moving in the y -axis, the suspension gets out of the dosing system of the nozzle with a controlled speed.

In order to control the thickness of the electrode, a dummy layer is tested before the fabrication of a stacked to control the conductivity of the future layers. The electrode is sprayed on an

elastomer layer of 3 mm thickness with the machine. The spraying parameters are evaluated, measuring the resistance of the electrode.

The resistance measuring station shown in Figure 4.5 is used to measure sheet resistances of elastic electrode materials. The conductive materials must be applied as a rectangular area on an elastic material. A 4-point measuring instrument is used for the determination of the film electric resistance (SD510, NAGY measuring systems). Several resistance measurements are done before the fabrication of a stacked in order to optimize the nozzle parameters. Previous experiments demonstrated a constant layer resistance after the fabrication of more than 100 layers. Within this method, the parameters of the spray nozzle are defined to obtain a precise thickness of the electrode layers.

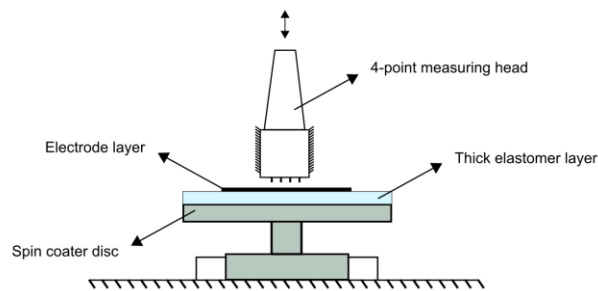


Figure 4.5: Resistance measuring station for the determination of the film resistance (SD510, NAGY measuring systems). Adapted and modified from [175].

The mechanical structures of the process modules are supported by a basic framework, which also includes the process infrastructure in the form of electrical energy and compressed air. Each module has its own control electronics, which are controlled centrally via LabVIEW, but also a user interface for manual operation is included. A control program on the computer manages the central process sequence.

Table 4.1: Summary of the degrees of freedom of the different elements of the automatic machine for the fabrication of DESA.

	Axis x	Axis y	Axis z
Rotational disc	✓		
Mixer			✓
Heating system			✓
Mask stage		✓ #	✓
Nozzle		✓	

#The mask stage changes in the y-axis, only when the type of mask is changed. As mentioned before, each spraying stage has the possibility to spray through two different masks.

The entire manufacturing process described above is designed for elastomeric devices with a maximum diameter of 100 mm. Within this area, actuator elements with almost any shape can be manufactured.

For a better understanding of the entire process, Figure 4.6 shows the different positions in the linear stage. The movements of the elements in the axis are summarized in Table 4.1.

4.1.3. FABRICATION OF A PUMPING MICROMIXER

The fabrication technique employed for the processing of the micromixer is based on the steps mentioned above [187]: mixing of the PDMS Elastosil® P7670 component A and B, ratio 1:1; spin coating of the mixed solution at different speeds in order to obtain a homogeneous film; curing of the PDMS at 80 °C during 2 minutes; and electrode deposition by spraying graphite powder over a shadow mask with the desired shape. The steps just mentioned are summarized in Figure 4.6.

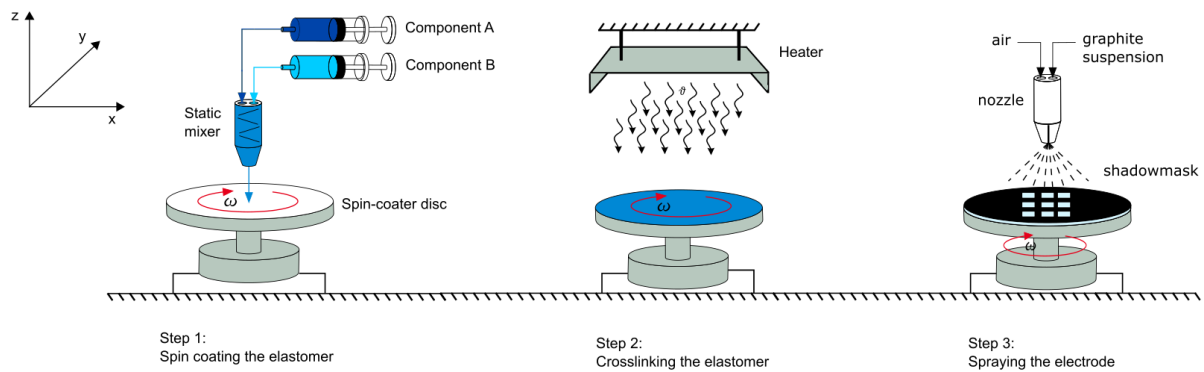


Figure 4.6: Automatic fabrication process of dielectric stacked actuators. The three steps for fabricating EAP in TU-Darmstadt, from left to right: dielectric deposition, elastomer crosslinking/heating step and electrode deposition. On the top left of the figure, a layout with the axis helps understanding the movements of the stages. Adapted and modified from [175].

For the fabrication of the micromixer presented in section 3.2.1, two spray stages with three different masks are used, two for ground and driving voltage electrodes and the third one for the fabrication of the channel. Figure 4.7 shows the three needed masks in grey. Figure 4.7 (a) and (b) show the masks with the pattern of the ground electrodes, represented with blue stroke rectangles, and the driving voltage electrodes, highlighted with red stroke rectangles. Figure 4.7 (c) is the mask used for spraying the channel.

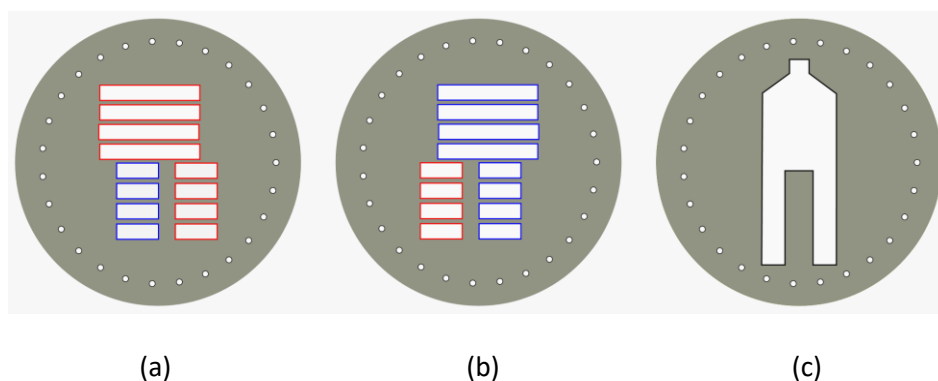


Figure 4.7: Shadow masks needed for the fabrication of a pumping micromixer: (a) and (b) masks for the electrodes and (c) mask for the channel fabrication.

When 15 actuator layers (half of the device) have been produced, the fabrication of the channel starts. The shadow mask in Figure 4.7 (c)), or channel mask, is placed on top of the last elastomer layer, or protection layer. This layer is meant to protect the fluids to be directly in contact with the

electrodes when the micromixer is in operation mode. Afterwards, a nozzle sprays the graphite suspension several times until the required thickness of the channel (40 μm) is obtained. Figure 4.8 shows an image of the actuator right after the fabrication of the channel. Then, on top of it, the fabrication of the next 15 layers of actuators continues, starting with the next silicone protection layer. The entire manufacturing process described above is designed for an elastomeric disc of 40 mm diameter. The fabrication of one full micromixer device takes approximately 3 hours with this automatic procedure.

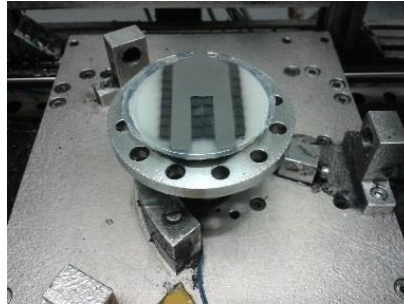


Figure 4.8: Fabrication process after spraying 40 μm graphite suspension on top of the protective elastomer layer of the micromixer to form a microfluidic channel.

Once the micromixer layers have been produced, the channel is rinsed with isopropanol and water to remove the graphite and leave the channel open. This procedure is repeated until no waste of graphite is found at the outlet and until the space between electrodes remains transparent. Other solution options, like water-soluble polymers in isopropanol, have been considered, but these solutions tend to dry out and cause plenty of problems in the nozzle unit and inside the small pipes, normally clogging them up. Afterwards, it is difficult to remove these solid polymers from the system without damaging it.

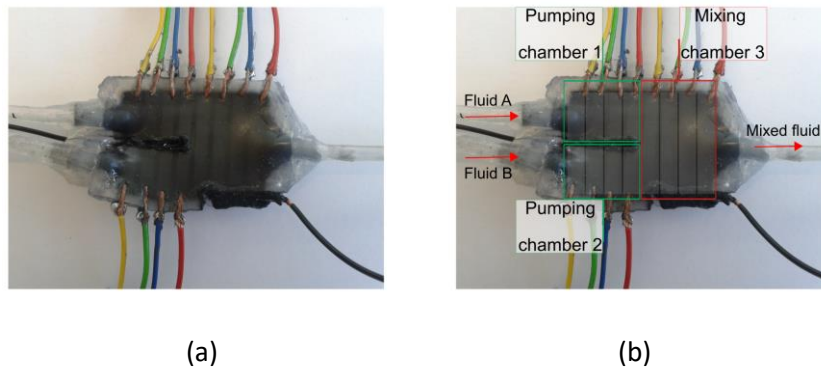


Figure 4.9: (a) A photograph of a finished fabricated micromixer, and (b) the same photo, modified with grey rectangles to clarify where the actuators are. The different chambers are indicated (pumping chambers in green, mixing chamber in red). Both inlets and the outlet with the mixed fluid can be observed.

The micromixer manufactured as mentioned above is 33 mm long and 25 mm wide. Figure 4.9(a) and (b) show a photograph of the manufactured micromixer. The micromixer is based on twelve stacked actuators distributed in: two different pumping chambers, chambers 1 and 2, consisting of four parallel actuators each; and a mixing chamber, chamber 3, made of four parallel actuators. The size of the actuators in the pumping chambers is 3 mm width and 6 mm length, while in the mixing chamber the actuators have 3 mm width and 15 mm length. In section 3.2.1 in

this thesis, Figure 3.8 shows a layout with more details about the layers. In the same section, Table 3.2 provides an overview of all the dimensions.

4.1.4. MICROMIXER CONNECTIONS

For the integration of the micromixer as a working device, it is necessary connecting it to a power supply in order to provide the electric field to the actuators. For this purpose, each layer of one stacked should be connected together and afterwards to a power supply with the controlling system. On the other hand, the micromixer has to be connected to reservoirs and tubing in order to be in contact with fluids.

A. Electric connections

After manufacturing the micromixer device has a circular geometry due to the spin coating process. First of all, the device is cut with a laser cutting machine in order to have a more homogeneous cut for the electrical connections. The cut is intended to be close to the edge of the electrodes in order to easily connect layer by layer via wire connection.

In this device, the connection technique used to electrically connect the driving voltage electrodes is different to that of the ground electrodes. Driving voltage electrode connections are based on graphite powder (MF 2/99,5-99,9E, NGS Naturgraphit GmbH), conductive paste (silver conductive grease, CW7100, Circuit Works®) and a copper wire through a hole which connects to every single driving voltage electrode layer in a stack. Figure 4.10(a) shows how the connection is done for this particular case.

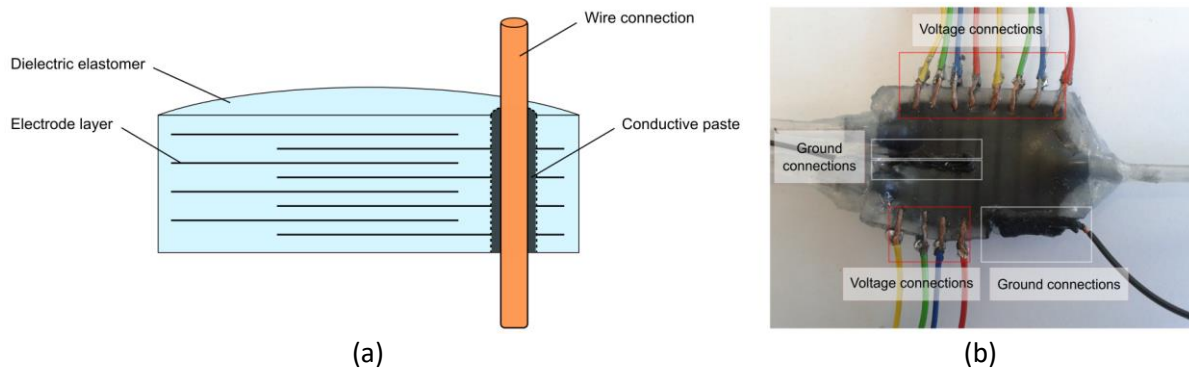


Figure 4.10: (a) A layout of the electrical connection of the voltage electrodes of the micromixer. (b) A photograph of the fabricated microfluidic device with tubes and electrical interconnections. White stroke rectangles show the ground connection driven by a black wire. Red stroke rectangles, the driving voltage connections with coloured wires.

Figure 4.10(b) shows the complete micromixer with electrical interconnections. White stroke rectangles are for ground electrodes connected via a black wire, while red stroke rectangles correspond to the driving voltage connections. Since each voltage connection has to be driven in different phases, each single stacked actuator has an individual connection ending in a single wire.

To decrease the amount of wire connections, ground electrodes are connected by means of conductive PDMS (Elastosil® LR3162, Wacker GmbH) and a copper wire in groups. This means, both pumping chambers ground electrodes are connected together and all ground electrodes in the mixing chamber are also connected together. The ground electrodes are always connected to

ground. Switching on and off a stacked actuator is only obtained by turning on/off the driving voltage.

The number of connected layers achieved by these methods is typically greater than 90 % of the total amount of layers. This can be estimated by the overall capacity determined with impedance measurements for each stacked actuator. When the ratio of connected layers in a stacked is lower than 90 %, connection will be renewed to ensure a maximum of deformation, and thereby displaced volume, in a chamber.

The twelve actuator elements are driven by rectangular signals with a variable phase shift which allow simulating a peristaltic motion through the whole device. The fluid flows through a channel in the middle of the micromixer, firstly in the pumping chamber and afterwards in the mixing chamber.

As described before, the actuator layers are separated from the fluid by two protective layers of Elastosil® PDMS P7670. The nearest electrode to the channel is a ground electrode, to prevent contact of the fluid with the voltage in case of rupture of the protective layer.

Figure 4.11 shows the basic setup for controlling the voltage applied to the actuators. Each stacked actuator is connected to an electrically switchable circuit on a printed circuit board. Phase shift, switching frequency and duty cycle are controlled by an Advantech USB 4750 data acquisition device and a LabVIEW application. A high voltage power supply (Matusada-AMT 5B20) is used to power the actuators.

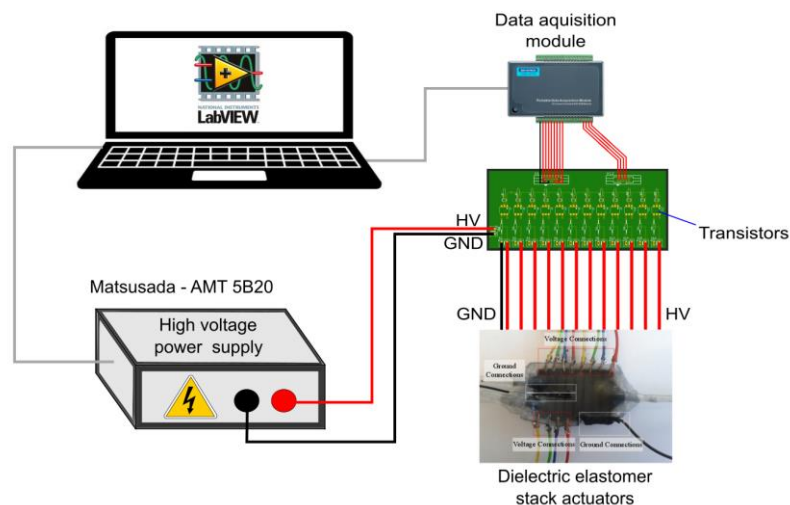


Figure 4.11: Set up for controlling the actuation of the micromixer.

B. Fluidic connections

The last step in the fabrication of the micromixer device is the fluidic connection. For this purpose, firstly, 3-D printing connectors are used to contact the micromixer channel with the tubing. The connectors are made of Polylactic Acid (PLA) and they have a flat opened area which connects to the micromixer and a rounded opened surface for the tubing. The flat aperture is glued to the micromixer channel by using the same PDMS as for the elastomer fabrication (Elastosil® P7670). Thanks to the self-healing properties of the silicone, it is possible to attach the PLA connector to the protective PDMS layers that surround the channel. Three PLA connectors are necessary, two

for the inlets and one for the outlet. The pipes get attached to the connectors by only applying force.

The tubes are connected to the inlets and outlets of the device. The micromixer device is connected to 3 pipes of 3.2 mm diameter. The pipes are at the same time connected to three reservoirs. The reservoirs R.1 and R.2 are at the inlet, while R.3 is at the outlet of the micromixer.

4.2. CHARACTERIZATION

After the fabrication of the pumping micromixer, the characterization of the device is necessary. First, measurements of the elastomer layer thickness are performed to confirm the success in the spin coating process. This step is only needed once for all the devices. Then, the electrical connection of each actuator is checked, or in other words, number of layers connected. This experiment is repeated for each device. Lastly, the deformation of the stacked actuator layers is characterized to have an estimation of the deformation acquired in the channel, or change in volume of the chambers.

4.2.1. CHARACTERIZATION OF THE LAYER THICKNESS

As previously mentioned, the layer thickness of the elastomer is relevant to the actuation of DEA in determining the highest possible electric field E that can be applied without dielectric breakdown.

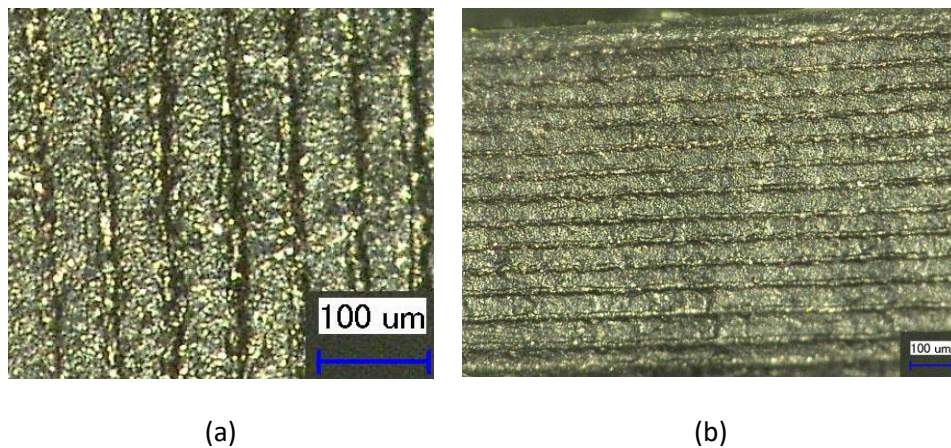


Figure 4.12: Images of the cross section of a pumping micromixer. (a) A magnified image of a couple of layers of elastomer separated by graphite layers. (b) Half of a micromixer under the microscope (Keyence VHX-600).

The layer thickness homogeneity is characterized using a digital microscope Keyence VHX-600. Half of the devices are fabricated with the same procedure exposed in section 4.1.2, and laser cut in the middle of the electrode. Afterwards, the thickness is measured with a digital microscope and the values are evaluated.

Figure 4.12 shows two images of the cross section of half pumping micromixer. Figure 4.12(a) shows in detail the difference between elastomer layers (Elastosil® P7670) and thin electrode layers out of graphite (MF 2/99,5-99,9E, NGS Naturgraphit GmbH), while Figure 4.12(b) shows half of a pumping micromixer.

The thickness of the elastomer layers is measured for two half pumping devices and different actuators (pumping actuators and mixing actuators). The actuators in the middle of the device showed a greater difference in thickness than those nearer to the edges of the device. The thickness of the elastomer layer measured is 50.3 μm and the thickness of the electrode layer is 9.8 μm .

Figure 4.13 shows a cross section of the connection zone of the pumping micromixer. It is possible to observe where the ground electrodes and the driving voltage electrodes end. The electrical connection takes place there by means of copper wires.

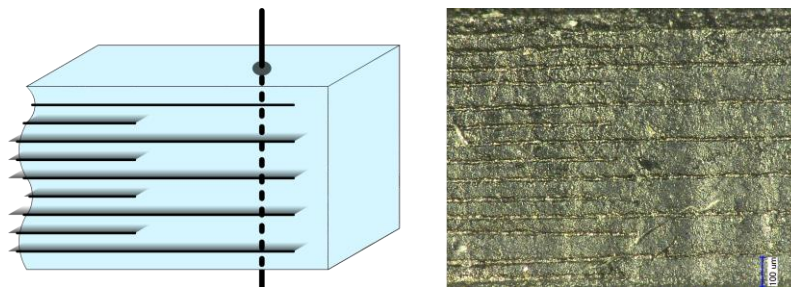


Figure 4.13: Layout of the connection cross section of a pumping micromixer (left) and cross section of the pumping micromixer in the connection zone (right).

4.2.2. CHARACTERIZATION OF THE ELECTRICAL CONNECTION

In a stacked actuator, it is important to know the number of active layers that are actuating each time to predict the deformation of the stack. To know how many layers are connected, impedance measurements are necessary.

The total capacitance in a stacked actuator is N times the capacity of a single capacitor. Considering the rectangular actuators of the mixing chamber (3 mm x 15 mm of 30 layers), the PDMS relative permittivity of 3 and the distance between plates (the thickness of the dielectric layer of 50 μm), the theoretical capacity of the stacked actuators is 0.8606 nF.

Table 4.2 summarizes the values of capacity for the actuators in the pumping chamber and in the mixing chamber, and the minimal value for considering a successful electric connection of the stacked actuator. The criterion for this value is to have at least the 95 % of the total capacity of the stack.

Table 4.2: Summary of the values of capacity for the actuators.

	Area	Theoretical capacity	Min. capacity (>95 %)
Pumping actuator	3 mm x 6 mm	0.2869 nF	0.2726 nF
Mixing actuator	3 mm x 15 mm	0.7173 nF	0.6815 nF

The capacitance measurements needed for the characterization of the micromixer pump are 4 measurements per actuator. As each device comprises 12 stacked actuators, 48 impedance measurements are needed to fully characterize the number of connected layers, considering that the first connection is successful for all stacked actuators.

4.2.3. DEFORMATION OF THE LAYERS

The deformation of a 15-layer actuator (half of a micromixer) is measured using a high accuracy Keyence laser triangulator, LK-G32. In particular, the analysis of the deformation measurements in a complete micromixer produced non-reliable results in our measurement setup, therefore half of a micromixer device is fabricated and used for the measurements.

Figure 4.14 represents a schematic of the general electrical connection of the micromixer and the specific set up for applying voltage. A laser triangulator (LK-G32) points to a single actuator. It sends the information to a computer, which at the same time controls the voltage signal with a LabVIEW program. The high voltage power supply is a Matsusada-AMT 5B20.

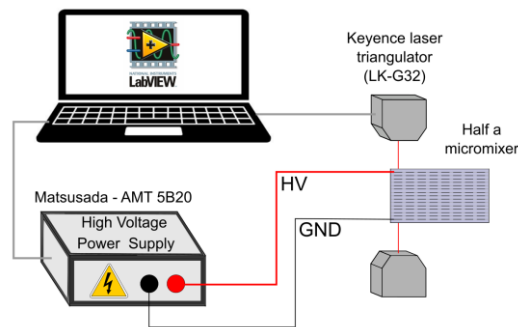


Figure 4.14: Layout of the deformation measurement set up.

The purpose of these experiments is the measurement of the displacement of the actuators, to get an impression of the maximal deformation of the walls of the channel and therefore the maximal amount of chamber volume change achievable with these actuators. The measurements shown here are performed on the pumping chamber actuators, which are critical for the fluid to be pumped in into the micromixer. In order to get reproducible data, three different pumping micromixers are tested. Within these three pumping micromixers, the first pumping actuator in Inlet A is chosen to be measured.

Different input signals and frequencies are applied at varying voltages. Firstly, rectangular signals are supplied from 1000 V to 1500 V in 50 V steps. Each thickness measurement is carried out 30 s after the beginning of the actuation.

Figure 4.15 shows the deformation as a function of voltage for rectangular input signals. Measured data points are shown for different frequencies: 1 Hz, 2 Hz and 10 Hz.

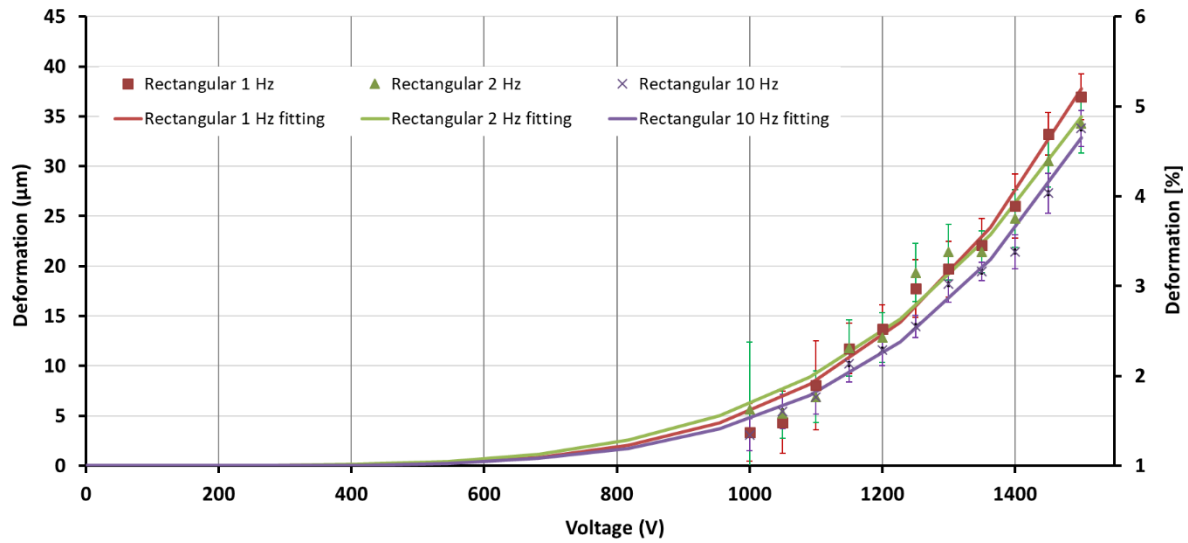


Figure 4.15: Deformation vs voltage for rectangular input signals. The x-axis represents the voltage applied to the stacked actuator, while the y-axis represents the deformation of the stack. The y-axis on the left refers to the displacement of the actuator in height and the y-axis on the right relates to the relative deformation. The error bars correspond to the standard deviation of the observed deformation.

The rectangular signals with 1500 V driving voltage produce deformations of 36.95, 34.25 and 33.8 μm for 1, 2 and 10 Hz, respectively. As it can be observed, the deformation of the pumping chamber stacked actuators is greater at lower frequencies.

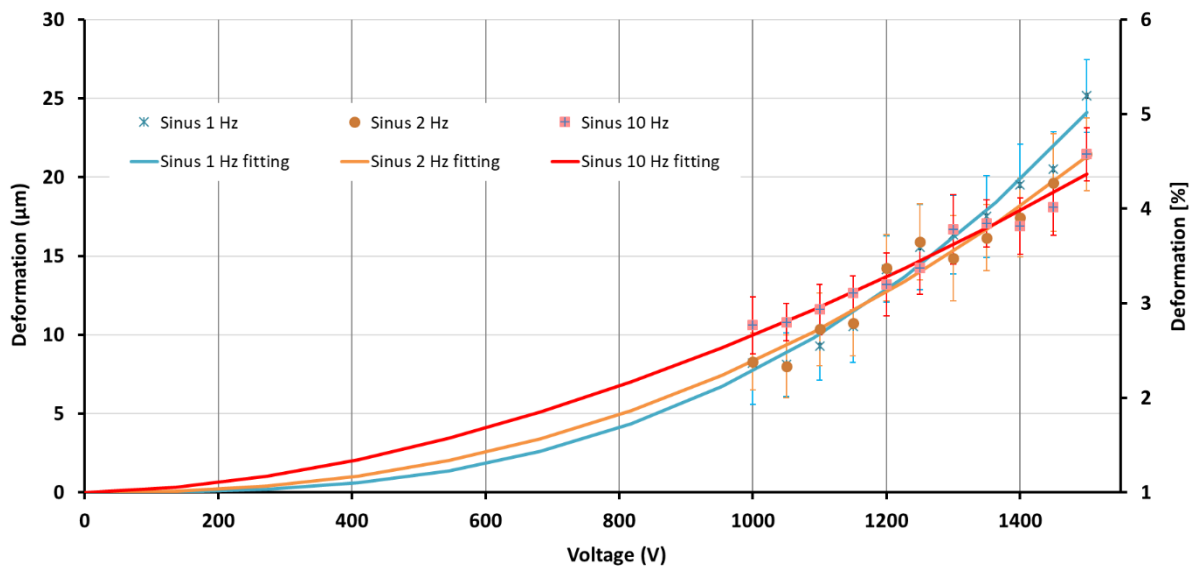


Figure 4.16: Deformation vs voltage for sinusoidal input signals. The x-axis represents the voltage applied to the stacked actuator, while the y-axis represents the deformation of the stack. The y-axis on the left refers to the displacement of the actuator in height and the y-axis on the right relates to the relative deformation. The error bars correspond to the standard deviation of the observed deformation.

The sinusoidal signals represented in Figure 4.16 produce deformations of 25.15, 21.45 and 21.23 μm at 1500 V (peak-to-peak voltage) for 1, 2 and 10 Hz, respectively. As in the previous case, the deformation of the stacked actuators is greater at lower frequencies. In this case, since it is a

sinusoidal signal, the holding time at maximum voltage to fully charge the actuator is lower than in the case of rectangular signals, thus a lower deformation of the actuator is expected.

Figure 4.17 shows all the fitting curves obtained after the analysis of the deformation of the stacked actuators with different input signals. In the graph, rectangular signals and sinusoidal signals are represented with the same colours as for the previous graphs. Here, rectangular signals at peak-to-peak voltages above 1200 V prove to perform better than sinusoidal signals. For the three frequencies under study, 1, 2 and 10 Hz, the rectangular signals have a bigger deformation of the stacked actuators. A difference of at least 1.6 % of deformation for each frequency in the stacks is observed, which means approximately a 32 % less deformation by using a sinusoidal signal than by using a rectangular signal.

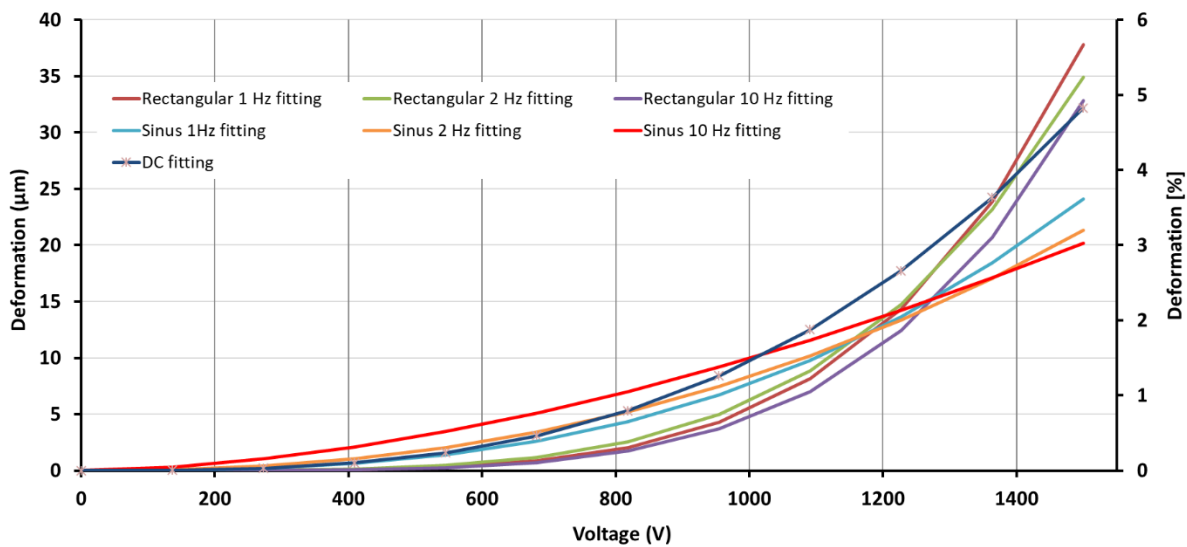


Figure 4.17: Summary of all the applied signals at different frequencies to compare the deformation. For the sake of simplicity, only the fitting lines are shown, with the same colours as previously. The DC fitting line is also shown.

The deformation with DC voltage is also shown in Figure 4.17, corresponding to 30 s of actuation of the stack. The deformation obtained for DC voltage at 1500 V is 40.5 µm, which is the maximum deformation possible. Obviously, an alternating voltage is necessary to move the channel walls and allow the fluid to experience a pressure difference in the chambers.

The rectangular signal is therefore chosen for the actuation of the micromixer, due to its larger deformation. When the actuators are driven with a rectangular signal of 1 Hz at 1500 V (dielectric breakdown of Elastosil® P7670 is 30 V/µm [176]), the channel gap increases from 40 µm (initially open due to the manufacturing process) to 113.9 µm, which represents an increase of approximately 200 %. When no voltage is applied, the actuators return to the passive state, partially closing the channel.

The working principle of the micromixer is based on the opening and closing of the channel walls between the actuators. When the voltage is applied, the actuators expand in area and compress in thickness. By reducing the thickness of the stacked actuators with a certain phase shift and duty cycle, the volume of the channel increases. This produces a pressure gradient that makes the fluid flow along the device.

4.3. EXPERIMENTAL RESULTS OF PUMPING MICROMIXER

In this section, preliminary results of the pumping micromixer are shown. The first characterization of the pumping quality of the device and the mixing efficiency are demonstrated.

4.3.1. FLOW RATE

In order to get the fluid to flow, the pumping micromixer has to switch the actuators on and off coordinately, with a specific phase shift, to achieve the peristaltic movements mentioned in section 3.2.3. The concept is to work in a similar behaviour as in organ's movements. For this reason, the actuators act like valves, which allow the fluid to pass through a specific section and partially close to not allow the fluid flow backwards. Figure 4.18 shows the numbering of the actuators in the micromixer for a better understanding of the actuation phase.

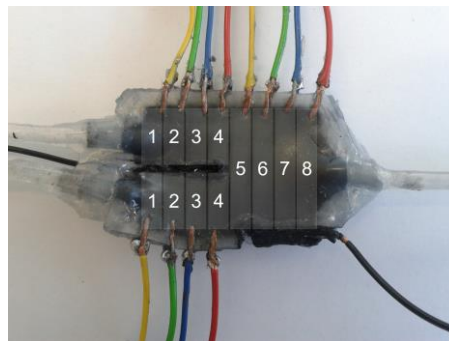


Figure 4.18: Numerical designation of the actuators in the pumping micromixer.

Figure 4.19 shows the eight actuator elements of a single line, A or B, driven by rectangular signals with a variable phase shift, which allows simulating a peristaltic motion through the whole device. The fluid flows through the channel in the middle of the micromixer, first into the pumping chambers and afterwards into the mixing chamber.

In Figure 4.19, the timing of different actuation configurations is described. The y -axis shows stacked actuators, numbered from the inlet in the pumping chamber (stacked actuators 1, 2, 3 and 4) to the outlet in the mixing chamber (stacked actuators 5, 6, 7 and 8). The x -axis represents the actuation time. The period, defined as the inverse of the frequency, and the phase shift ($\Delta\varphi$) are indicated.

The stacked actuators are tested with different configurations. In Figure 4.19(a), the 1:1 configuration is represented: the stacked actuators are activated sequentially with a rectangular phase. When the third stacked actuator turns on, the first stacked actuator turns off. The same behaviour continues in order to obtain a propagation of the fluid along the channel. In Figure 4.19 (b), the 2:2 configuration is represented. In this case, two stacked actuators turn on and off at the same time, so that the volume of the liquid transported is bigger than that in the 1:1 configuration.

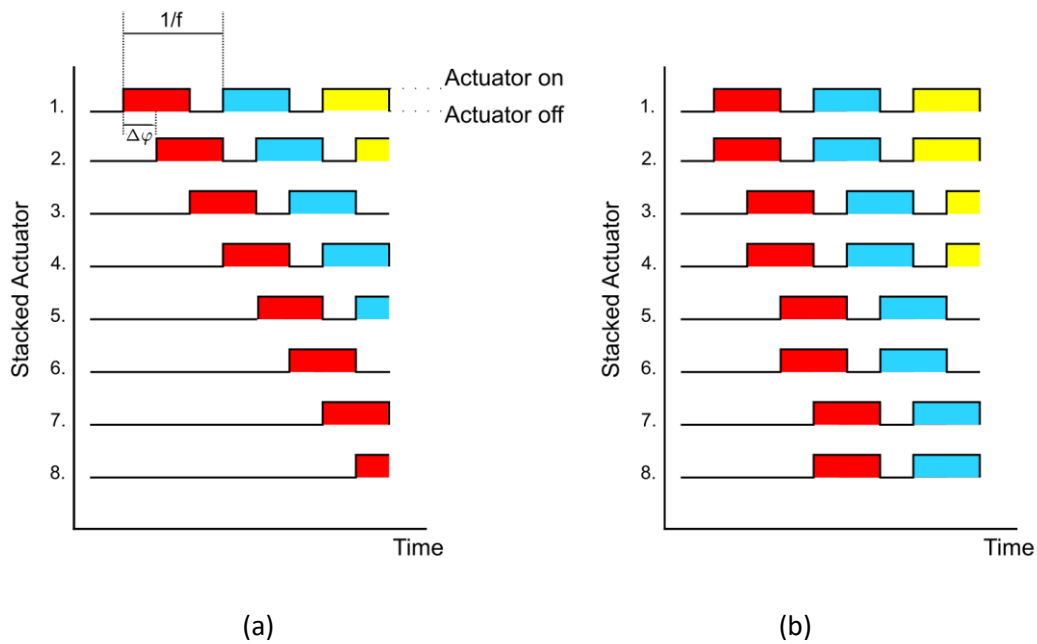


Figure 4.19: (a) Stacked actuators performing a 1:1 configuration or single driving stacked actuators and (b) stacked actuators performing a 2:2 configuration or 2 stacked actuators actuated at a time. Each colour represents a propagating wave.

To initiate the characterization of the fluid flow of the pumping micromixer, electrical and fluidic connections are installed in the system. Here, the electrical connections provide the high voltage input signal to the actuators to perform with specific phase shifts and sequences. Following the configuration 1:1 or 2:2 exposed above. The procedure is based on the method described in section 4.1.4. Moreover, fluidic connectors are added to the system. Firstly, 3-D printed structures of PLA are inserted into the open channels at the inlets and at the outlets. These structures are fluidic connectors that vary from a circular shape to a rectangular shape. The rectangular cross section is inserted in the micromixer channels and glued, while the circular shape is inserted in commercial tubes. The tubes have a 3.2 mm diameter. These are also connected to three reservoirs. The reservoirs R.1 and R.2 are at the inlet, while R.3 is at the outlet of the micromixer. All the tubes have the same length in order to provide the same pressure loss to the system and are connected at the same height of the reservoirs to avoid a difference of fluid pressure and thus, a non-desired fluid flow.

In Figure 4.20, a block diagram with the relation between the different elements in the measurement set up is shown. Two main parts can be distinguished: the electrical and the fluidic connections. More details about the electrical connection elements can be found in section 4.1.4.

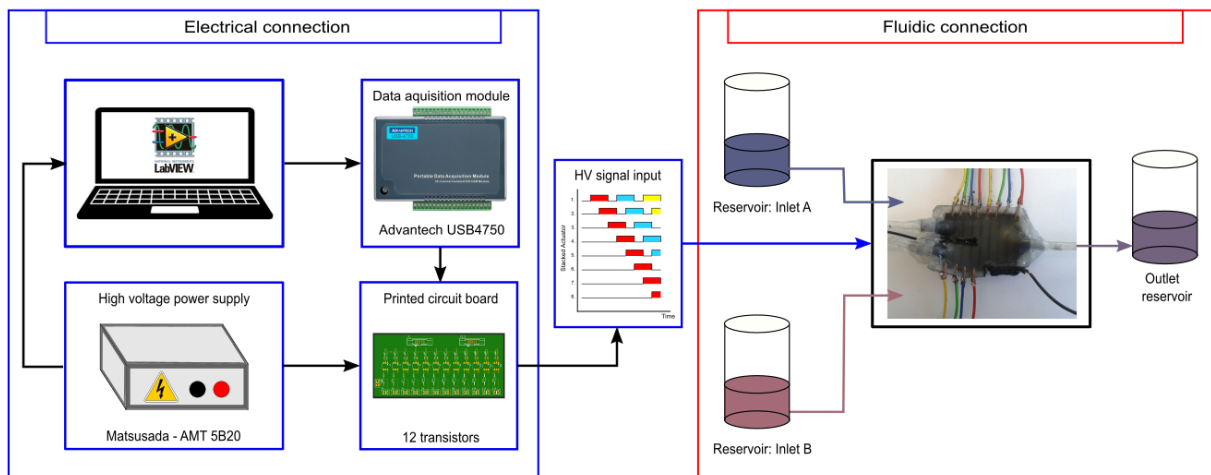


Figure 4.20: Block diagram of the full measurement set up. Both electrical and fluidic connections are represented in the sketch.

First tests concerning the flow rate are made for the pumping micromixer prototype. In order to properly choose the fluids in use, an analysis of PDMS properties is important. PDMS channels are excellent from the manufacturing point of view. The fabrication process tends to be low cost and simple, while the fabricated devices are in general biocompatible and robust, which enables many applications related to biology or medical fields. However, PDMS is highly hydrophobic, thus, flowing water-based solutions within the channels might be troublesome. In the previous devices from chapter 2, surface treatments like oxygen plasma of the channel have been implemented to overcome these challenges. Due to the continuous fabrication process of the stacked actuators, surface treatment methods to modify or increase the hydrophilicity of PDMS like Oxygen plasma, UV-radiation, silanization or chemical vapour deposition are not possible. Instead of using a surface method treatment, a surfactant (20 g/L) in DI water is used as the solution to be pumped to reduce the hydrophobicity of the PDMS channels to DI water.

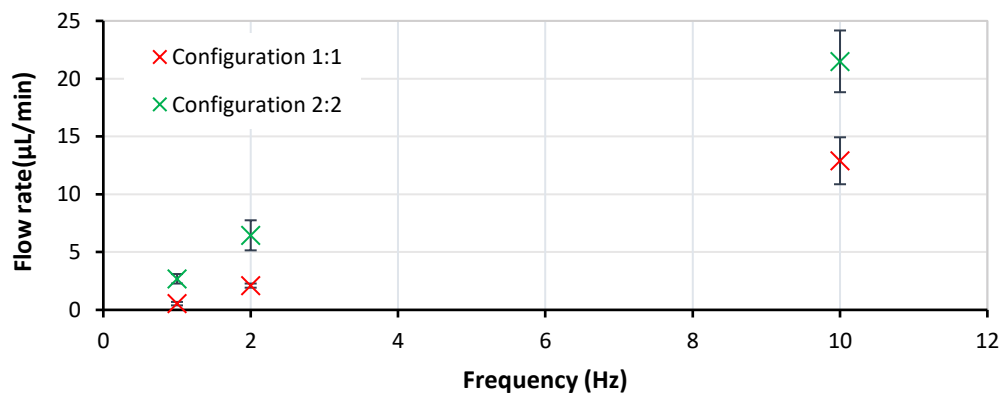


Figure 4.21: Flow rate at the outlet of the micromixer for different frequencies and actuation configurations at 1500 V with a rectangular signal. The error bars correspond to the standard deviation.

In the previous section, the deformation of the actuators at different input signals, sinusoidal and rectangular, was tested. It was proved that for the micromixer at high electric field rectangular signals provided a greater actuator deformation. Thus, rectangular signals with 1500 V driving voltages and a DC-bias half the amplitude, are here used. The stacked actuators are acting with 0.5 duty cycle and 90° phase shift. The two configurations, 1:1 and 2:2, are tested at the same frequencies, to compare the obtained flows. In Figure 4.21, the flow rate versus the frequency for

the 1:1 configuration, in red, and the 2:2 configuration, in green, are plotted. Both configurations show a linear behaviour.

The analysed frequencies are 1, 2 and 10 Hz for each configuration. For each frequency, the 2:2 configuration provides a higher flow rate performance than the 1:1 configuration at the same actuation voltage, 1500 V.

A peristaltic pump needs at least 3 chambers or valves to be able to generate a flow. For a single inlet A or B, the configuration 1:1 works as 8 different valves: 4 stacked pumping actuators and 4 stacked mixing actuators. Whereas the configuration 2:2 performs as 4 valves, 2 double stacked pumping actuators and 2 double stacked mixing actuators.

The flow rate difference at all frequencies between both configurations can be explained due to the difference in net volume transported per cycle. Configuration 2:2 delivers double the volume per actuation cycle as the configuration 1:1. Table 4.3 details the geometrical values of the stacked actuators in the pumping chamber. As it can be observed, the volume difference between on and off states of the actuators (Δ Volume) decreases with increasing frequencies for both configurations. This Δ Volume does not refer to the total volume transported per cycle. As it is a permanently open channel (40 μ m thickness gap), the fluid flows both forwards and backwards when the actuator switches from on to off. This open channel refers to the off state represented in the table as "OFF". The data considered here for the volume differences are taken from the deformation measurements for rectangular input signals at 1500 V and a DC-bias half of the amplitude from section 4.2.3.

The highest flow, obtained at 1500 V, 10 Hz and with the 2:2 configuration, is 21.5 μ L/min at the outlet. Although the deformation of the stacked actuators at 10 Hz is slightly lower (implying a lower displaced volume per actuation), the flow rate is larger due to the higher number of actuations per unit of time. The flow rate is measured after 30 min of actuation, measuring the displacement of the liquid into the outlet tube.

Table 4.3: Geometry and volume difference between on and off states for the pumping actuators at various frequencies.

Actuation	Length (mm)	Width (mm)	Thickness Def. (μ m)	Final Thickness (mm)	Volume On (μ L)	Δ Volume (μ L)
Configuration 1:1						
OFF	3	6	0	0.040	0.720	0
1 Hz	3	6	2 x 36.95	0.114	2.050	1.330
2 Hz	3	6	2 x 34.25	0.109	1.953	1.233
10 Hz	3	6	2 x 33.80	0.108	1.937	1.217
Configuration 2:2						
OFF	6	6	0	0.040	1.440	0
1 Hz	6	6	2 x 36.95	0.114	4.100	2.660
2 Hz	6	6	2 x 34.25	0.109	3.906	2.466
10 Hz	6	6	2 x 33.80	0.108	3.874	2.434

Further measurements at higher frequencies are necessary to know the potential of the pumping micromixer. No more measurements with the pumping micromixer were possible along this thesis due to fabrication problems with the automatic manufacturing setup

Higher flow rates are expected at higher frequencies for the pumping micromixer. In fact, the highest flow rate should be obtained at the resonance frequency of the stacked actuators. At the resonance frequency, the deformation of the actuator gets to a maximum peak. The combination of a very high deformation of the actuator at the resonance frequency and the movements of the walls at the resonance frequency itself leads to a great increase of the displacement volume of each chamber and thus to a much higher fluid flow than the one already obtained experimentally, which makes the pumping micromixer a promising device. In chapter 5, COMSOL Multiphysics® simulations of the pumping micromixer are performed to understand the pumping behaviour of the system and its limits.

4.3.2. MIXING OF FLUIDS

After the evaluation of the pumping behaviour of the device, the characterization of the mixing is necessary. Several methods are available to examine the mixture quality of a sample. Some of these imaging techniques are two-dimensional optical microscopy, two-dimensional fluorescence microscopy and confocal laser scanning microscopy.

Optical microscopy [188] is a technique employed to closely view a sample through the magnification of a lens with visible light. The wavelength spectrum corresponds to that of the human eye, from approximately 400 nm to approximately 750 nm. Optical microscopy is a non-invasive technique.

In fluorescence microscopy [189], the image observed is the result of electromagnetic radiation emitted by the molecules that have absorbed the primary excitation and re-emitted light with a longer wavelength. To let only the desired secondary emission pass, appropriate filters must be placed under the capacitor and above the lens. Fluorescence is a phenomenon of short-time luminescence that certain molecules called fluorochromes and fluorophores have.

Confocal laser scanning microscopy [190] is a method available for obtaining the optical equivalent of thin fluorescent sections. The optical principle of confocal microscopy is simple: it optically takes two-dimensional sections of an object to form a three-dimensional image of the object. In confocal microscopy, both condenser lens and objective lens must have the same point of focus.

Apart from the optical system and light source, the acquisition and processing of the images are important. They can be performed with image sensors like charge-coupled devices (CCDs), complementary metal oxide semiconductor (CMOS) image sensors or digital images. In this work, the digital imaging is used to analyse the mixing quality. Images are captured while the micromixer is mixing. The images are analysed afterwards.

The mixing is evaluated using two additives of different colours at the inlet and by observing the colour of the mixture at the outlet. Two water soluble colorants, red and blue, are separately solved in 100 mL DI water with 2 g surfactant. The colorants at the inlets A and B are light blue and red, respectively. After applying a rectangular signal at 1500 V, 10 Hz and 2:2 configuration, the outlet shows a change in the colorant.

Figure 4.22 shows how the colorants at the outlet have completely changed the colour to dark-purple. Moreover, it can also be observed that the mixture of the colours is rather homogeneous at the outlet.

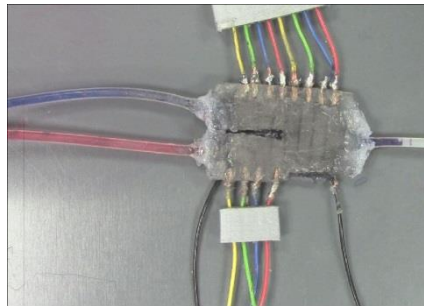


Figure 4.22: Micromixer used with different colorants, blue and red, for the inlets. The observed output is dark-purple.

Direct statistical methods are used to analyse the data obtained. A code in MATLAB is used to determine the value of the pixels. The three-dimensional coordinates RGB (red, green, blue) model is used to determine the mixing quality.

With the RGB triplet, it is possible to know the colour similarity between several colours, based on the distance between the colours in the cube shown in Figure 4.23. The shorter the distance between two points, the higher the similarity between colours.

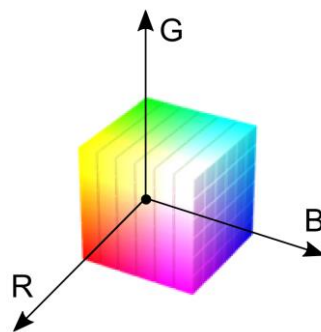


Figure 4.23: The RGB colour model mapped to a cube. The origin, black, is the hidden vertex [191].

Knowing the distance between different colours is difficult to describe without a quantification method. The Euclidean distance is often used to measure the distance between colours. The RGB colour ranges from 0 to 255. The higher the number, the closer to the pure colour. For example:

- (255, 0, 0) corresponds to pure red colour
- (0, 255, 0) refers to pure green colour
- (0, 0, 255) corresponds to pure blue colour

The MATLAB script code for the characterization of the mixing is based on: the “upload image” function; the RGB function for analysing the colour of a photo in RGB format for each pixel; a function for saving the RGB coordinates of the selected points in each tube; and the basic equations for calculating the median and the standard deviation.

The colour analysis in MATABL follows three steps:

- a) Upload image function
- b) Read each pixel in RGB format: `"imread ('photo.png')"`
- c) Manually select points in a photo and recording their RGB values: `"impixel"`

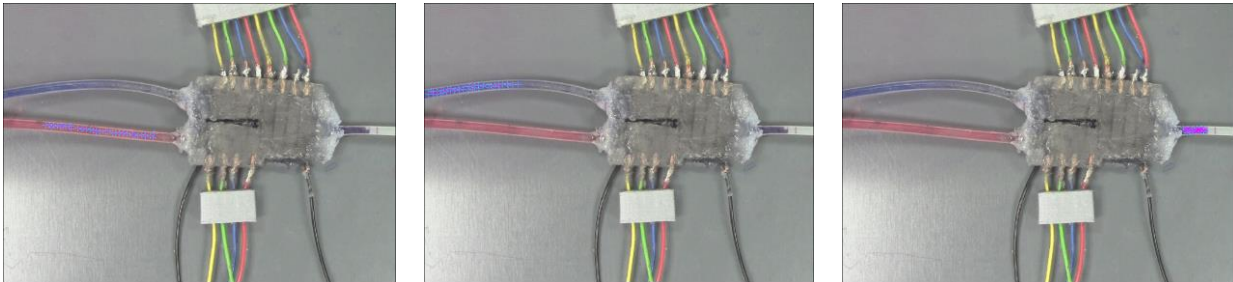


Figure 4.24: Micromixer picture of the mixing: 40 pixels, indicated with blue crosses, were analysed per tube.

By using this script, 40 pixels in the photo are selected for each colour, i.e., 40 points for red inlet, 40 points for blue inlet and 40 points for the outlet. Figure 4.24 shows the image used for analysing the mixing. The three images are the same, but with different indications.

Figure 4.25 shows a histogram with the data obtained directly from the MATLAB script. The values are expressed as the mean value of the 40 points, while the variance is shown as bars. As it is shown, for the case of the red inlet the maximum value corresponds to the R value, and for the blue inlet to the B value. The outlet corresponds approximately to the average value of both inlets.

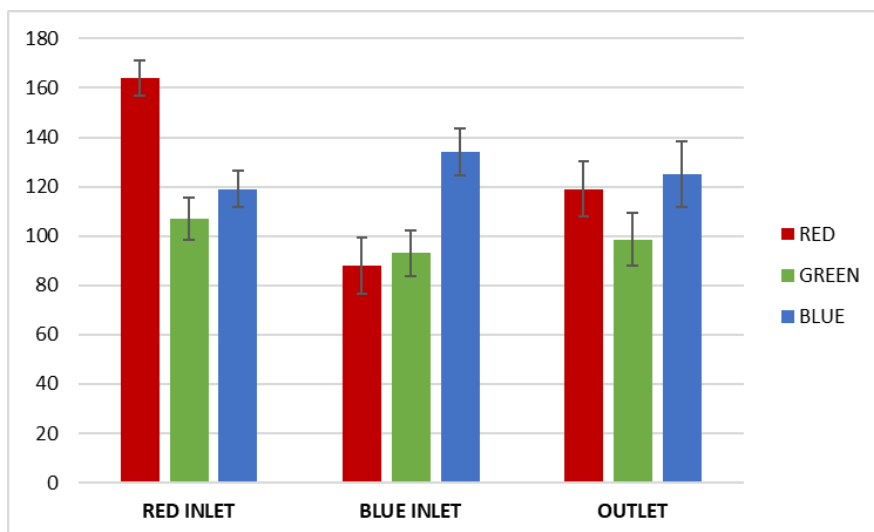


Figure 4.25: The histogram represents the direct value obtained from the pixel selection in MATLAB. The bars represent the variance of the values.

Figure 4.26 represents the theoretical RGB values for the mixture of both red inlet and blue inlet considering the mean value of the 40 pixels previously evaluated. The x -axis represents the concentration of blue colorant in the mixture from 0 to 100 %: 0 % corresponds to the red colorant at the inlet, while 100 % corresponds to the blue colorant at the inlet. The pixel RGB value at the inlets was measured using an analysis tool in MATLAB. Considering the Euclidean distances between the RGB values of the red and blue colorants at the inlets, the values for intermediate concentrations are calculated and expressed in Figure 4.26.

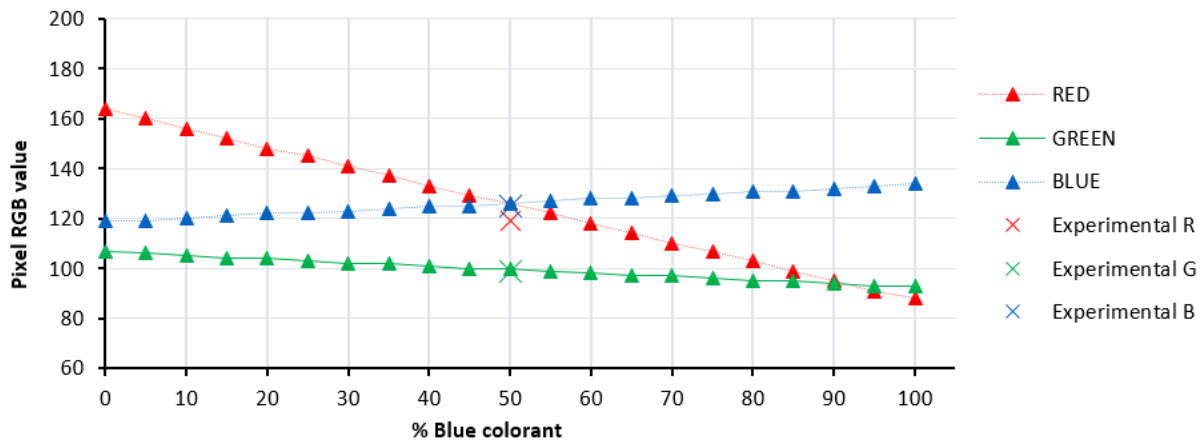


Figure 4.26: The plot represents the theoretical values obtained from the mixture of the blue and red colorants. Crosses represent the values in the RGB scale at the outlet obtained by a pixel analysis in MATLAB.

The theoretical values for 50 % concentration of blue colorant (and consequently 50 % of red colorant) are 126, 100, 126 (R, G, B). These values are marked with triangles at 50 % concentration in Figure 4.26. However, the results obtained with the analysis of 40 pixels at the outlet with MATLAB point to an experimental value for the mixture of 119, 98.5, 125 (R, G, B). These experimental values are represented in Figure 4.26 with three crosses, each one for a R, G, B value.

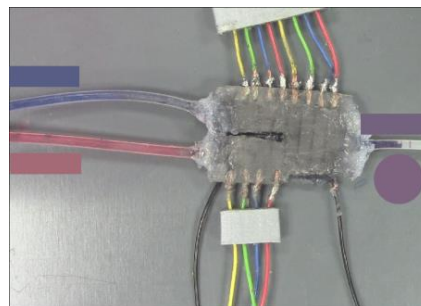


Figure 4.27: Modified photo of the micromixer. In rectangles, the colours of the mean value of the tubes obtained after the analysis of 40 pixels in each one with MATLAB. The purple circle represents the theoretical value obtained from the 50 % blue inlet (from the mean value) and 50 % red inlet (from the mean value).

Figure 4.27 shows rectangles coloured with the mean values obtained with the MATLAB analysis of the pixels. The colours of the rectangles slightly differ from the colours of the tubes from which they were taken due to the high variance in the 40 pixels taken. The circle at the outlet shows the theoretical value obtained from the mean value of the inlet's colours. By eye, only a small difference can be seen between the experimental (rectangle) and the theoretical (circle) purple colours.

Like for vectors, it is possible to measure the distance between two colours in order to know the similarities between them. The distance between colours in the RGB system can be expressed as:

$$\text{distance} = \sqrt{(R_2 - R_1)^2 + (G_2 - G_1)^2 + (B_2 - B_1)^2} \quad \text{Eq 4.2}$$

Where the subscript 1 refers to the purple colour of the theoretically obtained value and subscript 2 corresponds to the experimental one. R, G and B are the numbers from 0 to 255 of the RGB system for each colour.

The distance obtained between both purple colours is 7.14. This value is smaller than the variance of the purple colour obtained with MATLAB. The variance of the values R, G, B is (11.11, 10.76, 13.26). Thus, it is proved that the 50 % mixture of blue and red colorants is successfully achieved by the micromixer.

This micromixer has shown the capability to homogeneously mix solutions. Further investigations involving this device might include the mixing of well-known solutions to test the efficiency of the reactions and conversions. In this way, the optimal residence time can be experimentally obtained to maximize the conversion of the reactants. Mixing different ratios of solutions by only changing the frequency of actuation of the actuators in pumping chamber 1 with respect to the pumping chamber 2 and synchronising the frequency of both chambers with the mixing chamber might be the following step in the research of this device.

In this chapter, active pumping micromixers have been fabricated and characterized. Pumping micromixers have been fabricated using the layer-by-layer deposition method. An automatic procedure for the fabrication of stacked actuators based on the repetition of three steps (spin coating of the elastomer layer, crosslinking of the elastomer layer and spraying of an electrode solution through a mask), has been used. The method lasts 3 hours until the production of a full pumping micromixer. Hence, the procedure has proved the ability to manufacture complex structures as the pumping micromixer.

Several properties have been characterized: dielectric and electrode layer thicknesses; electrical connections; actuator deformation at various input signals and frequencies; flow rates at various frequencies and configurations; and the mixing quality.

Firstly, the thickness of the dielectric and the compliant electrodes were measured. The values obtained are 50.3 μm thick for the elastomer layer and 9.8 μm for the electrode layer.

Then, the electrical connections have been tested for the stacked actuators. As a criterion, 95 % of the dielectric layers must be electrically connected. Impedance measurements of each stacked actuator are performed to verify the quality of the electrical connections. For stacked actuators with a capacitance less than the 95 %, the electrical connections are re-established until more than 95 % of the layers are electrically connected. For the pumping actuators (6 mm x 3 mm, width x length), minimum capacity corresponds to 0.2726 nF, while for the mixing actuators (15 mm x 3 mm, width x length) 0.6815 nF.

Once the electrode layers are electrically connected, the deformation of the layers is studied. As far as pumping is concerned, stacked actuators in the pumping chambers are the bottleneck for the fluid flow due to their smaller size compared to the stacked actuators in the mixing chamber. For this reason, it is important to quantify their deformation, as it limits the fluid flow in the micromixer. Two input signals have been used: rectangular and sinusoidal. Table 4.4 summarizes the main results obtained for the deformation of half of stacked actuators layers for the stacked actuators in the pumping chambers. In the table, 1 Hz, 2 Hz and 10 Hz are represented for 1500 V with a DC-bias of half the amplitude (750 V). The maximal values obtained are 25.15 μm for the sinusoidal input signal at 1 Hz and 36.95 μm for the rectangular input signal.

Table 4.4: Pumping micromixer main results obtained.

1. Sinusoidal signal (DC-bias): 1500 V (750V)			
	1 Hz	2 Hz	10 Hz
Actuator Deformation #	25.2 ± 2.3 μm	21.4 ± 2.3 μm	21.3 ± 1.7 μm
2. Rectangular signal (DC-bias): 1500 V (750V)			
	1 Hz	2 Hz	10 Hz
Actuator Deformation #	36.9 ± 2.3 μm	34.3 ± 2.9 μm	33.8 ± 1.8 μm
Flow rate (Config 1:1)	0.54 ± 0.15 μL/min	2.14 ± 0.18 μL/min	12.90 ± 2.03 μL/min
Flow rate (Config 2:2)	2.69 ± 0.41 μL/min	6.45 ± 1.3 μL/min	21.51 ± 2.67 μL/min

Deformation of half of the stacked actuator layers (15 layers) for the pumping chamber actuators.

For driving voltages above 1200 V, rectangular input signals prove a better deformation of the stacked actuators. For this reason, the rectangular input signal is chosen for all the following operations with the micromixer. As mentioned above, when using electroactive polymers, the highest possible electric field is used without reaching dielectric breakdown. This is done to achieve maximum deformation. Therefore, since rectangular signals show a higher strain than sinusoidal signals at 1200 V and above, they are used for both fluid flow and mixing measurements.

The next step in the characterization of the micromixer is its operation as a peristaltic micropump. For this purpose, complete micromixers are manufactured and electrically connected. Due to the hydrophobic character of silicone, the material of which the micromixer is made, a solution of distilled water with surfactants (20 g/L) is used.

A rectangular input signal at the maximum electric field before breakdown is applied (1500 V) with a DC-bias of half the amplitude. The flow rate for this signal at different frequencies, 1 Hz, 2 Hz and 10 Hz, is tested. Two different configurations of the actuation order are used: the so-called configuration 1:1, in which each stacked actuator is individually on and off after the define phase shift; and the configuration 2:2, in which two consecutive stacked actuators are on and off at the same time.

As expected, configuration 2:2 provides a higher fluid flow at all tested frequencies. The volume difference between on and off states of the actuators for configuration 2:2 doubles that of configuration 1:1. For one propagating wave, the fluid volume displaced increases in configuration 2:2. Thus, the flow rate increases for configuration 2:2 at least 1.6 times with respect to configuration 1:1 for the tested frequencies. Table 4.4 summarizes the main results obtained for the characterization of the pumping micromixer in terms of deformation and flow rate at various signal inputs and frequencies.

Finally, the mixing of the pumping micromixer has been evaluated using direct statistical methods. MATLAB is used to determine the coordinates in the RGB model of the pixels at the inlets A and B and at the outlet. The comparison between the theoretical values obtained at the outlet and the experimental values proved a 50 % mixing of the fluids at the outlet.

These results of the pumping micromixer confirm the goal of this thesis. First, it is possible to manufacture a pumping micromixer with the layer-by-layer deposition method and second, the DESA technology allows the fabrication of complex microfluidic devices. Although the fabricated

devices meet expectations for a preliminary prototype, the relatively large size of the devices with respect to their low fluid flow encourages the search for pathways to improve the performance of these devices.

Improvements to the current design of the pumping micromixer are proposed in the next section. To this end, two routes are chosen: on the one hand, improvements on the fluid flow and pumping pressure of the system, for example, by encapsulating the micromixer; and on the other hand, improvements on the mixing efficiency by increasing the contact between fluid layers (T-type pumping micromixer). Moreover, limitations and future perspective of the research are exposed.

4.4. IMPROVED PUMPING DESIGNS AND OUTLOOK

In this section, further experiments and prototypes on the pumping micromixer fabricated in the previous sections, are proposed. This research focuses on the improvement of the fluid flow and back pressure of the previous devices, as well as on the mixing by changing the geometry of the pumping micromixer. These can be performed upon success in the fabrication of the Y-type pumping micromixer. At the end of the section, the limitations and perspectives for this device are also included.

4.4.1. ENCAPSULATED MICROMIXER

The previous fabricated Y-type pumping micromixer is modified here to increase the fluid flow and the pressure at the outlet. To do so, the same prototype has been used. The improvement consists in the encapsulation of the device. This means that a rigid layer is added to the top and bottom layers of the micromixer. It ensures that the fluid channel remains closed when there is no actuation.

The concept is based on the restriction of the free deformation of the actuators, allowing the actuator to move more in the z -direction to open and close the walls surrounding the channel. With this restriction, it is also possible to fully close the channels when the actuators are inactive, in order to increase the pressure and the fluid flow. The inner channel will exhibit no height when not actuated, in contrast to the $40\ \mu\text{m}$ height from the previous micromixer. Figure 4.28(a) shows a layout of the previous prototype ($40\ \mu\text{m}$ initial channel thickness) and Figure 4.28(b) presents the working concept of the encapsulating micromixer. More details about the elements in Figure 4.28 can be found in chapter 3 in Figure 3.8.

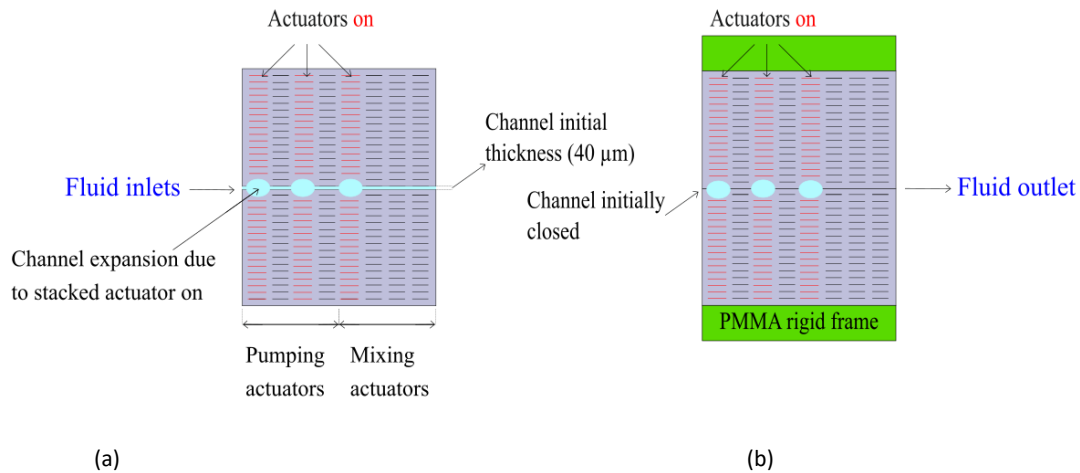


Figure 4.28: (a) Profile view of the Y-type pumping micromixer previously fabricated with an initial channel thickness of 40 μm . (b) Y-type pumping micromixer encapsulated by two rigid PMMA layers on top and bottom of the device.

As mentioned above, due to the layer-by-layer deposition manufacturing process of the micromixers, it is not possible to obtain an initially closed channel. The encapsulation of the micromixer proposed here is done to overcome this issue. By encapsulating the micromixer, an increase of the fluid flow and pressure at the outlet are expected. At each propagating wave, the inactive actuators are closed, not allowing the fluid to move backwards, i.e., inactive actuators serve as closed valves. The fluid contained in the chambers is always displaced towards the outlet.

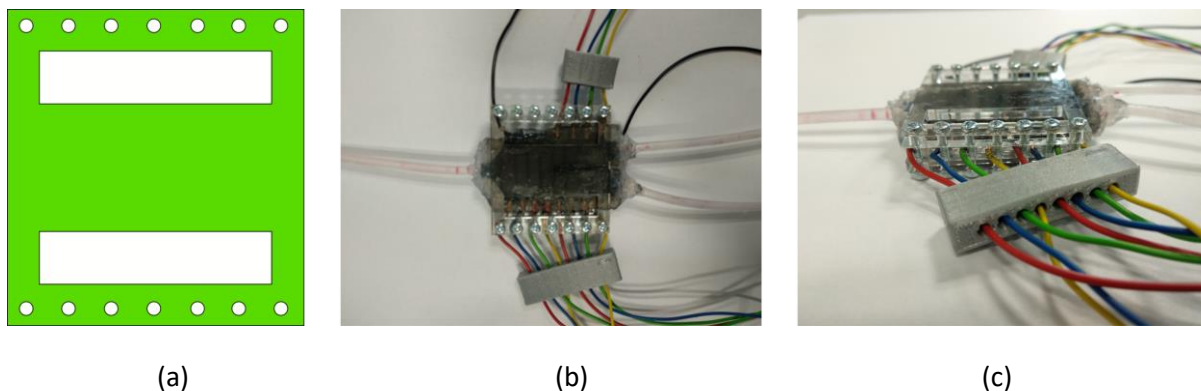


Figure 4.29: (a) A schematic of the rigid PMMA frame fabricated to avoid free deformation of the actuators. (b) A pumping micromixer with the rigid part on top and on bottom. (c) A profile photo of the encapsulated micromixer.

Figure 4.29(a) shows a schematic of the rigid part fabricated. It consists of a 3 mm thick PMMA surface in which holes have been laser cut to add screws. Seven holes have been cut to separate each high voltage wire. The holes have a diameter of 2 mm and two rectangles, 7.5 x 33 mm, as windows to favour the heat dissipation of the electrical connections, here directly in contact with air.

Figure 4.29(b) and (c) show the final device set up with the transparent PMMA attached to the top and bottom layers. The material used for attaching the PMMA to the elastomer layer is a double-sided Tape 3M[®] 96042. Several pumping micromixers were tested with this rigid part;

however, they have been broken after a short time of operation. During this research, it was firstly tested with no acceptable results.

The hypothesis for this break is thermal breakdown due to the loss of heat dissipation or overheating of the actuators. Fume and bubbles were created in the actuators while voltage was applied.

Christensen et al. [192] performed COMSOL simulations of the thermal breakdown of DESA varying the number of actuator layers and the diameter of the stack. They determined that if the diameter of the stacked is large, it is suitable to assume thermal insulation of the cylindrical surface of the stack. Furthermore, they found out that increasing the applied electric field or the temperature of the surroundings greatly decreases the number of possible fabricated layers in a stacked DEA.

4.4.2. T-TYPE PUMPING MICROMIXER

Based on the pumping micromixer already tested and proved, it is possible to develop new devices. Here, a prototype to increase the mixing efficiency of the pumping micromixer is manufactured. To this end, a pumping micromixer with a design similar to a passive T-type micromixer is proposed.

As already stated in section 3.1.1, for the same size and geometry, T-type micromixers offer a higher mixing efficiency than the Y-type micromixer. This is caused by the contact of the fluid layers at the junction of the inlets. In the T-type, the flows from the A and B inlets get in contact from opposing directions, leading to an increase of the turbulences. Whereas in the Y-type, both streams flow in the same direction when they meet.

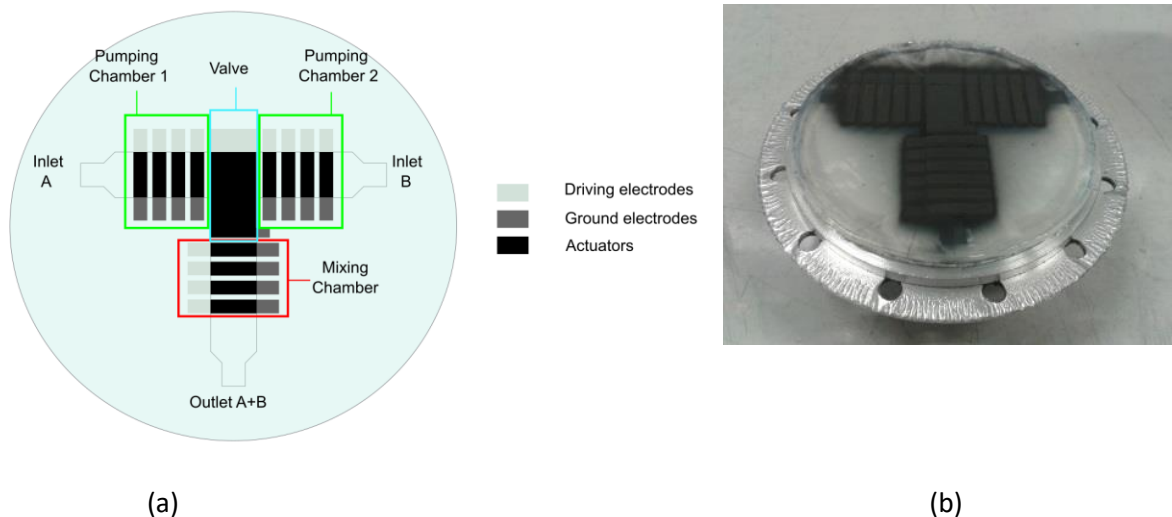


Figure 4.30: (a) Sketch of a proposed active pumping micromixer with a T-type shape. The active mixer is based on the dielectric elastomer stacked actuators. (b) Photo of a fabricated T-type pumping micromixer device.

Due to its geometry, the fabrication of a T-type micromixer results much more complex than that of the Y-type. Thus, only the Y-type was fabricated. In T-type micromixers the two inlet channels

are straight and the mixing junction has a T-form. In order to keep the 3 mm length for the actuators, it is necessary to use a bigger disc size in this new configuration.

The sketch in Figure 4.30(a) shows the different chambers and actuators designed for this prototype. As for the Y-type micromixer, three chambers are necessary. Two pumping chambers (namely 1 and 2), one for each inlet (A and B), and a mixing chamber plus a single valve. Each chamber has four actuators of 3 mm x 10 mm size. The electrodes are located so that the electrical connections can be simplified for the ground electrodes. As for the Y-type pumping micromixer, the electrical connections for this device are designed differently for driving electrodes and ground electrodes. Driving electrodes are connected with a single wire per stacked actuator, whereas ground electrodes are all connected together for the same chamber.

In the layout, both ground electrodes (in dark grey) and driving electrodes (in light grey) are represented. The area in which ground electrodes and driving electrodes are superimposed is coloured in black, representing the actuation area. The T-channel is also drawn in the layout with a black area. Inlets A and B can be observed, as well as the corresponding outlet A+B.

The photo in Figure 4.30(b) demonstrates that this device can be fabricated with the same procedure as the one for the Y-type micromixer. The device in the photo has also PDMS protective layers and a channel in between the two half 15 actuator layers. The total number of layers for the actuators are also 30 layers, each 50 µm thick. The materials employed for the manufacturing are the same as the ones for the Y-type pumping micromixer. Unlike the Y-type micromixer, the rotatory disc used in this case corresponds to a 75 mm diameter disc. Due to the geometry requirements of the T-channel, a larger surface is necessary and therefore, more PDMS material is needed for the fabrication of this device. The rest of parameters like rotational speed, crosslinking temperature and time, spraying time, etc, are the same as for the Y-type micromixer, leading to a fabrication time of approximately 3 hours for this device.

Table 4.5: Geometric dimensions for the proposed T-type pumping micromixer.

Nº of actuators:		15+15
Pumping Chamber		
Actuators length		3 mm
Actuators width		10 mm
Mixing Chamber		
Actuators length		3 mm
Actuators width		10 mm
Valve		
Actuator length		10 mm
Actuator width		18 mm

Table 4.5 summarizes the most important values of the actuators in the T-type pumping micromixer. The dimensions of the micromixer can be further reduced in order to obtain a smaller device.

Here, it is proved that such a complex device with a high number of stacked actuators and chambers can be fabricated with the layer-by-layer deposition method. Further investigations in

terms of flow rate, mixing quality and deformation need to be studied to obtain more information about the functionality of this device and its potential use.

4.4.3. ARRAY OF MICROFLUIDIC MIXERS

The Y-micromixer prototype fabricated in this work is considered the first step for further fabrication of diverse microfluidic devices. Within this thesis, it has already been proved that EAP technology is an appropriate technology for this purpose. Pumping and mixing fluids have been already tested.

The technology showed in section 4.1.2 for the fabrication of stacked actuators has also proved the capability of fabricating actuators of 1 mm² area. Figure 4.31(a) shows a layout of the already fabricated system as a tactile display by Matysek [193] and in Figure 4.31(b), a photo of the device with more details can be observed. This decrease in size geometry of the fabrication procedure leads to the possibility of increasing the number of inlets and outlets from micromixer devices, giving the possibility to mix plenty of fluids in arbitrary ways, thus forming arrays for mixing fluids.

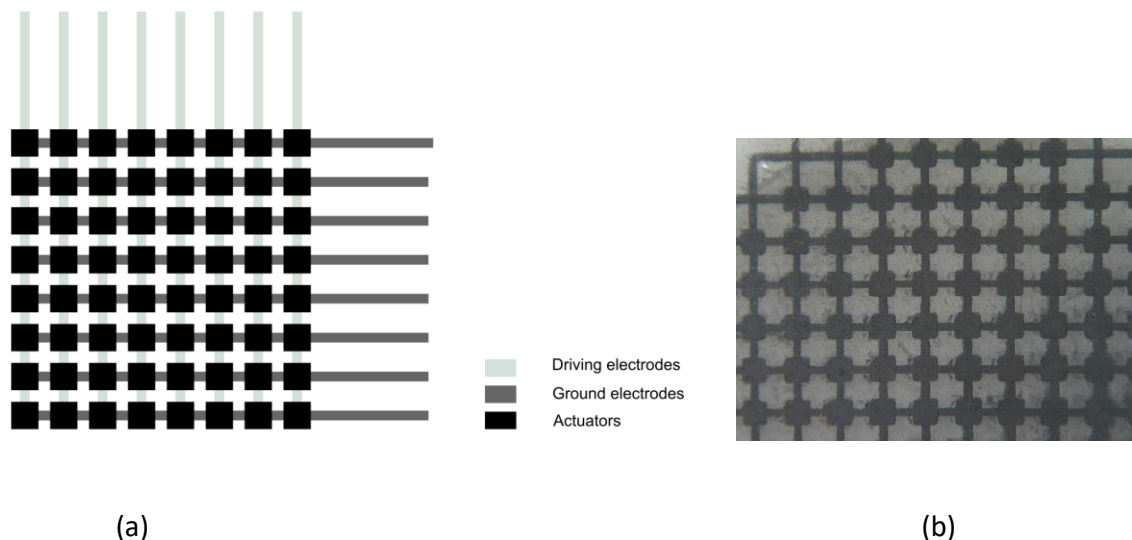


Figure 4.31: (a) Sketch of the already fabricated system as a tactile display by Matysek and (b) a photo of the device where more details can be observed [193]. For a better understanding of the sketch, ground electrodes, in dark grey, and driving electrodes, in light grey, have been differently coloured. The surfaces, where ground electrodes and driving electrodes converge, are coloured in black and correspond to the actuator area.

New fabrication techniques like 3D-printing allows the fabrication of the present actuators in a small scale. Systems like the ones shown in Figure 4.32 will be reality in the closer future. Furthermore, due to the advance in the manufacturing of thin layer elastomers and electrodes, the high voltage needed will no longer be a disadvantage for the use of this technology together with biological samples and for human interaction. As mentioned in section 1.6, driving DEAs at 100 V will be possible. Figure 4.32 shows the diverse possibilities offered by an array of four inlets and one or two outlets.

More ambitious scenarios can be thought by combining more inlets and outlets in different directions within the same device.

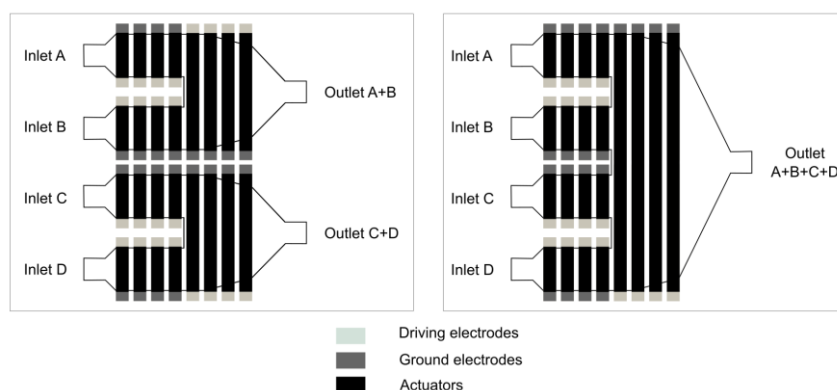


Figure 4.32: Diverse possibilities offered by an array of four inlets and one or two outlets. Ground electrodes (in dark grey) and driving electrodes (in light grey) have been differently coloured. The areas, where ground electrodes and driving electrodes converge, are coloured in black and correspond to the actuator area.

4.5. APPLICATIONS

The application of the pumping micromixer corresponds to a great range of possibilities, from the chemical industry to the analysis of chemical and biological samples. In the chemical industry, this device can be used not only as a micromixer but also as a microreactor. Micromixers play a significant role in both homogeneous [194][195][196] and heterogeneous [197][198] reaction.

Micromixers are also useful in the case of costly substances where no waste is economically desirable, for example expensive catalysers [199]. It is possible to test the reaction in a small scale and save material or investigate plenty of operating conditions like temperature, concentration of reactants, etc, thus, to determine the most efficient parameters and then extrapolate these conditions to a macrodevice. Microreactors are also used in the explosives field, where testing small amounts of explosives reduces the danger of the testing operations.

Micromixers are often used in the analysis of chemical, biological and medical samples. For example, it is used for the detection of ammonia in aqueous solutions [200]. They also play an important role in combinatorics chemistry, the synthesis of proteins for drug discovery [201], in enzyme assays [202][203] and for biochemical sensors [204][205].

4.5.1. LIMITATIONS OF THE MICROMIXER

It is also necessary to point out, not only in which fields pumping micromixers can be used, but also their limitations. The constraints mentioned here are based on two concepts: materials interaction and pumping limit.

The pumping micromixer will not be able to neither pump nor mix substances that dissolve the materials in which the pumping micromixer is based on. This means any solvent that dissolves PDMS, or more specifically, Elastosil® P7670, cannot be used. Mata et al. [77] studied the properties of PDMS for biomedical micro/nanosystems and studied the possible reactants for dissolving PDMS. Some of the solvents are summarized by Lee et al. [206]. Lee et al. did experiments to demonstrate the compatibility of PDMS with organic solvents. They considered the swelling of PDMS in a solvent, the partitioning of solutes between a solvent and PDMS and the

dissolution of PDMS oligomers in a solvent. They found that the solvents that swell PDMS the most are diisopropylamine, trimethylamine, pentane and xylenes.

The operating temperature range in which PDMS does not change properties is an important parameter. In this sense, PDMS is a very suitable material, because it can withstand hundreds of degrees before starting decomposing. On the other hand, with increasing the temperature, as expressed in section 1.3, a thermal degradation of the actuators and a thermal breakdown are possible. High voltages with high temperatures favour the breakdown of the actuators.

Reactions that need to be visually monitored, like those using fluorescent substances, cannot be used with this pumping micromixer due to the materials opacity of the graphite electrodes. Other transparent electrodes are possible, like those used in the fabrication of lenses of dielectric elastomer actuators (for example hydrogels) containing electrolyte that can work as ionic conductors to actuate DEAs [207].

At the moment, the pumping limit is 21.5 $\mu\text{L}/\text{min}$ with the possibility to be increased by simply increasing the frequency of the actuators or optimizing duty cycle and phase shift of the actuators. Simulations of this optimization are further studied in chapter 5 in this thesis. A higher flow rate in such a device corresponds to the optimized phase shift and duty cycle combined with the resonance frequency of the actuators. When an actuator operates at its resonant frequency, typically in the order of a couple of hundred Hertz for EAPs, the deformation of the actuators reaches its maximum. The combination of a high actuation rate at the resonance frequency and the maximum deformation of the actuators leads to a large increase in fluid flow compared to other configurations. Reactions or mixing of substances that need less residence time than the time, the pumping can provide for the mixture, cannot be performed with this device.

4.6. CONCLUSION

Herein, the fabrication of a pumping micromixer consisting of DESA is demonstrated. This micromixer is not only able to mix two solutions, but also to pump in and out the resulting mixture.

In this chapter, it is proved that prototypes of a Y-type active micromixer can successfully be fabricated using the layer-by-layer deposition method. The automatic method used here is based on the spin coating of the dielectric layer, the *in-situ* crosslinking of the elastomer layer and the spraying of the electrodes as thin graphite layers. The repetition of these steps enables the manufacture of multiple layers or stacked actuators. It should be noted the complexity of the micromixer structure based on a total of 12 dielectric stacked actuators and a channel in the middle of the device.

In this chapter, the pumping micromixer has been examined. First, the thickness of the layers is measured. The elastomer layer is 50.3 μm thick and the electrode layer is 9.8 μm thick. Then, the response of the pumping actuators to different input signals and electric fields has been tested. For driving voltages higher than 1200 V, it is proved that rectangular signals offer a greater deformation of the stacked actuators than the same driving voltages with sinusoidal signals. The maximum deformation obtained corresponds to 36.95 μm for half the stacked actuator layers. This is reached at a frequency of 1 Hz for a rectangular input signal of 1500 V with a DC-bias half the amplitude.

Concerning the pumping, the micromixer has been tested at different frequencies (1, 2 and 10 Hz) at 1500 V (the maximal voltage, shortly below the electric breakdown of the elastomer), displaying a maximal flow rate of 21.5 $\mu\text{L}/\text{min}$ at 10 Hz.

The mixing capability of the device was tested and a 50 %/50 % mixture was obtained. The analysis of these results was done by means of digital imaging. Images are captured while the micromixer is mixing and the images are afterwards investigated using a MATLAB program. This micromixer has proven its capability to homogeneously mix solutions. Future investigations on the micromixer might include mixing different ratios of solutions by only changing the frequency of actuation of the actuators in pumping chamber 1 respecting to the pumping chamber 2 and synchronising the frequency of both chambers with the mixing chamber. Within this work, the possibility of using DESA as a pumping micromixer has been demonstrated. Further measurements in the pumping and mixing ranges are necessary to fully characterize the micromixer.

The pumping micromixer, as it is designed, minimizes the apparatus necessary for mixing by decreasing the number of elements of the setup, compared to classical micromixers. Unlike rotatory pumps, the proposed micromixer is based on peristaltic movements of its walls, avoiding the contact with external parts, which may contaminate the samples. Peristalsis involves an actuation principle where energy is transferred from the periodic motion of the walls to a fluid volume. It is the common transport phenomenon in the human body due to the gentle treatment to the samples. Therefore, the use in biological samples is very interesting, where the stress in cells may cause the death or their unusable behaviour. Moreover, DESA micromixers are also of interest in the analysis of chemical, biological and medical samples, due to the biocompatibility [208][174] of the used materials (PDMS and graphite).

Parallel to this work other technologies have been used to fabricate thinner stacked DEAs and therefore with the need of a lower driving voltage. Examples of these techniques are 3D printing techniques [62][209] and dip coating [210], with a very high range of applications like artificial muscles, tubular DEA for energy harvesting acting as buoys. Poulin et al. [211] 3D-printed a 3 μm dielectric membrane and reported 7.5 % strain at 245 V. Afterwards, McCoul et al. [212] from the same research group improved the method to allow inkjet 3D printing of UV curable DEAs. The advantages of 3D printing DESA are the thinner membranes created and the possibility of fabricating complex geometries. Regarding stacked actuator, each layer can be differently manufactured by only changing the parameters of the 3D-printer and even introducing passive elements that can be afterwards removed from the structure, for example, dissolving them. Klug et al. [210] developed an automatic fabrication method for manufacturing tubular DESA of 10 layers of 100 mm length. Ji et al. [213] introduced the prestretch for micro-fabricated DESA based on the Langmuir-Schaefer method to increase the actuation ratio. They fabricated a 1.4 μm -thick prestretched PDMS membrane and reported about 4 % strain at 100 V.

These studies provide unique contributions for miniaturization of DEAs and reducing the operating voltage of DEAs to sub-kV ranges. Using these technologies, the fabrication of biocompatible pumping micromixers able to operate at low voltages seems to be a reality in the near future. Furthermore, these technologies will also help in the miniaturization of the exposed mixer, allowing it to get into the micro level and be more competitive. At the end of this chapter, different approaches for new prototypes and mixers have been proposed.



5. SIMULATIONS WITH THE PUMPING MICROMIXER

In this chapter, the Y-type pumping micromixer explained in chapter 3 and fabricated in chapter 4 is studied using COMSOL Multiphysics® Modelling Software.

Firstly, the deformation of the stacked actuator layers under an applied voltage is examined. Then, the fluid dynamic behaviour of the pumping chamber actuators is analysed at different duty cycles, phase shifts and frequencies. Finally, the pressure at the outlet of the channel in the pumping chamber is determined, in order to have a full vision of the versatility of the pumping micromixer.

5.1. DISPLACEMENT VERSUS ELECTRIC FIELD

The modelling of the pumping micromixer helps to understand the behaviour of the dielectric elastomer stacked actuators, including their deformation and influence on the fluid channel. COMSOL Multiphysics® Modelling Software is used for simulating the device performance.

Within this software, different multiphysics modules are used for dielectric elastomer actuators: the electrostatic module to calculate the electrostatic force applied to the actuators, and the solid mechanics module to determine the deformation or displacement of the actuators. The electrostatic module is coupled to the mechanical structure module (solid mechanics), in order to evaluate the electrostatic pressure exerted on a DEA sandwiched between two compliant electrodes, according to the Maxwell pressure equation (Eq.1.1). In the mechanical structure module, a hyperelastic model is used.

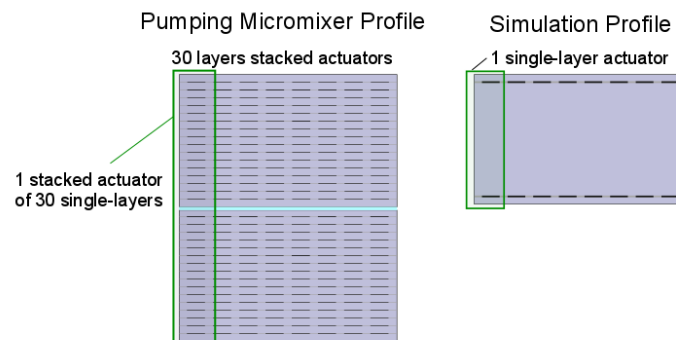


Figure 5.1: Simulation geometry. On the left, a sketch of the fabricated pumping micromixer consisting of 12 stacked actuators of 30 single-layers, each with a thickness of 50 μm . On the right, the simulated geometry in COMSOL Multiphysics®. The device consists of 12 single-layer actuators with a thickness of 750 μm .

For the purpose of simplifying the simulations, instead of multiple layers, each stacked actuator is considered as a single layer capacitor, whose effective capacity is determined by the contribution of each layer in its stack. Thus, one single layer with the thickness of the total amount of layers is evaluated. The total thickness of the actuators is then 750 μm for the top part of the device and 750 μm for the bottom part. Figure 5.1 shows a sketch of the considered geometry for the study in COMSOL Multiphysics®. On the left, a profile sketch of a full pumping micromixer and on the

right, the considered model. To simplify the calculations, only 15 layers are simulated (half of the device).

For a more precise modelling of the actuators, the properties of the materials for the pumping micromixer are the same as those of the fabricated micromixer, i.e., Elastosil® P7670 PDMS from Wacker®, for the dielectric and the passive layers, and MF 2/99,5-99,9E graphite powder, for the electrodes. The basic properties of these materials are summarized in section 3.2.2, more specifically in Table 3.3.

5.1.1. MODULES AND PARAMETERS

The modules used in COMSOL Multiphysics®, as mentioned before, are the electrostatics and solid mechanics. The electrostatic module is configured including the ground, terminal and force components. The bottom layer electrodes are considered as working electrodes and the top layer electrodes act as ground electrodes.

The first assumption made in the COMSOL Multiphysics® geometry, the stacked layers are considered as a single thick layer, leads to a change in the electric field applied to the dielectric. Thus, the applied voltage to get the same deformation corresponds to n times the voltage applied to one-single layer actuator, where n is the number of layers of the stack. In this particular case, that voltage corresponds to 1500 V x 15 layers (22.5 kV) for a 750 μm thick one-layer capacitor (half the thickness of the micromixer). Null passivation due to the electrode rigidity is assumed. The main electrical properties used for the simulations are summarized in Table 5.1.

Table 5.1: Parameters used in the electrostatic module.

Parameter	Symbol	Value
Relative permittivity	ϵ_r	3
Terminal electrodes voltage	V_T	22.5 kV
Ground electrodes voltage	V_G	0 V

The electrostatic pressure exerted on the one-layer actuator is calculated by the electrostatic module, based on the Maxwell pressure equation (Eq 1.1). Then, this pressure is consequently added as an input value to the solid mechanics module to determine the deformation of the layer.

In this study, the dielectric material is assumed as an incompressible hyperelastic solid, since the elastic effect is predominant compared to the visco-elastic one. The stress state in the hyperelastic material is determined by taking the derivatives of the strain energy density with respect to the strain components.

The Mooney-Rivlin hyperelastic model with five parameters is used for the simulation. The strain energy function of Mooney-Rivlin hyperelastic constitutive model is explained in detail in section 1.2.1A. Here, equation 1.26 is used to obtain the values of deformation of the elastomer.

Former colleagues in the department have previously investigated the mechanical properties of the dielectric material, PDMS Elastosil® P7670, and have fitted the measured points to the hyperelastic model of Mooney Rivlin for five parameters [214]. These values, summarized in Table 5.2, are used in the solid mechanics module to determine the deformation of the stacked in all directions.



Table 5.2: Parameters used in the solid mechanics module for hyperelastic model of Mooney Rivlin 5 parameters.

Parameter	Symbol	Value
Young's Modulus	Y	165 kPa
Poisson's ratio	ν	0.49
Hyperelastic Mooney-Rivlin: 5 parameters		
Incompressibility	d	0
Constant 1	C_{10}	31357 Pa
Constant 2	C_{01}	1138.7 Pa
Constant 3	C_{20}	2174 Pa
Constant 4	C_{02}	1044.9 Pa
Constant 5	C_{11}	-3718.1 Pa

5.1.2. DISPLACEMENT RESULTS

Displacement simulations with respect to the applied voltage were performed. As expected, the highest electric field reveals the greatest deformation and thus larger area expansion and thickness contraction.

Figure 5.2 shows the 3D plot obtained from the solid mechanics module. The displacement in x, y, and z is plotted for half the stacked actuator layers. The maximal displacement obtained in the z direction is 148 μm , while in the x and y axes are 23 μm and 41.5 μm , respectively. Due to symmetry, the z-axis deformation of the full device is double the simulated deformation. As mentioned above, only half of the micromixer is simulated.

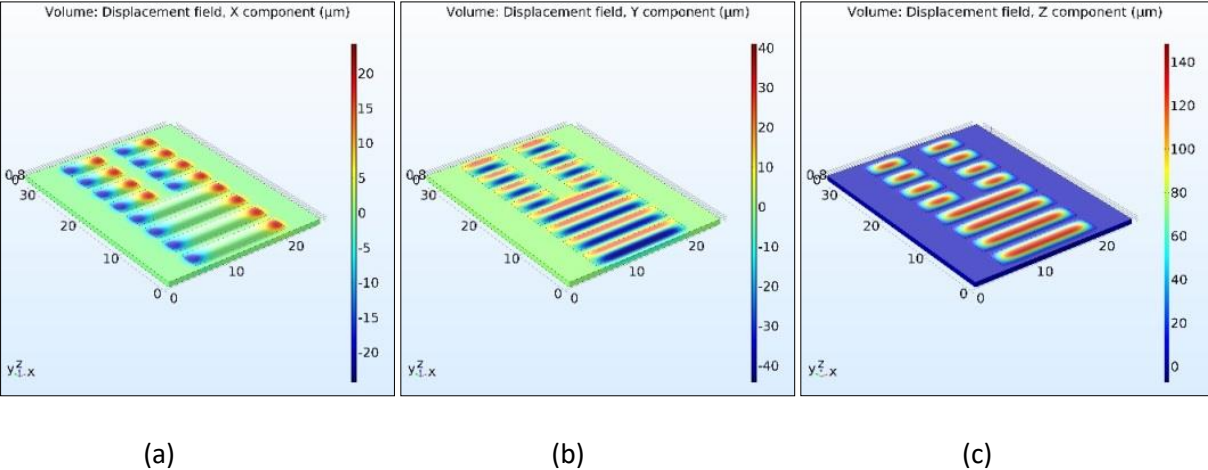


Figure 5.2: Displacement in x, y and z direction of half a pumping micromixer using both the solid mechanics and the electrostatic module in COMSOL Multiphysics®. (a) Corresponds to the displacement field in the x-axis, (b) to the y-axis and (c) to the z-axis. The colour bar, from blue to red, shows the displacement field in μm of the actuators according to the axis they represent.

The upper wall of the channel shrinks by 148 μm into the positive z-direction and the bottom part of the channel moves 148 μm into the negative direction of the z-axis. The channel increases 7.4 times in height with respect to the initial height of the channel of 40 μm .

Experimental measurements of the deformation of the dielectric stacked actuators (half of a fabricated pumping micromixer) showed a maximal displacement of 40.5 μm in z-direction,

holding a DC voltage of 1500 V for 30 seconds. More details about these measurements can be found in section 4.2.3.

Upon comparison of the theoretical and experimental results of deformation of the dielectric stacked actuators, a considerable discrepancy was observed. The simulations indicate an increase in displacement by a factor of 3.65, as compared to the experimental results. The reasons behind this deviation could be attributed to several factors, such as the rigidity of the electrodes, non-electrically connected layers within the stack, and the presence of protective layers above and below the stack actuator, among others.

In terms of the rigidity of the electrodes, the simulations do not account for the presence of graphite electrodes. Instead, the simulations assume pure deformation of the hyperelastic material, driven solely by its elastic properties. As previously noted, the stacks comprise layers of hyperelastic material with a thickness of 50 μm , sandwiched between two layers of 10 μm -thick graphite electrodes. The hyperelastic material, PDMS Elastosil[®] P7670, possesses a Young's modulus of 165 kPa, while the graphite electrodes exhibit a Young's modulus of approximately 10 GPa [175]. The significant difference in elasticity between the two materials underscores the need to consider the passivation generated by the electrodes when simulating stack deformation.

In a previous study conducted by our research group [175], [193], the influence of the ratio between film thickness and electrode thickness on the final deformation achieved by stack actuators was investigated using the same materials as in this thesis. Dielectric thicknesses of 20 μm , 10 μm , and 5 μm were evaluated with a range of electrode layer thicknesses between 0.1 μm and 10 μm . The results show that the maximal stack deformation is approximately 10% for 10 μm and 20 μm film thicknesses with a dielectric thickness between 0.1 μm and 1 μm electrode thickness. For thicker electrodes, the deformation decreases, reaching a minimum of 5% for 10 μm and 7% for 20 μm film at an electrode thickness of 10 μm . In the case of a 1 μm thick film, the deformation follows a very pronounced negative slope, leading to a 10% deformation at an electrode thickness of 0.1 μm and a 3% deformation at an electrode thickness of 10 μm . Therefore, this research concluded that for optimal stacking actuator performance, the electrode thickness should be less than 10% of the dielectric film thickness, preferably closer to 1%. However, in this thesis, the electrode thickness is 20% thinner than the dielectric film thickness. This electrode thickness was required to manufacture functional devices, as the stack layers were not electrically connected when thinner electrodes were used.

In their study [175], [193], a relationship between the normalized stack deformation and the ratio of electrode thickness to film thickness was established. The normalized stack deformation is defined as 100% when the deformation of the stack with and without electrodes is the same, and 50% when the deformation of the stack is half of that of the actuators without electrodes. For a film thickness of 50 μm and an electrode thickness of 10 μm , corresponding to a 20% ratio of electrode thickness to film thickness, the normalized stack deformation was found to be 85% of the stack deformation based on their calculations. Therefore, the simulations performed in this study should show only 15% higher deformation value than the experimental values.

Additionally, based on the investigation described above, the graphite electrodes with a Young's modulus of 10 GPa should have a ratio of electrode thickness to dielectric thickness of 110% to achieve a passivation of 3.65 times lower deformation of the stacks. This means that the electrode thickness should be 55 μm . Despite the thinness of the electrode layers and their graphite powder-

based composition, they still offer significant resistance to the dielectric, however, this factor alone can only partially explain the difference between simulation and experimental results.

The simulated case presented in this work assumes an ideal case wherein all the layers are interconnected and operating at their maximum capacitive potential, while disregarding the impact of protective layers located above and beneath the electrodes that only deform under the influence of the active layers. These protective layers, nevertheless, also contribute to the passivation of the actuators. Based on the discerned impact of the stiffer electrodes on the overall deformation, it can be inferred that the passive layers' contribution to the deviation in the experimental and simulated results is minimal. Hence, other aspects associated with the hyperelastic model used in the simulations, such as the parameters or boundary conditions, necessitate further investigation to identify the root cause of this deviation. Due to time limitation, this discrepancy was not further studied. From this point on, the experimental values of deformation will be used for future simulations of the fluid flow and pressure of the devices.

The pumping micromixer in this thesis operates in two states: 1) the actuators are off and the channel is partially opened (40 μm height, caused by the fabrication process) and 2) the actuators are on and the channel is opened with a height equal to 40 μm plus the deformation of the actuators in the z-axis. In both states, the channel is opened and thus, while changing from state 2 to state 1, the fluid is able to flow backwards. From this point of view, it is important to perform various simulations to determine the actual flow that ideally can be achieved within these conditions. The following section provides a study to perform simulations of pumping micromixers out of electroactive polymers in terms of fluid flow and pressure.

5.2. FLUID DYNAMIC CHARACTERIZATION

In the following simulations, only the pumping characteristics of the pumping micromixer are under study. No mixing is characterized. Moreover, the complexity of the whole geometry of the device makes it very hard to simulate the system as it is. Here, only the pumping chambers are studied. Actuators are smaller in the pumping chamber than in the mixing chamber. Thus, the volume difference in the channel between the active and inactive state of the actuators is smaller in the pumping chambers than in the mixing chambers. Hence, the pumping chambers are the bottle neck for the fluid flow. In this section, the flow in the pumping chambers is calculated and simulated, which is equivalent to the half of the fluid flow of the full system.

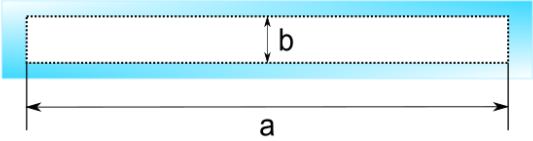
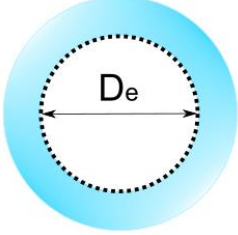
The fluid dynamic characterization requires the use of the following modules in COMSOL Multiphysics[®]: the solid mechanics, the laminar flow, and the fluid structure interaction module to combine the results from both modules.

Since the simulated deformation of the actuators shows a great variance with respect to the experimental one, the experimental values of the deformation are used to obtain more realistic fluidic calculations. The deformation of half a micromixer in the z-direction is set as the one corresponding to a rectangular signal at 1500 V, namely 36.95 μm height change (see section 4.2.3 for more details).

To simplify the modelling of the fluid flow, a 2D axisymmetric model is used. The cross-section geometry of the channel is changed from rectangular to circular. Table 5.3 shows the geometry change and the corresponding channel values. Symmetry conditions help to reduce the number

of variables that need to be defined initially in the program. In addition, the simulation is solved more quickly and more accurately.

Table 5.3: Simplified model from rectangular cross-section channel (real) to circular cross-section channel (simulated).

	
<p>Rectangular cross-section (state 1: off)</p> <p>a is the width of the actuator (6 mm)</p> <p>b is the initial height of the channel (40 μm)</p>	<p>Circular cross-section (state 1: off)</p> <p>D_{e1} is the equivalent diameter for state 1 (340 μm)</p>
<p>Rectangular cross-section (state 2: on)</p> <p>a is the width of the actuator (6 mm)</p> <p>b corresponds to the height of the channel. Here, the initial channel height plus twice the deformation of half the micromixer (40 $\mu\text{m} + 2 \cdot 36.95 \mu\text{m} = 113.9 \mu\text{m}$)</p>	<p>Circular cross-section (state 2: on)</p> <p>D_{e2} is the equivalent diameter for state 2 (652 μm)</p> <p>Diameter diff. (state 2 - state 1) = 312 μm</p>

To obtain the same results as for the rectangular channel, the Huebscher equation is used to calculate the equivalent diameter D_e of the channel (Eq. 2.2, section 2.1).

By introducing the size values of the pumping chamber in Eq 2.2, the equivalent diameter for the passive state of the channel (state 1), and also for the channel when maximal voltage is applied (state 2), are calculated. The equivalent diameter is 340 μm for the passive state, (when no voltage is applied), and 652 μm when maximal voltage is applied for a circular cross-section. These values are summarized in Table 5.3.

5.2.1. SOLID MECHANICS MODULE

The geometry used in the solid mechanics module for the fluid characterization of the micromixer is a 2D axisymmetric model, using the previously calculated equivalent diameter.

The solid mechanics module is configured including the force needed in each actuator to provide a displacement of 156 μm . Both inlet and outlet of the channel are included in the solid mechanics module. The boundary conditions used for the solid mechanics module are:

-
- All edges of the device that are not in contact with the actuators are considered fixed or rigid. These edges are shown in blue in Figure 5.3(a).
 - The rest of the geometry is considered free of movement, except for the edges of the actuators.
 - The displacement of the actuators is described by using the function boundary load. Each actuator has its own boundary load condition.

Figure 5.3(a) corresponds to the geometry under study. The 2D axisymmetric model is drawn. In the x -axis the height in metres of the device is represented, and in the y -axis its length, also in metres. In the x -axis, the equivalent radius of the channel and the equivalent radius of the actuators are visible. The symmetry axis of the device can be observed as a dashed red line, for $r=0$. Blue edges represent the boundary conditions for the solid mechanics module, defining these zones as rigid parts. The geometry between the blue lines correspond to the actuators. Four pumping actuators are simulated here. For clarity, a zoom-in sketch of the width of the system is represented in the same figure. The equivalent radius R_e , define as the half of the equivalent diameter D_e , is shown for the two states: on and off.

For the coupling of the solid mechanics module with the fluid dynamics module, it is necessary that the solid mechanics deformation is done as a boundary load over time and not as a sudden displacement of the full actuator. A highly smooth boundary load over the actuator's length is implemented.

The boundary load over the actuators is defined as a function of the distance in the electrode. Figure 5.3(b) shows the deformation with respect to time for an actuator. In the x -axis a hypothetical time is drawn, from -1 until 2 seconds. In the y -axis, a non-dimensional parameter for the length of the actuator is shown. In the z -axis, the step function from 0 until 1 is shown for the boundary load. In this particular example, at 0.5 seconds the maximal deformation on the centre of the actuator or at 1.5 mm is shown. The colour bar shows the change in deformation for the step function, from dark blue (0 displacement) until dark red (100 % displacement or 1).

The total solid deformation is obtained by multiplying the force applied to the actuators by the load function in time leading to a slightly smoothed signal for the deformation of the actuators with time and length.

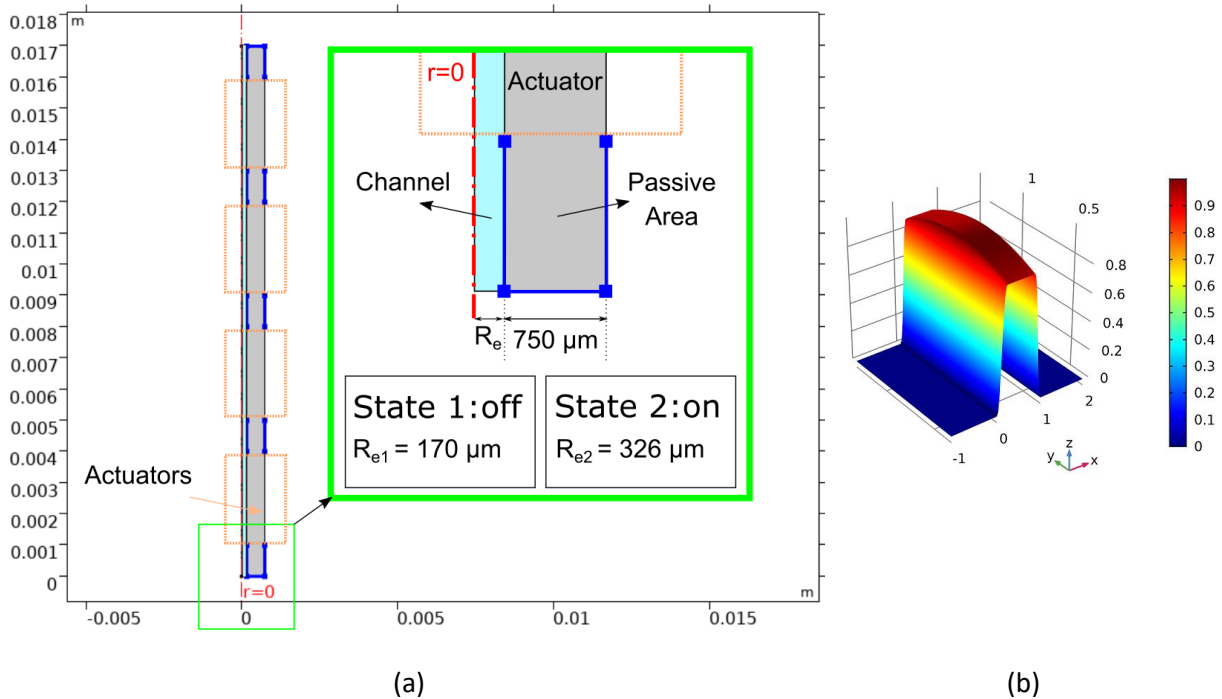


Figure 5.3: (a) Representation of the geometry. (b) Step function for the calculation of displacement of the actuator.

The load inputs in the solid mechanics modules are based on rectangular signals with a time dependency. The time steps are 10^{-3} , and 10^{-4} s for higher frequencies. For each frequency, at least every 1 ms a data point is obtained. The simulations start from 0 s and run until 5 s for the lower frequencies and 1s for the higher ones.

5.2.2. LAMINAR FLOW MODULE

Laminar flow module helps to understand the change in velocity and pressure for fluids at low Reynolds numbers. The conservation equations are used for these simulations (more details in Appendix A) for a single phase of homogeneous composition in a continuum level.

The conservation equations of mass (continuity equation), of momentum (Newton's second law or Navier-Stokes equation, motion equation) and of energy (first law of thermodynamics or energy equation) provide information about the velocity, the pressure and the temperature field. Other properties can also be deduced from the previous ones like viscosity, density, enthalpy, etc.

The fluid is considered to be incompressible, initially at room temperature and at atmospheric pressure. Due to the very laminar regime of the system, or very low Reynolds number, no turbulences are added. It is considered a fluid flow profile where the fluid velocity at the wall is null. For the laminar flow module, water was chosen as the liquid to be pumped.

Both inlet and outlet are designed as open boundary, so fluids can flow in and out of the system. Moreover, both parts can allow reverse flow. In the case of peristaltic pumps, reverse flow is important because a progression and regression of the fluid is common for each step. Disregarding the back flow will lead to a fully mistaken simulation. Initially, the fluid is considered to be static. Only the inside part of the channel is subjected to the laminar flow.

5.2.3. FLUID-STRUCTURE INTERACTION

The Fluid-Structure Interaction Multiphysics interface combines fluid flow with solid mechanics to calculate the interaction between the fluid and the solid structure. The solid mechanics interface models the solid, while a single-phase flow interface models the fluid. The Fluid-Structure Interaction coupling appears on the boundaries between the fluid and the solid.

Depending on the precision expected for the modelling or the influence between the laminar flow and the solid mechanics, it is possible to consider their effect on each other. In these simulations, fully coupling is considered to be more effective and provides more relevant information. On one hand, it is clear that the deformation of the actuators leads to the filling of the channel chamber with the fluid. On the other hand, when the actuator gets in off-state, it needs to have enough stroke to push the water to the next chamber and also backwards. Ideally, the coupling of both will help to evaluate whether the force of the actuator is sufficient for pumping or not.

5.2.4. DEFINITION OF MESH

Choosing a right mesh for modelling a system is quite important in general, but it increases its importance when two multiphysics modules are interacting with each other. In this case, the fluid dynamics module is applied inside the channel, which requires a very precise meshing. The solid mechanics module covers the whole geometry and does not require a fine mesh.

Three different mesh systems are considered in this simulation. First, the inside channel mesh, which corresponds entirely to the laminar flow module. Free triangular mesh with a fine refinement has been used for this section. Free triangular mesh is interesting in applications of high aspect ratio because triangular mesh is a quick and simple way to obtain meshes of high element quality that cover very different geometries.

Secondly, boundary layers are implemented. These layers connect the solid mechanics module with the laminar flow multiphysics module in the solid/liquid interface. This interface is composed of free triangular and mapped layers, also in fine mesh refinement. Mapped meshes can be particularly powerful for 2D simulations because they provide extremely good control over element size, quality, and growth rate since all elements possess the same geometry and size. The term mesh quality refers to a dimensionless quantity between 0 and 1, where 1 states for a perfectly regular element, and 0 represents a degenerated element. The growth rate of a mesh is defined as the change in element size from one element to the size of its neighbours. In order to get accurate results, the growth rate should be small.

Finally, a free triangular mesh covers the surface of the wall, for the solid mechanics calculations with a fine refinement. As it can be observed, it increases the triangular geometries from the channel until the outer part of the actuators.

Figure 5.4 shows a plot where the chosen mesh is drawn for a zoomed section of the device. As in Figure 5.3, x-axis represents the equivalent radius of the device. The red dashed line in $r=0$ represents the symmetry axis. The y-axis displays the length of a part of the device. Here the edges of the channel are drawn in blue to distinguish the areas between the inner channel and the outer channel.

As it is depicted in Figure 5.4, the size of the triangular mesh varies with the channel thickness. The closer the triangles are to the solid-liquid interface, the smaller the triangles are. Therefore, the larger the radius of the walls, the larger the mesh geometries.

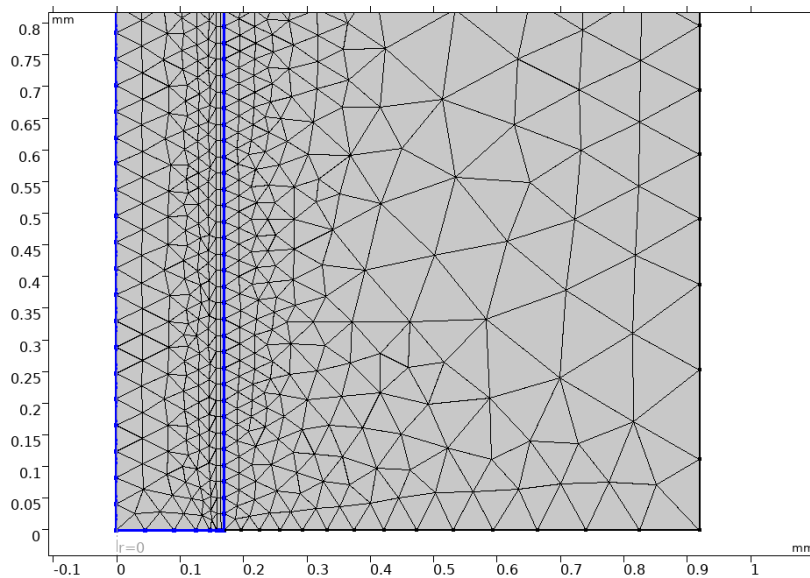


Figure 5.4: A zoomed-in view of the mesh resulting from the physics-induced meshing sequence for the peristaltic model: channel on the left (within blue edges) and wall on the right. Three different mesh systems are considered in this simulation. For the inside channel, a free triangular mesh with a fine refinement has been used. Secondly, a boundary layer which connects both interfaces, solid mechanics and laminar flow. This section is composed of free triangular and mapped layers, also in fine mesh refinement. Finally, a free triangular mesh covers the surface of the walls with a fine refinement, which increases the triangular geometries from the channel until the outer part of the actuators.

Both geometries for the inner channel and the channel itself in the laminar flow module are solved based on a freely moving deformed mesh, in order to vary when the equivalent diameter gets bigger due to the deformation of the actuators. Based on the main properties of PDMS, the change in shape is controlled by using a hyperelastic smoothing. On the solid-fluid boundary at the tube's inner wall, the moving mesh follows the structural deformation.

It is possible to get more accurate simulations with a finer mesh. However, as the simulations of these sections are time-based and the number of calculations required for the three modules is quite high, a compromise between mesh size and calculation time needs to be taken.

A proof of the mesh quality is performed by comparing simulations with coarse, normal and fine mesh refinements. Simulations have been performed at 1 Hz with a 0.5 duty cycle and 90° phase shift with a variable mesh size. The fluid flow and the number of elements have been studied.

As depicted in Table 5.4, the total number of mesh elements increases with the mesh refinement. The number of elements in the channel increases approximately triples when using a fine mesh compared to a coarse mesh. In addition, the average element quality achieved increases with increasing refinement. As stated above, the element quality is a value provided by COMSOL Multiphysics® that defines the homogeneity of the individual elements in a mesh. This ranges from 0 to 1, with 1 being a perfect element. In the simulation, an average value of 0.836 element quality has been obtained for the fine mesh refinement. Coarse and normal meshes provided a slightly lower average element quality. The flow rate obtained by the simulations between coarse, normal and fine has also been evaluated. Values of 18.611, 18.897 and 18.865 $\mu\text{L}/\text{min}$ were obtained,

respectively. Here, no significant differences between normal and fine refinement are detected. The deviations are minimal and only the second significant figure varies. Both normal and fine refinement could be used for these simulations. However, to ensure the quality of the simulations for other duty cycles, phase shifts and frequencies, fine refinement is used to have a larger number of elements within the channel.

Table 5.4: Mesh refinement test. Coarse, normal and fine mesh refinements are investigated.

Mesh refinement	Total number of elements	Elements in the inside channel: Triangles/Quads	Average element quality	Flow rate ($\mu\text{L}/\text{min}$)
Coarse	7711	2842/824	0.833	18.611
Normal	11495	4206/1054	0.834	18.897
Fine	16535	6818/1326	0.836	18.865

5.2.5. RESULTS

The simulated peristaltic micropump consists of four actuators located along a channel and driven by smooth rectangular signals with a particular sequence. Rectangular signals are preferred due to the higher deformation obtained in the experimental measurements (see section 4.2.3). The general parameters that quantify the pump performance are the maximum flow rate (Q) and the maximum pressure that can be generated between the pump inlet and outlet (P , called the pump head).

Given a number of actuators, parameters such actuation frequency, phase shift, response time and the volume that is moved, determine the performance of the pumping system. Time dependent measurements are performed at different frequencies to obtain a fluid flow and a pressure of the fluid after the actuation takes place.

A. Flow rate

In this first simulation at constant frequency, the phase shift is defined as half of the actuation time, or in other words, the second actuator starts its actuation at the middle point in time of actuation of the first actuator ($\Delta\varphi = 90^\circ$). Multiple duty cycles D from 0.25 until 0.67 are simulated. This configuration is named configuration 0.

Configuration 0:

The first simulations performed are at a constant frequency of 2 Hz. The representation of the flow rate Q in the y -axis versus the duty cycle D in the x -axis leads to a parabolic profile, shown in blue in Figure 5.5(a). The parabolic fit function for 2 Hz is:

$$Q_{0(2\text{Hz})} = -308.13D^2 + 212.46D - 0.0007 \quad \text{Eq 5.1}$$

with a regression coefficient of $R^2 = 0.9947$. The parabola maximum point states a maximum flow rate at duty cycle of 0.3447 of 36.62 $\mu\text{L}/\text{min}$, when the phase shift coincides with half the actuation time. At 0.6895 duty cycle the flow rate is again 0.

In the same way, if the results obtained with the same simulation parameters but a constant frequency of 20/3 Hz or 6.67 Hz are analysed (red plot in Figure 5.5(a)), the resulting parabolic function is:

$$Q_{0(6.67\text{Hz})} = -763.35D^2 + 532.48D + 0.8067 \quad \text{Eq 5.2}$$

with a regression coefficient of $R^2 = 0.9923$. For this particular case, the maximum flow rate is 93.67 $\mu\text{L}/\text{min}$ at a duty cycle of 0.3478, when the phase shift coincides with half the actuation time. Using the parabolic equation, at 0.699 duty cycle the flow rate is also 0. Note that the duty cycle at which the maximum flow rate is obtained and the duty cycle at the minimum flow, only slightly differ to those obtained for 2 Hz.

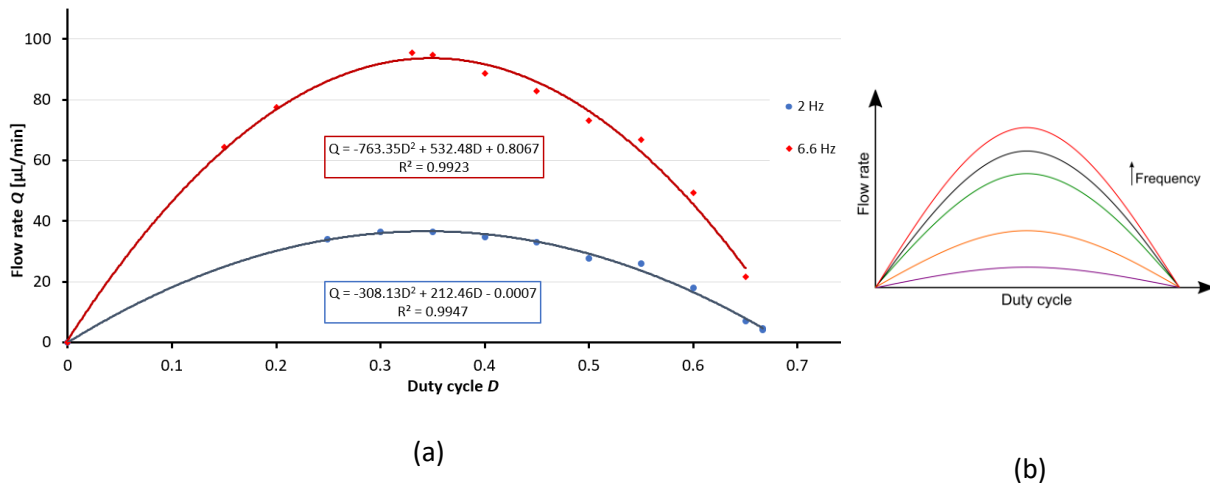


Figure 5.5: (a) Simulated flow rate versus duty cycle at constant frequencies for 2 Hz in blue and 20/3 Hz or 6.67 Hz in red. Duty cycle varies from 0.25 until 2/3. The phase shift was determined as half the actuation time of the previous actuator or 90° . A parabolic behaviour is observed. (b) Expected behaviour of the dependency of the flow rate and duty cycle at different frequencies.

Both 2 Hz and 20/3 Hz (6.67 Hz) graphs present the same parabolic behaviour. Curves start at duty cycle 0, but do not end at duty cycle 1. This behaviour is obtained for this particular case of the phase shift. Within this configuration, one actuator will turn on only when the previous actuator achieves the centre of its actuation time. For low duty cycles, although the time of actuation is very short, the actuators open and close with a peristaltic motion, meaning that not all the actuators are simultaneously on or off. In the case of high duty cycles, the actuators stay on for very long times, leading to periods when the majority of the actuators are open, or in other words, a propagating wave is not created and thus there is no net pumping. Details of both extremes (very low and very high duty cycle) can be observed in detail in Figure 5.6.

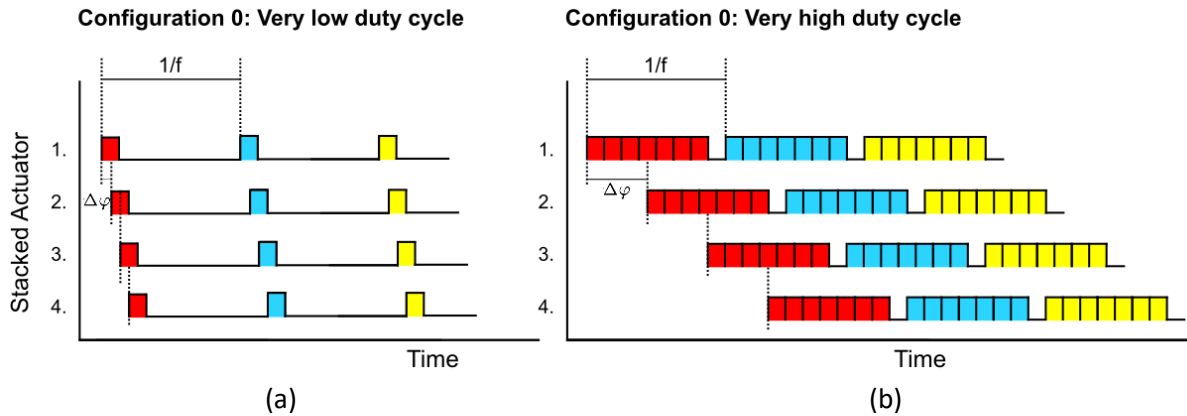


Figure 5.6: (a) Configuration 0 for very low duty cycle ($1/8$) and (b) configuration 0 for a very high duty cycle ($7/8$).

In Figure 5.6(a) an example of a very low duty cycle ($1/8$) is shown, while in Figure 5.6(b) a case with a very high duty cycle ($7/8$) is displayed. The first 3 actuation cycles for the 4 stacked actuators in the pumping chamber are represented. Colour sections belong to the actuation time when actuators are in on-state. Red colour represents the first actuation cycle for each actuator, light blue the second cycle and yellow the third cycle. The propagating wave in the low duty cycle lasts a short period of time and the actuators are in off-state for a long period. Meanwhile, for the high duty cycle the red propagating wave coincides in time with the blue one. The second, third and fourth actuator are still on during the first propagating wave when the second propagating wave starts, leading to a coupling and as a result there is no separation between one and other. Since there is no period where the channel is closed during a propagating wave, no net pumping is expected.

Similar behaviour to that shown for 2 and $20/3$ Hz is expected for lower and higher frequencies with these parameter configurations. The parabolas start at 0 duty cycle, getting a maximum flow rate at approximately 0.35 duty cycle and ending at approximately 0.69 duty cycle. Pattern replicas for different frequencies are expected, with parabolas with steeper slopes in the case of higher frequencies and lower slopes for smaller frequencies, as shown in the scheme in Figure 5.5(b).

In the previous chapter, the fluid flow in the pumping micromixer was tested in two different configurations, namely 1:1 and 2:2. In configuration 1:1, the stacked actuators are activated individually and sequentially with a rectangular phase, while in configuration 2:2, two stacked actuators turn on and off at the same time, also with a rectangular input signal. Experimental measurements of the pumping micromixer, described and analysed in section 4.3.1, were performed with a 0.5 duty cycle and a phase shift of 90° . The simulations of configuration 0 were also done with a phase shift of 90° .

Table 5.5 compares the values obtained both in simulations and experimentally. Only the case of the configuration 1:1 ("Experimental 1:1") is used here because its parameters match those simulated. The experimental values obtained for the fluid flow in the previous chapter correspond to twice the values included here. This is due to the fact that in the simulations only one fluidic inlet is considered.

Table 5.5: Comparison between Experimental 1:1 and simulation results for configuration 0 in terms of flow rate.

Phase shift	Duty cycle	Frequency (Hz)	Flow rate (µL/min)		Absolute error	Relative error (%)
			Experimental 1:1 [#]	Simulation		
90°	0.5	1	0.27	18.86	18.59	6885
		2	1.05	29.20	28.15	2681
		10	6.45	103.65	97.2	1507

[#]Only half the fluid flow is depicted here.

As it can be seen in the table, there is a large deviation between the experimental and the simulated values. The flow rate in the simulations is approximately 20 times higher than that obtained experimentally. Both absolute and relative errors are added in the table for better comparison of deviations at each frequency.

These deviations obtained between simulated and experimental measurements can be attributed to the ideal conditions imposed in the simulations.

Some of these ideal conditions are, for example, the measurement of the fluid flow at the outlet of the micromixer and the deformation of all the stacked actuator layers. In simulations, the fluid flow is measured right at the micromixer outlet, but in experimental measurements the fluid flow is measured in the reservoir. This means that the fluid has to flow through a tube into the reservoir with the resulting pressure loss due to the length of this tube. In other words, there is an extra resistance due to the transport of the fluid into the reservoir, which results in a loss of both pressure and flow rate. In the simulations, all actuator layers are deformed. A single layer with the thickness of the individual layers is considered and the corresponding voltage is applied to it. In the experimental case, although the number of connected layers per stacked actuator is determined individually before inserting the fluid, it cannot be guaranteed that during the process of measuring the fluid flow all layers of the actuators are still electrically connected.

Although there are large deviations between the simulations and the experimental results, the simulations provide relevant information on the best performance conditions of the pumping micromixer. An example of this are the curves shown in Figure 5.5, which determine the optimal duty cycle at a constant phase shift: in this case 90° to obtain the maximal fluid flow. These simulations prove that the experimental flow rate obtained with 0.5 duty cycle is not the optimum. The simulations determine a flow rate difference of approximately 20 % between duty cycle 0.35 and duty cycle 0.5. Thus, higher flow rates can be achieved with the pumping micromixer with a duty cycle of 0.35 and a phase shift of 90°.

The following simulations were done under three different configurations, where duty cycle and phase shift were changed. Table 5.6 summarizes the main parameters used in each case.

Table 5.6: Summary of the three simulated configurations

Configuration	Duty cycle	Phase shift
1	0.5	45° or 1/8 cycle
2	2/3	120° or 1/3 cycle
3	0.75	90° or 1/4 cycle

Configuration 1:

The first configuration has a duty cycle of 0.5 and a phase shift of 45° or 1/8. Figure 5.7(a) represents the configuration for a better visual understanding. The first 3 actuation cycles for the 4 stacked actuators in the pumping chamber are represented. Colour sections belong to the actuation time when actuators are in on-state. Red colour represents the first actuation cycle for each actuator, light blue the second cycle and yellow the third cycle.

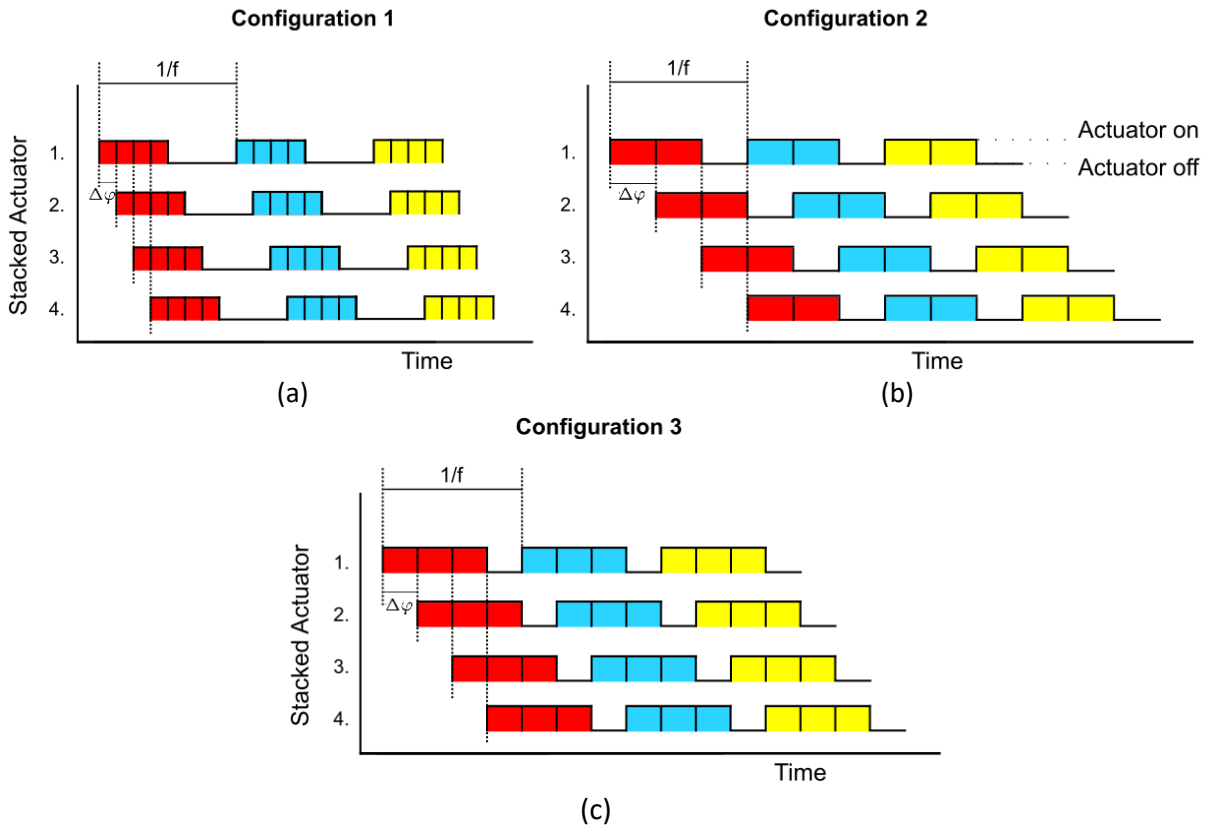


Figure 5.7: (a) Configuration 1 with a duty cycle of 0.5 and a phase shift of 45°. (b) Configuration 2 with a duty cycle of 2/3 and a phase shift of 45°. (c) Configuration 3 with a duty cycle of 0.75 and a phase shift of 90°.

Simulations at various frequencies are performed under the parameters previously explained. These frequencies are 1, 2, 5, 6.67, 20 and 200 Hz. Simulations are performed for the lower frequencies, which have also been experimentally tested, as well for higher frequencies. Higher frequencies are simulated to elucidate the full working capacity of the peristaltic pump from very low limits to very high.

The laminar flow module provides information about the fluid velocity vector u (components in both radial direction (u) and longitudinal direction along the channel (v)) and its pressure p . More details about the velocity vector in a circular section are found in Appendix A. The volumetric flow rate \dot{V} in m^3/s at a time t is obtained by a boundary integral over the channel's inlet and outlet boundary:

$$\dot{V}_{in} = - \int_{S_{in}} 2\pi r (n \cdot u) ds \quad \text{Eq 5.3}$$

$$\dot{V}_{out} = - \int_{s_{out}} 2\pi r (n \cdot u) ds \quad \text{Eq 5.4}$$

where n is the outward-pointing unit normal to the boundary, u is the velocity vector, and s is the boundary coordinate, along which the integration is done.

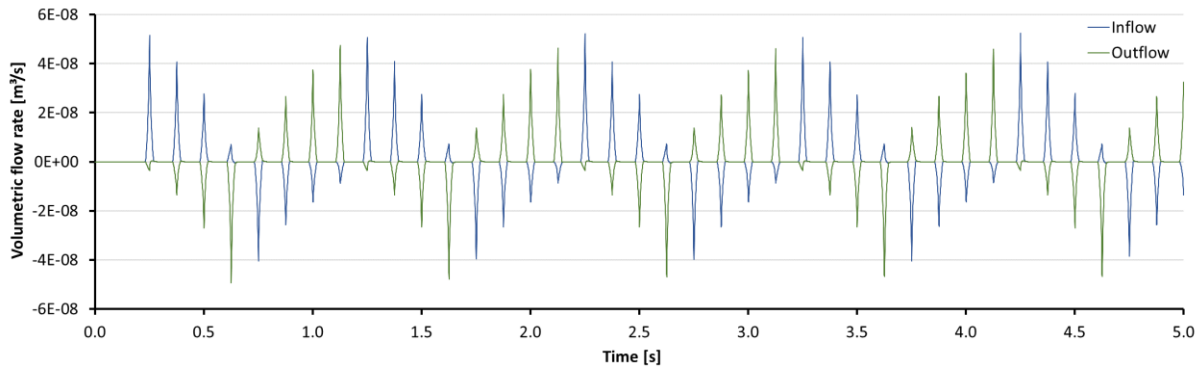


Figure 5.8: Inlet and outlet flow in m^3/s as functions of time. Volumetric flow rate at the inlet of the channel (in blue) and at the outlet (in green) for the configuration 1, at 1 Hz, 0.5 duty cycle and a phase shift of 45° . Positive values indicate that the fluid is flowing into the inlet and out of the outlet.

As a representative illustration, Figure 5.8 shows results about the volumetric flow rate at the inlet of the channel (in blue) and at the outlet (in green). Results are taken for the configuration 1, at 1 Hz, 0.5 duty cycle and a phase shift of 45° . Positive values indicate that the fluid is flowing into the inlet and out of the outlet, or that the fluid is travelling as desired. When for a full cycle the difference between positive and negative values is positive, the pump is correctly pumping. If the difference is negative, it means that the fluid is moving backwards, and a null difference states for a null net flow of the fluid.

If one complete cycle is considered for the analysis, the accumulated flow is obtained as the mean value between the inlet and outlet flow, as it can be observed in Figure 5.9 for 1 Hz. In blue, a positive accumulated flow at the outlet is observed. In the same figure in green, the volume conveyed is represented. The volume conveyed is defined as the accumulative outlet volume. During the first cycle, due to the difference of pressure acquired by the deformation of the actuator, the volume conveyed is initially negative because fluid is coming inside the pump from the outlet. As time passes, the pump starts to deliver fluid and the volume conveyed becomes positive and increases the transferred amount. At 1 Hz, the loss from the first cycle is recovered already at the second cycle (after 2 seconds of actuation).

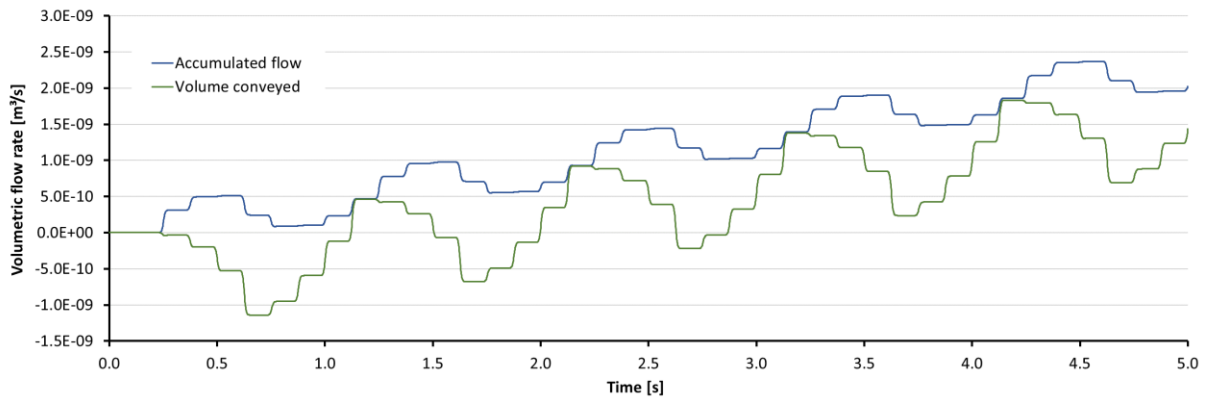


Figure 5.9: Representative volumetric flow rates for the configuration 1 (0.5 duty cycle, phase shift 45°) at 1 Hz. In blue, the accumulated flow defined as the mean value between the inlet and outlet flow. In green, the volume conveyed or, in other words, the accumulated outlet volume.

In the graph, steps can be observed for each cycle. These steps correspond to the opening and closing of the actuators, which lead to changes in the fluid flow and the pressure in the channel. This behaviour appears in all the configurations due to the working principle of the device.

Multiple simulations are done to determine the flow rate of the peristaltic pump at different frequencies. In Figure 5.10, configuration 1 with 0.5 duty cycle and a phase shift of 45° at diverse frequencies is plotted with the flow rate in $\mu\text{L}/\text{min}$ on the y-axis, and the frequency in Hz in a logarithm scale on the x-axis.

The simulated volumetric flow rate Q is 21.25 $\mu\text{L}/\text{min}$ at 1 Hz and 42.39 $\mu\text{L}/\text{min}$ at 2 Hz. The linear fitting leads to the equation $Q_1 = 8.1916f + 19.87$ and a coefficient of determination $R^2 = 0.9306$. For this particular configuration, at lower frequencies the simulated points converge in a better line fitting, as long as the actuation frequency increases.

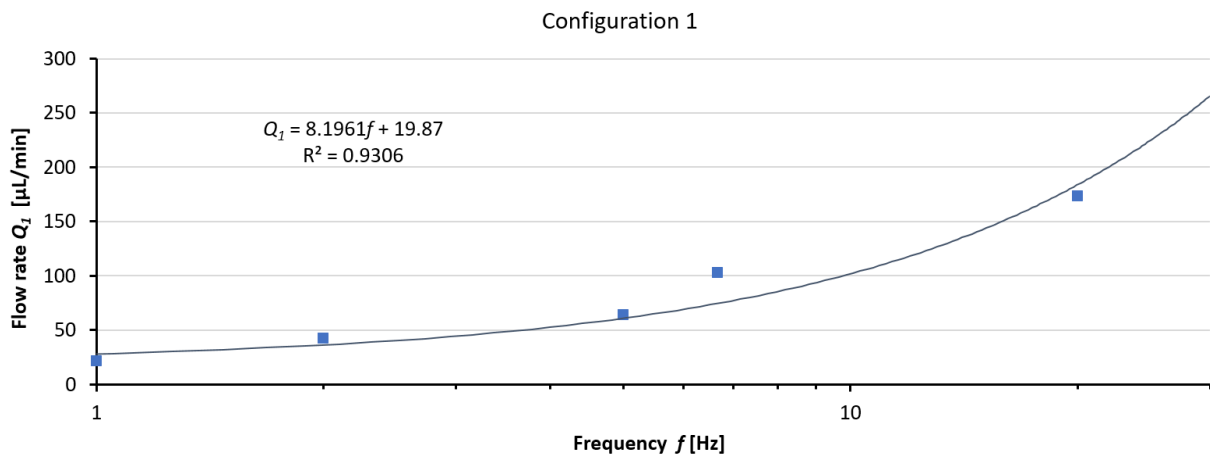


Figure 5.10: Plot of the flow rate Q_1 versus the actuation frequency f . For a better view of the lower frequencies' values, x-axis is plotted in a logarithm scale. Results correspond to the configuration 1 with 0.5 duty cycle and a phase shift of 45°.

Configuration 2:

The second configuration, with duty cycle 2/3 and phase shift 120°, is based in the sketch in Figure 5.7(b).

Figure 5.11 shows the values of the flow rate at several frequencies for configuration 2. Here, the values at 2 Hz and 10 Hz are highlighted. The simulations lead to a flow rate of 4.54 μL/min for 2 Hz and 16.83 μL/min for 10 Hz. The linear fitting of the simulated points leads to the equation $Q_2 = 1.8543f + 4.1478$ and a coefficient of determination $R^2 = 0.9969$. For this configuration, the results fit much better to a line than in the previous case, also for higher frequencies.

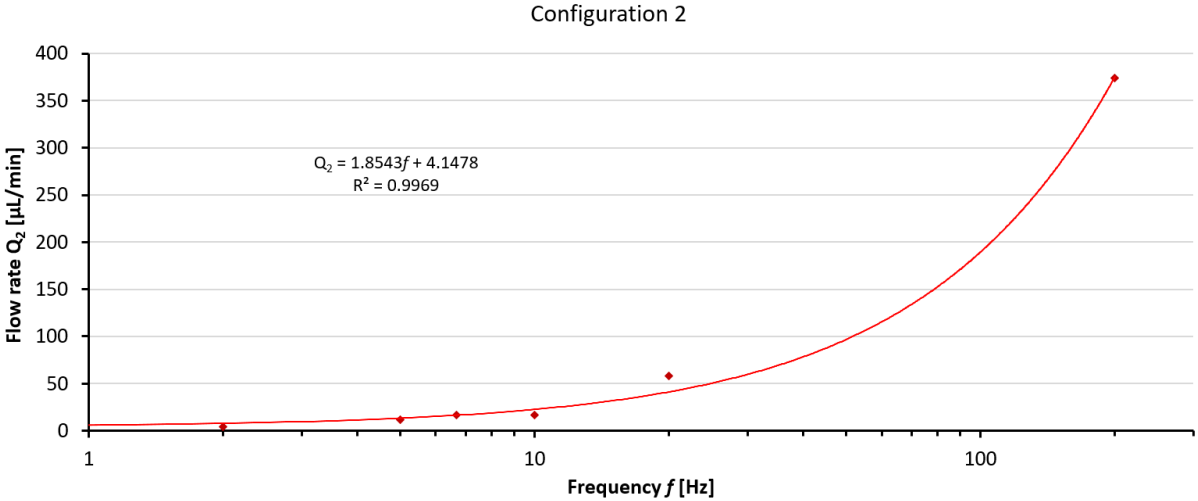


Figure 5.11: Values of volumetric flow rate at different frequencies for the configuration 2 or with 2/3 duty cycle and a phase shift of 120°. The red line corresponds to the fitting of the simulated points. For a better visualization of the lower frequencies' values, the x-axis is plotted in a logarithm scale.

Configuration 3:

Finally, the third configuration corresponds to a duty cycle of 0.75 and a phase shift of 90°, represented in Figure 5.7(c). In this case the frequencies highlighted are 1 and 2 Hz. The frequency of 1 Hz leads to a flow rate of 5.57 μL/min, while for 2 Hz the flow rate obtained is 7.62 μL/min. The linear fitting leads to the equation $Q_3 = 6.7765f - 19.724$ and a coefficient of determination $R^2 = 0.9973$. Data are presented in Figure 5.12.

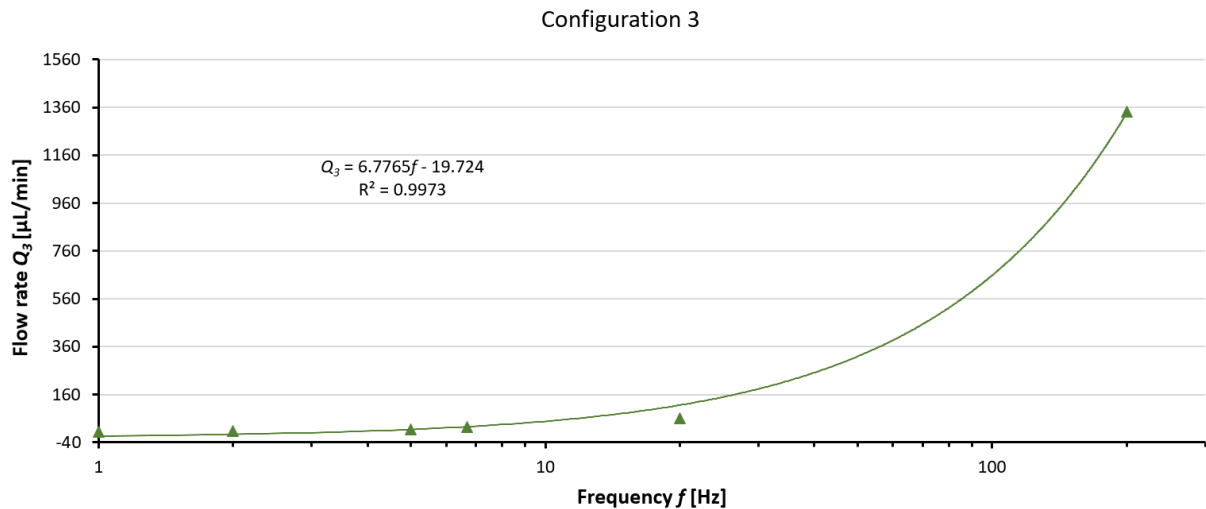


Figure 5.12: Values of volumetric flow rate at different frequencies for the configuration 3 or with 3/4 duty cycle and a phase shift of 90°. The green line corresponds to the fitting of the simulated points. For a better visualization of the lower frequencies' values, the x-axis is plotted in a logarithm scale.

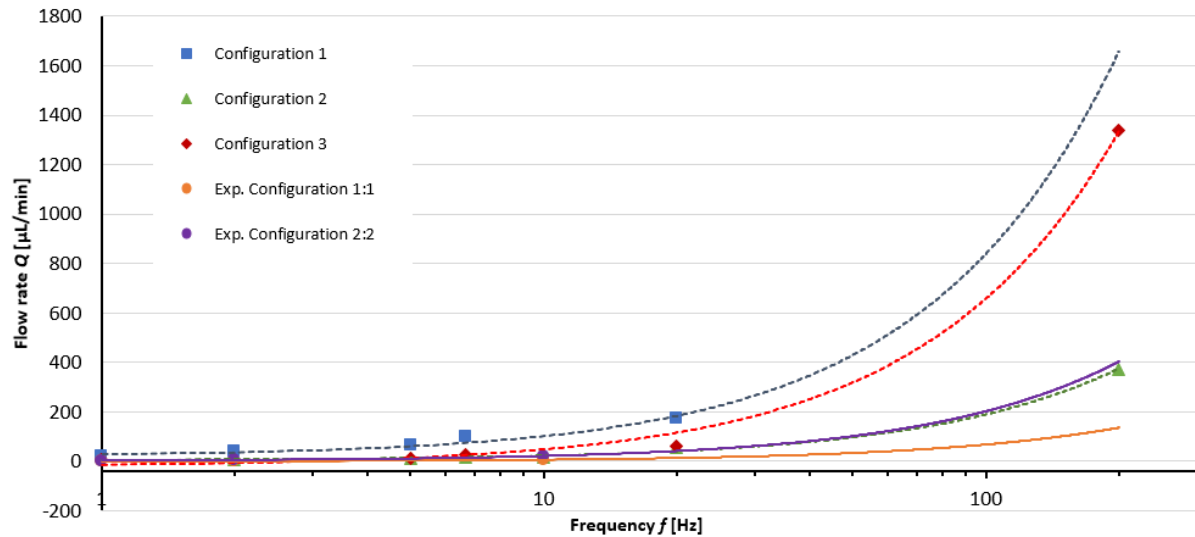
Comparison between simulated-configurations and experimental results

In the previous section, simulations have been performed for three configurations varying duty cycle and phase shift. The simulations have been carried out for four pumping actuators or, in other words, a single inlet, A or B. Within these configurations, different flow rates have been obtained at the same actuation frequency. In this section, not only the simulated configurations are compared, but also the results obtained in the experimental tests of the pumping micromixer shown in section 4.3.1. Here only half of the flow rate obtained by the experimental measurements is considered for a fair comparison between simulation and experimental data.

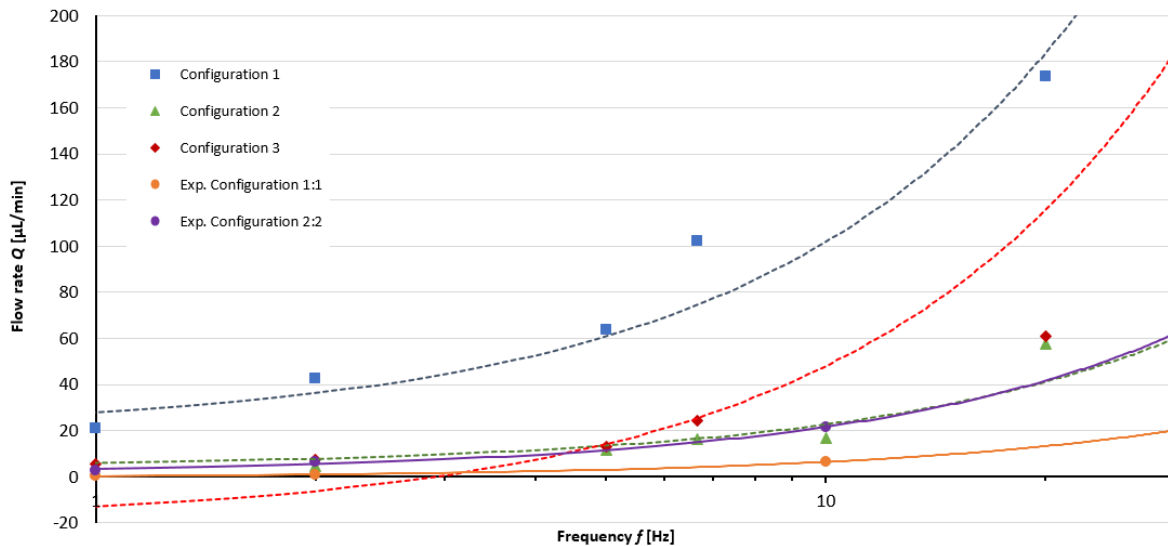
Figure 5.13 presents the data for the flow rate versus frequency for the three tested configurations and the experimental data obtained. Circular points correspond to the experimental results, which are fitted to solid lines, while simulated data are fitted with dashed lines.

In Figure 5.13, Exp. Configuration 1:1 and 2:2 stand for the data obtained with the fabricated pumping micromixer. The conditions of the experimental tests are 0.5 duty cycle and 90° phase shift. More details about these measurements and the measurement set up can be found in section 4.3.1.

Configuration 1 proves to be the best configuration tested in terms of flow rate, followed by configuration 3. Both configurations show a significant difference in flow rate compared to the other configurations tested at the same operating frequency. Configuration 2 and Exp. Configuration 2:2 show a similar behaviour in the tested frequencies, having Exp. Configuration 2:2 a slightly higher flow rate. This can be appreciated in more details in Figure 5.13(b).



(a)



(b)

Figure 5.13: Flow rate versus frequency for the three simulated configurations and for the experimental configurations 1:1 and 2:2. Frequency range: (a) From 1 Hz to 200 Hz and (b) from 1 Hz to 30 Hz (for a better visualization of the lower frequencies).

Table 5.7 includes the values of 1, 2 and 10 Hz for all simulated configurations, i.e. 0, 1, 2 and 3. These frequencies coincide with those measured experimentally. Moreover, a frequency of 200 Hz has also been simulated for configurations 1, 2 and 3. A frequency close to 200 Hz has been reported in the literature as the resonance frequency for some 50 μm thick EAP actuators and has therefore been chosen here as a reference [215].

In the simulations, it is remarkable how varying the phase shift and duty cycle at the same frequency results in a large difference in fluid flow in the same device. For example, for a frequency of 1 Hz, configuration 2 provides the lowest flow rate, 3.04 $\mu\text{L}/\text{min}$, while configuration 1 provides the highest, 21.25 $\mu\text{L}/\text{min}$, resulting in a flow rate 7 times higher. For a longer lifetime of the EAP

actuators, low frequencies are recommended. Hence, for the same flow rate, a lower actuation frequency is recommended and therefore configuration 1 is the most suitable for use in this system.

Table 5.7: Summary of the main results obtained in simulations in terms of flow rate for each configuration. Frequencies of 1,2,10 and 200 Hz have been chosen.

Configuration	Phase shift	Duty cycle	Frequency (Hz)	Flow rate ($\mu\text{L}/\text{min}$)
Exp. 1:1 [#]	90°	0.5	1	0.27
			2	1.05
			10	6.45
Exp. 2:2 [#]	90°	0.5	1	1.35
			2	3.23
			10	10.75
0	90°	0.5	1	18.86
			2	29.20
			10	103.65
1	45°	0.5	1	21.25
			2	42.40
			10	101.83
			200	1659.09
2	120°	2/3	1	3.04
			2	4.54
			10	16.83
			200	373.72
3	90°	0.75	1	5.57
			2	7.62
			10	48.04
			200	1340.92

Half of the values obtained by the experimental measurements are displayed here.

The highest simulated flow rate here corresponds to 1659.09 $\mu\text{L}/\text{min}$ (1.66 mL/min). It is obtained for configuration 1 at 200 Hz. As mentioned above, this frequency is simulated to estimate the flow rate that could be obtained near the resonance frequency of the material. In these simulations, the deformation of the stacked actuators is only considered as obtained in the experimental measurements for a frequency of 1 Hz. At the resonance frequency, the EAP actuators undergo an enormous deformation which would obviously lead to a huge change of the channel volume and thus to an extremely high fluid flow. However, at high frequencies, the lifetime of the actuators considerably decreases, leading to early breakdown of the devices. These simulations illustrate the potential of the pumping micromixer in terms of flow rate. More details about the comparison between experimental and simulations are included in the conclusion in section 5.3.

B. Pressure

A relevant parameter regarding peristaltic pumps is the fluid pressure at the outlet. The pressure was also simulated with COMSOL Multiphysics® for the previous configurations and frequencies. The laminar flow module allows the determination of the pressure at any simulating time and in any point, line or section inside the peristaltic pump.

As an example of a pressure profile at the outlet, Figure 5.14 represents the values of the pressure at the pump outlet for the whole outlet area and also at the pump inlet section. Data are taken from configuration 1 with a frequency of 1 Hz, for which a duration of 5 seconds has been simulated.

In Figure 5.14, the changes in the pressure at the inlet and outlet are observed. The pressure here also changes in pulses due to the actuation principle in which the peristaltic system is based. A zero pressure value here corresponds to atmospheric pressure. At each starting of the wave period, it can be observed that the pressure at the inlet is negative, which allows the liquid to flow inside the channel from the exterior of the device. As it can be observed, the peaks of the green line, corresponding to the outlet values, are higher than those of the blue line, which belong to the inlet section. This pressure difference allows the liquid to propagate in a wave form along the inlet channel, and afterwards outside the device.

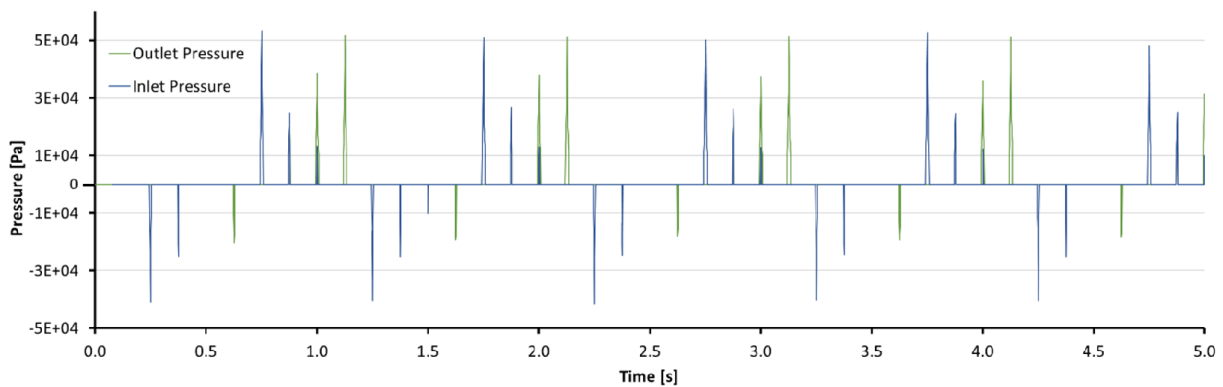


Figure 5.14: COMSOL Multiphysics® simulation of the change of pressure with time at the inlet (in blue) and at the outlet (in green) of the peristaltic pump. Configuration 1 at 1 Hz is here shown as an example. A zero pressure value here corresponds to atmospheric pressure.

Although there are pressure fluctuations at the outlet due to the actuators activation and deactivation, it is possible to estimate the backpressure of the system considering the maximum pressure at the outlet, ΔP_{max} , and the maximum flow rate, Q_{max} , obtained when the pump is used without any exit fluidic resistance. The maximum flow rate for each configuration is the one calculated in the previous simulations. The flow rate Q is obtained as a function of the backpressure ΔP_{back} using the following expression:

$$Q = Q_{max} \frac{\Delta P_{max} - \Delta P_{back}}{\Delta P_{max}} \quad \text{Eq 5.5}$$

where Q_{max} and ΔP_{max} are data directly obtained from the software simulations. It is then possible to obtain a linear dependency between the flow rate and the backpressure for the system. The expression corresponds to a linear drop of the fluid flow at the outlet with the back pressure.

For all the configurations, the maximum pressure at the outlet was also simulated leading to the same tendencies as that for the flow rate. Configuration 1, followed by configuration 3, presents the highest pressure at the outlet and configuration 2 provides the minimal pressure. The maximal pressure is reached at 200 Hz and configuration 1 (200 Hz corresponds to the highest frequency

calculated for this configuration), while the pressure obtained is 99.3 kPa. The lowest maximal pressure at the outlet is 0.41 Pa for the configuration 2 at 1 Hz.

5.3. CONCLUSION

In this chapter, simulations of the actuators displacement versus driving voltage considering half of the peristaltic micromixer are performed. As expected, the highest electric field applied leads to the maximal displacement. The maximal displacement values are: 23 μm , 41.5 μm and 148 μm , for the x , y and z axes, respectively. According to these simulations, the channel inside the micromixer is expanding from 40 μm initial height, to 296 μm corresponding to 148 μm into the positive direction of z and 148 μm into the negative direction of z . The channel is increasing 7.4 times in height with respect to the passive state.

Simulations in COMSOL Multiphysics® predict an increase of 3.65 times more displacement than that experimentally achieved. Assumptions like the lack of actuation passivation due to the Young's modulus of the electrodes or the consideration of the electrical connection of 100 % of the actuator layers in the simulations, cannot be neglected. In the subsequent simulations, the experimentally obtained deformation value is used. This value corresponds to 36.95 μm in the positive direction of z and 36.95 μm in the negative direction of z . The difference between the experimental value and the simulated value is very large. Hence, using the simulated value of deformation would cause the subsequently calculated fluid flow and pressure values to deviate substantially from the experimental values.

To fully characterize the behaviour of the pumping micromixer in terms of fluid dynamics, simulations of the flow rate versus frequency, duty cycle and phase shift are performed in this chapter. Moreover, the pressure at the outlet is under study. Four actuators of the pumping chamber considering their experimental deformation are used for this analysis.

Firstly, frequencies of 2 and 20/3 Hz are chosen to determine the behaviour of the flow rate while the duty cycle is varying. In this case, one actuator will turn on only when the previous actuator achieves the centre of its actuation time.

A parabolic behaviour is observed for the flow rate versus duty cycle for a constant frequency. Parabolas start at duty cycle 0, get their maximum at 0.35 duty cycle and end near 0.70 duty cycle. Pattern replicas for different frequencies are expected, with parabolas with steeper slopes in the case of higher frequencies and lower slopes for smaller frequencies, with similar starting, maximum and ending points for the duty cycle.

To summarize, it has been proven that larger flow rates than experimentally obtained are possible. Three different configurations have been checked, showing that the best configuration is the so-called configuration 1, with 0.5 duty cycle and a phase shift of 45°. This configuration presents a flow rate of 1545 $\mu\text{L}/\text{min}$ or, in other units, 1.545 mL/min at 200 Hz. This high frequency is easily achievable with the EAP technology.

Pressure at the outlet of the channel has also been under study in COMSOL Multiphysics®. The three configurations analysed present a similar behaviour as for the flow rate, due to the linear dependency of the pressure-flow rate. Configurations 1 and 3 present the highest back pressures, while configuration 2 provides the minimal pressure. On one hand, the maximal back pressure is

achieved at 200 Hz and configuration 1 with a peak value of 99.3 kPa. On the other hand, the lowest maximal back pressure (0.41 Pa) is obtained for the configuration 2 at 1 Hz.

As demonstrated, the deviations between simulation and experimental results are quite considerable. To elucidate the discrepancies between the simulations and experimental results, the assumptions and boundary conditions utilized in the simulations are further analysed.

First, the interaction between the solid walls of the actuators and the fluid are under evaluation. In simulations, these movements are mimicked through the use of the Fluid-Structure Interaction module in COMSOL Multiphysics®. Within this module, the resistance that the fluid exerts on the walls of the chambers or actuators when the electric potential is deactivated is included. The fluid must then be displaced according to the force exerted by the actuators when they return to their initial, deactivated position (a 40 µm open channel).

The force exerted on the actuators is evaluated using the Maxwell equation (Eq. 4.1) for dielectric stacked actuators, as described in section 4.1.1. In this analysis, only half of the actuator layers (15 layers) are considered, along with the actuator areas of 1.8 mm² and 4.5 mm² in the pumping and mixing chambers, respectively. The electric potential applied yields a force of 6.455 N and 16.137 N to deform half of the actuators in the pumping and mixing chambers, respectively, which corresponds to a pressure of 358.6 kPa for all half-stacked actuators. The application of electric potential results in the pressure acting on the top and bottom 15 layers, causing deformation of the channel and an expansion of the initial volume of the chambers.

As the initial volume of the chambers expands, there is an increase in the volume available for fluid flow. The increased volume creates a pressure gradient, causing fluid to be drawn into the chambers. Upon deactivation of the electric potential, the actuators - which form the walls of the chambers - return to their initial positions, partially closing the chambers. This closure restricts the available volume for fluid flow, generating a pressure gradient that propels fluid through the micromixer.

In the simulations, the electric field exerts pressure directly on the walls of the chamber. Specifically, a pressure of 358.6 kPa causes the top 15 layers of half-stacked actuators to deform upwards, while the bottom 15 layers deform downwards, resulting in an opening of 36.95 µm in both directions. These values were obtained experimentally for 15 layers of stacked actuators. However, as previously stated in section 4.2.3, the deformation of the full micromixer with 30 layers was 20 times smaller than predicted by the simulations.

In the simulations, it was assumed that the upper half-stacked actuators deform in a toward direction, while the lower half-stacked actuators displace towards the bottom of the micromixer, resulting in a symmetrical aperture of the channel. However, experimental validation of this assumption was not possible, and this could be a contributing factor to the lower fluid flow observed experimentally compared to the simulated flow. Furthermore, experimental data could not determine if the half-stacked actuators could move in both upward and downward directions. If only downward movement occurs, only half of the expected deformation would take place, which results in a significant mismatch between experimental and simulated results.

One potential factor contributing to the discrepancy between simulations and experimental results is the assumption in the simulations of 100% electrically connected layers and using the maximum deformation value observed during experimental analysis. During the experimental analysis of the deformation, it was observed that the degree of deformation varied according to

the applied electric potential, input signal, and frequency. Specifically, a rectangular signal with frequencies of 1 Hz, 2 Hz, and 10 Hz was used as input and the resulting deformations were 36.9 μm , 34.4 μm , and 33.8 μm , respectively. These variations of the deformations with the frequency were not implemented in the simulations.

As previously mentioned, the simulations conducted in this study aim to determine the optimal parameters, such as duty cycle, phase shift, frequency, etc., for the micromixer's operation. At the beginning of the experimental evaluation of the micromixer, there was no available information on the optimal parameters for achieving its optimal performance as a pumping system. Therefore, providing information on the optimal parameters for pumping system operation could be valuable to the scientific community and serve as a guide for future research, not only in the field of electroactive polymer actuators technology, but also for any pumping system that utilizes multiple actuating chambers.

Results show the versatility of the pumping characteristics of such a microdevice, from very few $\mu\text{L}/\text{min}$ until mL/min , and from a very low pressure in the range of Pa to hundreds of kPa, by only changing the actuation mode and the frequency. As stated in section 1.3, for a longer life cycle, it is recommended to have a smaller frequency than a larger one. Therefore, for the same flow rate a lower actuation frequency is recommended.

Comparing the DESA pumping micromixer with those presented in section 3.1.2, the performance of the DESA micromixer produced in this thesis provides higher flow rates and pressures.

Tseng et al. [171] developed a pumping micromixer out of pneumatic actuators. The rotatory pump has a flow rate of 165.7 $\mu\text{L}/\text{min}$ at a driving frequency of 17 Hz. It is not known whether this frequency is the maximum frequency measured by the rotary pump. At this same frequency, if configuration 1 is used in the micromixer, a value of 159.20 $\mu\text{L}/\text{min}$ is obtained by extrapolation using the regression equation in Figure 5.9. Similar values are obtained at this frequency for both devices.

Sheen et al. [172] fabricated a piezoelectric pumping micromixer. The maximum flow rate obtained was 50 $\mu\text{L}/\text{min}$ at 50 V and 2.2 kHz. In this case, although the voltage used is much lower than the 1500 V used for the deformation of the DESA pumping micromixer, the flow rate obtained at 2.2 kHz from the pump is much lower than the maximum obtained by our micromixer at a much lower frequency. At only 3.68 Hz with configuration 3, the same flow rate of 50 $\mu\text{L}/\text{min}$ was obtained using the regression equation in Figure 5.9.

New technologies in the DESA fabrication like 3D printing and the Langmuir-Schaffer method will allow the manufacturing of thinner elastomer and electrode layers, thus, lower voltage will be needed (more details in section 1.6). On the other hand, these technologies will also help in the miniaturization of the mixer proposed here, allowing it to get into a much smaller size and to be more competitive.



6. SUMMARY AND CONCLUSIONS

During the development of this thesis, the technology of Electroactive Polymers is employed to manufacture microfluidic devices. Firstly, prototypes of single-layer Electroactive Polymer peristaltic pumps are manufactured and secondly, a pumping micromixer is fabricated with Dielectric Stacked Actuators.

6.1. MICROPUMP PROTOTYPES

The main principle of the design of the one-layer peristaltic pumps is a single prestressed membrane made of elastomer material; on top and bottom of this membrane, several electrodes are located in series, forming actuators. On the upper electrodes, a channel fabricated out of a softer elastomer material is placed to safely hold a fluid. When actuation occurs, the channel deforms and expands in the same direction as the actuators (the perpendicular direction to the channel length). While actuating the actuators with different phases, the difference of pressure acquired along the channel allows the fluid to flow.

In chapter 2, two different prototypes are designed to fabricate a peristaltic pump. The first prototype, manufactured with the liquid film method and afterwards with the solid film method, is based on an array of three actuators located in series in a prestressed membrane. On top of the electrodes, an elastomeric channel is located. When actuation occurs, the channel deforms together with the actuators, leading to a volume change of the chamber. The pressure difference acquired along the channel is meant to allow the fluid to flow.

Before manufacturing the peristaltic pumps, the optimization of the parameters related to the deformation of the actuators is computed. Parameters like prestretch values in both directions, active ratio and maximal deformation are under study. This helps to understand the largest displacement of the actuators, and thus the largest change in the volume of the channel. The analytical method provides values for the bidirectional prestretch: $\lambda_{1ps} = 0.9$, for prestretch in the actuation direction, and $\lambda_{2ps} = 2.2$, for the perpendicular direction. This is translated into a stretch after actuation of $\lambda_{1a} = 1.24$, i.e., a theoretical deformation of 24 %.

The devices are fabricated according to the analytical methods. The deformation of the actuators is analysed in order to get more information about the system. The experimental values of actuation stretch are $\lambda_{1a} = 1.194$ for the desired direction and $\lambda_{2a} = 1.048$, for the perpendicular direction. A difference of 5 % between theoretical and experimental actuation stretch is observed.

The influence of the actuation of one actuator on the following one is also under study. A great influence is observed, due to the short distance between actuators (1 mm). While the upper actuator is under voltage (19 % deformation), the following actuator without driving voltage is holding a deformation of 14 % due to the influence of the upper one to it. The distance between actuators is then changed to 5.2 mm. This leads to a deformation of 1.4 % of the following actuator when the previous one is actuated.

Thinner dielectric layers (40 μm thickness) and a separation of 5.2 mm between actuators are investigated. The deformation for these actuators is 24 % (as the analytical method predicts). Moreover, an out of plane deformation is also present in these actuators.

After the experimental analysis of the actuator performance, the fluid channel is added to the device to continue with the analysis of the system. The obtained deformation when the channel is on top of the actuators decreases by 9 %. No fluid flow is observed. The bottom layer of the channel is taken out of the system. The deformation is only decreased in 0.1 to 1 %. The fluid to be pumped (DI water with surfactants) is introduced into the system and pumping of the fluid is observed. The liquid flows in the channel. Unfortunately, in all the cases there is a leaking of the DI water through the DEA-membrane (not observable by eye) leading to the electrolysis of water and the generation of H₂ and O₂. The dielectric membranes are systematically getting broken in very short periods of time. It is not possible to do long time measurements of the pump flowing.

The microfluidic system, as designed, is not suitable for pumping liquids due to its short time life attributed to the diffusion of the fluid through the membrane and continuously breakdown of the DEA membrane. This system needs a channel with a bottom layer, only in this case, the DEA membrane is not broken when the fluids are in the channel. Different materials for the fabrication of the channel and the actuators may lead to functional devices.

The prototype is again fabricated with different materials. The dielectric layer or elastomer, the electrodes and the manufacturing method are different (Single-layer peristaltic pump - type 1 solid film, section 2.4). The goal of fabricating this prototype again is to overcome the problems of low deformation when a full channel with top, wall and bottom layer is placed on top of the actuators. Results have proven that the deformation of the actuators with these materials leads to a lower deformation of the channel, resulting in an invalid device for pumping microfluidics, although materials with a theoretical better performance are used.

A second prototype of single layer peristaltic pump is proposed, named single-layer peristaltic pump-type 2 solid film (section 2.5). This device is based on the coupling of two parallel arrays of actuators, where a channel is located in the middle space between the arrays. Unlike the previous prototype where the channel width expands when the EAPs are active, herein the channel width contracts when the actuators are active, decreasing the total volume of the channel.

For this prototype the analytical modelling of the deformation leads to an actuation stretch of $\lambda_{1a} = 1.11$ at 168 V/ μm . The experimental results show a stretch upon actuation of $\lambda_{1a} = 1.09$ at 168 V/ μm . Including the channel in the design does not passivate much the deformation of the actuators. Without the channel, a deformation of 8.12 % is obtained, while adding the channel provides a deformation of 7.97 %. A channel with 1 mm width deforms 1/3 its width. Video recording the actuation proves that the top layer of the channel wrinkles and moves down and gets inserted inside the channel. No pumping liquid is observed with only 1/3 of channel deformation.

None of the prototypes using these configurations succeeds in pumping fluids. The microfluidic devices though can hold fluids inside an elastomeric, biocompatible channel and stretch this channel and compress with a maximal deformation of 33 % for a 1 mm channel width. The deformation is controlled with the voltage applied. For this reason, a deformation between 0 % and 33 % of a fluid in a direction is possible. Some of the most relevant properties of these microfluidic devices are: biocompatibility of the channel (PDMS); the channel can be easily detached/attached (very helpful for changing samples); transparency in some areas; the channel can be fully closed; the device deforms a channel almost 14 % unidirectionally for the first prototype and 33 % for the second prototype; possibility to increase the number of actuators to hold more samples.

Here, a different application for the fabricated devices is proposed: the use of the devices in chapter 2 as cell stretchers. Researchers have already used DEAs in the field of cell stretching [78][107][181].

In the human body, cells are continuously submitted to complex mechanical forces. The study of the influence of these deformations on certain biological functions of the cells are now being further studied due to its importance in biological functions like cells proliferation or gene expression. The response of cells to mechanical stimuli is important in a great amount of diseases such as lung and cardiovascular diseases and certain types of cancer. Depending on the location in the body of the human cells, the deformation varies in frequency and stretch amount. For example, in the blood vessel walls cells are stretched once per second [182], for a few seconds in the lungs, and for several minutes in the bladder and the intestine, where they do not remain stretched [183]. Therefore, a device able to apply a different stretch to the same kind of sample is advantageous since it allows to explore and study the cell viability with same external conditions, such as temperature, surrounding materials and medium conditions but submitted to different stretches.

The difference in this case is that the fluids are hold in a channel, contrary to that already used where the cells are deposited directly on top of an elastomeric layer on top of the actuators, without a cover to protect the fluids.

The prototypes fabricated in this thesis can be used for this purpose, moreover as the influence on the deformation of one actuator over the following one has also been studied with the distance. Not only one channel and stretch are possible for one device, several deformation sequences are possible in the prototypes described here. The channel fabrication method allows the fabrication of three different inlets and outlets to introduce different probes to measure this deformation. Due to the versatility of the channel fabrication, that is possible with one single device, introducing several different types of channel for diverse measurements. For example, a reference probe in the middle without stretching and two probes in upper and bottom electrode to study different deformations with time. As explained in section 1.3, the lifetime of EAP is very high, lasting over hundred thousand cycles of actuation. This allows plenty of cycles, considering there is no need for very high frequency deformation of cells.

Both prototypes can be used for the investigation of the mechanoresponsive behaviour of diverse cells of the human body at the same time in uniaxial and biaxial cases. The study of the influence of the deformation of cells in the proposed devices is out of the scope of this thesis.

6.2. PUMPING MICROMIXER

The technology of dielectric elastomer stacked actuator is employed to fabricate a pumping micromixer. This micromixer is not only able to mix two solutions, but also to pump in and out the resulting mixture.

For applications such as drug delivery of substances and reagents for chemical analysis, pumping micromixers are preferred as they simplify the parts needed for the mixing, where neither external valves nor pumps are required and the increase of the mixing quality is achieved. The micromixers are often active micromixers, or in other words, their working principle is not only based in the diffusion of the molecules, but an external energy is applied to them to enhance the mixing

capability, decreasing the time needed for a better mixing and often increasing the reaction efficiency, as very low laminar regimes are expected for these devices.

The fabricated pumping micromixer is based on peristalsis movements of its walls, avoiding the contact with external parts like in the rotatory pumps, which may contaminate the samples. Peristalsis involves an actuation principle where energy is transferred from the periodic motion of the walls to a fluid volume. It is the common transport phenomenon in the human body due to the gentle treatment to the samples. Therefore, it is very interesting to use in biological samples where the stress in cells may cause the death or their unusual behaviour. Moreover, DESA micromixers are also of interest in the analysis of chemical, biological and medical samples, due to the biocompatibility [163] [138] of the used materials (PDMS and graphite).

The pumping micromixer is composed of three chambers with 4 stacked actuators each. Two chambers are the so-called pumping chambers, in which fluids A and B are pumped into the system separately. The third chamber is known as the mixing chamber, where the fluids A and B are mixed and pumped out the device. Each stacked actuator consists of 30 single DEA layers.

The fabrication technique employed for the processing of the micromixer is based on the well-known automatic stacked actuator fabrication in TU-Darmstadt based on: mixing of the PDMS Elastosil® P7670 component A and B, ratio 1:1; spin coating of the mixed solution at different speeds in order to obtain a homogeneous film; curing of the PDMS at 80 °C during 2 minutes; and electrode deposition by spraying graphite powder over a shadow mask with the desired shape. The entire manufacturing process described is designed for an elastomeric disc of 40 mm diameter. The fabrication of one full pumping micromixer device takes approximately 3 hours with this automatic procedure.

The pumping micromixer is then characterised. First, the thickness of the dielectric layers to ensure the efficiency of the manufacturing method. Then, the electrical connections or number of layers connected. Finally, the deformation of the actuators with respect to voltage and input signal. The rectangular signal is chosen for the actuation of the micromixer, due to its larger deformation. When the actuators are driven with a rectangular signal of 1 Hz at 1500 V, the channel gap increases from 40 µm (initially open due to the manufacturing process) to 113.9 µm, which represents an increase of approximately 200 %. When no voltage is applied, the actuators return to the passive state, partially closing the channel.

The pumping abilities of the device are under study at different frequencies (1, 2 and 10 Hz) at 1500 V (which provides the maximal electric field shortly lower than the electric breakdown of the elastomer), displaying a maximal flow rate of 21.5 µL/min at 10 Hz.

The mixing in the micromixer is then analysed by means of digital imaging. At 10 Hz and 1500 V, the actuators are deforming and two different colorants are pumped in, mixed and pumped out by the action of the pumping micromixer. Images at the outlet are captured and analysed using MATLAB. Pixel analysis proves a 50 % mixing when all actuators are actuating at the same pace and voltage.

New technologies in the DESA fabrication, like 3D printing and the Langmuir-Schaffer method, will allow the manufacturing of thinner elastomer and electrode layers. Therefore, lower voltages will be needed, in contrast to the 1500 V needed to actuate the pumping micromixer. On the other hand, these technologies will also help in the miniaturization of the mixer proposed here, allowing it to get into a much smaller size and to be more competitive. In chapter 4, new prototypes for the

fabrication of pumping micromixers with different geometries but the same working principle are proposed.

In this thesis, the first steps towards the fabrication of microfluidic devices with EAPs are exposed. It is demonstrated that it is possible to fabricate microfluidic devices capable of pumping in, mixing and pumping out two different fluids. Due to problems with the automatic fabrication process of these devices and the overall time of this research, it has not been possible to perform further characterisation and analysis of the devices. Analysis at a wider range of frequencies, with different configurations of duty cycle, phase shift, and different frequencies in pumping chambers 1 and 2, to obtain a different degree of mixing, are of interest in this research. To provide more information about the properties of the micromixer, complex electromechanical and fluid dynamic simulations are carried out with the simulation software COMSOL Multiphysics®.

In chapter 5, various simulations of the pumping micromixer are developed. Firstly, the deformation versus applied voltage of the actuators, only considering the half of the micromixer. The solid mechanics module coupled with the electric module is used. The maximal applied voltage, 1500 V, provides a displacement for half of a micromixer of: 23 μm , 41.5 μm and 148 μm , for the x, y and z axes, respectively. In the passive state of the actuators, the open channel of the micromixer has a height of 40 μm . Simulations prove a change in height of 7.4 times when the actuators are active. Experimental characterizations are 3.65 times lower than that predicted with the simulations. Assumptions like the lack of actuation passivation due to the young modulus of the electrodes or the consideration of the electrical connection of 100 % of the actuator layers in the simulations, cannot be negligible. For the following fluid dynamic simulations, the experimental values are used.

After the electromechanical characterization of half a micromixer, the fluid dynamic analysis is performed. To simplify simulations, the equivalent diameters of the channel in active and passive state are calculated. A 2D axisymmetric model is used considering only the four actuators of one pumping chamber.

The first fluid dynamic simulation is performed with the so-called configuration 0, at constant frequencies (2 Hz and 20/3 Hz), 90° phase shift and multiple duty cycles from 0.25 until 0.67. A parabolic behaviour is observed for the flow rate versus duty cycle for a constant frequency. The maximum of the parabola or flow rate is at about 0.35 duty cycle and end near 0.70 duty cycle. Errors in simulations are obtained at higher duty cycles. Pattern replicas for different frequencies are expected, with parabolas with steeper slopes in the case of higher frequencies and lower slopes for smaller frequencies and similar starting, maximum and ending points for the duty cycle.

Three other configurations for constant phase shift, constant duty cycle and varying frequencies are under study. Configuration 1 with 0.5 duty cycle and a phase shift of 45° proved to be the best configuration in terms of flow rate between the tested ones. This configuration presents a flow rate of 1545 $\mu\text{L}/\text{min}$ or, in other units, 1.545 mL/min at 200 Hz. This high frequency is easily achievable with the EAP technology. It has been proven that larger flow rates than that experimentally obtained are possible with this device.

Not only the flow rate is under study, but also the pressure at the outlet of the channel. The linear dependency of the flow rate with the pressure derives in a similar performance for the pressure at the outlet. Configuration 1 also presents the highest back pressure with a value of 99.3 kPa at 200 Hz.

From the simulation records, it can be concluded that the pumping micromixer presents a high versatility. Flow rates from very few $\mu\text{L}/\text{min}$ to mL/min and from a very low pressure in the range of Pa to hundreds of kPa are possible by only changing the actuation mode and the frequency, deriving in a changing a couple of magnitude orders for a single device. If high precision at low flow rate is needed only by changing to configuration 2, it is possible to vary flow rate in smaller steps by changing frequency. On the other hand, as stated in section 1.3, for a longer life cycle, it is recommended to have a relatively low frequency, so for the same flow rate a lower actuation frequency is recommended, i.e., a more efficient configuration.

The comparison of the values of the DESA pumping micromixer, in terms of flow rate and pressure, with other previously fabricated pumping micromixers with other technologies such as pneumatic actuators or piezoelectric devices, showed the higher performance of the DESA pumping micromixer obtained with the COMSOL Multiphysics® simulations.

Due to the working principle in which the pumping micromixer is based, motion of actuators leading to a propagation wave, the pumping micromixer is able to move fluids forwards or backwards, or in other words, in two directions. The device can be used in two different ways: 1) two-single entrances leading to a unique outlet, working as a micromixer or a unification system; and 2) a unique entrance which is leading to two single outlets, commonly known as a fluid splitter, if the fluid is pumped backwards. By only changing the actuation order, this system can also work as a fluid splitter, obviously losing its mixing capability.



REFERENCES

- [1] R. E. Pelrine, R. D. Kornbluh, and J. P. Joseph, "Electrostriction of polymer dielectrics with compliant electrodes as a means of actuation.," vol. 4247, no. 97, pp. 77–85, 1998.
- [2] R. D. Kornbluh, R. E. Pelrine, and J. P. Joseph, "Elastomeric dielectric artificial muscle actuators for small robots," in *Proceedings of the 3rd IASTED International Conference on Robotics and Manufacturing*, 1995, pp. 1–6.
- [3] R. E. Pelrine, J. Eckerle, and S. Chiba, "Review of artificial muscle approaches," in *Proceedings of the 3rd International Symposium on Micro Machine and Human Science*, 1992, pp. 1–19.
- [4] P. Lochmatter and G. Kovacs, "Concept study on active shells driven by soft dielectric EAP," in *Proceedings of SPIE - Electroactive Polymer Actuators and Devices (EAPAD)*, 2007.
- [5] M. Matysek, P. Lotz, and H. F. Schlaak, "Development of Multilayer Dielectric Elastomer Actuators," in *Annex of the Conference proceedings: Actuator 2008, 11th International Conference on New Actuators and 5th International Exhibition on Smart Actuators and Drive Systems*, 2008.
- [6] A. Poulin, S. Rosset, and H. R. Shea, "Pad printing 1-10 mm thick elastomer membranes for DEAs," in *EuroEAP 2015 - Fifth International Conference on Electromechanically Active Polymer (EAP) Transducers & Artificial Muscles*, 2015.
- [7] O. A. Araromi, S. Rosset, and H. R. Shea, "High-resolution, large-area fabrication of compliant electrodes via laser ablation for robust, stretchable Dielectric Elastomer Actuators and sensors," *ACS Appl. Mater. Interfaces*, vol. 7, no. 32, pp. 18046–18053, 2015.
- [8] F. M. Weiss, T. Töpfer, B. Osmani, S. Peters, G. Kovacs, and B. Müller, "Electrospraying Nanometer-Thin Elastomer Films for Low-Voltage Dielectric Actuators," *Adv. Electron. Mater.*, vol. 2, no. 5, p. 1500476, 2016.
- [9] S. Hau, A. York, and S. Seelecke, "High-Force Dielectric Electroactive Polymer (DEAP) Membrane Actuator," in *Proceedings of SPIE - Electroactive Polymer Actuators and Devices (EAPAD)*, 2016.
- [10] O. A. Araromi *et al.*, "Optimization of thin-film highly-compliant elastomer sensors for contractility measurement of muscle cells," *Extrem. Mech. Lett.*, vol. 9, pp. 1–10, 2016.
- [11] R. Pelrine *et al.*, "Dielectric Elastomer Artificial Muscle Actuators : Toward Biomimetic Motion," in *Proceedings of SPIE - Electroactive Polymer Actuators and Devices (EAPAD)*, 2002, vol. 4695, pp. 126–137.

-
- [12] R. D. Kornbluh and R. E. Pelrine, "High-Performance Acrylic and Silicone Elastomers. Dielectric Elastomers as Electromechanical Transducers.," in *Dielectric Elastomers as Electromechanical Transducers*, 2008, pp. 33–42.
- [13] B. Kussmaul *et al.*, "New DEA materials by organic modification of silicone and polyurethane networks," in *Proceedings of SPIE - Electroactive Polymer Actuators and Devices (EAPAD)*, 2013, vol. 8687, pp. 750–757.
- [14] C. Renard, D. Wang, Y. Yang, S. Xiong, C.-Y. Shi, and Z.-M. Dang, "Plasticized thermoplastic polyurethanes for dielectric elastomers with improved electromechanical actuation," *J. Appl. Polym. Sci.*, vol. 134, no. 30, p. 45123, 2017.
- [15] G. Ştiubianu, A. Soroceanu, C. D. Varganici, C. Tugui, and M. Cazacu, "Dielectric elastomers based on silicones filled with transitional metal complexes," *Compos. Part B Eng.*, 2016.
- [16] L. Yu and A. L. Skov, "Silicone rubbers for dielectric elastomers with improved dielectric and mechanical properties as a result of substituting silica with titanium dioxide," *Int. J. Smart Nano Mater.*, vol. 6, no. 4, pp. 268–289, 2015.
- [17] G. Gallone, F. Carpi, D. De Rossi, G. Levita, and A. Marchetti, "Dielectric constant enhancement in a silicone elastomer filled with lead magnesium niobate-lead titanate," *Mater. Sci. Eng. C*, vol. 27, no. 1, pp. 110–116, 2007.
- [18] P. Mazurek, L. Yu, R. Gerhard, W. Wirges, and A. L. Skov, "Glycerol as high-permittivity liquid filler in dielectric silicone elastomers," *J. Appl. Polym. Sci.*, vol. 133, no. 43, p. 28, 2016.
- [19] F. B. Madsen, L. Yu, A. E. Daugaard, S. Hvilsted, and A. L. Skov, "Silicone elastomers with high dielectric permittivity and high dielectric breakdown strength based on dipolar copolymers," *Polymer (Guildf.)*, vol. 55, no. 24, pp. 6212–6219, 2014.
- [20] C. Tugui, S. Vlad, M. Iacob, C. D. Varganici, L. Pricop, and M. Cazacu, "Interpenetrating poly(urethane-urea)-polydimethylsiloxane networks designed as active elements in electromechanical transducers," *Polym. Chem.*, vol. 7, no. 15, pp. 2709–2719, 2016.
- [21] A. H. A. Razak, P. Szabo, and A. L. Skov, "Enhancement of dielectric permittivity by incorporating PDMS-PEG multiblock copolymers in silicone elastomers," *RSC Adv.*, vol. 5, no. 65, pp. 53054–53062, 2015.
- [22] A. H. A. Razak and A. L. Skov, "Silicone elastomers with covalently incorporated aromatic voltage stabilisers," *RSC Adv.*, vol. 7, no. 1, pp. 468–477, 2017.
- [23] A. Shakun, M. Poikelispää, A. Das, and J. Vuorinen, "Improved electromechanical response in acrylic rubber by different carbon-based fillers," *Polym. Eng. Sci.*, vol. 58, pp. 395–404, 2018.
- [24] G. Kofod and P. Sommer-larsen, "Silicone dielectric elastomer actuators: Finite-elasticity model of actuation," *Sensors Actuators, A Phys.*, vol. 122, pp. 273–283, 2005.

-
- [25] J. Bonet and R. D. Wood, *Nonlinear Continuum Mechanics for Finite Element Analysis*, 2nd ed. Cambridge University Press, 2008.
- [26] M. Mooney, "A theory of large elastic deformation," *J. Appl. Phys.*, vol. 11, no. 9, pp. 582–592, 1940.
- [27] R. S. Rivlin, "Large Elastic Deformations of Isotropic Materials. IV. Further Developments of the General Theory," *Philos. Trans. R. Soc. A Math. Phys. Eng. Sci.*, vol. 241, no. 835, pp. 379–397, 1948.
- [28] A. N. Gent, "A new constitutive relation for rubber," *Rubber Chem. Technol.*, vol. 69, no. 1, pp. 59–61, 1996.
- [29] P. Lotz, M. Matysek, and H. F. Schlaak, "Fabrication and application of miniaturized dielectric elastomer stack actuators," *IEEE/ASME Trans. Mechatronics*, vol. 16, no. 1, pp. 58–66, 2011.
- [30] O. A. Araromi, A. T. Conn, C. S. Ling, S. C. Burgess, and R. Vaidyanathan, "A novel fabrication set-up for the flexible production of silicone based EAP 'artificial muscle' actuators," *WIT Trans. Ecol. Environ.*, vol. 138, pp. 289–300, 2010.
- [31] F. Carpi, P. Chiarelli, A. Mazzoldi, and D. De Rossi, "Electromechanical characterisation of dielectric elastomer planar actuators: comparative evaluation of different electrode materials and different counterloads," *Sensors Actuators A Phys.*, vol. 107, pp. 85–95, 2003.
- [32] M. Kujawski, J. Pearse, and E. Smela, "PDMS/graphite stretchable electrodes for dielectric elastomer - Technische Informationsbibliothek (TIB)," in *Proceedings of SPIE - Electroactive Polymer Actuators and Devices (EAPAD)*, 2010, p. 9.
- [33] S. Kirkpatrick, "Percolation and Conduction," *Rev. Mod. Phys.*, vol. 45, no. 4, pp. 574–588, 1973.
- [34] C. Brosseau *et al.*, "Dielectric and microstructure properties of polymer carbon black composites," *J. Appl. Phys.*, vol. 81, no. 2, pp. 882–891, 1997.
- [35] Q. H. Zhang and D. J. Chen, "Percolation threshold and morphology of composites of conducting carbon black/polypropylene/EVA," *J. Mater. Sci.*, vol. 39, no. 5, pp. 1751–1757, 2004.
- [36] M. Benslimane, P. Gravesen, and P. Sommer-Larsen, "Mechanical properties of dielectric elastomer actuators with smart metallic compliant electrodes," in *Proceedings of SPIE - Electroactive Polymer Actuators and Devices (EAPAD)*, 2002, vol. 4695, pp. 150–157.
- [37] P. Dubois *et al.*, "Microactuators based on ion-implanted dielectric Electroactive Polymer Membranes (EAP)," in *Digest of Technical Papers - International Conference on Solid State Sensors and Actuators and Microsystems, TRANSDUCERS '05*, 2005, vol. 2, pp. 2048–2051.

-
- [38] S. Rosset, M. Niklaus, P. Dubois, and H. R. Shea, "Metal Ion Implantation for the Fabrication of Stretchable Electrodes on Elastomers," *Adv. Funct. Mater.*, vol. 19, no. 3, pp. 470–478, 2009.
- [39] F. Habrard, J. Patscheider, and G. Kovacs, "Stretchable metallic electrodes for electroactive polymer actuators," *Adv. Eng. Mater.*, vol. 16, no. 9, pp. 1133–1139, 2014.
- [40] K. C. Kao, *Dielectric Phenomena in Solids*. Elsevier Inc., 2004.
- [41] K. C. Kao, "New theory of electrical discharge and breakdown in low-mobility condensed insulators," *J. Appl. Phys.*, vol. 55, no. 3, pp. 752–755, 1984.
- [42] S. B. Zakaria, P. H. F. Morshuis, M. Y. Benslimane, K. V. Gernaey, and A. L. Skov, "The Electrical Breakdown of Thin Dielectric Elastomers: Thermal Effects," in *Proceedings of SPIE - Electroactive Polymer Actuators and Devices (EAPAD)*, 2014, p. 11.
- [43] M. Matysek, P. Lotz, and H. F. Schlaak, "Lifetime Investigation of Dielectric Elastomer Stack Actuators," *IEEE Trans. Dielectr. Electr. Insul.*, vol. 18, no. 1, pp. 89–96, 2011.
- [44] M. Zhang, I. Denes, Y. Xue, and M. R. Buchmeiser, "Ageing of Silicone-Based Dielectric Elastomers Prepared with Varying Stoichiometric Imbalance: Changes in Network Structure, Mechanical, and Electrical Properties," *Macromol. Chem. Phys.*, vol. 217, no. 15, pp. 1729–1736, 2016.
- [45] S. Rosset, C. De Saint-Aubin, A. Poulin, and H. R. Shea, "Assessing the degradation of compliant electrodes for soft actuators," *Rev. Sci. Instrum.*, vol. 88, no. 10, 2017.
- [46] A. O'Halloran, F. O'Malley, and P. McHugh, "A review on dielectric elastomer actuators, technology, applications, and challenges," *J. Appl. Phys.*, vol. 104, no. 7, 2008.
- [47] R. E. Pelrine, R. D. Kornbluh, Q. Pei, and J. P. Joseph, "High-Speed Electrically Actuated Elastomers with Strain Greater Than 100 %," *Science (80-.)*, vol. 287, no. 5454, pp. 836–839, 2000.
- [48] B. R. Pelrine and R. Kornbluh, "High-Strain Actuator Materials Based on Dielectric Elastomers," no. 16, pp. 1223–1225, 2000.
- [49] S. Rosset, P. Dubois, M. Niklaus, and H. R. Shea, "Large Stroke Miniaturized Dielectric Elastomer Actuators," pp. 2401–2404, 2009.
- [50] S. Hau and S. Seelecke, "Silicone based dielectric elastomer strip actuators coupled with non-linear biasing elements for large actuation strains," *EuroEAP 2017, Int. Conf. Electromechanically Act. Polym. Transducers Artif. Muscles*, vol. 22, no. June, p. 2017, 2017.
- [51] J. Eckerle, R. Schmidt, and T. Low, "Biologically inspired hexapedal robot using field-effect electroactive elastomer artificial muscles," no. June, 2001.
- [52] Q. Pei, M. Rosenthal, R. Pelrine, S. Stanford, and R. Kornbluh, "Multifunctional

-
- electroelastomer roll actuators and their application for biomimetic walking robots.”
- [53] M. Moscardo, X. Zhao, Z. Suo, and Y. Lapusta, “On designing dielectric elastomer actuators,” *J. Appl. Phys.*, vol. 104, no. 9, 2008.
- [54] Y. Bar-Cohen, “Biomimetic Actuators using Electroactive Polymers (EAP) as Artificial Muscles,” *J. Adv. Mater.*, 2006.
- [55] S. C. Burgess, C. S. Ling, A. Conn, S. Araromi, J. Wang, and R. Vaidyanathan, “Development of a novel Electro Active Polymer (EAP) actuator for driving the wings of flapping micro air vehicle,” *WIT Trans. Built Environ.*, vol. 106, no. May, pp. 207–217, 2009.
- [56] X. Ji *et al.*, “An autonomous untethered fast soft robotic insect driven by low-voltage dielectric elastomer actuators,” *Sci. Robot.*, vol. 4, no. 37, Dec. 2019.
- [57] E.-F. M. Henke, S. Schlatter, and I. A. Anderson, “Soft Dielectric Elastomer Oscillators Driving Bioinspired Robots,” *Soft Robot.*, vol. 4, no. 4, pp. 353–366, Dec. 2017.
- [58] J. Shintake, V. Cacucciolo, H. Shea, and D. Floreano, “Soft biomimetic fish robot made of dielectric elastomer actuators,” *Soft Robot.*, vol. 5, no. 4, pp. 466–474, Aug. 2018.
- [59] H. Godaba, J. Li, Y. Wang, and J. Zhu, “A Soft Jellyfish Robot Driven by a Dielectric Elastomer Actuator,” *IEEE Robot. Autom. Lett.*, vol. 1, no. 2, pp. 624–631, Jan. 2016.
- [60] J. Heim, R. E. Pelrine, R. D. Kornbluh, and J. S. Eckerle, “Electroactive polymer rotary clutch motors,” US6806621B2.
- [61] I. A. Anderson *et al.*, “A thin membrane artificial muscle rotary motor,” *Appl. Phys. A Mater. Sci. Process.*, vol. 98, no. 1, pp. 75–83, Jan. 2010.
- [62] F. Klug, S. Solano-Arana, H. Mößinger, F. Förster-Zügel, and H. F. Schlaak, “Fabrication of dielectric elastomer stack transducers (DEST) by liquid deposition modeling,” *Electroact. Polym. Actuators Devices 2017 10163 101632Q*, vol. 10163, p. 101632Q, 2017.
- [63] Y. Bar-Cohen, “Electroactive polymers for refreshable Braille displays,” *SPIE Newsroom*, 2009.
- [64] R. Heydt, R. Pelrine, J. Joseph, J. Eckerle, and R. Kornbluh, “Acoustical performance of an electrostrictive polymer film loudspeaker,” *J. Acoust. Soc. Am.*, vol. 107, no. 2, pp. 833–839, 2000.
- [65] F. Klug, C. Endl, S. Solano-Arana, and H. F. Schlaak, “Design, fabrication, and customized driving of dielectric loudspeaker arrays,” in *SPIE-Intl Soc Optical Eng*, 2019, p. 73.
- [66] L. Maffli, S. Rosset, M. Ghilardi, F. Carpi, and H. Shea, “Ultrafast all-polymer electrically tunable silicone lenses,” *Adv. Funct. Mater.*, vol. 25, no. 11, pp. 1656–1665, 2015.

-
- [67] "Sensors." [Online]. Available: <https://stretchsense.com/sensors/>. [Accessed: 03-Feb-2020].
- [68] R. D. Kornbluh *et al.*, "Dielectric elastomers: Stretching the capabilities of energy harvesting," *MRS Bull.*, vol. 37, no. 3, pp. 246–253, Mar. 2012.
- [69] J. Maas and C. Graf, "Dielectric elastomers for hydro power harvesting," *Smart Mater. Struct.*, vol. 21, no. 6, 2012.
- [70] C. Graf, J. Maas, and D. Schapeler, "Energy harvesting cycles based on electro active polymers," in *Electroactive Polymer Actuators and Devices (EAPAD) 2010 (2010) 7642 764217*, 2010, p. 764217.
- [71] C. Graf *et al.*, "Dielectric elastomer-based energy harvesting: Material, generator design, and optimization," *J. Intell. Mater. Syst. Struct.*, vol. 25, no. 8, pp. 951–966, 2014.
- [72] "The S3 Wave Energy Converter represents a Paradigm Shift to reinvent Wave Energy Conversion," 2019. [Online]. Available: https://www.sbmoffshore.com/wp-content/uploads/2019/11/SBM-Offshore_Technology_Wave-Energy-Converter.pdf. [Accessed: 03-Feb-2020].
- [73] A. Poulin, S. Rosset, and H. R. Shea, "Printing low-voltage dielectric elastomer actuators," *Appl. Phys. Lett.*, vol. 107, no. 24, 2015.
- [74] H. F. Matysek, M., Lotz, P., Flittner, K. and Schlaak, "High Performance Dielectric Elastomer Stack Actuators: Low Voltage and High Bandwidth," in *ACTUATOR 2010, 12th International Conference on New Actuators*, 2010, no. June, pp. 14–16.
- [75] T. Töpfer, F. Weiss, B. Osmani, C. Bippes, V. Leung, and B. Müller, "Siloxane-based thin films for biomimetic low-voltage dielectric actuators," *Sensors Actuators A Phys.*, vol. 233, pp. 32–41, Sep. 2015.
- [76] X. Ji *et al.*, "Stretchable composite monolayer electrodes for low voltage dielectric elastomer actuators," *Sensors Actuators, B Chem.*, vol. 261, pp. 135–143, 2018.
- [77] A. Mata and A. J. Fleischman, "Characterization of Polydimethylsiloxane (PDMS) Properties for Biomedical Micro / Nanosystems," vol. 2, pp. 281–293, 2005.
- [78] A. Poulin *et al.*, "An ultra-fast mechanically active cell culture substrate," *Sci. Rep.*, vol. 8, no. 1, pp. 1–10, 2018.
- [79] J. Costa *et al.*, "Bioreactor With Electrically Deformable Curved Membranes for Mechanical Stimulation of Cell Cultures," *Front. Bioeng. Biotechnol.*, vol. 8, Jan. 2020.
- [80] F. Xia, S. Tadigadapa, and Q. M. Zhang, 'Electroactive polymer based microfluidic pump,' *Sensors Actuators A Phys.*, vol. 125, no. 2, pp. 346–352, Jan. 2006.
- [81] F. M. Alsaleh, F. J. Smith, S. Keady, K. M. G Taylorà, and S. U. M Ma R Y, "Insulin pumps:

-
- from inception to the present and toward the future.”
- [82] T. G. Schleis and A. D. Tice, “Selecting infusion devices for use in ambulatory care,” *Am. J. Heal. Pharm.*, vol. 53, no. 8, pp. 868–877, Apr. 1996.
- [83] J. R. Lake, K. C. Heyde, and W. C. Ruder, “Low-cost feedback-controlled syringe pressure pumps for microfluidics applications,” *PLoS One*, vol. 12, no. 4, 2017.
- [84] F. Esser, T. Masselter, and T. Speck, “Silent Pumpers: A Comparative Topical Overview of the Peristaltic Pumping Principle in Living Nature, Engineering, and Biomimetics,” *Adv. Intell. Syst.*, vol. 1, no. 2, p. 1900009, Jun. 2019.
- [85] R. A. Freitas, “Basic Capabilities,” *Nanomedicine*, vol. 1, 1999.
- [86] J. D. Miller, D. F. Pegelow, A. J. Jacques, and J. A. Dempsey, “Skeletal muscle pump versus respiratory muscle pump: Modulation of venous return from the locomotor limb in humans,” *J. Physiol.*, vol. 563, no. 3, pp. 925–943, Mar. 2005.
- [87] J. Ren *et al.*, “Determinants of intrabolus pressure during esophageal peristaltic bolus transport,” *Am. J. Physiol.*, vol. 264, no. 3 Pt 1, 1993.
- [88] G. Bassotti, M. Gaburri, B. Pietro Imbimbo, A. Morelli, and W. E. Whitehead, “Distension-stimulated propagated contractions in human colon,” *Dig. Dis. Sci.*, vol. 39, no. 9, pp. 1955–1960, Sep. 1994.
- [89] Huebscher R. G., “Friction equivalents for round, square and rectangular ducts,” *ASHVE Trans. (Renamed ASHRAE Trans.)*, vol. 54, pp. 101–144, 1948.
- [90] A. V Lemoff and A. P. Lee, “An AC magnetohydrodynamic micropump,” *Sensors Actuators B Chem.*, vol. 63, no. 3, pp. 178–185, May 2000.
- [91] J. Seyed-Yagoobi, “Electrohydrodynamic pumping of dielectric liquids,” *J. Electrostat.*, vol. 63, no. 6–10, pp. 861–869, Jun. 2005.
- [92] X. Wang, C. Cheng, S. Wang, and S. Liu, “Electroosmotic pumps and their applications in microfluidic systems,” *Microfluid. Nanofluidics*.
- [93] C. Zhou, H. Zhang, Z. Li, and W. Wang, “Chemistry pumps: a review of chemically powered micropumps,” *Lab Chip*, vol. 16, no. 10, pp. 1797–1811, May 2016.
- [94] S. Herrlich, S. Spieth, S. Messner, and R. Zengerle, “Osmotic micropumps for drug delivery,” *Adv. Drug Deliv. Rev.*, vol. 64, no. 14, pp. 1617–1627, Nov. 2012.
- [95] D. Juncker *et al.*, “Autonomous microfluidic capillary system,” *Anal. Chem.*, vol. 74, no. 24, pp. 6139–6144, Dec. 2002.
- [96] K. S. Yun *et al.*, “A micropump driven by continuous electrowetting actuation for low voltage and low power operations,” *Proc. IEEE Micro Electro Mech. Syst.*, pp. 487–490, 2001.

-
- [97] E. D. Torniainen, A. N. Govyadinov, D. P. Markel, and P. E. Kornilovitch, "Bubble-driven inertial micropump," *Phys. Fluids*, vol. 24, no. 12, p. 122003, Dec. 2012.
- [98] V. Singhal and S. V. Garimella, "Induction electrohydrodynamics micropump for high heat flux cooling," *Sensors Actuators A Phys.*, vol. 134, no. 2, pp. 650–659, Mar. 2007.
- [99] A. Richter, H. Sandmaier, and A. Plettner, "An Electrohydrodynamic Injection Pump - A Novel Actuator for Microsystem Technology," in *Micro System Technologies 90*, Springer Berlin Heidelberg, 1990, pp. 812–817.
- [100] O. M. Stuetzer, "Ion Drag Pumps," *J. Appl. Phys.*, vol. 31, no. 1, p. 136, Jun. 2004.
- [101] A. Furuya, Shimokawa F, Matsuura T, and Sawada R, "Fabrication of fluorinated polyimide microgrids using magnetically controlled reactive ion etching (MC-RIE) and their applications to an ion drag integrated micropump," *J. Micromechanics Microengineering*, vol. 6, no. 3, Apr. 1996.
- [102] S.-H. Ahn and Y.-Kweon, "Fabrication and Experiment of Planar Micro Ion Drag Pump," *Sensors Actuators A Phys.*, vol. 70, no. 1–2, pp. 1–5, 1998.
- [103] K. R. Hencken and G. B. Sartor, "Electrokinetic pump," US 6,770,183 B1, 03-Aug-2004.
- [104] B. Gas, "ELECTROPHORESIS | Principles," *Encycl. Anal. Sci. Second Ed.*, pp. 363–370, Jan. 2005.
- [105] Dongqing Li, *Electrokinetics in Microfluidics*, vol. 2. 2004.
- [106] R. Zengerle, A. Richter, and H. Sandmaier, "A micro membrane pump with electrostatic actuation," in *IEEE.*, 1992, pp. 19–24.
- [107] H. Asadi Dereshgi, H. Dal, and M. Z. Yildiz, "Piezoelectric micropumps: state of the art review," *Microsyst. Technol.* 2021 2712, vol. 27, no. 12, pp. 4127–4155, Jan. 2021.
- [108] F. C. M. Van de Pol, H. T. G. Van Lintel, M. Elwenspoek, and J. H. J. Fluitman, "A thermopneumatic micropump based on micro-engineering techniques," *Sensors Actuators A Phys.*, vol. 21, no. 1–3, pp. 198–202, Feb. 1990.
- [109] W. L. Benard, H. Kahn, A. H. Heuer, and M. A. Huff, "Thin-film shape-memory alloy actuated micropumps," *J. Microelectromechanical Syst.*, vol. 7, no. 2, pp. 245–251, Jun. 1998.
- [110] C. Zhan, T. Lo, L. Liu, and T. Peihsin, "A silicon membrane micropump with integrated bimetallic actuator - HKUST SPD | The Institutional Repository," *Chinese J. Electron.*, vol. 5, no. 2, p. 3335, 1996.
- [111] M. Annabestani and M. Fardmanesh, "Ionic Electro active Polymer-Based Soft Actuators and Their Applications in Microfluidic Micropumps, Microvalves, and Micromixers: A Review," *Appl. Phys.*, Apr. 2019.

-
- [112] R. R. Gidde, P. M. Pawar, and V. P. Dhamgaye, "Fully coupled modeling and design of a piezoelectric actuation based valveless micropump for drug delivery application," *Microsyst. Technol.* 2019 262, vol. 26, no. 2, pp. 633–645, Jul. 2019.
- [113] T. Gerlach and H. Wurmus, "Working principle and performance of the dynamic micropump," *Sensors Actuators A Phys.*, vol. 50, no. 1–2, pp. 135–140, Aug. 1995.
- [114] A. Olsson, G. Stemme, and E. Stemme, "Diffuser-element design investigation for valveless pumps," *Sensors Actuators A Phys.*, vol. 57, no. 2, pp. 137–143, Nov. 1996.
- [115] A. R. Gamboa, C. J. Morris, and F. K. Forster, "Improvements in fixed-valve micropump performance through shape optimization of valves," *J. Fluids Eng. Trans. ASME*, vol. 127, no. 2, pp. 339–346, Mar. 2005.
- [116] A. Fadl, S. Demming, Z. Zhang, S. Büttgenbach, M. Krafczyk, and D. M. L. Meyer, "A multifunction and bidirectional valve-less rectification micropump based on bifurcation geometry," *Microfluid. Nanofluidics*, vol. 9, no. 2–3, pp. 267–280, Aug. 2010.
- [117] F. Forouzandeh, A. Arevalo, A. Alfarhel, and D. A. Borkholder, "A review of peristaltic micropumps," *Sensors Actuators A Phys.*, vol. 326, p. 112602, Aug. 2021.
- [118] L. Abrahao, V. Bhargava, A. Babaei, A. Ho, and R. K. Mittal, "Swallow induces a peristaltic wave of distension that marches in front of the peristaltic wave of contraction," *Neurogastroenterol. Motil.*, vol. 23, no. 3, pp. 201–e110, Mar. 2011.
- [119] T. Dow Chemical Company, "SYLGARD™ 186 Silicone Elastomer," 2017.
- [120] S. Rosset, O. A. Araromi, and H. R. Shea, "Maximizing the displacement of compact planar dielectric elastomer actuators," 2016.
- [121] S. Rosset, O. Araromi, H. Shea, S. Rosset, O. Araromi, and H. Shea, "Maximizing strain in miniaturized dielectric elastomer actuators," 2015.
- [122] M. Schimmelpfennig, F. Weimar, and K. Heinz, "Method and apparatus for the pulsation-free volumetric delivery of fluids and suspensions," 14-Apr-2013.
- [123] S. Rosset, O. A. Araromi, S. Schlatter, and H. R. Shea, "Fabrication Process of Silicone-based Dielectric Elastomer Actuators," *J. Vis. Exp.*, no. 108, pp. 1–13, 2016.
- [124] NuSil Company, "Datasheet MED-4086 Ultra-soft low consistency silicone elastomer."
- [125] S. Schlatter, P. Illenberger, and S. Rosset, "Peta-pico-Voltron: An open-source high voltage power supply," *HardwareX*, vol. 4, p. e00039, Oct. 2018.
- [126] H. Godaba, Z. Q. Zhang, U. Gupta, C. C. Foo, and J. Zhu, "Instabilities in dielectric elastomers: Buckling, wrinkling, and crumpling," *Soft Matter*, vol. 15, no. 36, pp. 7137–7144, 2019.
- [127] Wacker, "ELASTOSIL® Film 2030," 2020.

-
- [128] M. A. Unger, H. Chou, T. Thorsen, A. Scherer, and S. R. Quake, "Monolithic Microfabricated Valves and Pumps by Multilayer Soft Lithography," *Science* (80), vol. 288, no. April, 2000.
- [129] M. Zhang, J. Wu, L. Wang, K. Xiao, and W. Wen, "A simple method for fabricating multi-layer PDMS structures for 3D microfluidic chips," *Lab Chip*, vol. 10, no. 9, pp. 1199–1203, May 2010.
- [130] F. Förster-Zügel, S. Solano-Arana, F. Klug, and H. F. Schlaak, "Dielectric breakdown strength measurements with silicone-based single-layer dielectric elastomer transducers," *Smart Mater. Struct.*, vol. 28, no. 7, 2019.
- [131] A. Iannarelli, M. G. Niasar, and R. Ross, "The effects of static pre-stretching on the short and long-term reliability of dielectric elastomer actuators," *Smart Mater. Struct.*, 2019.
- [132] F. Förster-Zuegel, T. Grotepaß, and H. F. Schlaak, "Characterization of the dielectric breakdown field strength of PDMS thin films: thickness dependence and electrode shape," *Electroact. Polym. Actuators Devices 2015*, vol. 9430, p. 94300D, 2015.
- [133] P. H. Cazorla *et al.*, "A low voltage silicon micro-pump based on piezoelectric thin films," *Sensors Actuators, A Phys.*, vol. 250, pp. 35–39, 2016.
- [134] N. A. Hamid, B. Y. Majlis, J. Yunas, A. R. Syafeeza, Y. C. Wong, and M. Ibrahim, "A stack bonded thermo-pneumatic micro-pump utilizing polyimide based actuator membrane for biomedical applications," *Microsyst. Technol.*, vol. 23, no. 9, pp. 4037–4043, Sep. 2017.
- [135] S. A. M. Shaegh *et al.*, "Plug-and-play microvalve and micropump for rapid integration with microfluidic chips," *Microfluid. Nanofluidics*, vol. 19, no. 3, pp. 557–564, Sep. 2015.
- [136] A. Ehsani and A. Nejat, "Conceptual design and performance analysis of a novel flexible-valve micropump using magneto-fluid–solid interaction," *Smart Mater. Struct.*, vol. 26, no. 5, p. 055036, Apr. 2017.
- [137] A. Poulin, C. Saygili Demir, S. Rosset, T. V. Petrova, and H. R. Shea, "Dielectric elastomer actuator for mechanical loading of 2D cell cultures," *Lab Chip*, vol. 16, no. 19, pp. 3788–3794, 2016.
- [138] Z. Li *et al.*, "Cell Nanomechanics Based on Dielectric Elastomer Actuator Device," *Nano-Micro Letters*, vol. 11, no. 1. SpringerOpen, pp. 1–19, 01-Nov-2019.
- [139] V. Hessel, H. Löwe, and F. Schönfeld, "Micromixers — a review on passive and active mixing principles," in *Chemical Engineering Science*, 2005, vol. 60, pp. 2479–2501.
- [140] E. L. Paul, V. A. Atiemo-Obeng, and S. M. Kresta, *Handbook of industrial mixing : science and practice*. Wiley-Interscience, 2004.
- [141] J. R. Bourne, "Mixing and the Selectivity of Chemical Reactions," *Org. Process Res. Dev.*, vol. 7, pp. 471–508, 2003.

-
- [142] J. Liu, Y. F. Yap, and N. T. Nguyen, "Behavior of microdroplets in diffuser/nozzle structures," *Microfluid. Nanofluidics*, vol. 6, no. 6, pp. 835–846, 2009.
- [143] C. T. Wang and Y. C. Hu, "Mixing of liquids using obstacles in Y-type microchannels," *Tamkang J. Sci. Eng.*, vol. 13, no. 4, pp. 385–394, 2010.
- [144] H. Wang, P. Iovenitti, E. C. Harvey, S. Masood, and R. Deam, "Mixing of liquids using obstacles in microchannels," *BioMEMS and Smart Nanostructures*, vol. 4590, pp. 204–212, Nov. 2001.
- [145] N. T. Nguyen and Z. Wu, "Micromixers - A review," *J. Micromechanics Microengineering*, vol. 15, no. 2, 2005.
- [146] E. A. Mansur, Y. E. Mingxing, W. Yundong, and D. A. I. Youyuan, "A State-of-the-Art Review of Mixing in Microfluidic Mixers," *Chinese J. Chem. Eng.*, vol. 16, no. 4, pp. 503–516, 2008.
- [147] D. S. Kim, S. H. Lee, T. H. Kwon, and C. H. Ahn, "A serpentine laminating micromixer combining splitting/recombination and advection," *Lab Chip*, vol. 5, no. 7, pp. 739–747, Jun. 2005.
- [148] T. Tofteberg, M. Skolimowski, E. Andreassen, and O. Geschke, "A novel passive micromixer: Lamination in a planar channel system," *Microfluid. Nanofluidics*, vol. 8, no. 2, pp. 209–215, Feb. 2010.
- [149] N. T. Nguyen and X. Huang, "Modelling, fabrication and characterization of a polymeric micromixer based on sequential segmentation," *Biomed. Microdevices*, vol. 8, no. 2, pp. 133–139, Jun. 2006.
- [150] R. Sakurai, K. Yamamoto, and M. Motosuke, "Concentration-adjustable micromixers using droplet injection into a microchannel," *Analyst*, vol. 144, no. 8, pp. 2780–2787, Apr. 2019.
- [151] J. B. Knight, A. Vishwanath, J. P. Brody, and R. H. Austin, "Hydrodynamic focusing on a silicon chip: Mixing nanoliters in microseconds," *Phys. Rev. Lett.*, vol. 80, no. 17, pp. 3863–3866, Apr. 1998.
- [152] V. Rudyak and A. Minakov, "Modeling and Optimization of Y-Type Micromixers," *Micromachines*, vol. 5, no. 4, pp. 886–912, Oct. 2014.
- [153] D. Gobby, P. Angeli, and A. Gavriilidis, "Mixing characteristics of T-type microfluidic mixers," *J. Micromechanics Microengineering*, vol. 11, no. 2, pp. 126–132, Mar. 2001.
- [154] V. Hessel, S. Hardt, H. Löwe, and F. Schönfeld, "Laminar mixing in different interdigital micromixers: I. Experimental characterization," *AIChE J.*, vol. 49, no. 3, pp. 566–577, Mar. 2003.
- [155] F. G. Bessoth, A. J. deMello, and A. Manz, "Microstructure for efficient continuous flow mixing," *Anal. Commun.*, vol. 36, no. 6, pp. 213–215, Jan. 1999.

-
- [156] S. Hossain, M. A. Ansari, A. Husain, and K.-Y. Kim, "Analysis and optimization of a micromixer with a modified Tesla structure," *Chem. Eng. J.*, vol. 158, no. 2, pp. 305–314, Apr. 2010.
- [157] A. S. Yang *et al.*, "A high-performance micromixer using three-dimensional Tesla structures for bio-applications," *Chem. Eng. J.*, vol. 263, pp. 444–451, 2015.
- [158] L. T. Rao, S. Goel, S. K. Dubey, and A. Javed, "Performance Investigation of T-Shaped Micromixer with Different Obstacles," in *International Conference on Recent Advances in Fluid and Thermal Sciences*, 2019.
- [159] D. Bothe, C. Stemich, and H. J. Warnecke, "Fluid mixing in a T-shaped micro-mixer," *Chem. Eng. Sci.*, vol. 61, no. 9, pp. 2950–2958, May 2006.
- [160] G. Orsi, M. Roudgar, E. Brunazzi, C. Galletti, and R. Mauri, "Water-ethanol mixing in T-shaped microdevices," *undefined*, vol. 95, pp. 174–183, May 2013.
- [161] M. Hoffmann, M. Schlüter, and N. Rübiger, "Experimental investigation of liquid–liquid mixing in T-shaped micro-mixers using μ -LIF and μ -PIV," *Chem. Eng. Sci.*, vol. 61, no. 9, pp. 2968–2976, May 2006.
- [162] A. Fani, S. Camarri, and M. V. Salvetti, "Investigation of the steady engulfment regime in a three-dimensional T-mixer," *Phys. Fluids*, vol. 25, no. 6, p. 064102, Jun. 2013.
- [163] Z. Yang, S. Matsumoto, H. Goto, M. Matsumoto, and R. Maeda, "Ultrasonic micromixer for microfluidic systems," *Sensors Actuators A Phys.*, vol. 93, no. 3, pp. 266–272, Oct. 2001.
- [164] M. H. Oddy, J. G. Santiago, and J. C. Mikkelsen, "Electrokinetic Instability Micromixing," *Anal. Chem.*, vol. 73, no. 24, pp. 5822–5832, Dec. 2001.
- [165] P. Woias, K. Hauser, and E. Yacoub-George, "An Active Silicon Micromixer for μ TAS Applications," in *Micro Total Analysis Systems 2000*, Dordrecht: Springer Netherlands, 2000, pp. 277–282.
- [166] A. A. Deshmukh, D. Liepmann, A. P. Pisano, B. Sensor, and A. Center, "Continuous Micromixer With Pulsatile Micropumps," in *Transducer Research Foundation Inc. (TRF)*, 2020, pp. 73–76.
- [167] A. A. Deshmukh, D. Liepmann, A. P. Pisano, B. Sensor, and A. Center, "Continuous micromixer with pulsatile micropumps," in *Transducer Research Foundation Inc. (TRF)*., 2020, pp. 73–76.
- [168] T. Fujii, Y. Sando, K. Higashino, and Y. Fujii, "A plug and play microfluidic device," *Lab Chip*, vol. 3, no. 3, pp. 193–197, 2003.
- [169] C. Y. Lee and L. M. Fu, "Recent advances and applications of micromixers," *Sensors Actuators, B Chem.*, vol. 259, pp. 677–702, 2018.

-
- [170] M. S. Yoon, B. J. Kim, and H. J. Sung, "Pumping and mixing in a microchannel using AC asymmetric electrode arrays," *Int. J. Heat Fluid Flow*, vol. 29, no. 1, pp. 269–280, 2008.
- [171] H. Y. Tseng, C. H. Wang, W. Y. Lin, and G. Bin Lee, "Membrane-activated microfluidic rotary devices for pumping and mixing," *Biomed. Microdevices*, vol. 9, no. 4, pp. 545–554, 2007.
- [172] H. J. Sheen, C. J. Hsu, T. H. Wu, H. C. Chu, C. C. Chang, and U. Lei, "Experimental study of flow characteristics and mixing performance in a PZT self-pumping micromixer," *Sensors Actuators, A Phys.*, vol. 139, no. 1-2 SPEC. ISS., pp. 237–244, 2007.
- [173] A. Victor, J. Ribeiro, and F. S. Araújo, "Study of PDMS characterization and its applications in biomedicine: A review," *J. Mech. Eng. Biomech.*, vol. 4, no. 1.
- [174] M.-C. Bélanger and Y. Marois, "Hemocompatibility, biocompatibility, inflammatory and *in vivo* studies of primary reference materials low-density polyethylene and polydimethylsiloxane: A review," *J. Biomed. Mater. Res.*, vol. 58, no. 5, pp. 467–477, Jan. 2001.
- [175] P. Lotz, "Dielektrische Elastomerstapelaktoren für ein peristaltisches Fluidfördersystem," no. November, 2009.
- [176] D. Gatti, H. Haus, M. Matysek, B. Frohnäpfel, C. Tropea, and H. F. Schlaak, "The dielectric breakdown limit of silicone dielectric elastomer actuators," *Appl. Phys. Lett.*, vol. 104, no. 5, 2014.
- [177] M. Matysek, P. Lotz, T. Winterstein, and H. F. Schlaak, "Dielectric Elastomer Actuators for Tactile Displays," in *3rd Joint EuroHaptics Conference and Symposium on Haptic Interfaces for Virtual Environment and Teleoperator Systems, World Haptics*, 2009, pp. 290–295.
- [178] G. Kovacs and L. Düring, "Contractive tension force stack actuator based on soft dielectric EAP," 2009, p. 72870A.
- [179] W. Yuan *et al.*, "Fault-tolerant dielectric elastomer actuators using single-walled carbon nanotube electrodes," *Adv. Mater.*, vol. 20, no. 3, pp. 621–625, 2008.
- [180] X. Yu, R. Rajamani, K. A. Stelson, and T. Cui, "Carbon nanotube-based transparent thin film acoustic actuators and sensors," *Sensors Actuators, A Phys.*, vol. 132, no. 2, pp. 626–631, 2006.
- [181] W. Yuan, L. Hu, S. Ha, T. Lam, G. Grüner, and Q. Pei, "Self-clearable carbon nanotube electrodes for improved performance of dielectric elastomer actuators," in *Electroactive Polymer Actuators and Devices (EAPAD) 2008*, 2008, vol. 6927, p. 69270P.
- [182] F. Carpi and D. De Rossi, "Contractile dielectric elastomer actuator with folded shape," *Smart Struct. Mater. 2006 Electroact. Polym. Actuators Devices*, vol. 6168, p. 61680D, 2006.

-
- [183] J. Maas, D. Tepel, and T. Hoffstadt, "Actuator design and automated manufacturing process for DEAP-based multilayer stack-actuators," *Meccanica*, vol. 11, no. 50, pp. 2839–2854, Oct. 2015.
- [184] M. Matysek, P. Lotz, and H. F. Schlaak, "Development of Multilayer Dielectric Elastomer Actuators," in *Annex of the Conference proceedings: Actuator 2008, 11th International Conference on New Actuators and 5th International Exhibition on Smart Actuators and Drive Systems, 2008*.
- [185] M. Jungmann, "Entwicklung elektrostatischer Festkörperaktoren mit elastischen Dielektrika für den Einsatz in taktiken Anzeigefeldern."
- [186] Wacker GmbH, "Datasheet of ELASTOSIL® P 7670 A/B Room Temperature Curing Silicone Rubber (RTV-2)." [Online]. Available: www.wacker.com. [Accessed: 07-Feb-2020].
- [187] P. Lotz, M. Matysek, and H. F. Schlaak, "Fabrication and Application of Miniaturized Dielectric Elastomer Stack Actuators," *IEEE/ASME Trans. Mechatronics*, vol. 16, no. 1, pp. 58–66, 2011.
- [188] A. Diaspro and C. Usai, "Optical Microscopy," in *Wiley Encyclopedia of Biomedical Engineering*, Hoboken, NJ, USA: John Wiley & Sons, Inc., 2006.
- [189] M. J. Sanderson, I. Smith, I. Parker, and M. D. Bootman, "Fluorescence microscopy," *Cold Spring Harb. Protoc.*, vol. 2014, no. 10, pp. 1042–1065, Oct. 2014.
- [190] S. W. Paddock, "Confocal laser scanning microscopy," *BioTechniques*, vol. 27, no. 5. Future Science Ltd London, UK, pp. 992–1004, 22-Aug-1999.
- [191] SharkD, https://commons.wikimedia.org/wiki/File:RGB_color_solid_cube.png. [Online]. Available: https://commons.wikimedia.org/wiki/File:RGB_color_solid_cube.png. [Accessed: 29-Oct-2020].
- [192] L. R. Christensen, O. Hassager, and A. L. Skov, "Electro-Thermal model of thermal breakdown in multilayered dielectric elastomers," *AIChE J.*, vol. 65, no. 2, pp. 859–864, 2019.
- [193] M. Matysek, "Dielektrische Elastomeraktoren in Multilayer-Technologie für taktile Displays," no. November, 2009.
- [194] C. Wiles, P. Watts, S. J. Haswell, and E. Pombo-Villar, "The aldol reaction of silyl enol ethers within a micro reactor," *Lab Chip*, vol. 1, no. 2, pp. 100–101, Dec. 2001.
- [195] M. Sands *et al.*, "The investigation of an equilibrium dependent reaction for the formation of enamines in a microchemical system," *Lab Chip*, vol. 1, no. 1, pp. 64–65, Sep. 2001.
- [196] E. Garcia-Egido, S. Y. F. Wong, and B. H. Warrington, "A Hantzsch synthesis of 2-aminothiazoles performed in a heated microreactor system," *Lab Chip*, vol. 2, no. 1, pp.

-
- 31–33, Feb. 2002.
- [197] N. G. Wilson and T. McCreedy, “On-chip catalysis using a lithographically fabricated glass microreactor - The dehydration of alcohols using sulfated zirconia,” *Chem. Commun.*, no. 9, pp. 733–734, May 2000.
- [198] M. Ueno, H. Hisamoto, T. Kitamori, and S. Kobayashi, “Phase-transfer alkylation reactions using microreactors,” *Chem. Commun.*, vol. 3, no. 8, pp. 936–937, Apr. 2003.
- [199] G. M. Greenway, S. J. Haswell, D. O. Morgan, V. Skelton, and P. Styring, “Use of a novel microreactor for high throughput continuous flow organic synthesis,” *Sensors Actuators, B Chem.*, vol. 63, no. 3, pp. 153–158, May 2000.
- [200] T. T. Veenstra, T. S. J. Lammerink, M. C. Elwenspoek, and A. Van Den Berg, “Characterization method for a new diffusion mixer applicable in micro flow injection analysis systems,” *J. Micromechanics Microengineering*, vol. 9, no. 2, pp. 199–202, Jun. 1999.
- [201] Q. Lang *et al.*, “In-plane microvortices micromixer-based AC electrothermal for testing drug induced death of tumor cells,” *Biomicrofluidics*, vol. 10, no. 6, Nov. 2016.
- [202] B. J. Burke and F. E. Regnier, “Stopped-flow enzyme assays on a chip using a microfabricated mixer,” *Anal. Chem.*, vol. 75, no. 8, pp. 1786–1791, Apr. 2003.
- [203] A. G. Hadd, D. E. Raymond, J. W. Halliwell, S. C. Jacobson, and J. M. Ramsey, “Microchip Device for Performing Enzyme Assays,” *Anal. Chem.*, vol. 69, no. 17, pp. 3407–3412, Sep. 1997.
- [204] R. A. Vijayendran, K. M. Motsegood, D. J. Beebe, and D. E. Leckband, “Evaluation of a three-dimensional micromixer in a surface-based biosensor,” *Langmuir*, vol. 19, no. 5, pp. 1824–1828, Mar. 2003.
- [205] D. S. Kim, S. H. Lee, C. H. Ahn, J. Y. Lee, and T. H. Kwon, “Disposable integrated microfluidic biochip for blood typing by plastic microinjection moulding,” *Lab Chip*, vol. 6, no. 6, pp. 794–802, 2006.
- [206] J. N. Lee, C. Park, and G. M. Whitesides, “Solvent Compatibility of Poly(dimethylsiloxane)-Based Microfluidic Devices,” *Anal. Chem.*, vol. 75, no. 23, pp. 6544–6554, 2003.
- [207] H. Zhang, M. Dai, and Z. Zhang, “The analysis of transparent dielectric elastomer actuators for lens,” *Optik (Stuttg.)*, vol. 178, pp. 841–845, Feb. 2019.
- [208] A. Victor, J. Ribeiro, and F. S. Araújo, “Study of PDMS characterization and its applications in biomedicine: A review,” *J. Mech. Eng. Biomech.*, vol. 4, no. 1.
- [209] A. Chortos, E. Hajiesmaili, J. Morales, D. R. Clarke, and J. A. Lewis, “3D Printing of Interdigitated Dielectric Elastomer Actuators,” *Adv. Funct. Mater.*, vol. 30, no. 1, p. 1907375, Jan. 2020.

-
- [210] F. Klug, S. Solano-Arana, N. J. Hoffmann, and H. F. Schlaak, "Multilayer dielectric elastomer tubular transducers for soft robotic applications," *Smart Mater. Struct.*, vol. 28, no. 10, 2019.
- [211] A. Poulin, S. Rosset, and H. R. Shea, "Fully printed 3 microns thick dielectric elastomer actuator," *Electroact. Polym. Actuators Devices 2016*, vol. 9798, no. April 2016, p. 97980L, 2016.
- [212] D. McCoul, S. Rosset, S. Schlatter, and H. Shea, "Inkjet 3D printing of UV and thermal cure silicone elastomers for dielectric elastomer actuators," *Smart Mater. Struct.*, vol. 26, no. 12, Nov. 2017.
- [213] X. Ji *et al.*, "Stretchable composite monolayer electrodes for low voltage dielectric elastomer actuators," *Sensors Actuators, B Chem.*, vol. 261, pp. 135–143, 2018.
- [214] H. Mößinger, F. Förster-Zügel, and H. F. Schlaak, "Simulation of the transient electromechanical behaviour of dielectric elastomer transducers," in *Electroactive Polymer Actuators and Devices (EAPAD) 2016*, 2016, vol. 9798, p. 979831.
- [215] P. Dubois, S. Rosset, M. Niklaus, M. Dadras, and H. Shea, "Voltage control of the resonance frequency of dielectric electroactive polymer (DEAP) membranes," *J. Microelectromechanical Syst.*, vol. 17, no. 5, pp. 1072–1081, 2008.
- [216] N.-T. Nguyen and N.-T. Nguyen, "Chapter 1 – Introduction," in *Micromixers*, 2012, pp. 1–8.
- [217] D. Dutta, A. Ramachandran, and D. T. Leighton, "Effect of channel geometry on solute dispersion in pressure-driven microfluidic systems," *Microfluidics and Nanofluidics*, vol. 2, no. 4. pp. 275–290, Jul-2006.
- [218] J. H. E. Cartwright, M. Feingold, and O. Piro, *An Introduction to Chaotic Advection*, no. January. 1999.
- [219] B. H. Weigl, R. Bardell, and T. Schulte, "Design and Rapid Prototyping of Thin-Film Laminate-Based Microfluidic Devices," *Biomed. Microdevices*, vol. 3, no. 3, pp. 267–274, 2001.
- [220] R. Hiorns, *Polymer Handbook, 4th edn, John Wiley and Sons, New York, 1999, pp 2250*, vol. 49, no. 7. Wiley, 2000.

LIST OF PUBLICATIONS

- [1] S. Solano-Arana, H. Mößinger and H. F. Schlaak, "Biocompatible microfluidic systems based on dielectric electroactive actuators". In: EuroEAP 2016 Sixth international conference on Electromechanically Active Polymer (EAP) transducers & artificial muscles, *Proceedings of EuroEAP* Helsingor, Denmark, 2016.
- [2] S. Solano-Arana, F. Klug, H. Mößinger, F. Förster-Zügel and H. F. Schlaak, "Micromixer based on dielectric stack actuators for medical applications". In: *Proceedings of SPIE*. Bd. 10163. 1016332. *SPIE Smart Structures, Materials + Nondestructive Evaluation and Health Monitoring*, Portland, USA, 2017.
- [3] F. Klug, S. Solano-Arana, H. Mößinger, F. Förster-Zügel and H. F. Schlaak, "Fabrication of dielectric elastomer stack transducers (DEST) by liquid deposition modeling", In: *Proceedings of SPIE*. Bd. 10163. 1016332. *SPIE Smart Structures, Materials + Nondestructive Evaluation and Health Monitoring*, Portland, USA, 2017.
- [4] S. Solano-Arana, F. Klug, H. Mößinger, F. Förster-Zügel and H. F. Schlaak, "A novel application of dielectric stack actuators: a micromixer", In: EuroEAP 2017 Seventh international conference on Electromechanically Active Polymer (EAP) transducers & artificial muscles, *Proceedings of EuroEAP* Cartagena, Spain, 2017.
- [5] F. Klug, S. Solano-Arana, F. Förster-Zügel, H. F. Schlaak, G. Grötsch, C. Cornelißen, A. Streitenberger and M. Eulenburg, "Fabrication approaches of dielectric elastomer stack transducers for complex and large-scale production", In: EuroEAP 2017 Seventh international conference on Electromechanically Active Polymer (EAP) transducers & artificial muscles, *Proceedings of EuroEAP* Cartagena, Spain, 2017.
- [6] S. Solano-Arana, F. Klug, H. Mößinger, F. Förster-Zügel and H. F. Schlaak, "A novel application of dielectric stack actuators: a pumping micromixer" *Smart Materials and Structures*, Volume 27, N°7, 2018.
- [7] S. Solano-Arana, F. Klug, F. Förster-Zügel and H. F. Schlaak, "Characterization of pumping micromixers based on dielectric elastomer stack actuators", EuroEAP 2018, *Proceedings of 8th International Conference on Electromechanically Active Polymer (EAP) Transducers & Artificial Muscles*, Lyon, France, 2018.
- [8] F. Klug, S. Solano-Arana, F. Förster-Zügel and H. F. Schlaak, "Design of artificial muscles based on dielectric elastomers for soft exosuits to support grasping motion". *EuroEAP 2018, 8th International Conference on Electromechanically Active Polymer (EAP) Transducers & Artificial Muscles*, Lyon, France, 2018
- [9] F. Klug, C. Endl, S. Solano-Arana and H. F. Schlaak, "Design, fabrication, and customized driving of dielectric loudspeaker arrays". In: *Proceedings of SPIE*. Bd. 10966. 109662I. *SPIE Smart Structures, Materials + Nondestructive Evaluation and Health Monitoring*. Denver, USA, 2019.

-
- [10] F. Förster-Zügel, S. Solano-Arana, F. Klug and H. F. Schlaak, "Dielectric breakdown strength measurements with silicone-based single-layer dielectric elastomer transducers". *In Smart Materials and Structures* 28.7, 2019, S. 075042.
- [11] F. Klug, S. Solano-Arana, N. J. Hoffmann and H. F. Schlaak, "Multilayer dielectric elastomer tubular transducers for soft robotic applications", *In Smart Materials and Structures* 28.10, 2019, S. 104004.
- [12] E. Ricohermoso, E. Haripre, S. Solano-Arana, R. Riedel, and E. Ionescu, "Hierarchical microstructure growth in a precursor-derived SiOC thin film prepared on silicon substrate", *In International Journal of Applied Ceramic Technology* 2022, 20 (2), 735-746.
- [13] E. Ricohermoso, S. Solano-Arana, C. Fasel, R. Riedel, and E. Ionescu, "SiOC-Based Strain Gauge with Ultrahigh Piezoresistivity at High Temperatures", *In ACS Appl. Eng. Mater.* 2023, 1, 4, 1093-1105.



A. APPENDIX - TRANSPORT PHENOMENA IN MICROFLUIDICS

The equations for a single-phase fluid with homogeneous composition in a continuum level (i.e., disregarding molecular effects) are the conservation equations: conservations of mass (continuity equation), conservation of momentum (Newton's second law or Navier-Stokes equation, motion equation) and conservation of energy (first law of thermodynamics or energy equation). These equations provide information about the velocity, the pressure and the temperature field in a channel, very significant properties in the microfluidic field. Other properties can also be deduced from them.

In the following subsections, the conservation equations for fluids in a single phase and at continuum level are summarized. These equations are also used in chapter 5 for the COMSOL Multiphysics® simulations of the fluid flow in the pumping micromixer.

CONSERVATION OF MASS

In a continuum mechanics level, the conservation of mass is expressed by:

$$\frac{D\rho}{Dt} + \rho \operatorname{div}\nabla = 0 \quad \text{Eq A.1}$$

The equation above is the well-known continuity equation, where ∇ is the nabla operator, ρ the density and $\frac{D}{Dt}$ is the total derivative operator, defined as:

$$\frac{D}{Dt} = \frac{\partial}{\partial t} + u \frac{\partial}{\partial x} + v \frac{\partial}{\partial y} + w \frac{\partial}{\partial z} = \frac{\partial}{\partial t} + (\mathbf{v} \cdot \nabla) \quad \text{Eq A.2}$$

Where $\mathbf{v} = (u, v, w)$ is the velocity vector.

If the material is considered to be incompressible, then ρ is constant, and $\frac{D\rho}{Dt}$ is zero, and

$$\rho \operatorname{div}\nabla = 0 \quad \text{Eq A.3}$$

And then divide through by ρ (since it's not zero) to get

$$\operatorname{div}\nabla = 0 \quad \text{Eq A.4}$$

CONSERVATION OF MOMENTUM

The conservation of momentum is based on the statement that in a problem domain, the amount of momentum remains constant. The momentum is only changed through the action of forces as described by Newton's laws of motion. Newton's second law can be expressed as:

$$\rho \frac{Dv}{Dt} = f = f_{body} + f_{surface} \quad \text{Eq A.5}$$

In this equation, the acceleration force is equal to the forces per unit volume. The force term, f , can refer to body forces (for example, gravity g) or surface forces like electrostatic forces, viscous forces or surface stress. Here, if the viscosity and the density are constant, the only forces acting over the system are gravity and surface forces, like the ones caused by a pressure gradient or a viscous force. Therefore, the general conservation equation leads to the Navier-Stokes equation:

$$\rho \frac{Dv}{Dt} = \rho g - \nabla p + \mu_d \nabla^2 v \quad \text{Eq A.6}$$

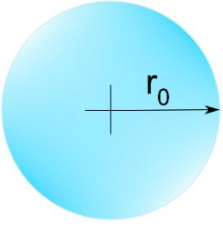
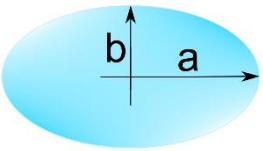
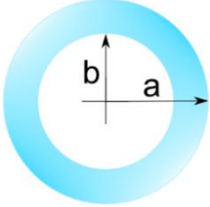
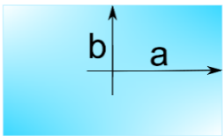
where μ_d is the dynamic viscosity of the fluid. It is possible to further derive the Navier-Stokes equation considering that the flow in the axial-x-direction is fully developed. A fully developed flow occurs, when the viscous effects due to the shear stress between the fluid particles and the walls generate a fully developed velocity profile. In order for this to occur the fluid must travel through a length of a straight pipe. In addition, the velocity of the fluid for a fully developed flow will be at its fastest at the centre line of the pipe. On the other hand, the velocity of the fluid at the walls of the pipe will theoretically be zero. As a result, fluid velocity should be expressed as an average velocity. The equation then satisfies that $v = w = 0$ and $du/dx = 0$.

Then the problem simplifies to a two-dimensional form:

$$\frac{\partial^2 u}{\partial y^2} + \frac{\partial^2 u}{\partial z^2} = \frac{1}{\mu} \frac{dp}{dx} \quad \text{Eq A.7}$$

where the last term of the equation is a constant. It is possible, depending on the channel geometry or configuration, to obtain an analytical expression for the velocity field within the walls. In Table A.1, the analytical expressions for the most common geometries are shown.

Table A.1: Velocity field inside a straight channel.

<p>Circle</p> 	$u^*(r) = 2 \left(1 - \frac{r^2}{r_0^2} \right)$ $\bar{u} = \frac{1}{8\mu} \left(-\frac{dp}{dx} \right) r^2$
<p>Ellipse</p> 	$u^*(y, z) = 2 \left(1 - \frac{y^2}{a^2} - \frac{z^2}{b^2} \right)$ $\bar{u} = \frac{1}{4\mu} \left(-\frac{dp}{dx} \right) \frac{a^2 b^2}{a^2 + b^2}$
<p>Concentric annulus</p> 	$u^*(r) = 2 \left[a^2 - r^2 + (a^2 - b^2) \frac{\ln(a/r)}{\ln(b/a)} \right] / \left[a^2 + b^2 - \frac{a^2 - b^2}{\ln(a/b)} \right]$ $\bar{u} = \frac{1}{8\mu} \left(-\frac{dp}{dx} \right) \left[a^2 + b^2 - \frac{a^2 - b^2}{\ln(a/b)} \right]$
<p>Rectangle</p> 	$u^*(y, z) = \frac{48}{\pi^3} \sum_{n=1}^{\infty} (-1)^{n-1} \left\{ \left[1 - \frac{\cosh[(2n-1)\pi z/2a]}{\cosh[(2n-1)\pi b/2a]} \right] \times \frac{\cos[(2n-1)\pi y/2a]}{(2n-1)^3} \right.$ $\left. / \left\{ 1 - \frac{192a}{\pi^5 b} \sum_{n=1}^{\infty} \frac{\tanh[(2n-1)\pi b/2a]}{(2n-1)^5} \right\} \right\}$ $\bar{u} = \frac{a^2}{3\mu} \left(-\frac{dp}{dx} \right) \left\{ 1 - \frac{192a}{\pi^5 b} \sum_{n=1}^{\infty} \frac{\tanh[(2n-1)\pi b/2a]}{(2n-1)^5} \right\}$

CONSERVATION OF ENERGY

As mentioned above, the conservation of energy is based on the first law of the thermodynamics, which states that the energy can be converted from one form to another with the interaction of heat, work, and internal energy, but it cannot be created nor destroyed. To summarize, the sum of the heat and work added to a system is equal to the change of the total energy:

$$dQ + dW = dE_{total} \quad \text{Eq A.8}$$

with dQ the heat, and dW the work added to the system and dE_{total} , the total energy obtained. The expression above in terms of absolute temperature T can be expressed as

$$\rho c_p \frac{DT}{Dt} = \beta T \frac{Dp}{Dt} + \text{div}(k_t \nabla T) + \Phi \quad \text{Eq A.9}$$

With c_p the specific heat at constant pressure, $\beta = -\frac{1}{\rho} \left(\frac{\partial \rho}{\partial T} \right)_p$, β is the thermal expansion coefficient, k_t is the thermal conductivity, and Φ is the dissipation function. For a Newtonian fluid, incompressible flow, a constant thermal conductivity and not considering the kinetic energy change, the energy equation transforms into the heat convection equation:

$$\rho c_p \frac{DT}{Dt} = k \nabla^2 T \quad \text{Eq A.10}$$

B. APPENDIX - TRANSPORT PHENOMENA IN MICROMIXERS

The fluid flow in micromixers also follows the conservation equations proposed in Appendix A. These equations are considered for a homogeneous composition in a continuum level: the conservations of mass (continuity equation), the conservation of momentum (Newton's second law or Navier-Stokes equation, motion equation) and conservation of energy (first law of thermodynamics or energy equation). Using these equations, it is possible to determine the velocity, pressure and temperature profile of the fluid. Further properties like viscosity, density and enthalpy can also be derived from the previous ones.

Micromixers involve multiple phases. In order to describe the mixing process, it is necessary to add more equations to the system. In the macroscale mixing, diverse transport of species mechanisms are involved, such as molecular diffusion, Eddy diffusion, advection, and Taylor dispersion. In the case of micromixing, it only makes sense to think about a laminar flow, due to the dominant viscous effect. The main transport phenomena in micromixing are molecular diffusion, advection and Taylor dispersion. Eddy diffusion is not considered in micromixing devices because it is based on the transport of a large group of species in a turbulent regime.

The conservation of species is the most used equation when mixing substances, where they change in phase. The conservation of species is based on the diffusion/convection equation:

$$\frac{Dc}{Dt} = D\nabla^2 c + r_g \quad \text{Eq B.1}$$

where c is the concentration of the species, D is the diffusivity or diffusion coefficient of the species (solute) in the carrier fluid (solvent) and r_g is the generation rate of the species per volume. For a chemical species, $r_g > 0$ means that a chemical reaction is creating more of the species, and $r_g < 0$ means that a chemical reaction is destroying the species.

In order to obtain equation B.1, it is necessary to determine the isotropic diffusion coefficient as a constant value. The terms of the equation can be regarded as follows:

- $\frac{Dc}{Dt}$ refers to the accumulation and convection of species
- $D\nabla^2 c$ represents molecular diffusion
- r_g is the generation rate of the species per volume

Molecular diffusion

Molecular diffusion is a mechanism based on the random motion of molecules. Two models are considered for the molecular diffusion of particles in a fluid: the random walk or Brownian motion, and the Stokes–Einstein model of diffusion.

For Brownian motion, a one-dimensional walk on a line is considered, where the particle can choose between two directions in each step, defined as

$$\frac{Dc}{Dt}x(n) = \sum_{i=1}^n s_i \quad \text{Eq B.2}$$

with s the displacement at each step, $x(n)$ the position at a step(n) and s_i a random step. Assuming that each step needs the same time($t \propto n$), the squared value of the position is thus:

$$x(n)^2 = \sum_{i=1}^n s_i^2 = ns^2 \propto Dt \quad \text{Eq B.3}$$

The diffusion coefficient is then proportional to the speed of the particles.

In the investigated microfluidic devices, the media in use are liquids, thus the only exposed equations are based on the diffusion in liquids. The diffusion coefficient in liquids follows the Stokes-Einstein equation. The Stokes-Einstein equation is based on a spherical particle following a Brownian motion at a uniform temperature T :

$$D = \frac{k_B T}{3\pi\mu_d\sigma_p} \quad \text{Eq B.4}$$

where D is the diffusion coefficient, k_B is the Boltzmann constant, μ is the viscosity of the fluid and σ_p is the radius of the particle p . The term $k_B T$ represents the kinetic energy of the molecule, while the term $3\pi\mu\sigma_p$ deals with the friction forces acting on the molecule.

Taylor dispersion

Taylor dispersion occurs in a distributed velocity field where a shear flow increases the diffusivity of particles. Instead of a uniform velocity profile, like in the case of molecular diffusion, an axial effect increases the effectivity of the mixing.

In Figure B.1(a), the particle distribution with time in a microchannel is shown for a uniform velocity profile, i.e. only considering molecular diffusion as a transport phenomenon. On the contrary, in Figure B.1(b) the particle distribution with time for a fluid subject to a parabolic

velocity profile due to Taylor dispersion is shown. The different concentration gradient in the section leads to a diffusion of the solute in the solvent in the axial direction with a faster velocity than in the case of simple molecular diffusion.

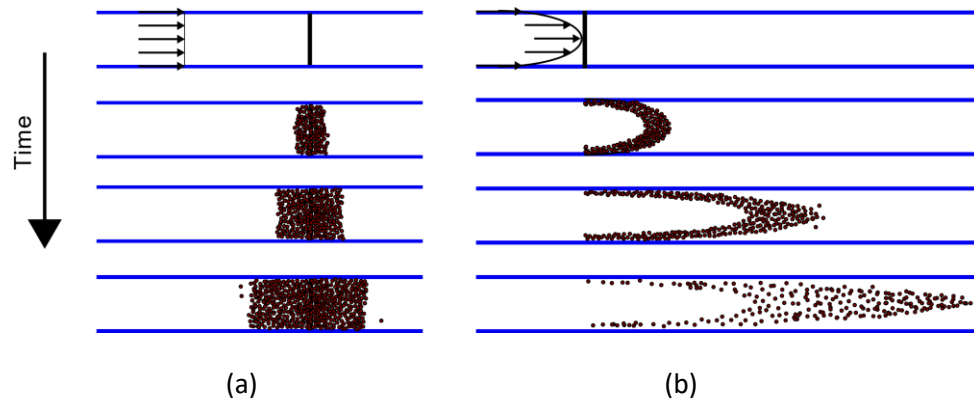


Figure B.1: Particle distribution in a microchannel. (a) Particle distribution with a uniform velocity profile and (b) particle distribution with a parabolic velocity profile. Adapted from [216].

The fabrication procedure for DEA micromixer leads to only rectangular cross section microchannels. Considering a 2-D system, the dispersion coefficient D^* in a Poiseuille flow between two parallel plates is defined as:

$$D^* = D + \frac{2h^2\bar{u}^2}{105D} \quad \text{Eq B.5}$$

where h is half of the height of the channel and \bar{u} is the mean velocity obtained from Table A.1, considering the symmetry conditions, the wall shape and the initial condition. Figure B.2 shows the geometry of a rectangular cross section channel for the determination of Taylor dispersion in Poiseuille flow between parallel plates.

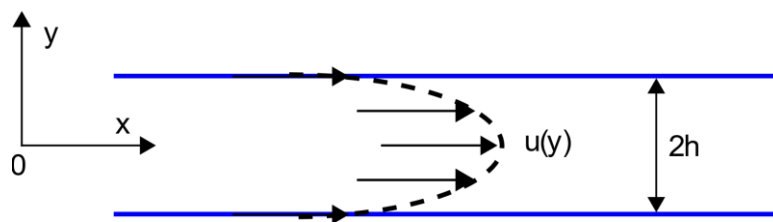


Figure B.2: Layout of a rectangular cross section channel with a parabolic velocity profile.

In order to take into account a three dimensional case, Dutta et al. [217] added a dispersion factor, named f , to extrapolate the 2-D case of Taylor Dispersion to a 3-D case. The equation is as follows:

$$D^* = D + \frac{d^2\bar{u}^2 f}{210D} \quad \text{Eq B.6}$$

with $d = 2h$ and $f = 1$, the previous case of Poiseuille flow between two parallel plates is obtained. The factor f is directly related to the aspect ratio d/W of the channel, being d the height of the channel and W its width.

Chaotic advection

Chaotic advection [218] is a phenomenon that not only takes part in turbulent regime but also in a laminar regime. It occurs when a simple Eulerian velocity field leads to a chaotic response in the distribution of a Lagrangian marker. Chaotic advection can be formed in two ways: a simple 2-D flow with time-dependent disturbance or a 3-D flow even without time-dependent disturbance.

In the case of non-disturbance, the velocity components at a point in space are constant over time. The condition of chaos takes place because the particles crash onto each other. For chaos advection, the particles are big enough not to be considered in a molecular diffusion state, but neither big enough to disturb the fluid flow. Here, it is considered that the particles move passively with the flow.

The transport mechanism is characterized by the following equations:

$$\begin{cases} dx/dt = u(x, y, z, t) \\ dy/dt = v(x, y, z, t) \\ dz/dt = w(x, y, z, t) \end{cases} \quad \text{Eq B.7}$$

The above equations can be solved and it is then possible to describe the motion of the fluid in a region, such as a microchannel. In general, with methods like fluorescence it is also possible to determine the trajectory of the particle in the fluid.

C. APPENDIX - LIQUID FILM FABRICATION METHOD

Here, a detailed description of the liquid film method for the fabrication of peristaltic micropumps out of dielectric elastomer actuators is presented.

A. Elastomer membrane fabrication

The elastomer membrane is made of Sylgard® 186 from Dow Chemical®. Sylgard® 186 is based on two components, A and B, and the mixing ratio used is 10:1, respectively. The two components and a solvent are mixed in a planetary mixer (Thinky mixer) to get a homogeneous solution.

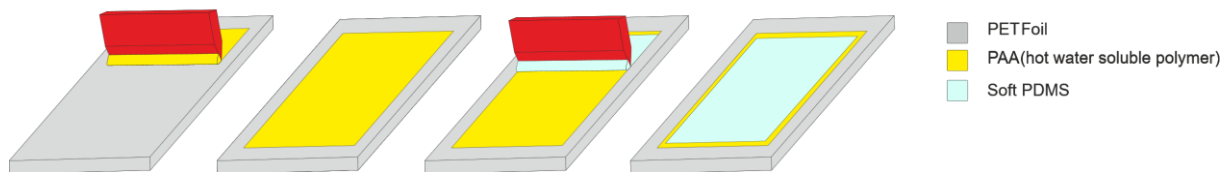


Figure C.1: Automatic casting procedure for fabricating PDMS membranes.

The thin membrane is fabricated by casting with a ZAA 2300 Automatic Film Applicator. Firstly, a High-Quality PET (polyethylene terephthalate) foil (Melinex, Dupont) of 125 μm with a DIN-A4 shape is placed on the applicator as a substrate. Then, a water-soluble solution of PAA (polyacrylic acid) as a sacrificial layer (4g PAA: 32g IPA PAA 5 %) is cast on top of the substrate with a speed of 25 mm/s with the film gap applicator. The PDMS solution is cast with a variable gap applicator, ZAA 2000.200 at a 1 mm/s speed. Figure C.1 shows the gap applicator layers fabrication.

The set of film on the substrate is located over a glass plate. After solvent evaporation, the set is introduced in the oven for 1 hour at 80°C. The thickness of the membrane is measured with a visible spectrometer, to compare it with the expected value. The initial thickness of the membranes is $95 \pm 2 \mu\text{m}$.

B. Membrane prestretching

As it has already been proven by different authors [130] [131], prestretching elastomer membranes greatly improves the dielectric breakdown strength of the material and also increases the final product performance.

The membrane is laser cut and released from the substrate and located on top of a bidirectional prestretcher. The membrane is prestretched following the numbers established in the analytical modelling. The prestretching is done bidirectionally in the directions 1 and 2, with magnitudes of 0.9 and 2.2, respectively.

A double frame of polymethyl methacrylate (PMMA) 3 mm thick, with an adapted shape for the pad printing system is attached with a double-sided tape to the membrane to hold the prestretch. The frames are located on top of the membrane and on the bottom.

After prestretching, the elastomer thickness is again measured with a transmission interferometer. The measurements show that the membrane is $47 \pm 2 \mu\text{m}$ thick. This thickness measurement is essential for all the films in order to avoid electrical breakdown, in case the

membrane is thinner than expected. The dielectric breakdown for Sylgard® 186 is 100 V/ μm . This leads to a maximal applied voltage of 4700 V for a 47 μm thick membrane.

C. Electrode deposition

The electrode material is based on a mixed of carbon black, silicone elastomer and isooctane. After the mixing, the solution is kept in a cool environment to avoid the crosslinking of the silicone material before its usage.

The fabrication of a mask for the pad printing of the desired design is done by laser cutting and engraving a PMMA foil (0.5 mm thick).

First, the mask is aligned to the membrane. Then, the top electrodes are pad printed. To speed up the cross-linking process, the device is heated 1 hour at 80°C. The same procedure follows for the bottom electrodes.

The thickness of the electrode with this method is approximately 3 μm . Due to the symmetry of the device, the same mask is employed for both top and bottom electrodes.

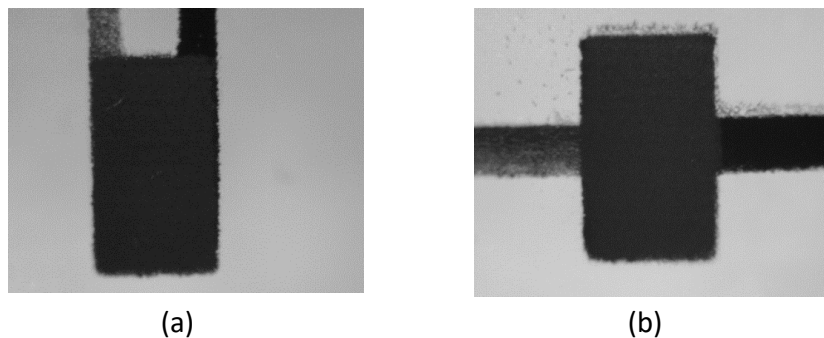


Figure C.2: Photos of the electrodes after pad printing. (a) Bottom actuator of the device. (b) Middle actuator.

Figure C. shows the appearance of the electrodes after the pad printing process. In the figure, the electrodes on the top and on the bottom are shown for the bottom and the middle actuators. Darker electrodes correspond to top electrode and the light black/grey electrodes to the lower electrodes.

After depositing the electrodes, RTV (room temperature vulcanizing) silicone is used between the PMMA frame and the membrane holder to avoid detachment of the prestretched membrane. PMMA frames (3 mm thickness) are stuck on top and bottom of the membrane to enhance the electrical connection and to have a defined passive region.

D. Electrical connections

The electrical connections are made by using a double-sided conductive carbon nanotube-silicone tape. At the end of the electrode, the tape is attached to its edge. The tape has a rectangular shape of 3 mm x 5 mm. On top of this double-sided tape, an aluminium strip is also attached and crocodile clips connect the aluminium strips to the voltage power supply.

E. Channel fabrication

The requirements for the channel fabrication process in this thesis are: a simple method which does not require clean room facilities, reproducibility and easy implementation. The fabrication process chosen for the channel rests on the lamination method [219]. The lamination method is based on stacking up of cut layers by bonding. The easiest fabrication method consists in three layers: a top layer, a flow layer or channel wall and a bottom layer. The process focuses on three steps: material selection, cutting the different layers in the desired shape and bonding the layers together.

There is a considerable amount of materials used in lamination, in general researchers use optically clear plastics and thermoplastics for this purpose. The most used materials, though, are adhesive transfer tapes, polymer layers (polycarbonate, PMMA) and glass. These polymer layers share a number of key features like optical clarity, low cost, and sample compatibility. For our particular application, apart from the above-mentioned properties, flexibility and low Young's modulus are necessary. The purpose of this microfluidic channel is the deformation due to the actuator displacement at the bottom of the channel. The material proposed for this case is also a PDMS but with a much lower Young's modulus than that of the elastomer layer of Sylgard® 186, MED4086 from NuSil® [124].

Here, the lamination process is based in: 1) PDMS as material, 2) Laser cutter for defining the pattern and 3) Plasma O₂ for bonding the layers.

The layers of the materials are fabricated out of PDMS, MED 4086. The properties of the material are summarized in Table C.1. The layers are deposited by using a cast film applicator at a determined height. Only rectangular channels are possible with this fabrication method.

Table C.1: Properties of the soft-PDMS used for the channels: MED4086 [124].

Property	Value
Viscosity	6.450 MPa·s
Tensile	0.28 MPa
Stress@Strain	0.06 MPa/200 %
Elongation	475 %
Curing Time	45 min/150°C
Mix ratio	1:1

Three different layers of PDMS are fabricated by casting with a film applicator; the casting procedure is shown in Figure C.3. The first layer or bottom layer (named A) is fabricated with a PET foil (A4 size) as substrate. On top of it, a PAA layer (approximately 1 µm thick) as a water-soluble polymer and a MED4086 layer (50 µm) are cast, respectively. A list of polymers and polymers solvents can be found with more details in the Polymer Handbook [220]. The second layer or channel wall (named B) is also fabricated with PET foil as substrate. On top of it, a layer (approximately 1 µm thick) of Polyvinil alcohol (PVA), from a 5 % solution and a MED4086 PDMS layer (of 500 µm) are cast, respectively. The height of a channel is then defined by the thickness of the material that is used to form the channel layer. Finally, the third layer (named C) is fabricated. Layer C is fabricated with PET foil as substrate, on top of it a PVA layer is cast (approximately 1 µm thick) and on top of it a PDMS layer out of MED4086 is cast to again 50 µm thick. After fabrication, all layers are placed in the oven for 1 hour at 150°C to crosslink the PDMS.

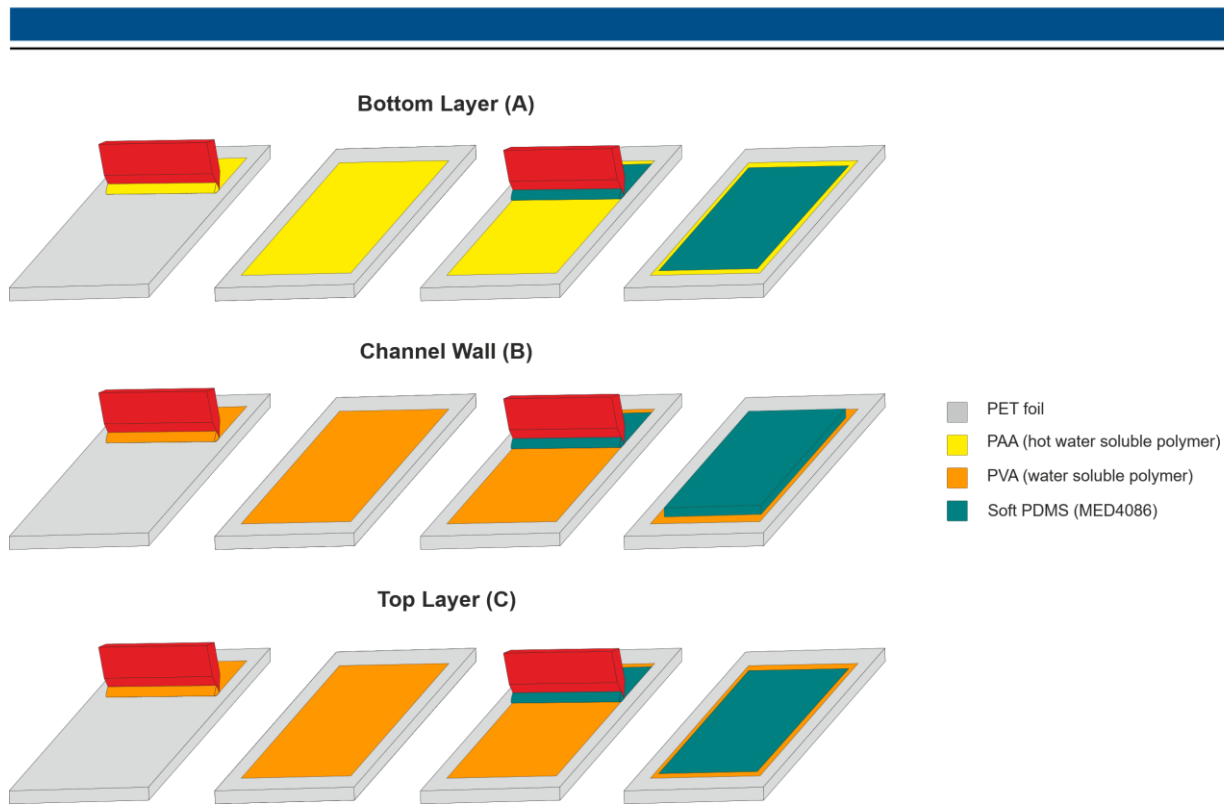


Figure C.3: Process for the fabrication of a completely soft channel

Layer A corresponds to the bottom layer of the channel, layer B to the walls of the channel and layer C to the top layer. The structure of the channel is shown in Figure 2.8, section 2.3.3, consisting of a PDMS layer of 50 μm at the bottom, a wall-channel of 500 μm and a PDMS layer of 50 μm at the top.

After casting and curing the PDMS, the layers are cut with a CO₂ laser cutter with the shapes shown in Figure C.4. Prior to cutting the layers, a protective layer of PET is located on top of the PDMS to prevent the accumulation of dust over the PDMS.

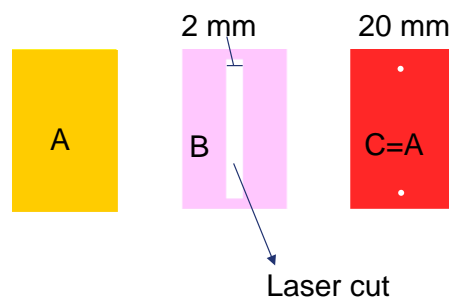


Figure C.4: Layers A (bottom), B (channel) and C (top) after being laser cut from the original A4 size sheet.

Layers A, B and C are 20 mm wide and 60 mm long. Layer B is also cut in the middle with a form of a rectangle 2 mm x 50 mm (channel geometry). Layer C has two holes of 1 mm diameter to favour the tubing connection of the microfluidics.

After cutting the rectangles, Layers A and B are plasma bonded with O₂ Plasma for 30 seconds, 50 % power or 100 W. The bonded layers are introduced in the oven at 80 °C for 30 minutes in order to increase the bonding strength. After 1 hour at room temperature, the layer A-B is

introduced in cold water for 20 minutes. Layer A is fabricated with PAA, a polymer soluble in hot water (fast), and layer B is made out of PVA, a polymer soluble in cold and hot water. The PET of layer B is easily detached and the remaining A-B layers is made, from bottom to top, of: PET foil, PVA layer (1 μm approximately), 50 μm PDMS layer and 500 μm PDMS layer (with a rectangular cavity in the middle).

After drying the A-B layers, they are bonded to the layer C. Plasma O_2 treatment is applied, also 30 seconds 75 % power or 150 W and then the resulting stacked layers introduce in the oven, at 80°C for 30 minutes. Using the same principle as in the previous step, the A-B layers are bonded to layer C.

The remaining layers after introducing layer A-B-C in cold water are: PET foil, PVA layer (1 μm approximately), 50 μm PDMS layer and 500 μm PDMS layer (with a rectangle cavity in the middle) and 50 μm PDMS layer. After this, a soft channel with a top, wall and bottom layer is produced.

Some of the advantages of this technique are the relatively inexpensive materials and instruments, simple process steps, rapid fabrication times, well-controlled layer depths (set by material thickness), optical access, and submillimetre feature sizes. With the possible exception of 3D printing, lamination is the fastest and easiest method to fabricate microfluidic channels for most applications.

F. Fluidic connection

The connection of the channel with the tubing is made using RTV double-sided tape, with a 3 mm thick PMMA connector of 6 mm x 6 mm. On top of this, a thin layer of acrylic glue prevents the leaking of the fluid. The tube, a low-density polyethylene polymer (LDPE) 0.5 mm inner diameter, 1 mm outer diameter and 5 cm length from RCT Reichelt Chemietechnik GmbH, is biologically compatible. Figure C.5 shows a layout of the connection system.

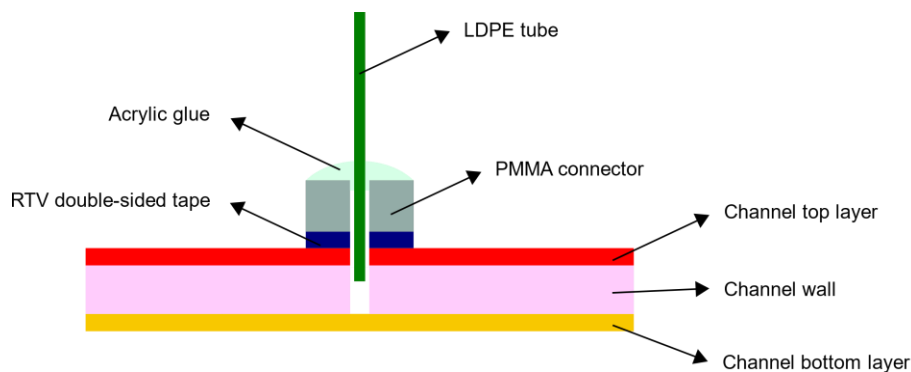


Figure C.5: Layout of the tubing connection with the channel



LIST OF FIGURES

Figure 1.1: Dielectric elastomer actuators working principle: in light blue, the elastic dielectric material and, in grey, compliant electrodes. In the left layout, the actuator is at zero voltage. The geometry of the actuator is defined by an initial area A_0 and an initial thickness of z_0 . The right layout represents the actuator when a voltage V is applied between the electrodes. The initial area A_0 expands, ending up in $A_0 + \Delta A$, while the final thickness is $z_0 - \Delta z$	8
Figure 1.2: (a) Elements needed to fabricate a single layer EAP: two rigid holding frames (normally made of PMMA); two rings of a double-sided tape, the top electrode, followed by the elastomer layer and the bottom electrode. (b) Assembled elements to form a single layer EAP. The bottom electrode is not visible in the layout.	9
Figure 1.3: Relation between force and strain for elastomers. Region a follows a linear behaviour, the Hooke's law for springs (the material in this region can be considered "hard"). In region b, the material gets softer and a plateau region is observed. In region c, no model is able to determine the relation between force and strain [24].	11
Figure 1.4: (a) Undeformed cube. (b) Deformation of the cube under external forces Fa	13
Figure 2.1: (a) Layout of a piezoelectric diaphragm pump (adapted from [104]). (b) Schematic view of a thermo-pneumatic micropump (adapted from [100]).	30
Figure 2.2: (a) Rotatory pump. (b) Valveless rectification pump.	30
Figure 2.3: Layout of the peristalsis in the human body (based on [110]).	33
Figure 2.4: Geometry of the proposed peristaltic pump. (a) Top view and (b) cross-section of the device.	34
Figure 2.5: (a) Top view of the device with the hollow channel on top of the actuators. (b) Cross-section of the full device.	35
Figure 2.6: Actuation stretch obtained for different bidirectional prestretches from 0 to 4.5 for direction 1 and from 1 to 4.5 for direction 2. The actuation stretch obtained is in the range between 1 and 1.269 (right bar).	38
Figure 2.7: (a) Photo of the preliminary device. (b) Preliminary device with the PMMA frames on top and bottom to obtain the exact active ratio.	40
Figure 2.8: Cross-section of the channel geometry: consisting of a layer of $50 \mu\text{m}$ at the bottom, a channel wall of $500 \mu\text{m}$ and a layer of $50 \mu\text{m}$ at the top.	41
Figure 2.9: Measurement setup for characterizing the displacement of the actuators.	42
Figure 2.10: Actuation stretch versus voltage in the direction 1 of actuation or desired direction. Rectangles correspond to measurement points, while dotted lines are only a visual guidance. On the top left of the graph, a photo of the device with red arrows along direction 1 is shown.	42
Figure 2.11: Actuation stretch versus voltage in the direction 2 of actuation. Rectangles are measurement points, while dashed lines are only a visual guidance. On the top left of the graph, a photo of the device with red arrows along direction 2 is shown.	43
Figure 2.12: Characterization of the deformation of the actuator with active ratio 0.12 (frame, F) and active ratio 0.05 (no frame, NF). Dotted lines are only a visual guidance. On the top left of the graph, a layout of the device with frame is shown. The middle or measured actuator is highlighted in green.	44
Figure 2.13: Layouts of the points taken for the measurement of interaction between actuators.	45

Figure 2.14: Deformation in the desired direction induced by the first actuator of the remaining actuators. Dotted lines are only a visual guidance.....	45
Figure 2.15: Deformation in the desired actuation direction of a thinner membrane (40 μm). Dotted lines are only a visual guidance. A picture of the bottom actuator with a deformation of 24 % and its loss of tension is shown (top left).	46
Figure 2.16: Series of ramps of the upper actuator of a 40 μm thick membrane device submitted to an electric field. Stretch obtained after four ramps in an actuator.	47
Figure 2.17: Characterization of the displacement of the actuation with channel (C, triangles) and without channel (NC, rectangles). Dotted lines are only a visual guidance.	47
Figure 2.18: Configuration for the peristaltic pump at 1 Hz frequency, 0.5 duty cycle and 1/3 phase shift.....	48
Figure 2.19: Actuator after detaching the channel. A part of the top electrode is also detached with the channel.....	48
Figure 2.20: The deformation of the actuator with the channel (C, only top layer and wall) is reduced between 0.1 % and 1 % of the maximal deformation obtained without the channel (NC).	49
Figure 2.21: Video frames where the actuators are driven at 4500 V with 1 Hz frequency and 1/3 phase shift. Blue lines point out the difference of the meniscus from one frame to the next one. The time difference between (a) and the (b) is 21.58 seconds.	50
Figure 2.22: Photos of the channel filled with DI water. (a) The meniscus of the fluid can be seen. (b) Bubbles in the fluid are shown. The displacement of the fluid towards the outlet can be observed.....	50
Figure 2.23: Single-layer peristaltic pump – type 1 solid film without the channel. (a) Photo of the device. (b) Layout of the top view and (c) of the cross-section of the device.....	52
Figure 2.24: Fabrication process of a single layer DEA. From left to right: first PDMS Elastosil E2030 membrane (1); bidirectional prestretch with a homemade device (2); attachment of a PMMA holding frame (3); and electrode deposition (4). Two possible methods for electrode deposition are shown: brushing the electrodes (A) and spraying the electrodes (B).	53
Figure 2.25: Relation between the deformation of a prestretched membrane and the electric field for two different electrode deposition methods: sample brushing (in red) and sample spraying (in blue) electrodes.	54
Figure 2.26: Photographs of the actuator. (a) Actuator at zero voltage. (b) Deformation of the actuator at applied voltage of 2600 V or 174 V/ μm . (c) Actuator at zero voltage after a previous actuation.	55
Figure 2.27: Three photographs of the actuator at (a) 0 V, (b) 2400 V and (c) 2750 V.....	55
Figure 2.28: Relation between the deformation of a prestretched membrane and the electric field with two different prestretches: prestretched 1, in blue (0.9 x 2.2) and prestretched type 2, in red (1.2 x 2.7). Measurements are taken until samples suffer from an electrical breakdown.	57
Figure 2.29: (a) Top view of the single-layer peristaltic pump – type 2 solid film with the channel on top of the elastomer layer. (b) Cross section of the device.	58
Figure 2.30: Active ratio versus prestretch in the direction 1 for the prototype 2. Prestretch in the direction 2 is constant, with a value of 2.7. The active ratio, defined as the ratio between the width of the actuator and the total width of the device, is represented from 0 to 1 against the prestretch in direction 1, from 0 to 1.8. The stretch after actuation obtained is displayed with a colour code. The colour bar gets from 1 to 1.31, or from blue to yellow.	59

Figure 2.31: (a) Photo of a prototype for the peristaltic pump 3. The prototype has three actuators in series located in parallel to other three actuators in series with an active ratio of 0.3. (b) Layout of the prototype with its legend.	61
Figure 2.32: Deformation versus electric field for the middle actuator at the left when it is the only actuator working (in purple), left actuator when two actuators at the same time are actuating (red squares), and right actuator when two actuators are acting at the same time (red triangles).....	62
Figure 2.33: Deformation versus electric field for the two actuators in the middle with and without the channel on top of the elastomeric membrane in blue and red, respectively.	63
Figure 2.34: Deformation of the channel of 1 mm width and 55 mm length.	63
Figure 2.35: Image of the channel on top of the membrane. (a) Actuators at 0 V/ μm . (b) Channel when the actuators are subjected to an electric field of 152 V/ μm	64
Figure 2.36: Configuration of one channel with multiple inlets and outlets to introduce one or several fluids and allowing different deforming conditions.	68
Figure 3.1: (a) Channel with a nozzle structure. (b) Channel with obstacles or passive elements.	72
Figure 3.2: Passive micromixers; (a) Y-form, (b) T-form and (c) interdigitated parallel lamination.....	73
Figure 3.3: Concentration distribution profiles in a T-type passive micromixer: (a) without an obstacle and (b) with a diamond shape passive element. Adapted and modified from [146].....	75
Figure 3.4: Mixing efficiency at 10.4 mm channel length (outlet) at different Re values. Adapted and modified from [146].	76
Figure 3.5: Cross sections of the mixing channel at Reynolds = 150 (vortex regime), at various lengths (a) 0.5 mm, (b) 5 mm and (c) 10 mm and at Reynolds= 250 (engulfment regime), at (d) 0.5 mm, (e) 5 mm and (f) 10 mm Adapted and modified from [149].	77
Figure 3.6: (a) Concept of an active micromixer based on pressure-driven disturbance. The fluids are delivered by integrated micropumps. Thermopneumatic actuators [155] drive the pump and generate the pressure disturbance. (b) Sketch of an active micromixer based on pressure-driven disturbance. The fluids are delivered by hybrid-integrated piezoelectric micropumps [156].	78
Figure 3.7: (a) Schematic illustration of a pumping micromixer composed of a Y-shaped microchannel, four PDMS membranes and two pneumatic microvalves [159]. (b) Schematic diagram of a pumping micromixer including two asymmetrical obstacles and one mixing region with triangular-wave structures.	80
Figure 3.8: (a) Top view of the micromixer with two pumping chambers (green boxes) and one mixing chamber (red box), each consisting of 4 actuated regions. (b) Working principle of the micromixer: cross sectional views of the micromixer when all the actuators are off (left) and when the voltage in some actuators is applied (right), where a change in the fluid channel height is observed.....	81
Figure 4.1: Dielectric stacked actuator working principle: in blue, the elastic dielectric material and, in grey, the compliant electrodes. After applying voltage to the stacked actuator (a), an area deformation of the dielectric occurs and thus, thanks to the conservation of volume, a decrease in thickness of the dielectric takes place (b).....	88
Figure 4.2: First step of the fabrication of DESA at Technische Universität Darmstadt, the spin coating process. The PDMS, in two syringes each with a component of it, namely A and B, is unified by a PET mixer. The resulting mixture is deposited on top of a spin-coater disc which rotates to provide the desired thickness. Adapted and modified from [163].	90
Figure 4.3: Elastomer crosslinking step. The disc arrives to a new stage, the heating area. The heating device descends and covers the spin coater disc surface. While the disc slowly rotates, the heater crosslinks the elastomer. Adapted and modified from [163].	90

Figure 4.4: Third step in the fabrication of DESA: spraying the electrodes. The spin coater disc is located in the new stage position. A mask holder supports two different masks, named Mask 1 and Mask 2. The desired mask is located on top of the elastomer layer. To do so, the desired mask moves first in the y-axis to the right position, vertically aligned to the spin coater disc. Then the mask moves down in the z-axis towards the elastomer layer in the spin coater disc until there is no gap between the dielectric layer and the mask. A tank holds the electrode suspension. The electrode suspension flows to the spray unit or nozzle by the action of a pump. The electrode solution enters the nozzle. While the nozzle head is moving in the y-direction, the electrode solution gets spread out of the nozzle and deposits on the elastomer layer with the mask shape. Adapted and modified from [163].	91
Figure 4.5: Resistance measuring station for the determination of the film resistance (SD510, NAGY measuring systems). Adapted and modified from [163].	92
Figure 4.6: Automatic fabrication process of dielectric stacked actuators. The three steps for fabricating EAP in TU-Darmstadt, from left to right: dielectric deposition, elastomer crosslinking/heating step and electrode deposition. On the top left of the figure, a layout with the axis helps understanding the movements of the stages. Adapted and modified from [163].	93
Figure 4.7: Shadow masks needed for the fabrication of a pumping micromixer: (a) and (b) masks for the electrodes and (c) mask for the channel fabrication.	93
Figure 4.8: Fabrication process after spraying 40 µm graphite suspension on top of the protective elastomer layer of the micromixer to form a microfluidic channel.	94
Figure 4.9: (a) A photograph of a finished fabricated micromixer, and (b) the same photo, modified with grey rectangles to clarify where the actuators are. The different chambers are indicated (pumping chambers in green, mixing chamber in red). Both inlets and the outlet with the mixed fluid can be observed.	94
Figure 4.10: (a) A layout of the electrical connection of the voltage electrodes of the micromixer. (b) A photograph of the fabricated microfluidic device with tubes and electrical interconnections. White stroke rectangles show the ground connection driven by a black wire. Red stroke rectangles, the driving voltage connections with coloured wires.	95
Figure 4.11: Set up for controlling the actuation of the micromixer.	96
Figure 4.12: Images of the cross section of a pumping micromixer. (a) A magnified image of a couple of layers of elastomer separated by graphite layers. (b) Half of a micromixer under the microscope (Keyence VHX-600).	97
Figure 4.13: Sketch of the connection cross section of a pumping micromixer (left) and cross section of the pumping micromixer in the connection zone (right).	98
Figure 4.14: Layout of the deformation measurement set up.	99
Figure 4.15: Deformation vs voltage for rectangular input signals. The x-axis represents the voltage applied to the stacked actuator, while the y-axis represents the deformation of the stack. The y-axis on the left refers to the displacement of the actuator in height and the y-axis on the right relates to the relative deformation. The error bars correspond to the standard deviation of the observed deformation.	100
Figure 4.16: Deformation vs voltage for sinusoidal input signals. The x-axis represents the voltage applied to the stacked actuator, while the y-axis represents the deformation of the stack. The y-axis on the left refers to the displacement of the actuator in height and the y-axis on the right relates to the relative deformation. The error bars correspond to the standard deviation of the observed deformation.	100

Figure 4.17: Summary of all the applied signals at different frequencies to compare the deformation. For the sake of simplicity, only the fitting lines are shown, with the same colours as previously. The DC fitting line is also shown.	101
Figure 4.18: Numerical designation of the actuators in the pumping micromixer.	102
Figure 4.19: (a) Stacked actuators performing a 1:1 configuration or single driving stacked actuators and (b) stacked actuators performing a 2:2 configuration or 2 stacked actuators actuated at a time. Each colour represents a propagating wave.	103
Figure 4.20: Block diagram of the full measurement set up. Both electrical and fluidic connections are represented in the sketch.	104
Figure 4.21: Flow rate at the outlet of the micromixer for different frequencies and actuation configurations at 1500 V with a rectangular signal. The error bars correspond to the standard deviation.	104
Figure 4.22: Micromixer used with different colorants, blue and red, for the inlets. The observed output is dark-purple.	107
Figure 4.23: The RGB colour model mapped to a cube. The origin, black, is the hidden vertex [179].	107
Figure 4.24: Micromixer picture of the mixing: 40 pixels, indicated with blue crosses, were analysed per tube.	108
Figure 4.25: The histogram represents the direct value obtained from the pixel selection in MATLAB. The bars represent the variance of the values.	108
Figure 4.26: The plot represents the theoretical values obtained from the mixture of the blue and red colorants. Crosses represent the values in the RGB scale at the outlet obtained by a pixel analysis in MATLAB.	109
Figure 4.27: Modified photo of the micromixer. In rectangles, the colours of the mean value of the tubes obtained after the analysis of 40 pixels in each one with MATLAB. The purple circle represents the theoretical value obtained from the 50 % blue inlet (from the mean value) and 50 % red inlet (from the mean value).	109
Figure 4.28: (a) Profile view of the Y-type pumping micromixer previously fabricated with an initial channel thickness of 40 μm . (b) Y-type pumping micromixer encapsulated by two rigid PMMA layers on top and bottom of the device.	113
Figure 4.29: (a) A schematic of the rigid PMMA frame fabricated to avoid free deformation of the actuators. (b) A pumping micromixer with the rigid part on top and on bottom. (c) A profile photo of the encapsulated micromixer.	113
Figure 4.30: (a) Sketch of a proposed active pumping micromixer with a T-type shape. The active mixer is based on the dielectric elastomer stacked actuators. (b) Photo of a fabricated T-type pumping micromixer device.	114
Figure 4.31: (a) Sketch of the already fabricated system as a tactile display by Matysek and (b) a photo of the device where more details can be observed [181]. For a better understanding of the sketch, ground electrodes, in dark grey, and driving electrodes, in light grey, have been differently coloured. The surfaces, where ground electrodes and driving electrodes converge, are coloured in black and correspond to the actuator area.	116
Figure 4.32: Diverse possibilities offered by an array of four inlets and one or two outlets. Ground electrodes (in dark grey) and driving electrodes (in light grey) have been differently coloured. The areas, where ground electrodes and driving electrodes converge, are coloured in black and correspond to the actuator area.	117
Figure 5.1: Simulation geometry. On the left, a sketch of the fabricated pumping micromixer consisting of 12 stacked actuators of 30 single-layers, each with a thickness of 50 μm . On the right, the simulated geometry in COMSOL Multiphysics®. The device consists of 12 single-layer actuators with a thickness of 750 μm	121

Figure 5.2: Displacement in x , y and z direction of half a pumping micromixer using both the solid mechanics and the electrostatic module in COMSOL Multiphysics®. (a) Corresponds to the displacement field in the x -axis, (b) to the y -axis and (c) to the z -axis. The colour bar, from blue to red, shows the displacement field in μm of the actuators according to the axis they represent.	123
Figure 5.3: (a) Representation of the geometry. (b) Step function for the calculation of displacement of the actuator.	128
Figure 5.4: A zoomed-in view of the mesh resulting from the physics-induced meshing sequence for the peristaltic model: channel on the left (within blue edges) and wall on the right. Three different mesh systems are considered in this simulation. For the inside channel, a free triangular mesh with a fine refinement has been used. Secondly, a boundary layer which connects both interfaces, solid mechanics and laminar flow. This section is composed of free triangular and mapped layers, also in fine mesh refinement. Finally, a free triangular mesh covers the surface of the walls with a fine refinement, which increases the triangular geometries from the channel until the outer part of the actuators.	130
Figure 5.5: (a) Simulated flow rate versus duty cycle at constant frequencies for 2 Hz in blue and 20/3 Hz or 6.67 Hz in red. Duty cycle varies from 0.25 until 2/3. The phase shift was determined as half the actuation time of the previous actuator or 90°. A parabolic behaviour is observed. (b) Expected behaviour of the dependency of the flow rate and duty cycle at different frequencies.	132
Figure 5.6: (a) Configuration 0 for very low duty cycle (1/8) and (b) configuration 0 for a very high duty cycle (7/8).	133
Figure 5.7: (a) Configuration 1 with a duty cycle of 0.5 and a phase shift of 45°. (b) Configuration 2 with a duty cycle of 2/3 and a phase shift of 45°. (c) Configuration 3 with a duty cycle of 0.75 and a phase shift of 90°.	135
Figure 5.8: Inlet and outlet flow in m^3/s as functions of time. Volumetric flow rate at the inlet of the channel (in blue) and at the outlet (in green) for the configuration 1, at 1 Hz, 0.5 duty cycle and a phase shift of 45°. Positive values indicate that the fluid is flowing into the inlet and out of the outlet.	136
Figure 5.9: Representative volumetric flow rates for the configuration 1 (0.5 duty cycle, phase shift 45°) at 1 Hz. In blue, the accumulated flow defined as the mean value between the inlet and outlet flow. In green, the volume conveyed or, in other words, the accumulated outlet volume.	137
Figure 5.10: Plot of the flow rate Q_1 versus the actuation frequency f . For a better view of the lower frequencies values, x -axis is plotted in a logarithm scale. Results correspond to the configuration 1 with 0.5 duty cycle and a phase shift of 45°.	137
Figure 5.11: Values of volumetric flow rate at different frequencies for the configuration 2 or with 2/3 duty cycle and a phase shift of 120°. The red line corresponds to the fitting of the simulated points. For a better visualization of the lower frequencies values, the x -axis is plotted in a logarithm scale.	138
Figure 5.12: Values of volumetric flow rate at different frequencies for the configuration 3 or with 3/4 duty cycle and a phase shift of 90°. The green line corresponds to the fitting of the simulated points. For a better visualization of the lower frequencies values, the x -axis is plotted in a logarithm scale.	139
Figure 5.13: Flow rate versus frequency for the three simulated configurations and for the experimental configurations 1:1 and 2:2. Frequency range: (a) From 1 Hz to 200 Hz and (b) from 1 Hz to 30 Hz (for a better visualization of the lower frequencies).	140
Figure 5.14: COMSOL Multiphysics® simulation of the change of pressure with time at the inlet (in blue) and at the outlet (in green) of the peristaltic pump. Configuration 1 at 1 Hz is here shown as an example. A zero pressure value here corresponds to atmospheric pressure.	142

Figure B.1: Particle distribution in a microchannel. (a) Particle distribution with a uniform velocity profile and (b) particle distribution with a parabolic velocity profile. Adapted from [201].	179
Figure B.2: Sketch of a rectangular cross section channel with a parabolic velocity profile.	179
Figure C.1: Automatic casting procedure for fabricating PDMS membranes.	181
Figure C.2: Photos of the electrodes after pad printing. (a) Bottom actuator of the device. (b) Middle actuator.	182
Figure C.3: Process for the fabrication of a completely soft channel	184
Figure C.4: Layers A (bottom), B (channel) and C (top) after being laser cut from the original A4 size sheet.	184
Figure C.5: Layout of the tubing connection with the channel	185

LIST OF TABLES

Table 1.1: Requirements for the dielectric material in terms of material properties, actuator performance and market requirements: high (H) or low (L).....	9
Table 1.2: Parameters of different materials used as dielectric in EAP systems	10
Table 1.3: Comparison of the properties of EAP with other technologies like SMA, EAC and EM (adapted from [46]).	20
Table 2.1: Fluid rate for various fluids in laminar ($Re = 1$, $Re = 1000$), transient ($Re = 3000$) and turbulent ($Re = 4000$) regimes.....	27
Table 2.2. Fixed parameters for the optimization.....	36
Table 2.3: Calculated Reynolds number for 1 Hz actuation and diverse fluids.....	39
Table 2.4: Characteristics of Elastosil® E2030 for DEA fabrication [119].....	51
Table 2.5: Main properties of the graphite used for the electrodes.....	52
Table 2.6: Different prestretch for the elastomer made out of Elastosil® E2030.....	56
Table 2.7: Geometry details about the actuator design	61
Table 3.1: Parameters used for the COMSOL Multiphysics® simulation [146].....	74
Table 3.2: Summary of the geometry of the system.....	82
Table 3.3: Properties of the dielectric and electrode material	84
Table 4.1: Summary of the degrees of freedom of the different elements of the automatic machine for the fabrication of DESA.	92
Table 4.2: Summary of the values of capacity for the actuators.	98
Table 4.3: Geometry and volume difference between on and off states for the pumping actuators at various frequencies.	105
Table 4.4: Pumping micromixer main results obtained.	111
Table 4.5: Geometric dimensions for the proposed T-type pumping micromixer.....	115
Table 5.1: Parameters used in the electrostatic module.	122
Table 5.2: Parameters used in the solid mechanics module for hyperelastic model of Mooney Rivlin 5 parameters.....	123
Table 5.3: Simplified model from rectangular cross-section channel (real) to circular cross-section channel (simulated).....	126
Table 5.4: Mesh refinement test. Coarse, normal and fine mesh refinements are investigated.	131
Table 5.5: Comparison between Experimental 1:1 and simulation results for configuration 0 in terms of flow rate.....	134
Table 5.6: Summary of the three simulated configurations	134
Table 5.7: Summary of the main results obtained in simulations in terms of flow rate for each configuration. Frequencies of 1,2,10 and 200 Hz have been chosen.....	141
Table A.1: Velocity field inside a straight channel.	175
Table C.1: Properties of the soft-PDMS used for the channels: MED4086 [116].....	183